



UNIVERSITAT DE
BARCELONA

Nanocrystals boost electrochemical oxidation of biomass-derived compounds

Guillem Montaña Mora

ADVERTIMENT. La consulta d'aquesta tesi queda condicionada a l'acceptació de les següents condicions d'ús: La difusió d'aquesta tesi per mitjà del servei TDX (www.tdx.cat) i a través del Dipòsit Digital de la UB (diposit.ub.edu) ha estat autoritzada pels titulars dels drets de propietat intel·lectual únicament per a usos privats emmarcats en activitats d'investigació i docència. No s'autoritza la seva reproducció amb finalitats de lucre ni la seva difusió i posada a disposició des d'un lloc aliè al servei TDX ni al Dipòsit Digital de la UB. No s'autoritza la presentació del seu contingut en una finestra o marc aliè a TDX o al Dipòsit Digital de la UB (framing). Aquesta reserva de drets afecta tant al resum de presentació de la tesi com als seus continguts. En la utilització o cita de parts de la tesi és obligat indicar el nom de la persona autora.

ADVERTENCIA. La consulta de esta tesis queda condicionada a la aceptación de las siguientes condiciones de uso: La difusión de esta tesis por medio del servicio TDR (www.tdx.cat) y a través del Repositorio Digital de la UB (diposit.ub.edu) ha sido autorizada por los titulares de los derechos de propiedad intelectual únicamente para usos privados enmarcados en actividades de investigación y docencia. No se autoriza su reproducción con finalidades de lucro ni su difusión y puesta a disposición desde un sitio ajeno al servicio TDR o al Repositorio Digital de la UB. No se autoriza la presentación de su contenido en una ventana o marco ajeno a TDR o al Repositorio Digital de la UB (framing). Esta reserva de derechos afecta tanto al resumen de presentación de la tesis como a sus contenidos. En la utilización o cita de partes de la tesis es obligado indicar el nombre de la persona autora.

WARNING. On having consulted this thesis you're accepting the following use conditions: Spreading this thesis by the TDX (www.tdx.cat) service and by the UB Digital Repository (diposit.ub.edu) has been authorized by the titular of the intellectual property rights only for private uses placed in investigation and teaching activities. Reproduction with lucrative aims is not authorized nor its spreading and availability from a site foreign to the TDX service or to the UB Digital Repository. Introducing its content in a window or frame foreign to the TDX service or to the UB Digital Repository is not authorized (framing). Those rights affect to the presentation summary of the thesis as well as to its contents. In the using or citation of parts of the thesis it's obliged to indicate the name of the author.

Doctoral thesis

Nanocrystals boost electrochemical
oxidation of biomass-derived compounds

Guillem Montaña Mora



UNIVERSITAT_{DE}
BARCELONA

Nanocrystals boost electrochemical oxidation of biomass-derived compounds

Memòria presentada per optar al grau de doctor per
la Universitat de Barcelona

Programa de doctorat en Nanociències

Autor:

Guillem Montaña Mora

Directors:

Dr. Andreu Cabot i Dr. Franc Güell Vilà

Tutor:

Dr. Franc Güell Vilà

Institut de Recerca en Energia de Catalunya (IREC)



UNIVERSITAT DE
BARCELONA

CONTENTS

AKNOWLEDGEMENTS	6
LIST OF ABBREVIATIONS AND ACRONYMS	8
LIST OF PUBLICATIONS AND AUTHOR'S CONTRIBUTIONS	11
PREFACE	13
SUMMARY OF RESULTS	15
RESUMEN DE RESULTADOS	17
CHAPTER 1	19
1.1. BIOMASS-DERIVED COMPOUNDS	19
1.1.1. Methods for biomass conversion.....	21
1.2. ELECTROCHEMICAL BIOMASS CONVERSION	22
1.2.1. Electrochemical cells	23
1.2.2. Fuel cells.....	24
1.2.3. Electrochemical valorization of biomass-derived intermediates	28
1.3. BASIC ELECTROCHEMICAL REACTIONS STUDIED	30
1.3.1. Oxygen evolution reaction	30
1.3.2. Formate oxidation reaction	31
1.3.3. Glucose oxidation reaction	32
1.3.4. Oxygen reduction reaction.....	33
1.3.5. Hydrogen evolution reaction	34
1.4. ELECTROCATALYSTS	35
1.4.1. Synthetic methods	35
1.4.2. Noble metal-based catalysts	37
1.5. OBJECTIVES.....	38
1.6. REFERENCES	39
CHAPTER 2	43
2.1. ABSTRACT	43
2.2. INTRODUCTION	44
2.3. EXPERIMENTAL.....	46
2.3.1. Synthesis of colloidal CoFeP NPs.....	46
2.3.2. Ligand removal.....	46
2.3.3. Electrode preparation	46
2.3.4. Morphological, Structural and Physicochemical characterization.....	47
2.3.5. Electrochemical measurements.....	47

2.4.	RESULTS AND DISCUSSION	48
2.4.1.	Characterization of the CoFeP NPs and the fabricated CoFeP/NF electrode	48
2.4.2.	Characterization of the CoFeP-based electrodes working as anodes for OER	50
2.4.3.	Electrochemical analysis of the electrodes using CoFeP as electrocatalyst	53
2.4.4.	Anion exchange membrane water electrolysis performance.....	57
2.5.	CONCLUSIONS	58
2.6.	REFERENCES	59
	SUPPORTING INFORMATION	63
2.7.	SI RESULTS	63
2.8.	SI REFERENCES	73
CHAPTER 3	75
3.1.	ABSTRACT	75
3.2.	INTRODUCTION	76
3.3.	RESULTS AND DISCUSSION	77
3.4.	CONCLUSION	83
3.5.	REFERENCES	83
	SUPPORTING INFORMATION	90
3.6.	SI EXPERIMENTAL SECTION	90
3.7.	SI REFERENCES	97
CHAPTER 4	101
4.1.	ABSTRACT	101
4.2.	INTRODUCTION	102
4.3.	RESULTS AND DISCUSSION	104
4.3.1.	Catalyst physico-chemical properties.	104
4.3.2.	Electrocatalytic formate oxidation.....	107
4.3.3.	DFT calculations	110
4.4.	CONCLUSIONS	112
4.5.	REFERENCES	113
	SUPPORTING INFORMATION	120
4.6.	SI EXPERIMENTAL AND THEORETICAL METHODS	120
4.7.	SI RESULTS	122
4.8.	SI REFERENCES	126
CHAPTER 5	127
5.1.	ABSTRACT	127
5.2.	INTRODUCTION	128

5.3.	EXPERIMENTAL SECTION.....	131
5.3.1.	Chemicals	131
5.3.2.	Synthesis of NiSn _{0.6} , NiSn _{1.8} and Ni nanoparticles	131
5.3.3.	Synthesis of NiSn _x /CNTs	132
5.3.4.	Characterization	132
5.3.5.	Electrochemical tests	132
5.3.6.	Product analysis	133
5.3.7.	DFT analysis.....	134
5.4.	RESULTS AND DISCUSSION.....	135
5.4.1.	Catalyst preparation and characterization	135
5.4.2.	Electrochemical characterization.....	138
5.4.3.	DFT calculations	147
5.5.	CONCLUSIONS	149
5.6.	REFERENCES	150
	SUPPORTING INFORMATION	153
5.7.	SI RESULTS	153
5.8.	SI REFERENCES	162
CHAPTER 6	165
	GENERAL DISCUSSION	165
	CONCLUSIONS	169
	FUTURE WORK.....	171
	CURRICULUM VITAE	173
	COLLECTION OF PUBLICATIONS PRESENTED IN THIS THESIS.....	176

AKNOWLEDGEMENTS

Moltes vegades, per no dir la majoria, no som capaços de evaluar un camí fins que aquest no ha acabat o fins no trobar-nos en la part final d'aquest. Moltes vegades, per no dir la majoria, al llarg del camí ens obsessionem en les petites coses dolentes, en els obstacles i frustracions del dia a dia, mentre que a l'acabar el nostre cervell te la virtut de destacar principalment les coses bones que ens han passat. Aquesta podria ser la definició d'aquests anys de tesis. Si haig de ser sincer amb mi mateix, reconec que ha estat un camí molt més dur del que pensava. La ciència, sobretot en la nostra societat pot arribar a ser dura, cruel, egoista, lluny de la idealitat que un té quan fa les primeres lliçons a l'escola. Principalment, els anys de tesis consisteixen en fallar un 95 % de les teories que es tenen i aconseguir encertar un molt baix percentatge quan gairebé no et queden forces per seguir. I a aquest camí tant complicat i irregular li vull dedicar el meu primer **gràcies**. Estic agraït per tot el que he après de la ciència i de mi mateix. He après a que tot i fallar, cal seguir endavant per aconseguir els objectius. Tot aquest camí m'ha ensenyat la veritable bellesa de fer ciència i ser científic. Vull agrair la oportunitat d'haver pogut investigar i poder posar el meu granet de sorra en millorar la nostra vida i la de les generacions futures.

El segon **gràcies** va dedicat a tots els companys/es que han estat present al llarg d'aquests anys. Primer de tot, agrair a tot el grup de *Functional Nanomaterials*. Han estat moltes les persones que he pogut conèixer en el grup, persones molt diverses, de moltes cultures i de moltes formes de pensar. La convivència, ha estat a vegades complicada i intensa però, després de tot, especial. **Gràcies** al grup per fer-me créixer com a persona i investigador. En segon lloc, vull agrair a tot el centre IREC i a totes les persones que m'han donat un cop de ma, per petit que sigui, encara que no formés part directe del seu departament o grup, en especial al grup *Energy Storage, Harvesting and Catalysis* i a tots els tècnics del centre. **Gràcies** a aquelles persones, Karol, Alberto, Cristhyan, Marisa, Sebastian, Martí,... amb les que he pogut treballar més aprop i heu fet del meu dia una mica més fàcil i agradable. Vull agrair també al centre IST-Austria per deixar-me viure l'experiència (o experiències) amb vosaltres durant els mesos que vaig estar vivint allà i, sobretot, a totes les persones amb les que pogut coincidir tant minuts, hores, dies o mesos. Sergi, Mariano, Juanca, Ozzy, Jeff, Seungho,... després de cadascuna de les estades he tornat sent una persona més completa **gràcies** a vosaltres. També vull donar les **gràcies** a aquelles persones, postdocs o professors que m'han ensenyat a pensar i raonar com un científic, ja no només en el doctorat sinó al llarg de la meva carrera d'investigació. Moltes gràcies també a l'Andreu i la Maria per fer possible aquesta etapa de la meva vida. Per últim, vull donar les **gràcies** especialment a en Jesús. Ets una persona increïble i sóc concient que sense per la teva

col·laboració altruista, el teu temps, els nostres cafès, els teus concells i les nostres xerrades, no hagués estat possible arribar fins al final. De veritat **gràcies**.

El meu tercer **GRÀCIES** va per totes les persones que han estat al meu costat animant-me i estimant-me. **Gràcies** a tots els amics que han sapigut treure'm un somriure quan he estat desanimat, i que han sapigut fer-me desconnectar per poder tornar amb més força el dia següent.

GRÀCIES a tota la meva increïble i no perfecta família. Als meus avis/es, **gràcies** a tots quatre pel vostre amor incondicional. **Gràcies** als meus tiets per tenir sempre una abraçada preparada i un somriure, tant si les coses no van tant bé com quan hi ha bones notícies. **Gràcies** als meus cosins per la vostre innocència i per empenyem a ser una persona a la que pogueu admirar. **MOLTES GRÀCIES** als meus tres pilars, mama, papa i Elisenda, per absolutament TOT. Sou el meu referent i sé que sóc qui sóc per vosaltres. Heu de tenir clar que aquest doctorat és **gràcies** a als tres, tant per tota la vostra ajuda durant aquests anys, com tot l'esforç que heu fet des de sempre i tot l'amor que m'heu donat. Us estimo moltíssim! Vull agrair també també a l'altra germana que ha arribat a la família un pel més tard però amb moltíssima alegria i força. Gràcia **GRÀCIES** per cuidar-me tant a mi com a tota la meva família. I al més petit de la família! **GRÀCIES** Martí per cuidar de les mamis però sobretot **gràcies** per tots els moments que ens esperen junts en un futur. Teniem ganes de tenir-te amb nosaltres!

Per últim, vull dedicar el meu últim **MOLTES GRÀCIES** a la meva petita nova família i, especialment, a la persona que ha patit tot aquest camí amb mi. Sé segur que res de tot això hagués sigut possible sense el teu suport, el teu positivisme constant, la teva força i tot el teu amor. Sé que el teu nom hauria d'apareixer en cadascun dels diferents apartats perquè en tots ells has estat fonamental. **Mil GRÀCIES** Sheila, amor, per tenir sempre la paraula i la força que necessitava en tot moment. **T'estimo! Moltes gràcies** i "*muchas veces*" també a tota la família Chumillas Moreno per ser-hi sempre aquests anys i per sempre tenir unes paraules d'ànim quan les coses no sortien i un somriure quan deia que anava per bon camí. I **gràcies**, també, al petit de la casa per la seva innocència i intensitat constant.

No sé si aquesta tesis significa un punt-i-final o un punt-i-seguit a la meva carrera professional com investigador però el que sé segur és que tot el que he après i la gent que he conegut formareu sempre part de mi. **GRÀCIES!**

LIST OF ABBREVIATIONS AND ACRONYMS

α_a	Charge transfer coefficient
Γ^*	Surface coverage
AA	Acetic acid
AC	aberration-corrected
acac	Acetylacetonate
AEM	Adsorbate evolution mechanism
AFC	Alkali fuel cell
BSE	Back scatter electron
CA	Chronoamperometry
CAA	Chloroanilic acid
CB	Carbon black
Cdl	Double layer capacitance
CHE	Computational hydrogen electrode
CNTs	Carbon nanotubes
CO2RR	CO ₂ reduction reaction
CP	Carbon paper
Cs	Specific capacitance
CV	Cyclic voltammetry
D	Proton diffusivity
DAD	Diode array detector
DFAFC	Direct formic acid fuel cells
DFFC	Direct formate fuel cell
DFT	Density functional theory
DLFC	Direct liquid fuel cells
DMF	N,N-dimethylformamide
E°	Standard theoretical potential
ECSA	Electrochemically active surface area
EDA	Ethylenediamine
EDS	Energy-dispersive X-ray spectroscopy
EELS	Electron energy-loss spectroscopy
EIS	Electrochemical impedance spectroscopy

FA	Formic acid
FE	Faradaic efficiency
FESEM	Field emission scanning electron microscope
FFT	Fast Fourier transform
FOR	Formate oxidation reaction
GC	Glassy carbon
GGA	Generalized gradient approximation
GOR	Glucose oxidation reaction
GRA	Glucaric acid
HAADF-STEM	High-angle annular dark-field
HAB	Hexaaminobenzene
HACO	Hexaketocyclohexane octahydrate
HAD	1-hexadecylamine
HER	Hydrogen evolution reaction
HMPT	Hexamethylphosphorous triamide
HPLC	High-performance liquid chromatography
HRTEM	High-resolution transmission electron microscopy
I2M	Interaction of two M-O units
I_a	Anodic current peak
ICP	Inductively coupled plasma
ICP-MS	Inductively coupled plasma mass spectrometry
ICP-OES	Inductively coupled plasma optical emission spectroscopy
LA	Lactic acid
LOM	Lattice oxygen mechanism
LSV	Linear sweep voltammetry
MAC	Methylamine hydrochloride
MCFC	Molten carbonate fuel cell
MWCNTs	Multi-walled carbon nanotubes
NC	Nanocrystal
NF	Nickel foam
NMP	N-methyl-2-pyrrolidone
NP	Nanoparticle
OAc	Acetate
OAm	Oleylamine

OCV	Open circuit voltage
ODE	1-octadecene
OER	Oxygen evolution reaction
OXA	Oxalic acid
PAFC	Phosphoric acid fuel cell
PAW	Projector-augmented-wave
PBE	Perdew–Burke–Ernzerhof
PDOS	Partial density of states
PEMFC	Polymer electrolyte membrane fuel cell
PTFE	Polytetrafluoroethylene
R	Resistance
RDE	Rotatory disc electrode
RDS	Rate determining step
RHE	Reversible hydrogen electrode
SEM	Scanning electron microscopy
SOFC	Solid oxide fuel cell
STEM	Scanning transmission electron microscopy
SUTW	Super ultra-thin window
TA	Tartronic acid
TBAB	Borane tert-butylamine
TEM	Transmission electron microscopy
TMPs	Transition metal phosphides
TOF	Turnover frequency
TOP	Tri-n-octylphosphine
TPOP	Triphenyl phosphite
VASP	Vienna ab-initio simulation package
XPS	X-ray photoelectron spectroscopy
XRD	X-ray diffraction

LIST OF PUBLICATIONS AND AUTHOR'S CONTRIBUTIONS

The thesis is based on research conducted in the Functional Nanomaterials Group at the Institut de Recerca en Energia de Catalunya (IREC), in Sant Adrià de Besòs (Barcelona), from 2020 to 2024, under the supervision of ICREA Prof. Andreu Cabot. Additionally, part of the work was carried out at the Institute of Science and Technology Austria (ISTA), in Klosterneuburg (Vienna), under the supervision of Prof. Maria Ibañez.

1. María Isabel Díez-García, Guillem Montaña-Mora, Marc Botifoll, Andreu Cabot, Jordi Arbiol, Mohammad Qamar, and Joan Ramon Morante. Cobalt–Iron Oxyhydroxide Obtained from the Metal Phosphide: A Highly Effective Electrocatalyst for the Oxygen Evolution Reaction at High Current Densities. *ACS Appl. Energy Mater.* **2023**, 6, 5690–5699

In this work, I carried out the synthesis of the nanoparticles and part of their characterization using SEM, EDS, and XRD. Additionally, I actively participated in the discussion of the results, contributing ideas to justify both the observed improvements and the unexpected outcomes. Dra. María Isabel designed the electrochemical experiments and wrote the paper. She also coordinated the high-resolution characterization results and actively participated in the discussion of the results.

2. Xiang Wang, Guillem Montaña-Mora, Xu Han, Jing Yu, Xueqiang Qi, Jordi Arbiol, Zhifu Liang, Andreu Cabot, and Junshan Li. Palladium Hydride on C₂N to Boost Formate Oxidation. *ACS Sustainable Chem. Eng.* **2023**, 11, 11399–11405

In this work, I carried out part of the synthesis of the supports and particles, and some of the electrochemical experimentation. Additionally, I actively participated in the discussion of the results. Dr. Xiang Wang contributed to the synthesis, characterization, and electrochemical application, and wrote the majority of the paper.

3. Guillem Montaña-Mora, Xueqiang Qi, Xiang Wang, Jesus Chacón-Borrero, Paulina R. Martinez-Alanis, Xiaoting Yu, Junshan Li, Qian Xue, Jordi Arbiol, Maria Ibañez, and Andreu Cabot. Phosphorous incorporation into palladium tin NPs for the electrocatalytic formate oxidation reaction, *Journal of Electroanalytical Chemistry*, 936, 2023, 117369

In this work, I conducted the synthesis of the material and performed most part of its characterization. Additionally, I designed the electrochemical experiments and led the

discussion of the results. Finally, I wrote most of the paper and coordinated the contributions from the other authors.

4. Guillem Montaña Mora, Karol V. Mejia-Centeno, Xueqiang Qi, Qian Xue, Jesus Chacón-Borrero, Francesco Salutarì, Maria Chiara Spadaro, Teresa Andreu, Germán Salazar-Alvarez, Frank Güell, Jordi Llorca, Jordi Arbiol, Paulina R. Martínez-Alanis, Andreu Cabot. Oxophilic Sn to promote glucose oxidation to formic acid in Ni nanoparticles. *ChemSusChem*, 2024, e202401256

In this work, I was responsible for synthesizing the materials and conducting most of the characterization. I also designed, executed, and analyzed the electrochemical experiments. Additionally, I led the discussion of the results, providing critical insights and suggesting ideas to solve various challenges.

PREFACE

Motivated by the desire to contribute to solving global energy crisis and the alarming environmental situation by using sustainable resources, this thesis is focused on the fabrication and characterization of nanostructured materials and their application as catalysts in electrochemical systems for biomass exploitation, with an emphasis on both electricity generation and the valorization of biomass-derived products.

Following this central goal, the work is structured into six chapters.

The first chapter introduces biomass as a sustainable alternative resource to fossil fuels and presents the objectives of this thesis. It outlines the advantages of biomass over conventional resources and describes current procedures used for its exploitation, both thermochemical and biological. Additionally, it introduces electrochemical methods, emphasizing their role in both energy generation and the further valorization of biomass-derived compounds, with a deeper explanation of the reactions studied in subsequent chapters.

Chapters 2 to 5 detail the experimental work conducted in this thesis. Each chapter illustrates the synthesis of the different materials, employing strategies to reduce the amount of noble metals, their subsequent characterization and their application as catalysts in electrochemical oxidation reactions.

According to the role that biomass plays in the electrochemical system, the experimental section can be divided into two sub-blocks: energy generation and further valorization of biomass-derived compounds

The first block, which includes chapters 2 to 4, focuses on the fabrication and application of several nanostructured materials as catalysts in OER and FOR, for electrical energy generation. In Chapter 2, the ternary material CoFeP is employed for the OER, while Chapters 3 and 4 investigate the FOR using Pd-based catalysts modified with light elements such as P and H.

In the second block, encompassing chapter 5, the synthesis of Ni-based catalysts and their use for the electrochemical valorization of glucose is details. GOR is studied due to the large number of high-value-added products that can be generated using a NiSn_{0.6} alloy, thereby avoiding the use of noble metals. By varying the reaction conditions, it has been possible to modulate the products and electrocatalytic activity, achieving a highly competitive Faradaic efficiency.

Finally, chapter 6 offers a general discussion of the experimental section and the obtained results, followed by the general conclusions of the thesis and a short section on future work of interest to be done.

SUMMARY OF RESULTS

The global energy situation coupled with the indiscriminate use of fossil fuels is currently a major problem for both human health and the prosperity of the planet. Biomass represents a highly promising renewable resource, and electrochemical processes can serve as an efficient technology for energy conversion and the sustainable generation of a wide variety of high-value products. However, the main current challenge is the development of competitive, efficient, and cost-effective catalysts.

Nanostructured materials are highly valuable in this field due to their large surface area and the ability to modulate their properties through structural, compositional, and morphological changes, providing them versatility across a wide range of application fields. Historically, noble metals such as Pt or Pd have been the primary choice as catalysts due to their remarkable electrochemical properties despite their high cost, limited availability, and susceptibility to contamination with CO.

In this context, in the different chapters of the thesis, I detail the work I have undertaken to produce and optimize different catalysts for application in electrochemical systems, either for electricity generation or for the valorization of compounds extracted from biomass. Among the four types of materials produced, two are based on Pd alloys modified to enhance both activity and stability. In the other two catalysts, I have replaced noble metals with more cost-effective and abundant transition metals.

In Chapter 2, the development of a bimetallic electrocatalyst based on cobalt-iron oxyhydroxide derived from cobalt-iron phosphide nanorods is detailed. This material is used in high-performance anodes for the OER at high current densities, exceeding 1 A cm^{-2} . Under alkaline conditions and anodic polarization, phosphorous depletion and a morphological transition occur, converting the initial CoFeP nanorods to CoFe oxyhydroxide nanoplates with a high ECSA. This procedure enables the preservation of the metal homogeneous distribution on the support, achieving a high density of active sites.

In Chapter 3, the application of the compound $\text{PdH}_{0.58}@\text{C}_2\text{N}$ as a catalyst in the FOR reaction is studied. The introduction of hydrogen modifies the electronic energy levels, increasing the specific activity to achieve a current density of up to $5.6 \text{ A} \cdot \text{mg}_{\text{Pd}}^{-1}$, which is 5.2 times higher than that of Pd/C. Additionally, the introduction of hydrogen reduces the onset potential and enhances stability, as it exhibits the slowest current decay compared to the reference

electrocatalysts. Analysing the results using DFT, it is observed that the d-band of the PdH_{0.58}@C₂N surface is downshifted, weakening the adsorbate binding and thus accelerating the rate-limiting step of the FOR.

In Chapter 4, the synthesis of the ternary compound Pd₂Sn_{0.8}P and the effect of phosphorus incorporation into the Pd-Sn alloy on the electrocatalytic response for formate oxidation are detailed. As a result, Pd₂Sn_{0.8}P exhibits very high catalytic activity, with record mass current densities of up to 10.0 A·mg_{Pd}⁻¹. Additionally, compared to Pd_{1.6}Sn, not only is the activity improved, but the stability of the catalyst is also enhanced. To understand how phosphorus affects the reaction mechanism, the system was studied using DFT calculations, which confirm that the presence of phosphorus favors the desorption of CO₂, thus reducing the energy barrier of the rate-limiting step.

In Chapter 5, I detail the effect of introducing an oxophilic element into Ni nanoparticles used as catalysts in the oxidation of glucose. We observed that incorporating Sn not only enhances the reaction kinetics but also that NiSn_{0.6} achieves excellent current densities and a Faradaic efficiency of 93% towards formic acid. A DFT study shows that Sn facilitates the adsorption of glucose on the Ni surface and promotes the formation of catalytically active Ni³⁺ species. At low concentrations and potentials, formic acid overoxidation to carbonates reduces the total Faradaic efficiency, while at high concentrations, the non-Faradaic glucose degradation pathway is promoted, increasing selectivity towards fructose, acetic acid, and lactic acid production.

RESUMEN DE RESULTADOS

La situación energética global, junto con el uso indiscriminado de combustibles fósiles, constituye actualmente un grave problema tanto para la salud humana como para la prosperidad del planeta. La biomasa representa un recurso renovable altamente prometedor, y los procesos electroquímicos pueden servir como una tecnología eficiente para la conversión de energía y la generación sostenible de una amplia variedad de productos de alto valor. Aun así, el principal desafío radica en el desarrollo de catalizadores competitivos, eficientes y rentables económicamente.

Los materiales nanoestructurados tienen un gran valor en este ámbito debido a su gran área superficial y a la capacidad de modular sus propiedades mediante cambios estructurales, composicionales y morfológicos, lo que les otorga versatilidad en una amplia gama de campos de aplicación. Históricamente, los metales nobles como el Pt o el Pd han sido la elección principal como catalizadores debido a sus notables propiedades electroquímicas, a pesar de su alto costo, disponibilidad limitada y susceptibilidad a la contaminación con CO.

En los diferentes capítulos de la tesis, he detallado el trabajo que he llevado a cabo en la fabricación y optimización de diferentes catalizadores y su aplicación en sistemas electroquímicos, ya sea para la generación de electricidad o para la valorización de compuestos extraídos de la biomasa. De los cuatro tipos de materiales producidos, dos están basados en aleaciones de Pd modificadas para mejorar tanto la actividad como la estabilidad. En los otros dos catalizadores, he reemplazado los metales nobles por metales de transición más abundantes y económicos.

En el Capítulo 2, se ha detallado el desarrollo de un electrocatalizador bimetálico basado en oxihidróxido de cobalto-hierro derivado de *nanorods* de fosfuro de cobalto-hierro. Este material es usado en ánodos de alto rendimiento para la OER a densidades de corriente elevadas, superiores a 1 A cm^{-2} . Bajo condiciones alcalinas y polarización anódica, ocurre una disminución de fósforo y una transición morfológica, convirtiendo los *nanorods* iniciales de CoFeP en *nanoplates* de oxihidróxido de CoFe con una alta ECSA. Este procedimiento permite la preservación de la distribución homogénea de metal en el soporte, logrando una alta densidad de sitios activos.

En el capítulo 3, se estudia la aplicación del compuesto $\text{PdH}_{0.58}@\text{C}_2\text{N}$ como catalizador en la reacción FOR. La introducción del hidrógeno modifica los niveles de energía electrónicos,

incrementando de la actividad específica, para obtener una densidad de corriente de hasta $5.6 \text{ A}\cdot\text{mg}_{\text{Pd}}^{-1}$, que es 5.2 veces mayor que la del Pd/C. Además, la introducción del hidrógeno reduce el potencial de inicio y aumenta la estabilidad, ya que exhibe la menor tasa de decaimiento de corriente en comparación con los electrocatalizadores de referencia. Analizando los resultados mediante DFT, se observa que el d-band de la superficie de $\text{PdH}_{0.58}\text{@C}_2\text{N}$ se desplaza hacia abajo, debilitando la unión del adsorbato y acelerando así el paso limitante de la reacción FOR.

En el capítulo 4, se detalla la síntesis del compuesto ternario $\text{Pd}_2\text{Sn}_{0.8}\text{P}$ y el efecto de la incorporación del fósforo en la aleación de Pd-Sn sobre la respuesta electrocatalítica para la oxidación de formato. Como resultado, $\text{Pd}_2\text{Sn}_{0.8}\text{P}$ presenta una actividad catalítica muy elevada, con densidades de corriente masiva récord de hasta $10.0 \text{ A}\cdot\text{mg}_{\text{Pd}}^{-1}$. Además, al comparar los resultados con $\text{Pd}_{1.6}\text{Sn}$, no solo se mejora la actividad, sino también la estabilidad del catalizador. Para comprender cómo afecta el fósforo al mecanismo de reacción, se ha estudiado el sistema mediante cálculos DFT los cuales confirman que la presencia de fósforo favorece la desorción de CO_2 , reduciendo así la barrera energética del paso limitante de la reacción.

En el capítulo 5, se estudia el efecto de introducir un elemento oxofílico en nanopartículas de Ni como catalizadores en la oxidación de la glucosa. Observamos que la incorporación de Sn no solo mejora la cinética de la reacción, sino que también el $\text{NiSn}_{0.6}$ alcanza excelentes densidades de corriente y una eficiencia Faradaica del 93% hacia el ácido fórmico. Un estudio DFT muestra que el Sn facilita la adsorción de glucosa en la superficie de Ni y promueve la formación de especies activas Ni^{3+} . A bajas concentraciones y potenciales, la sobreoxidación del ácido fórmico a carbonatos reduce la eficiencia Faradaica mientras que, a altas concentraciones, la degradación no Faradaica de la glucosa se promueve, aumentando la selectividad hacia la producción de fructosa, ácido acético y ácido láctico.

CHAPTER 1

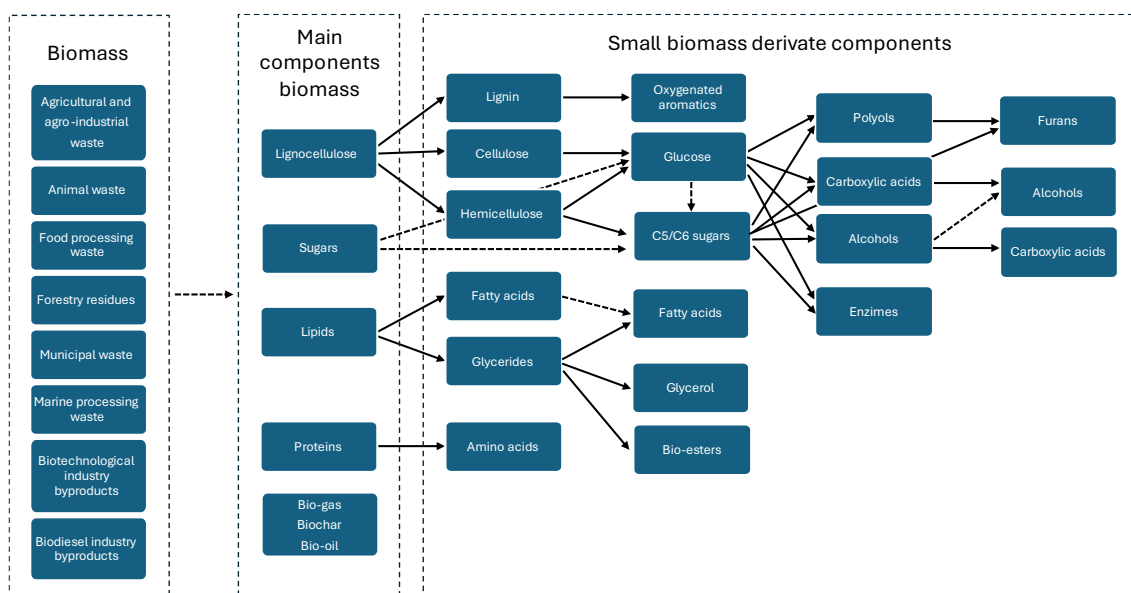
GENERAL INTRODUCTION

1.1. BIOMASS-DERIVED COMPOUNDS

Fossil fuels have played a crucial role as energy sources and chemical feedstocks since the Industrial Revolution to the present day. Their high energy density, low oxygen/hydroxide content, easy accessibility and simple implementation compared to other energy sources have propelled significant technological, social, and economic advancements in society. However, the exploitation of these compounds has also had several negative impacts on society and the environment. About 87% of global greenhouse gas emissions is due to the use of fossil resources, thus they are the primary contributors to global warming, local air pollution and acid rain. In addition to their harmful effects, fossil fuels pose a long-term challenge due to their status as non-renewable resources. As extraction becomes more difficult, the cost of these resources will gradually increase. This dilemma is aggravated by the continuous rise in energy demand, driven by global population growth, and industrial and technological development, among other factors. Despite efforts to increase awareness about the negative consequences of their use, their dominance in critical sectors such as transportation, electricity generation, and industrial production of chemicals hinders the transition to more sustainable alternatives.

The transition towards renewable and sustainable energy sources and chemical feedstocks has become indispensable not only to reduce current dependence on fossil fuels but also to mitigate the adverse effects on the planet. However, it is important to diversify energy supplies to avoid overexploitation of any of them. One of the foremost renewable energy sources, alongside solar, wind, and hydroelectric power, is energy derived from biomass, commonly referred to as bioenergy. Bioenergy accounts for 55% of renewable energy and contributes over 6% to the global energy supply. Furthermore, the utilization of modern bioenergy has been steadily increasing by an average of approximately 3% between 2010 and 2022, underscoring its current significance.¹

Biomass encompasses all organic matter derived from living organisms, including plants, animals, and microorganisms. It is a very heterogeneous and chemically complex renewable resource with a chemical composition comprised of C, H, O, and N. Lignocellulosic biomass stands out as the most abundant and cost-effective biomass source, composed of cellulose, hemicellulose, and lignin. While cellulose consists of a polysaccharide made exclusively of glucose molecules, hemicellulose can include a variety of sugars such as mannose, xylose, arabinose, galactose, among others. Due to its more amorphous structure compared to cellulose, hemicellulose can be degraded more easily. On the other hand, lignin represents the most complex and resistant biopolymer, composed of three different phenylpropanoid monomeric units: p-coumaric alcohol, coniferyl alcohol, and sinapyl alcohol. Additionally, various lipids can also be extracted from biomass and converted into biodiesel and glycerol.²



Scheme 1.1. Scheme of some of the possible biomass reaction pathways

The utilization of biomass is characterized by being a carbon-neutral process, which means that in net terms, it does not contribute to the increase in CO₂ emissions in the atmosphere. This is because the CO₂ released during its use is equivalent to the carbon previously absorbed during its growth, thus closing the carbon cycle. This aspect justifies the increasing trend in the use of biomass, as it helps to reduce associated CO₂ emissions.³

In developing countries, the consumption of fossil fuels is significantly lower compared to developed nations like the United States, Australia, or Germany. Additionally, in many of these countries, the generation of biomass waste is considerable due to predominant agricultural activity and the lack of efficient waste management systems. Despite this abundance, the reuse

of biomass for energy production remains limited due to the lack of infrastructure and appropriate technologies for its transformation, as well as a lack of awareness about its benefits.⁴

1.1.1. Methods for biomass conversion

The traditional use of biomass has often involved its direct combustion, especially in less economically developed countries. It remains one of the most utilized methods due to its simplicity and adaptability of technologies used for fossil fuels. However, comparable to the situation with fossil fuels, biomass combustion poses health and environmental problems due to the poor process efficiency.

Besides being an energy source, biomass exhibits remarkable versatility by offering a wide range of compounds that can be utilized in various applications. This biomass conversion process, where different compounds are decomposed and transformed into various high-value products, is known as biorefining.^{3,5} These compounds encompass not only fuels but also chemicals, pharmaceuticals, and a variety of bioproducts applicable to industry. The biorefining processes can be divided into two main categories: (1) thermochemical methods that include pyrolysis, gasification or hydrothermal liquefaction and (2) biochemical processes like enzymatic hydrolysis, anaerobic digestion, fermentation or transesterification.^{3,5-8}

In thermochemical methods, the organic matter is heated to high temperatures breaking down the molecules to obtain energy and other valuable compounds. A clear example is the direct combustion of biomass, in which molecules are heated under an excess amount of oxygen. Gasification and pyrolysis processes occur when this organic matter is heated under controlled oxygen levels (gasification) or in the absence of oxygen (pyrolysis). Through gasification, biomass is converted into primarily gaseous products like syngas, containing CH₄, CO₂, H₂, and CO, among others. Pyrolysis mainly yields bio-oil, biochar, and other gaseous and aerosol products, although varying experimental conditions can result in a greater variety of compounds. The hydrothermal liquefaction and aqueous phase reforming processes are thermochemical depolymerization methods performed in a liquid environment, taking place in a chamber at lower temperatures than the aforementioned processes. These methods involve subjecting biomass to high pressures, in the presence of water, to enhance the conversion efficiency. While the hydrothermal liquefaction process yields biocrude oil, fermentable sugars, along with other valuable byproducts, aqueous phase reforming systems focus on producing gaseous products

like hydrogen, but also other small carbon molecules, alcohols, and other chemically functionalized products.

On the other hand, biochemical processes involve the transformation of biomass using microorganisms, resulting in slower but milder conditions and greater selectivity. Enzymatic hydrolysis, as its name suggests, employs enzymes to depolymerize biomass to obtain simple sugars, such as glucose and xylose. Subsequently, these monosaccharides are converted into derivative compounds such as bioethanol or biobutanol through anaerobic digestion and fermentation. In anaerobic digestion, specialized bacteria break down organic materials in the absence of oxygen, producing biogas as a primary final product. Alternatively, fermentation involves the metabolic action of various microorganisms, such as yeast or bacteria. During fermentation, sugars are converted into alcohol and other byproducts through biochemical reactions. Depending on the specific microorganisms and substrate used, fermentation can yield various end products, with bioethanol being one of the most commonly produced. Transesterification is a chemical reaction commonly used in the conversion of biomass into biodiesel. In this process, triglycerides are broken down into fatty acid alkyl esters (biodiesel) and glycerol. The reaction proceeds through a series of steps where the alcohol molecule replaces the glycerol backbone of the triglyceride, resulting in the formation of biodiesel and glycerol as byproducts.

While both thermochemical and biochemical processes are effective, they present several disadvantages. In the case of thermochemical processes, they require high temperatures and pressures, leading to significant energy consumption and the generation of greenhouse gases, detrimental to the environment. Conversely, biochemical processes are known for their high selectivity and ability to operate under conditions close to ambient, but their main limitation lies in their relatively slow production rate. Moreover, both the processes and the microorganisms involved are sensitive to factors such as pH and temperature, meaning that any variation can negatively impact process efficiency.

1.2. ELECTROCHEMICAL BIOMASS CONVERSION

Electrochemical methods stand out as an alternative to these thermochemical and biochemical strategies.⁹ On one hand, these processes can be highly efficient and selective, with mild working conditions and lower environmental impact. Besides, they facilitate operation across a diverse pH range, with heightened reaction kinetics. Their scalability is readily achievable, owing to both process safety considerations and the compounds employed. Furthermore, electrochemical

methods can be integrated with thermochemical and biochemical processes, thus contributing to maximizing the performance and sustainability of the biomass value chain. Just like with previous methods, electrochemical processes can be employed both for energy generation, using fuel cells, and for obtaining a wide range of derivative products by applying energy to the system.^{2,10}

1.2.1. Electrochemical cells

Electrochemical cells serve as devices for electrochemical reactions. They consist of two electrodes, an anode and a cathode, an electrolyte, and an external circuit. At the anode, species undergo oxidation, releasing electrons that flow through the external circuit, generating electricity. These electrons are used at the cathode to undergo reduction reactions, thus closing the circuit. This configuration is primarily used in galvanic cells (fuel cells or batteries) where the cell voltage is driven by the reaction. In electrolytic cells, an external energy input drives the chemical reaction. A reference electrode is introduced to control the applied potential. The positive and negative ions created in the reaction travel through the electrolyte to complete the circuit and maintain charge neutrality.¹⁰

The different types of electrochemical cells can be classified in various ways according to their characteristics. For instance, they can be classified based on the state of the electrolyte used (solid, liquid, or gel), as well as by their nature (aqueous, organic, etc.). Additionally, they can also be categorized according to the membrane used, among other parameters such as electrode configuration, operating temperature, working pressure, electrode composition, and the specific application for which they are designed. Another important classification is based on their mode of operation: batch mode or continuous flow mode. In continuous flow mode, reactants are supplied continuously, allowing for continuous energy production. The electrochemical response is often more efficient due to a more effective contact between the electrolyte and the electrode, leading to higher reaction rates and increased energy conversion efficiency. However, this setup entails greater complexity in assembly and operation. Multiple additional factors must be considered, such as flow pressure, flow rate, and system tightness. On the other hand, in batch mode cells, a specific quantity of reactants is loaded, and the chemical reaction continues until the reactants are depleted or a specific goal is achieved. The process is simpler and more direct. By loading a specific quantity of reactants in a single operation cycle, the need for continuous material supply is avoided. This results in quicker and easier assembly and disassembly.

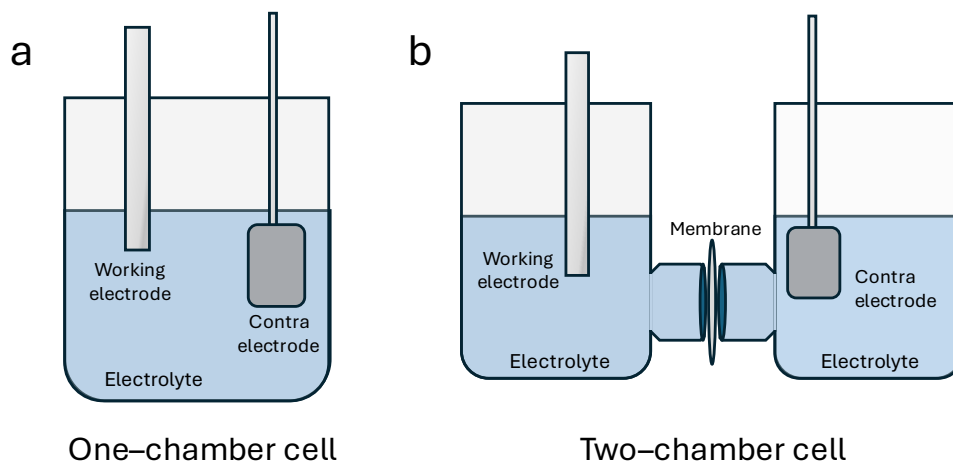


Figure 1.1. Schematic representation of the two main electrochemical cell configurations: Single-chamber (a) and two-chamber configuration (b).

Additionally, the first type of cells can also be classified according to whether they have a single-chamber or two-chamber configuration separated by a membrane (Figure 1.1). Those with a single chamber allow reactants to mix freely, while two-chamber cells separate the anodic and cathodic reactions using a selective membrane to prevent unwanted sub-processes. The main drawback of this second type is the increased system resistance due to the separation of the electrodes and the introduction of the membrane. Nonetheless, due to their simplicity and ease of assembly, both single-chamber and two-chamber configurations have been explored throughout the thesis.

1.2.2. Fuel cells

Fuel cells are devices where the chemical energy of the fuel is converted into electricity through redox reactions. When the fuel is supplied to the anode it oxidizes, releasing electrons that travel through an external circuit to the cathode, generating electricity. Fuel cells stand out in the search for sustainable solutions to satisfy energy demands for their high efficiency, eco-friendliness, and reliance on abundant and renewable fuel resources. Moreover, fuel cells facilitate the creation of simple and portable systems, demonstrating their versatility in application.

Fuel cells and batteries have the common aim of converting chemical energy into electricity.¹¹ Their operational distinction lies in the fact that while batteries harness the chemical energy stored in their electrodes, fuel cells rely on the chemical energy of a supplied fuel. Fuel cells theoretically offer unlimited operational time, subject to enough reactants in the electrolytic

medium and effective separation of the generated products. In contrast, batteries have a finite operational lifespan, requiring replacement or recharging after a certain period of use.¹²

In recent years, various types of fuel cells have been developed, such as SOFC, MCFC, AFC, PAFC or PEMFC (Table 1.1). Among them, PEMFCs have gained significant importance due to their versatility in various applications, especially in the automotive industry.¹³ They use a solid polymer as an electrolyte and Pt-based catalyst. These cells are known for their high-power density, fast start-up time, high efficiency, and low operating temperature. However, PEMFCs use pure H₂ as fuel, which needs to be stored under high pressure and handled properly. Additionally, H₂ is flammable and requires careful transportation.

As an alternative, DLFCs have been extensively investigated especially in mid-size power applications ranging from a few hundred watts to around 3 kW. In these cells, liquid fuel is introduced at the anode, while O₂ is used at the cathode. They exhibit a higher volumetric energy density, benefit from a well-established infrastructure, and are easier to store and transport compared to PEMFCs. Moreover, liquid fuel cells tend to have simpler system designs and can operate at lower temperatures, reducing the complexity and cost of thermal management systems. Besides the intrinsic characteristics of fuel cells, DLFCs can be categorized based on the type of fuel utilized in their operation.

Table 1.1. Overview of leading DLFC technologies. Adapted from Francisco et al published review.¹⁴

Fuel	E° (V)	Energy density (Wh L ⁻¹)	Anode Reaction	(Dis)Advantages
H ₂	1.23	2350	$H_2 \rightarrow 2 H^+ + 2 e^-$	<ul style="list-style-type: none"> • High energy density • Fast start-up • High efficiency • Clean technology • Careful storage and transport • Expensive infrastructure • Flammable
Methanol	1.21	4820	$CH_3OH + H_2O \rightarrow CO_2 + 6H^+ + 6e^-$	<ul style="list-style-type: none"> • High energy density • Cheap fuel • Easily handled, stored and transport • High fuel crossover • Toxic fuel • Low cell voltage and efficiency

Ethanol	1.15	6280	$C_2H_5OH + 3H_2O \rightarrow$ $2CO_2 + 12H^+ + 12e^-$ -	<ul style="list-style-type: none"> • Fuel easily produced and storage • Relative Non-toxic • high energy density • Slow oxidation • Difficult complete reaction, side products • Fuel crossover
Propanol	1.12	7080	$C_3H_7OH + 5H_2O \rightarrow$ $3CO_2 + 18H^+ + 18e^-$ -	<ul style="list-style-type: none"> • High electrochemical energy density • Safe handling • Many unwanted byproducts
Ethylene glycol	1.22	5800	$C_2H_6O_2 + 2H_2O \rightarrow$ $2CO_2 + 10H^+ + 10e^-$ -	<ul style="list-style-type: none"> • Non-volatile • High fuel volumetric energy density • Existence of distribution infrastructure • Difficult complete oxidation • Low power density and cell voltage • High cost • Fuel crossover • Pt usually used as catalyst.
Glycerol	1.21	6400	$C_3H_8O_3 + 3H_2O \rightarrow$ $3CO_2 + 14H^+ + 14e^-$ -	<ul style="list-style-type: none"> • Really low cost • Non-toxic, non-volatile, non-flammable • High energy density • Early research phase
FA	1.45	2110	$HCOOH \rightarrow$ $CO_2 + 2H^+ + 2e^-$	<ul style="list-style-type: none"> • Non-toxic, non-flammable • Mil operation conditions • Limited fuel crossover • Rapid electrooxidation • Higher theoretical cell potential and power energies • High fuel cost • Low volumetric energy density • CO poisoning
Dimethyl ether	1.20	5610	$(CH_3)_2O + 3H_2O \rightarrow$ $2CO_2 + 12H^+ + 12e^-$ -	<ul style="list-style-type: none"> • Well established storing and handling technologies • Non-carcinogenic, non-toxic, non-teratogenic and non-mutagenic • Less toxic than methanol • volatile • formaldehyde and methanol as byproducts • Electrochemical activity lower than methanol
Furfural	1.16	3915	-	<ul style="list-style-type: none"> • High energy density
Cyclohexane	1.06	1578	-	<ul style="list-style-type: none"> • Regenerative fuel cell • Low power density • Need a development of effective catalyst
Decalin	1.09	1893	-	<ul style="list-style-type: none"> • Non-volatile • CO free

Dodecahydro-N-ethylcarbazole	1.18	1715	-	<ul style="list-style-type: none"> • High OCV • Regenerative fuel cell • Low current density • Need a development of effective catalyst
Glucose	1.26	4430	$C_6H_{12}O_6 + H_2O \rightarrow C_6H_{12}O_7 + 2H^+ + 2e^-$	<ul style="list-style-type: none"> • Fuel availability and cheap. • Non-toxic • High energy density • Low electrochemical efficiency • Many Byproducts • Difficult complete oxidation
Ammonia borane	1.62	8400	$NH_3BH_3 + 6OH^- \rightarrow NH_4^+ + BO_2^- + 4H_2O + 6e^-$	<ul style="list-style-type: none"> • Chemically stable, available • High energy density • Non-toxic, inexpensive • The hydrolysis lower cell efficiency • Crossover • Complex equipment to eliminate H₂ • Far from commercialization
Ammonia	1.17	1704 (35 wt%)	$1/3NH_3 + OH^- \rightarrow 1/6N_2 + 1/2H_2O + e^-$	<ul style="list-style-type: none"> • Clean oxidation • Power density higher than H₂ • Need to be used in aqueous solution • Toxic • Catalyst degradation • Crossover
Sodium borohydride	1.64	2940 (30 wt%)	$BH_4^- + 8 OH^- \rightarrow BO_2^- + 6H_2O + 8e^-$	<ul style="list-style-type: none"> • No CO produced • High power density • High open circuit potential • Quite toxic • Hydrogen oxidation competition • Observed OCV much lower • Commercialization problems • Noble metal catalysts
Urea	1.15	4694	$CO(NH_2)_2 + 6OH^- \rightarrow CO_2 + N_2 + 5H_2O + 6e^-$	<ul style="list-style-type: none"> • High energy density • Easy transport, • Non-flammable, non-toxic • Non-volatile • Sluggish electrokinetics • Dominant OER • Low durability • Declined power output
Ascorbic acid	1.23	-	$L-C_6H_8O_6 \rightarrow C_6H_6O_6 + 2H^+ + 2e^-$	<ul style="list-style-type: none"> • High reaction rate • Non-toxic, environment-friendly • Inexpensive • Low crossover • Low power • Early research phase • Far from commercial

1.2.3. Electrochemical valorization of biomass-derived intermediates

Once the biomass is fractioned, the small constituent molecules can be further modified precisely into a variety of high-value products through electrochemical methods, either by adding or removing functional groups (Table 1.2). This ability for molecular manipulation quickly and efficiently not only offers great flexibility in organic compound synthesis but can also be tailored to various industrial needs and specific applications. Additionally, the low energy consumption associated with electrochemical methods makes them an attractive environmental option. Thus, they contribute to the sustainability of biomass transformation processes.^{15–18}

Table 1.2. Summary of electrochemical valorization chain from biomass-derived compounds. Adapted from Francisco et al published review.¹⁸

Biomass groups	Intermediate products	Final product
Polyols	Glycerol	Glyceraldehyde, glyceric acid, formic acid, glycolic acid, oxalic acid, tartronic acid, 1,3-dihydroxypropan-2-one, 2-oxomalonic acid, lactic acid
	Acetol	1,2-propanediol, acetone, 2-propanol
	Ethanol	Acetaldehyde, acetic acid, ethyl acetate
	Xylose	Xylonic acid, xylitol, d-valerolactone
	Glucose	Gluconic acid, glucaric acid, glyceraldehyde, glyceric acid, tartronic acid, glycolic acid, oxalic acid, formic acid, sorbitol,
	Galactose	Galactonic acid
	Mannose	Mannonic acid
Furans	Hydroxymethyl furfural	2,5-dihydroxymethyl furan, furandicarboxylic acid, 2,5-diformylfuran, 2,5-dihydroxymethylfurfural, 2,5-hexanediol, 5-methylfurfural
	Furfural	2-methylfuran, furfuryl alcohol, furoic acid, maleic acid, 5-hydroxyfuroic acid, 5-hydroxy-2(5H)-furanone, 1,5-pentanediol, hydroxyfuroin, 2,5-dimethyltetrahydrofuran
Carboxylic acids	Levulinic acid	Valeric acid, valerolactone, 2,7-octanedione
	2,7-octanedione	n-octane

	4-hydroxy-2-butanone	1-butanol
	Valeric acid	n-octane
	Lactic acid	Lactaldehyde, acetic acid
	Pyruvic acid	Lactic acid
	Itaconic acid	Methylsuccinic acid, 2,5-dimethyladipic acid
	Maleic acid	Succinic acid
Amino acids	L-glutamic acid	3-cyanopropanoic acid
	3-cyanopropanoic acid	Adiponitrile
	L-cysteine	L-cysteric acid
	L-phenylalanine	Benzyl cyanide
	L-isoleucine	2-methylbutyronitrile
	L-alanine	Acetonitrile, 2-aminopropan-1-ol
	L-valine	Isobutyronitrile
	L-serine	Glycolonitrile, ethanolamine, 2-aminopropane-1,3-diol
	L-threonine	Lactonitrile, 1-amino-2-propanol
	L-glutamine	3-cyanopropionamide
	L-asparagine	Acetamide
	L-aspartic acid	3-cyanopropionic acid, pyruvic acid, succinonitrile, 2-aminobutane-1,4-diol, 2-oxosuccinic acid
	L-arginine	N-(3-cyanopropyl)-guanidine
	L-lysine	5-aminopentanenitrile, 1,5-pentanediamine, 5-aminopentanamide
L-prolyne	2-pyrrolidone	

1.3. BASIC ELECTROCHEMICAL REACTIONS STUDIED

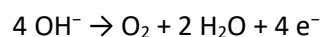
Numerous electrochemical reactions have been observed to employ both biomass and its constituent molecules, obtained through biorefinery processes, for both energy generation and subsequent modification to obtain derivative compounds. To optimize the response of each of these processes and make them more efficient, understanding their mechanisms and characteristics is essential.

One of the most important reactions studied in energy-generating devices is the OER mainly for its involvement in key energy technologies such as electrolyzers and metal-air batteries. Understanding this reaction is also crucial because it competes with biomass oxidation reactions, potentially reducing their efficiency.

The oxidation reaction of FA/formate has been also extensively researched for its application in DLFCs. This reaction enables rapid electrooxidation, higher theoretical cell potential, and power energies under mild conditions. On the other hand, the oxidation reaction of glucose has been extensively studied for its versatility in obtaining derivative products, which is of great interest to the industry. Finally, ORR and HER are the primary reactions occurring at the cathode of an electrochemical system, where they capture the electrons generated at the anode.

1.3.1. Oxygen evolution reaction

The OER is an important electrochemical process applied to energy storage, in metal-air batteries, or coupled with cathodic electrochemical conversions such as CO₂RR or water splitting. The OER in alkaline media follows the overall four-electron transfer process with a formal potential of 1.23 V vs RHE:



However, the reaction proceeds through different elementary steps, and they require the application of an overpotential to take place. The oxygen precursors involved in the reaction depend on the pH of the medium. Under basic conditions (Figure 1.2), the precursor is OH⁻, whereas under neutral or acidic conditions, it is H₂O. The OER typically proceeds through two possible pathways:¹⁹

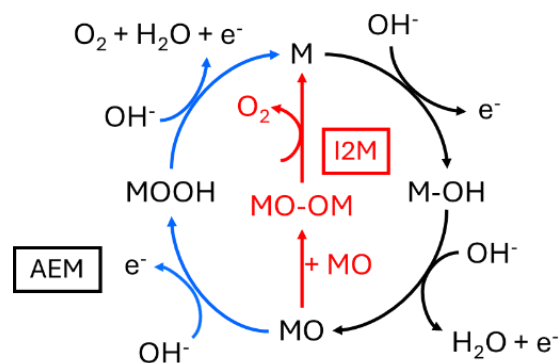


Figure 1.2. Conventional OER mechanism under alkaline conditions.

On one hand, the reaction can proceed via the AEM. In this reaction, a molecule of OH^- is adsorbed onto an active site and undergoes oxidation progressively until forming O_2 , which is then desorbed. On the other hand, the OER can also occur via the I2M mechanism. In this pathway, M-O species are formed through the same process as in the AEM, but instead of oxidizing to MOOH, this MO species couples with another MO species to form first the M-O-O-M species and finally O_2 , which desorbs.

These reaction mechanisms are suggested with the premise that OER is a surface phenomenon on the catalyst, involving the adsorption and transformation of various precursors in solution and a change in valence state at the active sites. However, in certain transition metal oxides, destabilization occurs, elucidated by another mechanism involving oxygen from within the catalyst structure. This mechanism is referred to as the LOM. In these pathways, the release of oxygen creates a vacancy in the lattice that is subsequently filled by the insertion of $\text{OH}^-/\text{H}_2\text{O}$ species.

1.3.2. Formate oxidation reaction

FA, with the chemical formula HCOOH , is the shortest chain carboxylic acid, composed of a single carbon atom. It is a biodegradable compound, relatively non-toxic, and mildly corrosive. Moreover, it is more economical compared to similar compounds. These properties make it widely utilized in the chemical industry, it serves as a preservative and finds application in the production of pharmaceuticals, dyes, agricultural products, and cleaning agents, among other uses. It is also a common additive and preservative in the food industry.

Recently, it has gained considerable interest as a hydrogen donor agent, being employed in various chemical processes. Compared to molecular hydrogen, it is more advantageous in terms of transportation and storage safety. Its short-chain structure ensures that its dehydrogenation

results in only CO₂ and H₂, making it a promising candidate as a hydrogen storage material. With a high volumetric hydrogen content, 1L of liquid FA contains 26.5 moles of H₂ (53 g H₂/L). Additionally, this dehydrogenation reaction can be achieved under mild conditions. Similarly, it can also be utilized for CO storage, as the dehydration reaction produces H₂O and CO.

In addition to the previously mentioned applications, FA/formate is gaining interest as a precursor in DLFCs.²⁰ This type of cell is appealing due to its high effectiveness in operating portable devices, in terms of transportation, storage, utilization, and safety of liquid fuels. Although traditionally acidic conditions and other compounds like methanol or ethanol have been used, direct formate fuel cells have stood out for their high oxidation kinetics and high theoretical cell voltage of 1.45 V, but also for their ease of transportation and storage due to being a solid compound under ambient conditions.

The main drawback of using formate as an energy source in an electrocatalytic process is the catalyst contamination and deactivation during the oxidation process. The oxidation of formate is a 2-electron process, but the reaction mechanism has two possible pathways. On one hand, there is direct oxidation where formate is converted to CO₂, which is the most efficient and favourable reaction. On the other hand, there is indirect oxidation which generates CO as an intermediate. This CO can strongly adsorb to the surface of catalysts, leading to the deactivation of active sites and thus inhibiting the process.

1.3.3. Glucose oxidation reaction

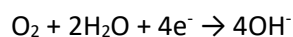
Glucose is a monosaccharide aldohexose containing six carbon atoms, one of which forms part of an aldehyde group, while the others are bonded to hydroxyl groups. Glucose stands out for its abundance, making it an attractive option for various applications. Besides being a key component in human nutrition, it is used in the production of biofuels, bioplastics, and industrial chemicals. Its availability, low cost, and non-toxicity make it particularly valuable in fields such as biotechnology and medicine, where it is utilized in drug manufacturing and tissue engineering, among other innovative applications. Primarily, glucose is derived from biomass sources such as cellulose and hemicellulose through enzymatic or chemical hydrolysis processes.

The oxidation of glucose has been extensively studied for its application in both biotic (enzymatic and microbial) and abiotic fuel cells, as well as in sensors. In most of these applications, glucose reactivity is based on the oxidation of the two functional groups located at the end of the molecule. Initially, the oxidation of the aldehyde group to form an acid group results in gluconic acid. Subsequently, the oxidation of the hydroxyl group yields glucuronic acid and glucaric acid.

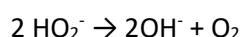
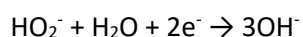
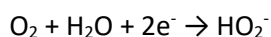
The performance of fuel cells using glucose as a fuel is inferior to that of other compounds such as ethanol, methanol, FA or glycerol. For this reason, and due to the wide range of products obtained through its oxidation, glucose has recently been investigated as a precursor for obtaining other industrially and medically relevant products. In addition to the products resulting from the oxidation of the functional groups, such as gluconic acid and glucaric acid, other compounds with shorter chains can be obtained through C-C bond cleavage. Some notable examples include glyceric aldehyde, tartronic acid, glycolic acid, glyceric acid, oxalic acid, and especially FA. Furthermore, through isomerization reactions, fructose can be obtained, from which lactic and acetic acid, among others, can be derived.

1.3.4. Oxygen reduction reaction

As previously explained, fuel cells involve two interconnected processes. While oxidation reactions such as FOR or GOR occur at the anode, reduction reactions take place at the cathode, utilizing electrons provided in the other half-reaction. Typically, during FOR or GOR processes, the ORR occurs at the cathode.^{13,21} This reaction is not only important in fuel cells but also in storage devices, such as metal–air batteries. The ORR is a multi-step reaction that follows a four-electron pathway, directly resulting in the production of H₂O in acidic medium, or OH⁻ in alkaline medium:



Despite the reaction being possible in both acidic and basic pH, in alkaline media, a less corrosive environment is provided to the catalysts, and the kinetics of the ORR are faster compared to acidic media. There are two main pathways in the ORR. On one hand, the reaction can occur via the direct pathway, which involves 4 electrons. On the other hand, it can also take place via the indirect conversion:



The GOR can be also coupled with the HER, as an alternative to the OER (1.23V vs RHE) due to the lower oxidation potential (0.05 V vs RHE) that presents GOR.

1.3.5. Hydrogen evolution reaction

The search for sustainable alternatives to fossil fuels has triggered renewed interest in hydrogen as a clean and highly efficient energy source. Currently, it has been demonstrated to be a fuel of significant interest for various types of vehicles, as its combustion only yields water, unlike fossil fuels. From its negligible levels in 2020, the production of clean hydrogen, both for its direct use as well as for the production of derivative fuels, is expected to increase to more than 500 million tons by the year 2050. This significant increase in clean hydrogen production underscores the need to seek and optimize different methods for its generation.²²

There are indeed various methods for obtaining H₂ from biomass, such as gasification or pyrolysis. However, it has been observed that electrochemical methods are a sustainable and efficient alternative for production.²³

The HER is one of the fundamental reactions in electrochemistry, in which H₂ is obtained through the reduction of H⁺ or H₂O from the electrolytic medium. There are two reaction mechanisms during water electrolysis depending on how H_{ads} reacts: Volmer-Tafel, where H_{ads} reacts with another nearby H_{ads}, and Volmer-Heyrovsky, where H_{ads} reacts with precursors in the medium. Moreover, the HER mechanism varies significantly depending on the pH conditions (Figure 1.3) in which it occurs.^{24,25}

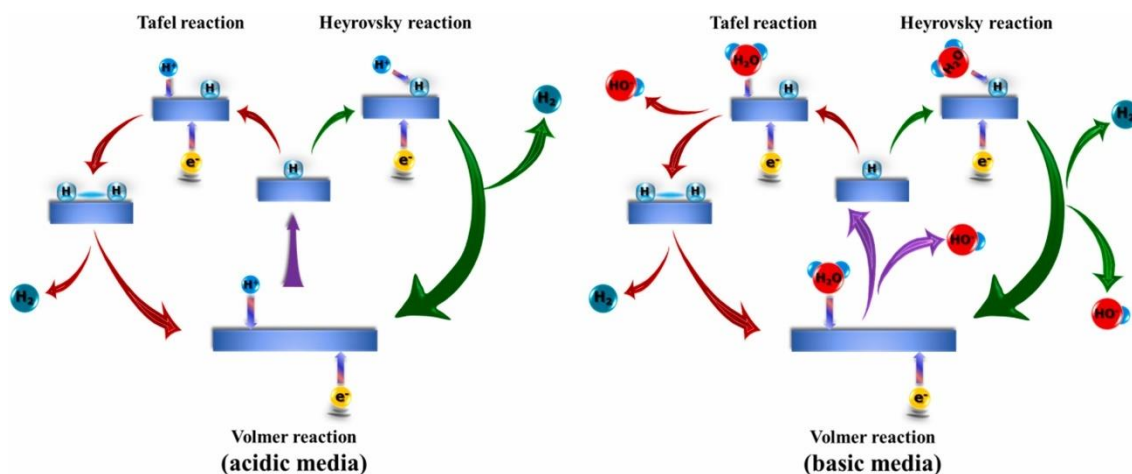


Figure 1.3. Reaction mechanisms of HER on an electrode surface in acid (left) and alkaline (right) conditions. (Extracted from: Copyright 2019, Elsevier Ltd.²⁶)

The first step of the reaction involves reducing a precursor to obtain adsorbed hydrogen on the catalyst surface. Subsequently, the formation of H₂ occurs through two possible processes: on one hand, via the Heyrovsky step, where H_{ads} reacts with a species in solution, undergoing

reduction, or through the Tafel step, where the reaction takes place between two adsorbed hydrogen species.

1.4. ELECTROCATALYSTS

The cost-effective implementation of electrochemical processes for biomass conversion depends largely on the process's effectiveness. In biomass electrooxidation processes, the OER can pose a challenge because these reactions are typically performed in alkaline media with a higher concentration of OH^- than biomass reagent. This concentration disparity leads to competition between the OER and biomass conversion, which reduces the biomass conversion efficiency. To address this challenge, working potentials are adjusted to hinder or reduce the OER intensity. In this context, catalysts play a crucial role by being selected in a manner that not only inhibits the OER but also enhances the desired conversion, thus ensuring an optimal and sustainable process.²⁷

Electrocatalysts are fundamental. In electrocatalytic reactions, the interface between the catalyst and the reaction medium is critical, as it is the surface atoms that dictate the specific reaction rate. The low coordination of surface atoms on the catalyst is the essence of catalysis, as surfaces with low coordination exhibit higher surface energy, resulting in increased reactivity for reagent adsorption. Nanomaterials providing high surface areas are fundamental.^{28–30}

1.4.1. Synthetic methods

The performance of electrocatalytic nanomaterials is heavily influenced not just by their composition but also by their structure and morphology. Hence, ensuring precise control and uniformity over the particles produced becomes imperative for their optimization. There are numerous techniques for synthesizing these materials, which can be classified into two main groups: bottom-up and top-down. While top-down methods involve the degradation or breaking down of macroscopic materials to reduce their size to the nanoscale, bottom-up methods involve the combination of atoms or molecules to form particles or compounds within the required range, with colloidal methods being an example of this second approach.

Thermal decomposition methods are widely used for their ability to precisely control both the morphology and composition of particles, all without the requirement of extreme pressure or temperature conditions or costly equipment. Moreover, they enable the production of a diverse array of NCs, ranging from simple oxides, chalcogenides or metals to more complex structures like core-shells or Janus particles.³¹

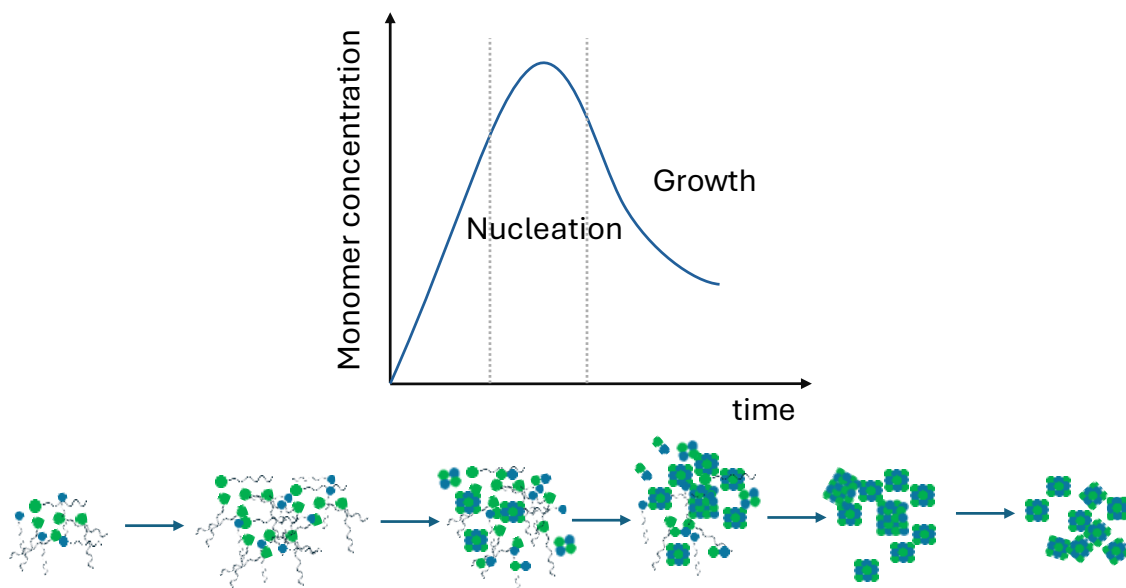


Figure 1.4. Schematic representation of the steps involved in the NCs formation.

In these methods (Figure 1.4), the soluble precursors decompose with temperature, typically within the range of 180 to 340°C, leading to the formation of atomic units (or monomers). In the presence of a reducing agent, monomers assemble to form small nuclei, which subsequently grow to eventually form nanostructures. Ensuring monodispersity of the NCs requires a distinct separation of the nucleation and growth phases. This is accomplished by inducing supersaturation to accelerate nucleation. Once nucleation initiates, the concentration diminishes, thereby halting further nucleation. The remaining monomers then bind to the nuclei to facilitate the continuation of the growth process.^{32–34}

There are two main types of thermal degradation methods: heat-up and hot-injection methods.³⁵ Both methods are based on the same principle of creating supersaturation but differ in the timing of adding the reactants. In the hot-injection method, compounds are injected at high temperatures, creating an instantaneous supersaturation of monomers, leading to rapid nucleation.³⁶ In contrast, in the heat-up method, precursors are first added, and then the temperature is gradually increased. In this latter method, nucleation takes place once the concentration reaches a critical value, which depends on the nature of the reactants and the reducing agent.³⁷

The main issue with these compounds is that their high surface energy makes them more reactive and prone to aggregation. To prevent particle aggregation and control their morphology, capping agents (as surfactants, polymers or polyelectrolytes) are employed. These substances adhere to the surface of NPs, preventing their aggregation either through steric

hindrance or electrostatic repulsion, thereby inhibiting their union with other particles. Moreover, these surfactants preferentially adhere to specific structural faces, depending on the nature of the compounds involved. This selective adhesion enables control over particle shape, allowing for the synthesis of spheres, cubes, rods, and so forth.

The high reactivity of the particles, as well as some of the reagents used, makes them prone to oxidation, especially at the relatively high temperatures involved. For this reason, the Schlenk line is used for their synthesis. Before synthesis, vacuum conditions at around 100°C are applied to remove oxygen, water, and other organic impurities, thus preventing the uncontrolled oxidation of the precursors. Subsequently, an inert atmosphere is introduced.

1.4.2. Noble metal-based catalysts

As previously mentioned, the presence of catalysts has become crucial for the application of electrochemistry and the development of various reactions. Noble metals exhibit remarkable versatility, demonstrating high performance across a diverse range of reaction conditions. They are capable of maintaining their catalytic activity under varying pH levels, temperatures, and reaction environments.

The main drawback of these noble elements lies in their scarcity and high cost, which limits their widespread application in many industrial processes and emerging technologies. Consequently, there is a continuous need to search for alternatives and strategies to reduce dependency and maximize their efficiency and sustainable use in industry and technology.⁹

Different strategies can be considered to reduce dependency on noble elements as catalysts: (1) reducing the amount, (2) alloying, or (3) substitution with other elements.

To decrease this dependency, taking into account their high cost, the first strategy involves modifying these compounds to increase their activity. This way, the amount used can be reduced while maintaining the same effectiveness. There are multiple strategies available for this purpose, such as structural and morphological modification of catalysts, as these factors play a fundamental role in NCs. Additionally, reducing the particle size or improving their dispersion on different substrates can increase the available surface area, thus enhancing catalytic performance.

The incorporation of other elements has emerged as the main strategy for reducing the utilization of noble metals. Research efforts have been directed towards the formation of a

diverse array of compounds, including metal alloys, oxides, chalcogenides, phosphides, and more. However, a challenge associated with these compounds lies in their synthesis. Given their complexity, precise control over nucleation and growth of the two or more elements introduced is essential. Nevertheless, thanks to extensive research over the past decades, significant progress has been made in achieving this control.

These compounds not only enhance the activity of monometallic catalysts but also introduce new properties or modify existing ones. In the field of heterogeneous catalysis, the incorporation of multiple elements opens a range of possibilities due to finely tuning the electronic structure through controlled modification of the composition and structure of NPs. For example, the presence of certain elements can promote the adsorption and activation of specific substrates, promoting biomass oxidation reactions and inhibiting oxygen evolution. Another advantage of introducing a second or third element is the improvement in catalyst stability. Depending on the reaction being used, especially in the oxidation of organic compounds such as FA or methanol, noble elements like Pt or Pd can become contaminated due to the production of intermediates such as CO. The introduction of poisoning-tolerant materials such as Ni, Co, Fe or Sn promotes the degradation of poisoning species, extending the material's durability.

Finally, another strategy to reduce dependency on noble metals is their substitution with other, more cost-effective elements. In biomass oxidation reactions, transition metals such as Fe, Co, Ni, or Cu have shown significant activity, often surpassing that of Pd or Pt. However, the primary challenge with these compounds lies in their low stability under extreme pH conditions, particularly in acidic environments. Nonetheless, oxidation reactions of compounds like FA or glucose tend to be more efficient under alkaline conditions. In such conditions, metal surfaces tend to oxidize, forming oxyhydroxides at working potentials, which have demonstrated considerable oxidizing activity and high stability.

1.5. OBJECTIVES

The general objective is to fabricate efficient catalysts to exploit completely the properties of biomass and its derivatives, thereby reducing the reliance on fossil fuels and initiating a reversal of the pollution and global warming situation. To achieve this, the thesis focuses on the synthesis of nanostructured materials using chemical methods to attain high activity and stability for oxidation reactions under alkaline conditions. To achieve this, this thesis presents several main objectives:

1. Develop and optimize colloidal synthetic methods to prepare NPs with controlled composition, structure, and morphology.
2. Establish the possibility of reducing or entirely eradicating the utilization of toxic or costly elements while achieving a material with superior electrochemical properties compared to previously documented analogues.
3. Elucidate the mechanism governing electrochemical reactions, investigating the processes and interactions dictating the conversion.
4. Establish a correlation between the electrocatalytic behaviour and the composition of the nanostructured compounds employed in the different oxidation reactions.

To achieve these general goals, more specific objectives have been established for each of the chapters of these thesis.

In the second chapter, the goal is to fabricate CoFeP nanoparticles as catalysts for the OER reaction and determine the mechanism by which phosphorus modifies the material electrocatalytic properties.

In the third and fourth chapters, the objective is to enhance the electrocatalytic properties of Pd by incorporating light elements such as P or H, as well as other metals like Sn. The aim is to establish experimentally and theoretically how these elements affect the active sites in the formic acid oxidation reaction.

In the fifth chapter, the goal is to introduce an oxophilic element, such as Sn, to Ni nanoparticles to enhance their activity and efficiency in the GOR. In addition to elucidating the mechanism of GOR, the objective is to establish theoretically and experimentally the effect of Sn on Ni active sites and glucose molecules.

1.6. REFERENCES

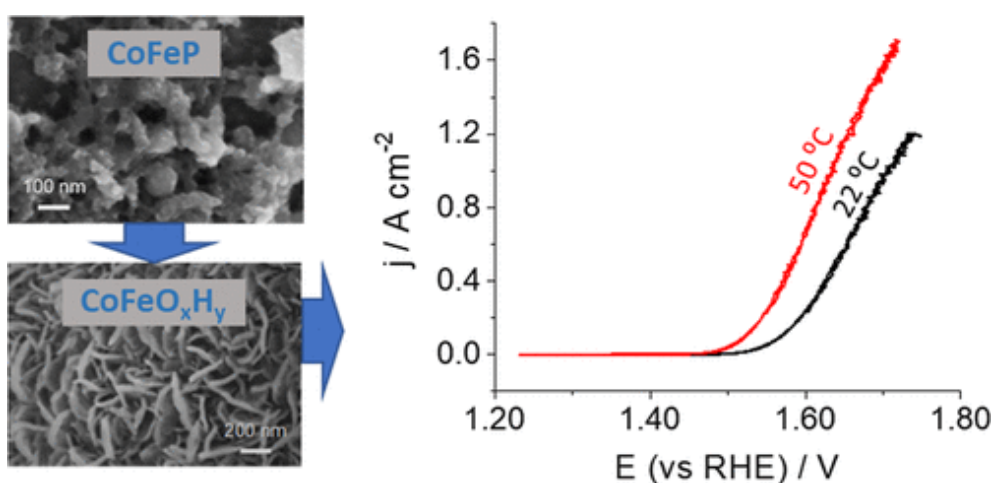
- 1 I. E. Agency, Net Zero Roadmap.
- 2 C. Xiong, C. Zheng, X. Jiang, X. Xiao, H. Wei, Q. S. Zhou and Y. Ni, *J. Energy Storage*, 2023, **72**, 108633.
- 3 R. K. Srivastava, N. P. Shetti, K. R. Reddy, E. E. Kwon, M. N. Nadagouda and T. M. Aminabhavi, *Environ. Pollut.*, 2021, **276**, 116731.
- 4 M. Antar, D. Lyu, M. Nazari, A. Shah, X. Zhou and D. L. Smith, *Renew. Sustain. Energy Rev.*, 2021, **139**, 110691.
- 5 H. Kargbo, J. S. Harris and A. N. Phan, *Renew. Sustain. Energy Rev.*, 2021, **135**, 110168.

- 6 V. K. Vaithyanathan, B. Goyette and R. Rajagopal, *Environ. Challenges*, 2023, **11**, 100700.
- 7 D. M. Alonso, J. Q. Bond and J. A. Dumesic, *Green Chem.*, 2010, **12**, 1493–1513.
- 8 K. Alper, K. Tekin, S. Karagöz and A. J. Ragauskas, *Sustain. Energy Fuels*, 2020, **4**, 4390–4414.
- 9 G. Yang, Y. Jiao, H. Yan, C. Tian and H. Fu, *Small Struct.*, 2021, **2**, 1–20.
- 10 S. A. Akhade, N. Singh, O. Y. Gutierrez, J. Lopez-Ruiz, H. Wang, J. D. Holladay, Y. Liu, A. Karkamkar, R. S. Weber, A. B. Padmaperuma, M. S. Lee, G. A. Whyatt, M. Elliott, J. E. Holladay, J. L. Male, J. A. Lercher, R. Rousseau and V. A. Glezakou, *Chem. Rev.*, 2020, **120**, 11370–11419.
- 11 G. Zhang, X. Liu, L. Wang and H. Fu, *J. Mater. Chem. A*, 2022, **10**, 9277–9307.
- 12 W. Liu, C. Liu, P. Gogoi and Y. Deng, *Engineering*, 2020, **6**, 1351–1363.
- 13 C. W. Anson and S. S. Stahl, *Chem. Rev.*, 2020, **120**, 3749–3786.
- 14 B. C. Ong, S. K. Kamarudin and S. Basri, *Int. J. Hydrogen Energy*, 2017, **42**, 10142–10157.
- 15 H. Luo, J. Barrio, N. Sunny, A. Li, L. Steier, N. Shah, I. E. L. Stephens and M. M. Titirici, *Adv. Energy Mater.*, , DOI:10.1002/aenm.202101180.
- 16 K. Li and Y. Sun, *Chem. - A Eur. J.*, 2018, **24**, 18258–18270.
- 17 K. Wang, Z. Li, Z. Guo, J. Huang, T. Liu, M. Zhou, J. Hu and H. Li, *Green Chem.*, 2024, **26**, 2454–2475.
- 18 F. W. S. Lucas, R. G. Grim, S. A. Tacey, C. A. Downes, J. Hasse, A. M. Roman, C. A. Farberow, J. A. Schaidle and A. Holewinski, *ACS Energy Lett.*, 2021, **6**, 1205–1270.
- 19 Z. Wang, W. A. Goddard and H. Xiao, *Nat. Commun.*, 2023, **14**, 38–44.
- 20 X. Su, Z. Pan and L. An, *Int. J. Energy Res.*, 2019, **43**, 7433–7443.
- 21 A. Dessalle, J. Quílez-Bermejo, V. Fierro, F. Xu and A. Celzard, *Carbon N. Y.*, 2023, **203**, 237–260.
- 22 B. Senthil Rathi, P. Senthil Kumar, G. Rangasamy and S. Rajendran, *Int. J. Hydrogen Energy*, 2024, **52**, 115–138.
- 23 T. Lepage, M. Kammoun, Q. Schmetz and A. Richel, *Biomass and Bioenergy*, 2021, **144**, 105920.
- 24 A. Lasia, *Int. J. Hydrogen Energy*, 2019, **44**, 19484–19518.
- 25 W. Zhang, R. Xi, Y. Li, Y. Zhang, P. Wang and D. Hu, *Int. J. Hydrogen Energy*, 2022, **47**, 32436–32454.
- 26 P. Yu, F. Wang, T. A. Shifa, X. Zhan, X. Lou, F. Xia and J. He, *Nano Energy*, 2019, **58**, 244–276.
- 27 Y. Qi, H. Guo, J. Li, L. Ma, Y. Xu, H. Liu, C. Wang and Z. Zhang, *ChemPhysMater*, 2024, **3**,

- 157–186.
- 28 Y. Li, Y. Wu, S. A. Delbari, A. Kim, A. S. Namini, Q. Van Le, C. Xia, R. Luque, H. W. Jang, M. Shokouhimehr and R. S. Varma, *Mol. Catal.*, DOI:10.1016/j.mcat.2023.113003.
- 29 R. Chakraborty, K. Vilya, M. Pradhan and A. K. Nayak, *J. Mater. Chem. A*, 2022, **10**, 6965–7005.
- 30 Q. Zhang, E. Uchaker, S. L. Candelaria and G. Cao, *Chem. Soc. Rev.*, 2013, **42**, 3127–3171.
- 31 X. Liu, D. Wang and Y. Li, *Nano Today*, 2012, **7**, 448–466.
- 32 F. Wang, V. N. Richards, S. P. Shields and W. E. Buhro, *Chem. Mater.*, 2014, **26**, 5–21.
- 33 N. T. K. Thanh, N. Maclean and S. Mahiddine, *Chem. Rev.*, 2014, **114**, 7610–7630.
- 34 A. L. Rogach, D. V. Talapin, E. V. Shevchenko, A. Kornowski, M. Haase and H. Weller, *Adv. Funct. Mater.*, 2002, **12**, 653–664.
- 35 S. G. Kwon and T. Hyeon, *Small*, 2011, **7**, 2685–2702.
- 36 A. Y. Singapati and C. Ravikumar, *Langmuir*, 2023, **39**, 9325–9342.
- 37 G. K. Soon, Y. Piao, J. Park, S. Angappane, Y. Jo, N. M. Hwang, J. G. Park and T. Hyeon, *J. Am. Chem. Soc.*, 2007, **129**, 12571–12584.

CHAPTER 2

Cobalt-iron oxyhydroxide obtained from the metal phosphide: a highly effective electrocatalyst for the oxygen evolution reaction at high current densities.



2.1. ABSTRACT

The development of high current density anodes for the OER is fundamental to manufacturing practical and reliable electrochemical cells. In this work, we have developed a bimetallic electrocatalyst based on cobalt-iron oxyhydroxide that shows outstanding performance for water oxidation. Such a catalyst is obtained from cobalt-iron phosphide nanorods that serve as sacrificial structures for the formation of an oxyhydroxide through phosphorous loss concomitantly to oxygen/hydroxide incorporation. CoFeP nanorods are synthesized using a scalable method using TPOP as a phosphorous precursor. They are deposited without the use of binders on NF to enable fast electron transport, a highly effective surface area and a high density of active sites. The morphological and chemical transformation of the CoFeP NPs is analysed and compared with the monometallic cobalt phosphide, based on the structural and chemical characterization of the materials in alkaline media and under anodic potentials. The resulting bimetallic electrode presents a Tafel slope as low as 42 mV dec⁻¹ and low overpotentials for OER.

For the first time, an anion exchange membrane electrolysis device with an integrated CoFeP-based anode was tested at high current densities of 1 A cm^{-2} , demonstrating excellent stability and Faradaic efficiency near 100%. This work opens up a way for using metal phosphide-based anodes for practical fuel electrosynthesis devices.

2.2. INTRODUCTION

The production of fuels by electroconversion coupled with renewable sources is one of the backbones of a sustainable energy future. In most of these systems, such as the electrosynthesis of H_2 , NH_3 , or CO_2 reduction products, the corresponding cathodic reaction is usually coupled to the OER. Nevertheless, OER is the most sluggish reaction in the overall process and its complexity derives from the four reaction steps associated with this reaction. Consequently, a rational design of the anode requires strategies for overcoming these drawbacks. The use of multi-metallic catalysts is advantageous as can provide appropriate metallic sites for achieving a more effective reduction of the energy barriers associated with each step.^{1,2} To this end, a dispersion of metallic atoms in the electrode frame and skeleton should be ensured to achieve an adequate density of active sites with adjacent locations of the metallic sites to reach high production rates. Furthermore, this rational design of the anode must take into account its electrical conductivity to guarantee adequate electron transport, the mass transport to or from the active sites to prevent diffusion limitations and also the increase of the kinetic rate constant associated with the reactions taking place in the active site.

The use of metal oxides as electrocatalysts has the limitation of their low conductivity. Among the alternative compounds proposed, TMPs are excellent candidates, as some of them present metallic-like properties and exhibit much higher conductivities³ than the corresponding metal oxides. TMPs have attracted much interest as electrocatalysts for water splitting for both half-reactions, HER and OER.^{1,4-7} In this context, cobalt, iron and the corresponding bimetallic phosphides have been reported as electrocatalysts for OER, displaying low overpotentials.^{1,7,8} So far, most of these studies have been focused on the electrocatalytic activity at low and medium currents ($10\text{-}50 \text{ mA cm}^{-2}$) while working at high current densities, $> 1 \text{ A cm}^{-2}$, has barely been studied despite its relevance concerning the demonstration of industrial feasibility. For achieving such high production rates, more attention must be paid to different features such as high active site density, high turnover frequency and efficient mass transport of the chemical species from and toward the electrocatalysts to optimize the reaction overpotentials.

However, most metal transition compounds are not stable under the oxidizing conditions of OER and the influence of the chemical transformation of these materials in the catalytic reaction should be considered.^{8–11} Usually, metal (oxy)hydroxides are generated in situ at the surface of oxides, selenides, or even phosphides.^{3,9,10,12–14} In some cases, the transformation is not only limited to the surface, and also affects the electrocatalyst bulk, which can be detrimental if the new material possesses low conductivity. A detailed analysis of the material conversion and the role of the non-metallic element needs to be faced for a complete rational design of the anode. Metal (oxy)hydroxides are well known to have a high electrocatalytic performance, providing highly active sites for OER,^{9,15–17} especially those containing Fe, Co or Ni.^{18–20} In fact, for these materials, the combination of Fe with Ni or Co has led to improved activity.²¹ The enhancement of the electrochemical activity for OER in bimetallic CoFe-based electrocatalysts compared with the corresponding monometallic compounds has also been corroborated by observing a decrease in the overvoltages.^{9,22–24} This is a critical aspect in the design of the anodes for achieving commercially viable electrolyzers for fuel production.

In this work, we report on a detailed investigation of CoFe bimetallic phosphide and the transformation mechanism in alkaline electrolyte leading to high performance anodes for OER at high current densities, $>1 \text{ A cm}^{-2}$. The rational procedure to prepare the electrodes involves as the first step, the synthesis of tiny nanorods mainly composed of CoFeP. They are obtained by a “heating up” process, using triphenyl phosphite which is advantageous against other phosphorous precursors because is air-stable and inexpensive.²⁵ A NF substrate has been selected as a 3D scaffold of the electroactive material because of its high conductivity and porous structure. The simplicity of the method employed for loading the electrocatalyst should be highlighted because of its potential scalability and the fact that no additives or heat treatments are used. The CoFeP/NF electrodes were characterized from a morphological, structural, physicochemical and functional point of view before and after OER in alkaline electrolyte. The most significant results concern the depletion of phosphorus (linked to the formation of CoFe oxyhydroxide) and the radically different morphology between the initial nanorod-like shape found in the CoFeP powder and the nanoplate-like shape of the oxyhydroxide after OER. All of these characteristics allow a rational design of the anode for working at high current densities. Then, the effectivity of the proposed strategy for the anode design is tested for reaching 1 A cm^{-2} for OER. The significance of the transformation of the bimetallic phosphide into a bimetal oxyhydroxide and the role played by phosphorus have been corroborated.

2.3. EXPERIMENTAL

2.3.1. Synthesis of colloidal CoFeP NPs

For the synthesis of the CoFeP NPs,²⁶ 2.4 g (10 mmol) of HDA (90%, Acros Organics) were mixed with 10.0 mL of ODE (90%, ACROS Organics) and 2.6 mL (10 mmol) of TPOP (99%, ACROS Organics) in a 50 mL flask. The system was degassed, heated to 130 °C and kept at this temperature for 1 h to remove low boiling point impurities, moisture, and oxygen. Then, the mixture was cooled down to 60 °C and 4 mL of ODE containing 380 mg (1 mmol) $\text{Co}_2(\text{CO})_8$ (95%, ACROS Organics) and 0.3 mL (2 mmol) $\text{Fe}(\text{CO})_5$ (Sigma Aldrich) were added. Firstly, the temperature was increased to 230 °C, and then stirred for 30 min, secondly heated to 300 °C for 40 min and kept at this temperature for 1 h. Finally, the system was allowed to cool down to 200 °C by removing the heating mantle and subsequently cooled rapidly down to room temperature with a water bath. The product was precipitated using acetone and centrifuged for 3 min at 7500 rpm. To remove organics, three dispersion and precipitation cycles using chloroform and acetone were additionally carried out to obtain a cleaner CoFeP precipitate. To synthesize the Co_2P NPs used as reference material, an identical procedure was followed but without adding the iron precursor.

2.3.2. Ligand removal

10 mL of a dispersion CoFeP or Co_2P in hexane (10 mg mL^{-1}) was mixed with 10 mL acetonitrile to form a two-phase mixture. Afterward, 1 mL HBF_4 solution (48%) was added. The resulting solution was sonicated until the NPs transferred from the upper to the bottom layer. Finally, these NPs were washed with ethanol three times and dispersed in 10 mL ethanol with around 0.5 mL of DMF for further use.

2.3.3. Electrode preparation

First, NF substrates were cleaned in an ultrasonic bath in 1 M HCl, water and ethanol for 10 min in each one. A suspension of 10 mg mL^{-1} of the CoFeP NPs in ethanol was prepared and sonicated for 30 min. The cleaned NF substrates were dipped into this suspension for 30 s and subsequently, the dispersion excess was removed. Finally, the electrode was dried at ambient temperature. The deposited amount of catalyst used for the objective of this work was estimated to be enough to guarantee enough active site density $> 10^{18} \text{ cm}^{-2}$ to facilitate reaching a current density higher than 1 A cm^{-2} . Electrodes with a higher amount of electrocatalyst have been prepared by repeating the immersion and drying steps up to four times. Unless otherwise

stated, the electrodes were prepared with a single immersion and the samples named “after OER” were subjected to a current density of ca. 120 mA cm⁻² during 2 h.

2.3.4. Morphological, Structural and Physicochemical characterization

Structural characterization was performed by XRD using a Bruker D8 Advance diffractometer equipped with a Cu K α (1.5406 Å) radiation source, LYNXEYE super speed detector and Ni filter. A Bragg–Brentano (θ – 2θ) configuration was used with a step size of 0.025°. The morphology of the electrodes was analysed by a Zeiss Auriga 60 FESEM. Both the HRTEM and STEM-EELS are obtained in an FEI F20 at 200kV. The HRTEM was acquired with a condenser aperture of 100 μ m, no objective aperture, spot size 3 and a BM-UltraScan CCD camera. The STEM-EELS was acquired with a condenser aperture of 70 μ m, no objective aperture, nominal camera length 30 mm, spot size 6, and Gatan EF-CCD camera. The same conditions apply for STEM-EDS, with a detector EDAX SUTW X-Ray detector, 136 eV resolution ($Z > Z(\text{Be})$), and a detector area of 30 mm². The EELS and EDS supporting STEM images are from an annular dark field detector (DF4). For analysing the samples, the initial CoFeP or Co₂P samples were diluted in hexane before deposition on the grid. For the analysis of the electrode after OER, the electrocatalyst was scraped from the NF substrate, and the resulting powder was dispersed in hexane by sonication before the deposition on the HRTEM grid. For the XPS analysis, a monochromatic X-ray source Al K α line was used in both a PHI 5500 Multitechnique System (Physical Electronics) for the electrodes before OER and a NEXSA X-Ray Photoelectron Spectrometer (Thermo-Scientific) for the electrodes after OER.

2.3.5. Electrochemical measurements

The electrochemical performance of the CoFeP-based electrodes was analysed with a Biologic VMP-300 potentiostat using a three-electrode cell. All the potentials were measured against an Ag/AgCl reference electrode. The potentials in the RHE scale are calculated according to: $E(\text{vs RHE}) = E(\text{vs Ag/AgCl}) + 0.205 \text{ V} + 0.059 \cdot \text{pH}$. To evaluate the oxygen evolution reaction activity, LSV and CV were performed at a scan rate of 5 mV s⁻¹ in 1 M KOH. All the potentials were corrected with the IR drop, and the corresponding R was determined by EIS. The overpotentials were calculated in all cases as $\eta = E - 1.23 \text{ V}$, where E is the applied potential vs RHE. The determination of C_{dl} by CV was performed between 0.1 and 0.2 V vs Ag/AgCl, a potential region with no faradaic processes, at different scan rates. The electrochemically ECSA was calculated as C_{dl}/C_s , where C_s is a reference capacitance for a planar surface taken as 40 μ F cm⁻².^{27,28} Nyquist plots were obtained by EIS in the frequency range of 50 kHz to 100 mHz and employing a signal

amplitude of 10 mV. The fitting of the experimental EIS curves to the equivalent circuit was performed with the Biologic software. The calculation of the TOF can differ from study to study.²⁷ In this work, TOF is calculated as the number of product molecules (O_2) per second and active site: $TOF = j A / (4 N e)$, where j is the current density, A is the area, N is the number of active sites and e is the elementary charge constant ($1.6 \cdot 10^{-19}$ C). The calculated number of active sites is $3.2 \cdot 10^{18}$ and $2.3 \cdot 10^{18}$ for CoFeP and Co_2P , respectively. They are estimated considering that both Co and Fe metallic atoms at the surface act as active sites. The metallic content was calculated from the measure of the electrode mass before and after the electrocatalyst loading and the elemental ratios obtained by EDS in the as prepared electrodes. In the full cell assembly, water splitting was performed in a two-electrode configuration with the two compartments separated by a Sustainion (Dioxide Materials) alkaline exchange membrane. The gas outlets from the anodic and cathodic compartments were connected to two inverted graduated cylinders filled with water to measure accumulated O_2 and H_2 , respectively. For the theoretical calculation of the volumes, they are considered ideal gases. The presence of H_2 was corroborated by gas chromatography using He as a carrier gas.

2.4. RESULTS AND DISCUSSION

2.4.1. Characterization of the CoFeP NPs and the fabricated CoFeP/NF electrode

The bimetallic CoFeP NPs obtained by the TPOP route were characterized in terms of morphology, crystallinity and composition. HRTEM images were performed to obtain information about the nanostructure morphology. Figure 2.1a and b and Figure 2.S1 show the synthesized CoFeP NPs exhibiting a nanorod-like shape with lengths up to about 18 nm and a diameter of 2-3 nm. FFT in Figure 2.1b reveals the presence of the CoFeP PNMA 62 phase that is according to the XRD analysis in Figure 2.S2. Importantly, the planes observed in isolated nanorods (Figure 2.1a) can be ascribed to the (020) and (210) planes of CoFeP PNMA. Figure 2.1a shows a sketch of the nanorod crystallographic arrangement. It was observed that these rods present a growth direction [010] (and its corresponding (020) observed planes), that coincides with the longitudinal axis of the nanorods, which is further supported by its relative orientation with the resolved (210) planes of CoFeP. Additionally, EELS compositional maps of Co, Fe and P were also performed to get insights into the nanostructure composition. Figure 2.1c shows a particle composed of the coalescence of different nanorods. A similar spatial distribution of the three elements along all the particles was found, coherent with the expected stoichiometry of the CoFeP. Nevertheless, EELS quantification reveals a slightly higher concentration of Co against Fe, $Co/Fe \approx 1.5$. Monometallic Co_2P NPs were also analysed by

HRTEM. They also exhibit rod-like shapes (Figure 2.S3), having similar sizes to the bimetallic nanorods. The planes found have interplanar distances similar to that of CoFeP and are according to the Co₂P PNMA, which was further corroborated by FFT (Figure 2.S4). As in the case of CoFeP, Co and P, are homogeneously distributed through the Co₂P nanorods as revealed by EELS (Figure 2.S5). In both, CoFeP and Co₂P NPs the metal to phosphorous ratio, based on the atomic concentration obtained by EDS, was near 1.3, which is lower than the stoichiometric. This can be partly due to the presence of oxygenated species such as metal phosphates or the presence of CoP as a secondary phase.

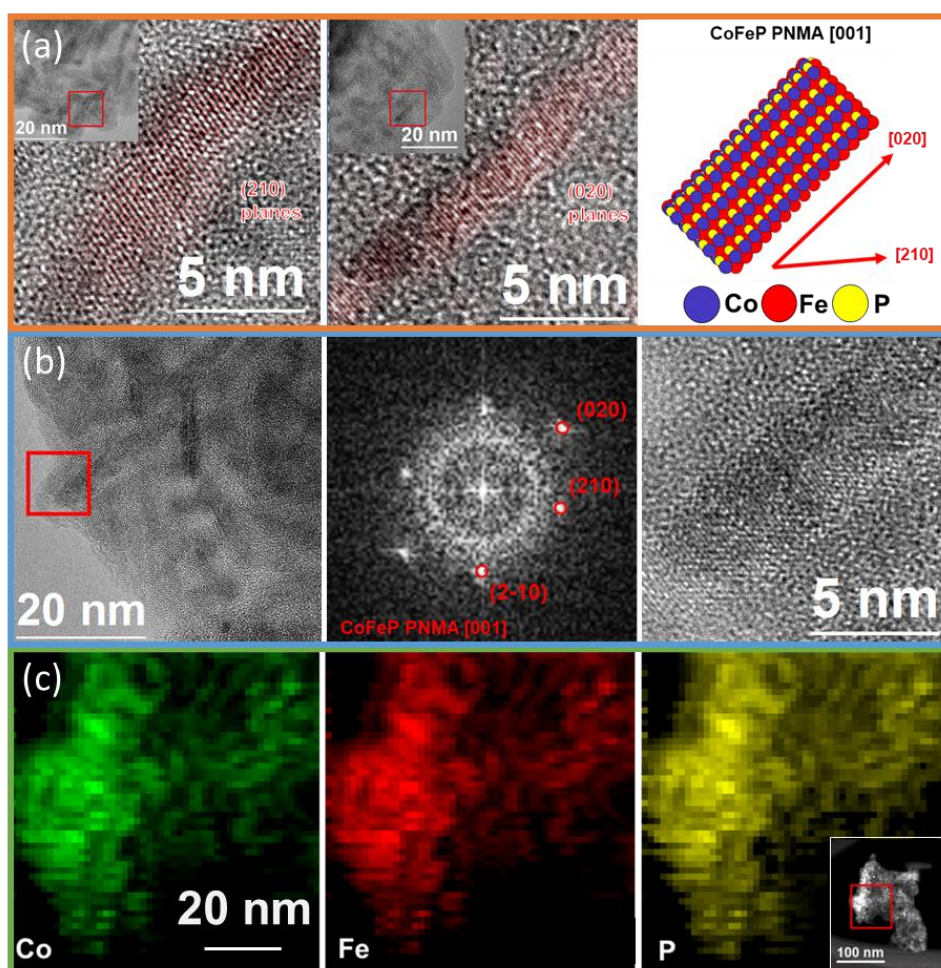


Figure 2.1. (a) HRTEM images showing individual nanorods (from the red squared region in the lower magnification images in the inset) and the schematic illustration of the orientation of the nanorods on the right side. (b) FFT spectrum of the HRTEM image on the right that corresponds to the red squared region of the image on the left showing the planes ascribed to the CoFeP PNMA 62. (c) EELS compositional maps of Co, Fe and P in CoFeP nanorods. The inset shows the corresponding STEM-ADF image.

XPS is used to gather information about the first fourth or sixth atomic monolayers (2-3 nm) at the sample surface. This has been employed to characterize the surface composition and chemical nature of the synthesized electrocatalyst, although it can be altered after its deposition on the NF by the interaction with the ambient air. The full survey spectrum of a bare CoFeP/NF electrode shown in Figure 2.S6 reveals the presence of Co, Fe, P, O and C. In the P 2p spectra (Figure 2.S7), the largest peak is located near 133.3 eV and can be correlated with the presence of phosphate species.^{9,10} This confirms that the surface of the electrocatalyst is composed of metal phosphate rather than phosphide after air exposure, which usually occurs in metal phosphides.^{15,23} The Co 2p spectrum in Figure 2.S7 exhibits the 2p_{3/2} and 2p_{1/2} signals with the overlapping of different contributions including satellite peaks. The fact that the position of the strongest peak in the Co 2p^{3/2} region (781.2 eV) was higher than the typical metal peak positions of oxides, together with the predominant peak in the O 1s region at 531.1 eV (Figure 2.S7) are in agreement with the presence of metal phosphate.^{29,30} The small peak located at 778.1 eV in the Co 2p^{3/2} could be assigned according to some authors to the presence of metal phosphides, but the corresponding Co 2p^{1/2} signal is challenging to be identified because of the small amount of phosphide detected at the surface.^{9,24} Accordingly, a very small peak at 130.1 eV in the P 2p spectrum can be attributed to metal phosphide. The Fe 2p^{3/2} signal (Figure 2.S7) revealed the presence of oxidized iron species.⁹ Therefore, the results from the XPS characterization indicate that the outer layer of the electrocatalyst surface shows a transformation from metal phosphide to phosphate, even when the samples were stored in a protective atmosphere before the analysis.

2.4.2. Characterization of the CoFeP-based electrodes working as anodes for OER

Metal phosphides can be unstable in alkaline media (1 M KOH) under anodic conditions, then, a detailed physicochemical characterization was performed before and after OER to study the material transformation and especially the role of phosphorous. Despite the transformation, the electrodes were stable for OER and any significant decay of the current was observed at about 100 mA cm⁻² (Figure 2.S8). Figure 2.2a-d show the morphology of the CoFeP NPs on the NF surface before and after OER by FESEM images. The small particle size of the CoFeP nanorods favors a good dispersion of the electrocatalyst on the NF surface. In the as-prepared electrodes, a porous network of interconnected NPs with spherical shape is observed (Figure 2.2a), probably derived from the coalescence of the initial CoFeP nanorods observed in Figure 2.1a and the oxidation of the surface leading to an outer metal phosphate layer. The CoFeP/NF electrodes were analyzed after CA at different times selecting a potential in the OER region with a current

density near 100 mA cm^{-2} . A radical change of the overall morphology was observed (Figure 2.2b-d) after OER, now displaying nanostructures with a plate-like shape resembling 2D units and thus conferring high effective area to the electrode. However, there was no significant evolution of the morphology from 5 to 120 min of OER. The approximate dimensions of the nanoplates are 200-400 nm and 10-40 nm in length and thickness, respectively. For comparison purposes, the $\text{Co}_2\text{P}/\text{NF}$ electrodes were also analyzed by SEM before and after OER (Figure 2.S9). A similar morphological change was observed after 120 min of OER, although in this case, the nanoplates were smaller with approximated lengths of 60 nm and thickness of 10 nm.

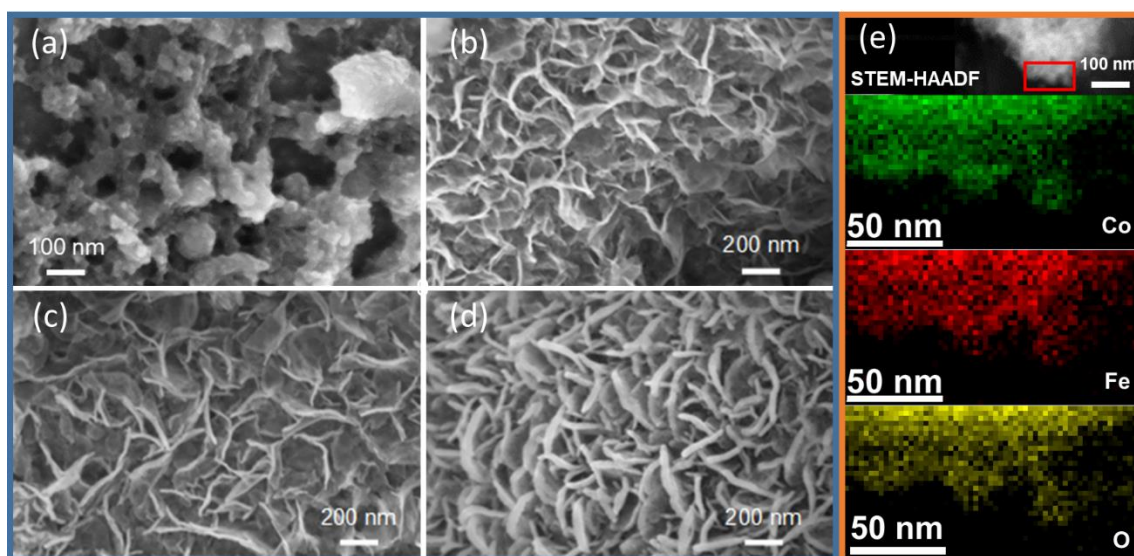


Figure 2.2. SEM micrographs showing the morphology of the (a) as prepared and after (b) 5, (c) 30 and (d) 120 min of OER for a CoFeP/NF electrode. (e) EELS compositional maps of the powder obtained by scrapping the electrocatalyst from the electrode surface of the CoFeP/NF electrode after 120 min of OER.

Despite the huge transformation of the material, a homogeneous distribution of Co and Fe is observed in the EELS maps as shown in Figure 2.2e. Remarkably, we could not observe any presence of crystalline planes in the HRTEM images neither in the corresponding FFT patterns obtained in the samples after OER, pointing out the amorphous nature of the transformed material. Furthermore, the high oxygen signal together with the absence of phosphorous, suggests that oxygenated phases as oxygen and hydroxyl groups have replaced the initial phosphide/phosphate species forming oxyhydroxide structures. To further investigate these assumptions, high resolution XPS spectra in Figure 2.3 and S10 in the electrodes after OER are compared with the previous results using fresh samples (Figure 2.S7). To increase the intensity of the XPS signal, the analysis was performed in a sample synthesized by four immersions in the iron precursor dispersion. We must stand out on several significant features. On one hand, there

is a low concentration of residual phosphorous at the surface (see Table 2.S1). On the other hand, a significant change in the O 1s spectrum is noticeable after OER (Figure 2.3). Apart from the peak around 532.5 eV that can be attributed to absorbed H₂O, the main signal can be deconvoluted in two peaks. The one at 529.4 eV is according to M-O and the largest peak at 530.8 eV would correspond to M-OH species supporting the presence of metal oxyhydroxides.¹⁵ These characteristics are endorsed for the measured spectra in the 2p regions of cobalt and iron in Figure 2.3, 2.S7 and 2.S10, in which the most intense peaks are shifted to lower energies in agreement with the expected values of oxyhydroxides compared to the initial phosphates. Concretely, the peak at 779.8 eV in the Co 2p region can be correlated with Co³⁺. Therefore, after the electrochemical measurements in alkaline media, the material is transformed in terms of morphology and composition from the initial CoFeP to CoFeO_xH_y material. After immersing in the 1 M KOH solution, a morphological change already occurs, afterwards, the cyclic voltammogram of the CoFeP (Figure 2.S11) shows an anodic irreversible peak appearing at 1.35 V vs RHE that is only present in the first cycle. This peak has been attributed to the irreversible evolution of CoOOH.^{19,31,32} Accordingly, a peak near the same potential region was also observed in the Co₂P/NF electrodes. After this anodic peak, the current densities for OER remain constant as evidenced by the overlapping of the first and second voltametric curves in Figure 2.S11. The complete morphological transformation of the CoFeP structure together with the phosphorous loss leading to CoFeO_xH_y is favoured by the small size of the initial NPs and the interconnected porous network of these NPs that facilitate the permeability of the alkaline electrolyte. Raman analysis in Figure 2.S12 supports the presence of metal oxyhydroxide. Concretely, the bands at 575 and 675 cm⁻¹ can be correlated with cobalt and iron oxyhydroxides,³³⁻³⁵ although the presence of oxides/hydroxides as secondary phases cannot be discarded. On the other hand, Co₂P/NF electrodes were also analysed by XPS after OER (Figure 2.S13). No evidence of different oxidation states of cobalt with respect to the bimetallic material is found as the Co 2p region presents the same characteristics.

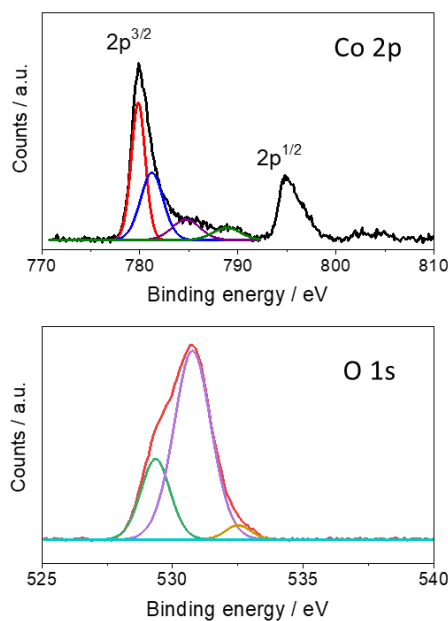


Figure 2.3. XPS spectra in the Co 2p and O 1s regions for the CoFeP/NF electrodes after OER.

2.4.3. Electrochemical analysis of the electrodes using CoFeP as electrocatalyst

The electrochemical activity of the initial bimetallic CoFeP/NF transformed to CoFeO_xH_y/NF has been investigated in 1 M KOH electrolyte. Figure 2.4a shows the cyclic voltammograms after IR correction for the CoFeP/NF electrodes, compared with both the Co₂P/NF electrode and the bare NF scaffold. The bimetallic CoFeP/NF electrode presents the best catalytic activity for OER, outperforming the monometallic Co₂P/NF. The overpotentials for OER at 10 and 100 mA cm⁻², are 285 and 335 mV for CoFeP/NF and 345 and 410 mV for Co₂P/NF, respectively. The bare NF also presents electrochemical activity for OER in alkaline media,^{36–38} but significantly lower than the bimetallic phosphide-loaded electrodes. The Tafel representation depicted in Figure 2.4b further confirms the favourable OER kinetics in the bimetallic electrocatalyst. The Tafel slope for Co₂P/NF is 53 mV dec⁻¹, while for CoFeP/NF is as low as 42 mV dec⁻¹. To the best of our knowledge, the latter value is the lowest reported for cobalt iron phosphide-based anodes without using a hybrid material (as compared in Table 2.S2). Additionally, the behaviour of the CoFeP/NF electrodes was tested during cycling for OER displaying good stability after 500 cycles (Figure 2.S14).

The effect of the deposited amount of electrocatalysts was studied by repeating different cycles of immersion in the CoFeP dispersion and drying up to four times, leading to different catalyst loading (see inset of Figure 2.S15a). The potentials for a given current density are reduced as the catalyst loading increases as expected. For 10 mA cm⁻², the overpotential is 360 mV for four

immersions, 15 mV lower than for the one of a single immersion (Figure 2.S15a). However, as the catalyst loading increases the current density normalized by the mass loading decreases (Figure 2.S15b). Then, for the lowest loaded amount of catalyst, there is an optimum dispersion of the CoFeP on the NF maximizing the number of reactive sites available per overall amount of catalyst. The overpotentials achieved in this work, considering the loaded amount of electrocatalyst, are one of the lowest reported for CoFeP-based anodes for OER without the addition of other binders or conductive materials (see Table 2.S2).

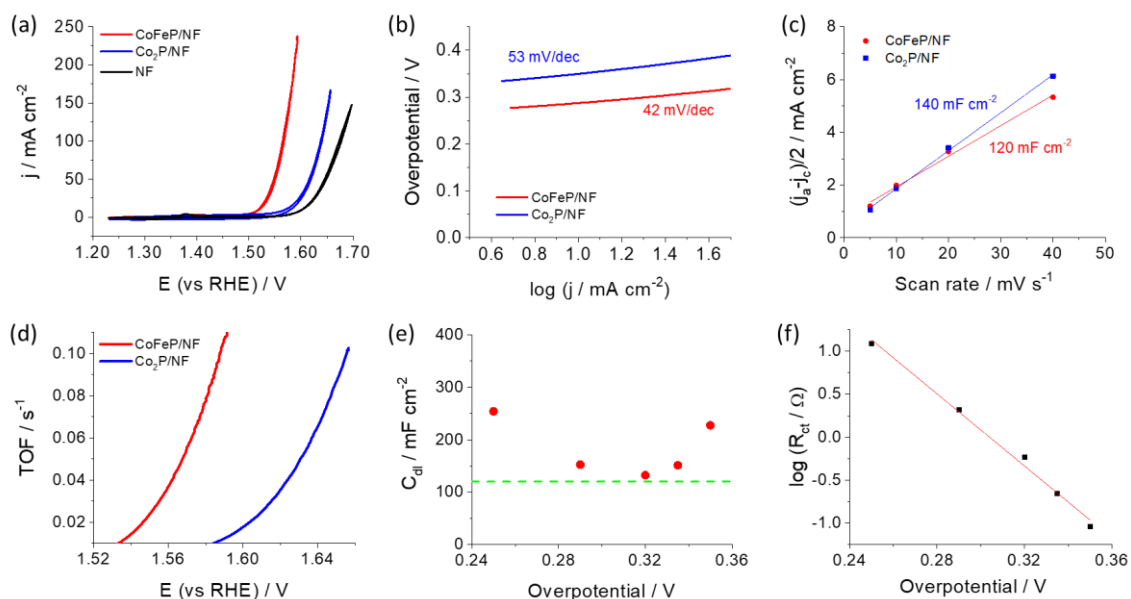


Figure 2.4. (a) Cyclic voltammogram recorded at 5 mV s^{-1} , (b) Tafel plots, (c) $(j_a - j_c)/2$ vs scan rate plot and (d) calculated TOF values as a function of the potential for CoFeP/NF and Co₂P/NF in 1 M KOH. (e) C_{dl} and (f) $\log(R_{ct} / \Omega)$ vs overpotential from the Nyquist plots for CoFeP/NF in 1 M KOH. The green line in (e) indicates the C_{dl} value obtained from cyclic voltammograms in Figure 2.4c and the red line in (f) the linear fitting of the points.

To get more insights into the origin of the catalytic activity of CoFeO_xH_y obtained from the bimetallic phosphide, the double-layer capacitances were calculated from the $(j_a - j_c)/2$ versus the scan rate plot obtained from Figure 2.S16. The calculated C_{dl} values are similar for the CoFeP/NF and Co₂P/NF and are estimated as 120 and 140 mF cm^{-2} , respectively, as shown in Figure 2.4c. Then, ECSA values of 3000 and 3500 cm^2 are obtained for CoFeP/NF and Co₂P/NF, respectively, referred to a planar surface. The huge ECSA values can be correlated with a high density of active sites due to good dispersion of the material favoured by the low particle size and the porous structure of the electrode scaffold that allow the full penetration of the electrolyte.

Figure 2.4d displays TOF values deduced from the calculated number of active sites based on the loaded amounts of electrocatalysts. A TOF value of 0.1 s^{-1} is reached at 358 mV for the CoFeP/NF, while for Co₂P/NF 425 mV is required. This demonstrates that despite both electrodes possessing similar ECSA and estimated number of active sites, the bimetallic phosphide exhibits a faster kinetic toward OER. This may be caused by the catalytic combined effects of the metallic Co and Fe adjacent sites cooperating on the four steps of the water oxidation reaction. This is supported by the lower value of Tafel slope in the CoFeP/NF electrode. In this regard, the concentration of iron is not critical in the OER activity, as when the concentration of iron decreases by 40%, the bimetallic electrode produces similar overpotentials. This is in agreement with a previous work using comparable Co/Fe ratios.¹⁵ A contribution derived from the nickel substrate cannot be discarded as active nickel species for OER can be generated in the alkaline electrolyte.

Nyquist plots obtained from electrochemical impedance spectroscopy are useful to better understand the electrocatalyst kinetics for OER. Then, they were recorded at different applied potentials (Figure 2.S17a), and the obtained spectra were fitted according to the model circuit displayed in Figure 2.S17b. R_{Ω} is the electrolyte resistance and the R_i and Q_i (a constant phase element) at high frequencies can be tentatively associated with the Ni/electrocatalyst interface or to the presence of a passive film.³⁹ C_{dl} and R_{ct} are related to the charge transfer to the electrolyte and they can provide information about the OER kinetic parameters. Concretely, the exchange current density (j_0) and the Tafel slope (b) can be estimated from the Nyquist plots using the following expression:⁴⁰⁻⁴²

$$\log\left(\frac{1}{R_{ct}}\right) = \log\left(\frac{di}{d\eta}\right) = \frac{1}{b}\eta + \log\left(\frac{2.3j_0}{b}\right) \quad (1)$$

where $b=2.3RT/\alpha_a F$ in mV dec^{-1} , being α_a the overall transfer coefficient given by $\alpha_a=(n_f/v+n_r\beta_a)$, where n_f is the number of electrons transferred before the RDS, v is the stoichiometric number with a typical value of one, n_r is the number of electrons transferred in each occurrence of the RDS, and β_a is correlated with the symmetry factor.^{43,44} On one hand, C_{dl} values calculated from Figure 2.S17 are represented in Figure 2.4e as a function of the overpotential. Although they are in the same order of magnitude as that obtained by cyclic voltammograms in the region without faradaic currents (Figure 2.4c), there exists some dispersion of values in the considered range of potentials. On the other hand, according to equation (1), Figure 2.4f shows a linear relationship between $\log(R_{ct})$ and η . The points in Figure 2.4f can be fitted to a straight line with good fitting ($R^2 = 0.996$). The Tafel slope (b) can be calculated as 48 mV dec^{-1} while a value of 42 mV dec^{-1}

was determined from the voltammogram in Figure 2.4b. Then, the overall α_a can be calculated as 1.24-1.41. Such values suggest that a step subsequent to the first electron transfer is the RDS with $\nu=1$, $n_f=1$ and $n_r=1$.⁴⁴ According to equation (1), from the intercept with the y-axis the exchange current density is calculated to be $1.1 \cdot 10^{-5} \text{ mA cm}^{-2}$.

The excellent characteristics based on the kinetics and the active site density suggest that the synthesized CoFe-based anodes are good candidates for working at high current densities as feasible and reliable electrodes. Thus, the electrochemical activity of these anodes was evaluated at higher applied potentials and the effect of the temperature was studied. Figure 2.5a shows the potential region of current densities $> 1 \text{ A cm}^{-2}$ at 22 °C and 50 °C. For reaching 1 A cm^{-2} , the overpotential is only 475 mV, and they decrease by 80 mV when the temperature rises to 50 °C. Furthermore, the stability tests at 1 A cm^{-2} in Figure 2.5b show that the current density remains constant at 22 °C while at 50 °C there is a slight decrease with time may be due to a lack of thermal stability of the experimental set-up. Table 2.1 summarizes the approximate overpotential values achieved for 10, 100 and 1000 mA cm^{-2} based on Figure 2.5a.

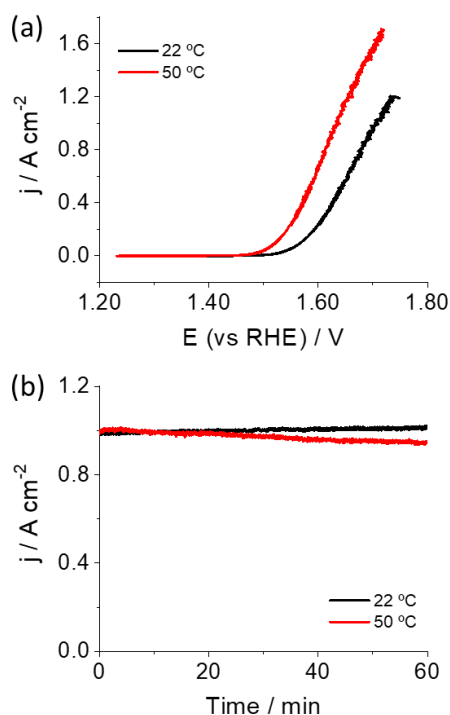


Figure 2.5. (a) Cyclic voltammogram and (b) chronoamperogram at a current density of ca. 1 A cm^{-2} at 22 °C and 50 °C for the CoFeP/NF electrode in 1 M KOH.

Table 2.1. Overvoltage for OER at selected current density values at 22 and 50 °C.

$j / \text{mA cm}^{-2}$	η / mV	
	22 °C	50 °C
10	285	240
100	335	290
1000	475	405

2.4.4. Anion exchange membrane water electrolysis performance

The stability of the electrocatalysts is a critical issue in fuel production and should be tested under more realistic conditions of continuous electrolyte flow to better evaluate its commercial viability. For this goal, the developed cobalt iron oxyhydroxide anode was integrated into an electrolyser schematized in Figure 2.6a for H₂ and O₂ production, which is a relevant configuration for an industrial application. The cell comprises two compartments separated by an alkaline anion membrane, with the anolyte and catholyte recirculating at a high flow rate through the respective compartments. Consequently, this configuration allows for the separation and collection of both produced gases, where hydrogen is evolving in the Ti/Pt plate (10 cm²), and oxygen is evolving in the CoFeO_xH_y/NF anode with a geometric area of 1 cm².

The stability of the full cell was examined at a high current density of nearly 1 A by heating the electrolytes at 50 °C. Figure 2.6b shows good stability of the current during 2 h, without any significant decay. Additionally, the volumes of H₂ and O₂ were measured for 10 min after 2 h at 1 A in the same conditions. The inset of Figure 2.6b displays the points corresponding to the measured gas volumes while the straight lines correspond to the calculated values. An excellent agreement between the experimental and theoretic values was found, which means that the faradaic efficiency for OER and HER in both processes is near 100%. The outlet gas stream from the cathode was analysed by gas chromatography confirming the presence of hydrogen gas. Similar results were obtained at room temperature (Figure 2.S18) displaying also good stability. In that case, because of the lack of temperature control, an initial increase in the current was reported before thermal equilibration.

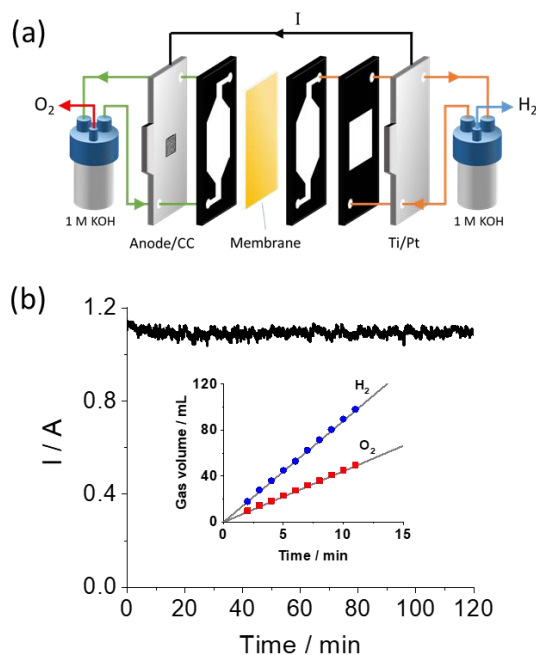


Figure 2.6. (a) Sketch of the alkaline exchange membrane electrolyser using geometric electrodic areas of 1 cm^2 in the anode and 10 cm^2 for the Ti/Pt cathode. (b) Chronoamperogram in the full cell depicted in (a) at a current density near 1 A and heating the electrolyte to $50 \text{ }^\circ\text{C}$. Inset: experimental (points) and calculated accumulated (solid lines) volumes of H_2 and O_2 .

2.5. CONCLUSIONS

In this work, an efficient anode for OER obtained by the in-situ generation of amorphous cobalt iron oxyhydroxide from the corresponding bimetallic phosphide on NF is reported. In the chemical conversion, phosphorous acts as a sacrificial element for homogeneous metal oxyhydroxide formation facilitated by the electrolyte permeation within the nanoporous structure. The initial CoFeP/NF electrode is synthesized from tiny rod-like NPs of bimetallic phosphide obtained by a feasible and scalable synthesis. These nanorods were dispersed in a 3D framework of a highly conductive metallic NF as a key element in the anode design. It ensures a high density of active sites as well as an appropriate pore size to guarantee the release of oxygen gas. Under alkaline media and anodic polarization, apart from the phosphorous depletion, the morphology radically changes from the initial nanorods to CoFe-oxyhydroxide nanoplates with a high electrochemically active surface area. Remarkably, this procedure guarantees maintaining a homogeneous distribution of metal atoms on a NF that allows for a rational design of the anodes to achieve a high density of active sites. The presence of Co and Fe atoms promotes favourable catalytic effects on the four-step reaction of water oxidation. Then, this rational anode design allows achieving working conditions of high current densities (higher than 1 A cm^{-2}) at optimized overpotentials lower than 500 mV for 1 A and Tafel slope as low as 42 mV dec^{-1} .

Remarkably, apart from the feasible and scalable manufacturing route of the CoFeO_xH_y/NF electrode, its stability was excellent in an alkaline exchange membrane flow cell at 1 A, which makes this electrode a robust and promising anode in high production rate devices for fuel electrosynthesis.

2.6. REFERENCES

1. Li, Y.; Dong, Z.; Jiao, L. Multifunctional Transition Metal-Based Phosphides in Energy-Related Electrocatalysis. *Adv. Energy Mater.* **2020**, *10*, 1902104.
2. Zhang, T.; Han, X.; Liu, H.; Biset-Peiró, M.; Zhang, X.; Tan, P.; Tang, P.; Yang, B.; Zheng, L.; Morante, J. R.; Arbiol, J. Quasi-Double-Star Nickel and Iron Active Sites for High-Efficiency Carbon Dioxide Electroreduction. *Energy Environ. Sci.* **2021**, *14*, 4847–4857.
3. Jin, Z.; Li, P.; Xiao, D. Metallic Co₂P Ultrathin Nanowires Distinguished from CoP as Robust Electrocatalysts for Overall Water-Splitting. *Green Chem.* **2016**, *18*, 1459–1464.
4. Xiao, P.; Chen, W.; Wang, X. A Review of Phosphide-Based Materials for Electrocatalytic Hydrogen Evolution. *Adv. Energy Mater.* **2015**, *5*, 1500985.
5. Pei, Y.; Cheng, Y.; Chen, J.; Smith, W.; Dong, P.; Ajayan, P. M.; Ye, M.; Shen, J. Recent Developments of Transition Metal Phosphides as Catalysts in the Energy Conversion Field. *J. Mater. Chem.* **2018**, *6*, 23220–23243.
6. Xu, S.; Zhao, H.; Li, T.; Liang, J.; Lu, S.; Chen, G.; Gao, S.; Asiri, A. M.; Wu, Q.; Sun, X. Iron-Based Phosphides as Electrocatalysts for the Hydrogen Evolution Reaction: Recent Advances and Future Prospects. *J. Mater. Chem. A* **2020**, *8*, 19729–19745.
7. Dutta, A.; Pradhan, N. Developments of Metal Phosphides as Efficient OER Precatalysts. *J. Phys. Chem. Lett.* **2017**, *8*, 144–152.
8. Zhang, H.; Maijenburg, A. W.; Li, X.; Schweizer, S. L.; Wehrspohn, R. B. Bifunctional Heterostructured Transition Metal Phosphides for Efficient Electrochemical Water Splitting. *Adv. Funct. Mater.* **2020**, *30*, 2003261.
9. Liu, X.; Yao, Y.; Zhang, H.; Pan, L.; Shi, C.; Zhang, X.; Huang, Z. F.; Zou, J. J. In Situ-Grown Cobalt-Iron Phosphide-Based Integrated Electrode for Long-Term Water Splitting under a Large Current Density at the Industrial Electrolysis Temperature. *ACS Sustain. Chem. Eng.* **2020**, *8*, 17828–17838.
10. Peng, Z.; Qiu, X.; Cai, G.; Zhang, X.; Dong, Z. Simultaneous Tuning of the Cation Content and Pore Structure of Cobalt-Iron Bimetal Phosphide to Enhance the Electrochemical Oxygen Evolution. *J. Alloys Compd.* **2020**, *842*, 155784.
11. Wang, G. B.; Hsu, C. S.; Chen, H. M. The Individual Role of Active Sites in Bimetallic Oxygen Evolution Reaction Catalysts. *Dalt. Trans.* **2020**, *49*, 17505–17510.

12. Burke, M. S.; Enman, L. J.; Batchellor, A. S.; Zou, S.; Boettcher, S. W. Oxygen Evolution Reaction Electrocatalysis on Transition Metal Oxides and (Oxy)Hydroxides: Activity Trends and Design Principles. *Chem. Mater.* **2015**, *27*, 7549–7558. Wu, Z. P.; Lu, X. F.; Zang, S. Q.; Lou, X. W. Non-Noble-Metal-Based Electrocatalysts toward the Oxygen Evolution Reaction. *Adv. Funct. Mater.* **2020**, *30*, 1910274.
13. Abed, J.; Ahmadi, S.; Laverdure, L.; Abdellah, A.; O'Brien, C. P.; Cole, K.; Sobrinho, P.; Sinton, D.; Higgins, D.; Mosey, N. J.; Thorpe, S. J.; Sargent, E. H. In Situ Formation of Nano Ni–Co Oxyhydroxide Enables Water Oxidation Electrocatalysts Durable at High Current Densities. *Adv. Mater.* **2021**, *33*, 2103812.
14. Zhang, X.; Zhang, X.; Xu, H.; Wu, Z.; Wang, H.; Liang, Y. Iron-Doped Cobalt Monophosphide Nanosheet/Carbon Nanotube Hybrids as Active and Stable Electrocatalysts for Water Splitting. *Adv. Funct. Mater.* **2017**, *27*, 1606635.
15. Wang, Y.; Kong, B.; Zhao, D.; Wang, H.; Selomulya, C. Strategies for Developing Transition Metal Phosphides as Heterogeneous Electrocatalysts for Water Splitting. *Nano Today* **2017**, *15*, 26–55. Hung, S. F.; Zhu, Y.; Tzeng, G. Q.; Chen, H. C.; Hsu, C. S.; Liao, Y. F.; Ishii, H.; Hiraoka, N.; Chen, H. M. In Situ Spatially Coherent Identification of Phosphide-Based Catalysts: Crystallographic Latching for Highly Efficient Overall Water Electrolysis. *ACS Energy Lett.* **2019**, *4*, 2813–2820.
16. Trotochaud, L.; Young, S. L.; Ranney, J. K.; Boettcher, S. W. Nickel-Iron Oxyhydroxide Oxygen-Evolution Electrocatalysts: The Role of Intentional and Incidental Iron Incorporation. *J. Am. Chem. Soc.* **2014**, *136*, 6744–6753.
17. Burke, M. S.; Kast, M. G.; Trotochaud, L.; Smith, A. M.; Boettcher, S. W. Cobalt-Iron (Oxy)Hydroxide Oxygen Evolution Electrocatalysts: The Role of Structure and Composition on Activity, Stability, and Mechanism. *J. Am. Chem. Soc.* **2015**, *137*, 3638–3648.
18. Pei, Y.; Ge, Y.; Chu, H.; Smith, W.; Dong, P.; Ajayan, P. M.; Ye, M.; Shen, J. Controlled Synthesis of 3D Porous Structured Cobalt-Iron Based Nanosheets by Electrodeposition as Asymmetric Electrodes for Ultra-Efficient Water Splitting. *Appl. Catal. B Environ.* **2019**, *244*, 583–593.
19. Chung, D. Y.; Lopes, P. P.; Farinazzo Bergamo Dias Martins, P.; He, H.; Kawaguchi, T.; Zapol, P.; You, H.; Tripkovic, D.; Strmcnik, D.; Zhu, Y.; Seifert, S.; Lee, S.; Stamenkovic, V. R.; Markovic, N. M. Dynamic Stability of Active Sites in Hydr(Oxy)Oxides for the Oxygen Evolution Reaction. *Nat. Energy* **2020**, *5*, 222–230. Inohara, D.; Maruyama, H.; Kakihara, Y.; Kurokawa, H.; Nakayama, M. Cobalt-Doped Goethite-Type Iron Oxyhydroxide (α -FeOOH) for Highly Efficient Oxygen Evolution Catalysis. *ACS Omega* **2018**, *3*, 7840–7845.
20. Zhang, W.; Li, Y.; Zhou, L.; Zheng, Q.; Xie, F.; Ho Lam, K.; Lin, D. Ultrathin Amorphous CoFeP

- Nanosheets Derived from CoFe LDHs by Partial Phosphating as Excellent Bifunctional Catalysts for Overall Water Splitting. *Electrochim. Acta* **2019**, *323*, 134595.
21. Tang, Y. J.; You, L.; Zhou, K. Enhanced Oxygen Evolution Reaction Activity of a Co₂P@NC-Fe₂P Composite Boosted by Interfaces between a N-Doped Carbon Matrix and Fe₂P Microspheres. *ACS Appl. Mater. Interfaces* **2020**, *12*, 25884–25894.
 22. Liu, J.; Meyns, M.; Zhang, T.; Arbiol, J.; Cabot, A.; Shavel, A. Triphenyl Phosphite as the Phosphorus Source for the Scalable and Cost-Effective Production of Transition Metal Phosphides. *Chem. Mater.* **2018**, *30*, 1799–1807.
 23. Zhang, C.; Du, R.; Biendicho, J. J.; Yi, M.; Xiao, K.; Yang, D.; Zhang, T.; Wang, X.; Arbiol, J.; Llorca, J.; Zhou, Y.; Morante, J. R.; Cabot, A. Tubular CoFeP@CN as a Mott–Schottky Catalyst with Multiple Adsorption Sites for Robust Lithium–Sulfur Batteries. *Adv. Energy Mater.* **2021**, *11*, 2100432.
 24. McCrory, C. C. L.; Jung, S.; Peters, J. C.; Jaramillo, T. F. Benchmarking Heterogeneous Electrocatalysts for the Oxygen Evolution Reaction. *J. Am. Chem. Soc.* **2013**, *135*, 16977–16987.
 25. Xue, Y.; Hui, L.; Yu, H.; Liu, Y.; Fang, Y.; Huang, B.; Zhao, Y.; Li, Z.; Li, Y. Rationally Engineered Active Sites for Efficient and Durable Hydrogen Generation. *Nat. Commun.* **2019**, *10*, 2281.
 26. Sankar, S. S.; Rathishkumar, A.; Geetha, K.; Kundu, S. A Simple Route for the Synthesis of Cobalt Phosphate Nanoparticles for Electrocatalytic Water Oxidation in Alkaline Medium. *Energy and Fuels* **2020**, *34*, 12891–12899.
 27. Yuan, C. Z.; Jiang, Y. F.; Wang, Z.; Xie, X.; Yang, Z. K.; Yousaf, A. Bin; Xu, A. W. Cobalt Phosphate Nanoparticles Decorated with Nitrogen-Doped Carbon Layers as Highly Active and Stable Electrocatalysts for the Oxygen Evolution Reaction. *J. Mater. Chem. A* **2016**, *4*, 8155–8160.
 28. Koza, J. A.; Hull, C. M.; Liu, Y. C.; Switzer, J. A. Deposition of β-Co(OH)₂ Films by Electrochemical Reduction of Tris(Ethylenediamine)Cobalt(III) in Alkaline Solution. *Chem. Mater.* **2013**, *25*, 1922–1926.
 29. Smith, R. D. L.; Prévot, M. S.; Fagan, R. D.; Trudel, S.; Berlinguette, C. P. Water Oxidation Catalysis: Electrocatalytic Response to Metal Stoichiometry in Amorphous Metal Oxide Films Containing Iron, Cobalt, and Nickel. *J. Am. Chem. Soc.* **2013**, *135*, 11580–11586.
 30. Zhou, J.; Yu, L.; Zhou, Q.; Huang, C.; Zhang, Y.; Yu, B.; Yu, Y. Ultrafast Fabrication of Porous Transition Metal Foams for Efficient Electrocatalytic Water Splitting. *Appl. Catal. B Environ.* **2021**, *288*, 120002.
 31. Liu, Y. C.; Koza, J. A.; Switzer, J. A. Conversion of Electrodeposited Co(OH)₂ to CoOOH and

- Co 3O₄, and Comparison of Their Catalytic Activity for the Oxygen Evolution Reaction. *Electrochim. Acta* **2014**, *140*, 359–365.
32. Hu, J.; Li, S.; Chu, J.; Niu, S.; Wang, J.; Du, Y.; Li, Z.; Han, X.; Xu, P. Understanding the Phase-Induced Electrocatalytic Oxygen Evolution Reaction Activity on FeOOH Nanostructures. *ACS Catal.* **2019**, 10705–10711.
33. Dong, G.; Fang, M.; Zhang, J.; Wei, R.; Shu, L.; Liang, X.; Yip, S.; Wang, F.; Guan, L.; Zheng, Z.; Ho, J. C. In Situ Formation of Highly Active Ni-Fe Based Oxygen-Evolving Electrocatalysts via Simple Reactive Dip-Coating. *J. Mater. Chem. A* **2017**, *5*, 11009–11015.
34. Urbain, F.; Du, R.; Tang, P.; Smirnov, V.; Andreu, T.; Finger, F.; Jimenez Divins, N.; Llorca, J.; Arbiol, J.; Cabot, A.; Morante, J. R. Upscaling High Activity Oxygen Evolution Catalysts Based on CoFe₂O₄ Nanoparticles Supported on Nickel Foam for Power-to-Gas Electrochemical Conversion with Energy Efficiencies above 80%. *Appl. Catal. B Environ.* **2019**, *259*, 118055.
35. Nie, J.; Hong, M.; Zhang, X.; Huang, J.; Meng, Q.; Du, C.; Chen, J. 3D Amorphous NiFe LDH Nanosheets Electrodeposited on: In Situ Grown NiCoP@NC on Nickel Foam for Remarkably Enhanced OER Electrocatalytic Performance. *Dalt. Trans.* **2020**, *49*, 4896–4903.
36. Lyons, M. E. G.; Brandon, M. P. The Oxygen Evolution Reaction on Passive Oxide Covered Transition Metal Electrodes in Alkaline Solution. Part III - Iron. *Int. J. Electrochem. Sci.* **2008**, *3*, 1463–1503.
37. Doyle, R. L.; Lyons, M. E. G. An Electrochemical Impedance Study of the Oxygen Evolution Reaction at Hydrous Iron Oxide in Base. *Phys. Chem. Chem. Phys.* **2013**, *15*, 5224–5237.
38. Lyons, M. E. G.; Brandon, M. P. The Oxygen Evolution Reaction on Passive Oxide Covered Transition Metal Electrodes in Aqueous Alkaline Solution. Part 1-Nickel. *Int. J. Electrochem. Sci.* **2008**, *3*, 1386–1424.
39. Han, L.; Tang, P.; Reyes-Carmona, Á.; Rodríguez-García, B.; Torrén, M.; Morante, J. R.; Arbiol, J.; Galan-Mascaros, J. R. Enhanced Activity and Acid PH Stability of Prussian Blue-Type Oxygen Evolution Electrocatalysts Processed by Chemical Etching. *J. Am. Chem. Soc.* **2016**, *138*, 16037–16045.
40. Exner, K. S.; Over, H. Beyond the Rate-Determining Step in the Oxygen Evolution Reaction over a Single-Crystalline IrO₂(110) Model Electrode: Kinetic Scaling Relations. *ACS Catal.* **2019**, *9*, 6755–6765.
41. Negahdar, L.; Zeng, F.; Palkovits, S.; Broicher, C.; Palkovits, R. Mechanistic Aspects of the Electrocatalytic Oxygen Evolution Reaction over Ni–Co Oxides. *ChemElectroChem* **2019**, *6*, 5588–5595.

SUPPORTING INFORMATION

2.7. SI RESULTS

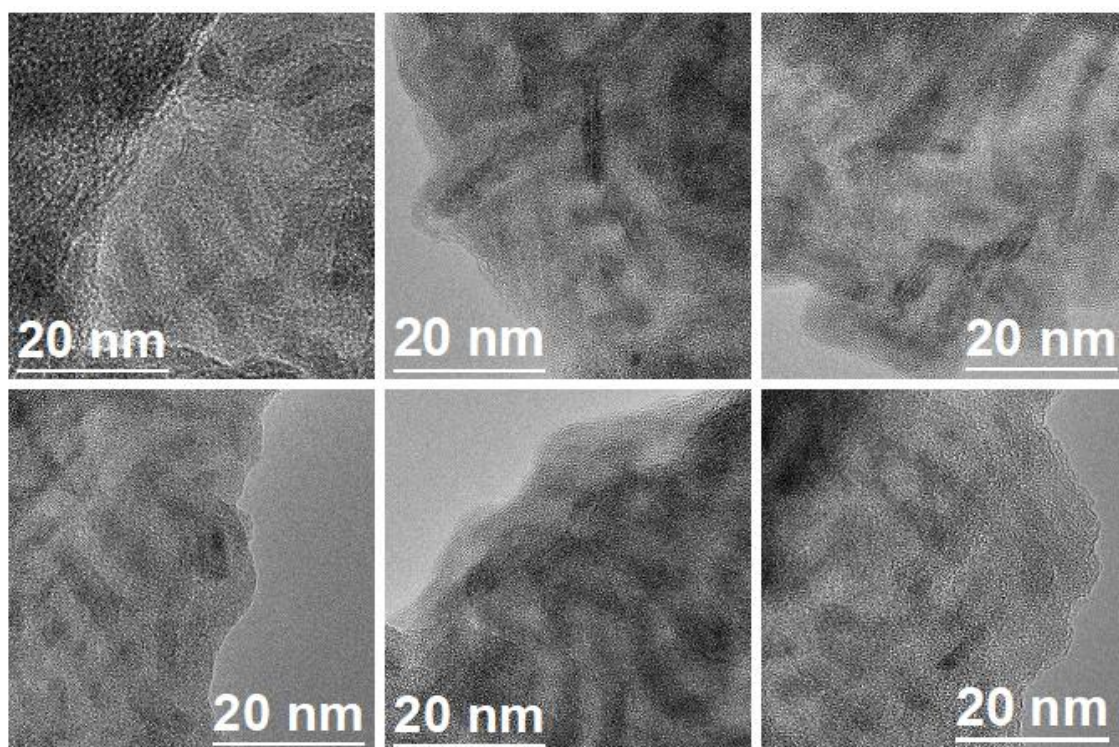


Figure 2.S1. HRTEM images of the CoFeP nanorods.

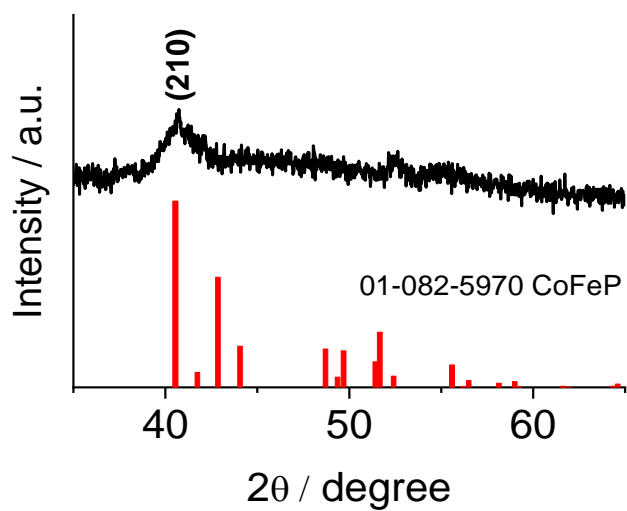


Figure 2.S2. XRD pattern of the CoFeP powder before the ligand removal.

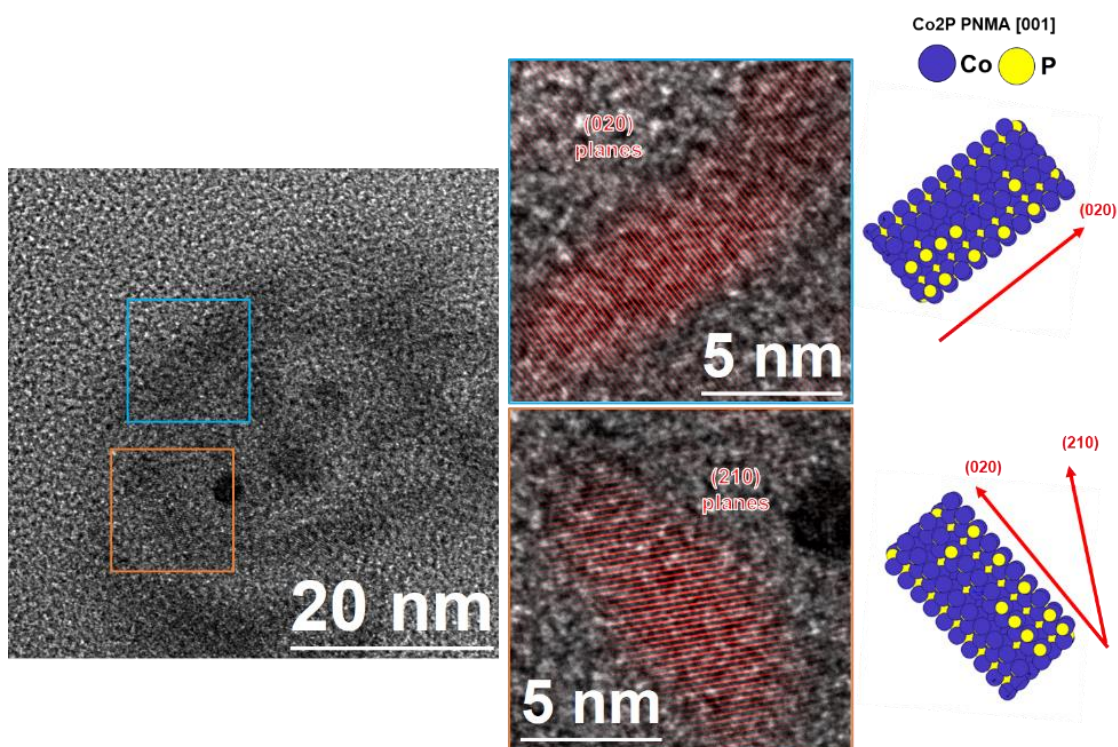


Figure 2.S3. HRTEM images of Co₂P nanorods and the schemes displaying the orientation of these nanorods.

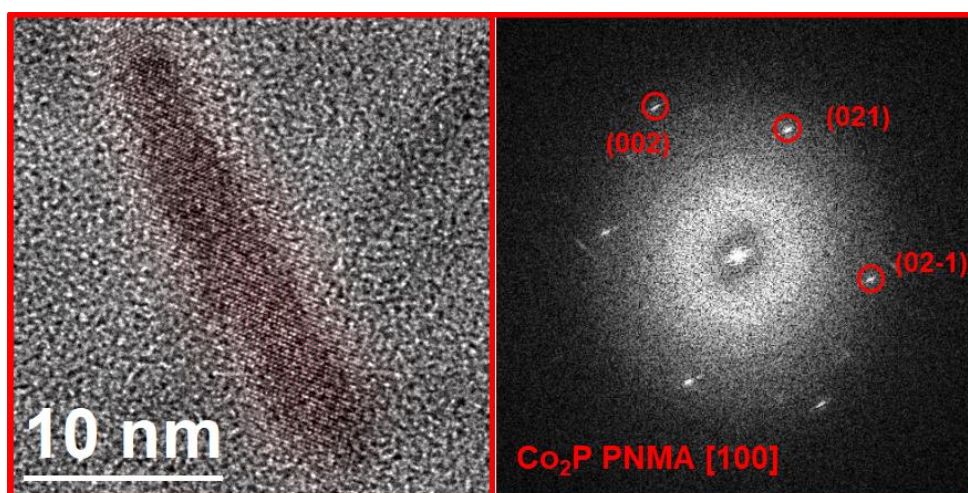


Figure 2.S4. a) HRTEM image of an individual nanorod and (b) the corresponding FFT spectrum showing the planes ascribed to the Co₂P PNMA.

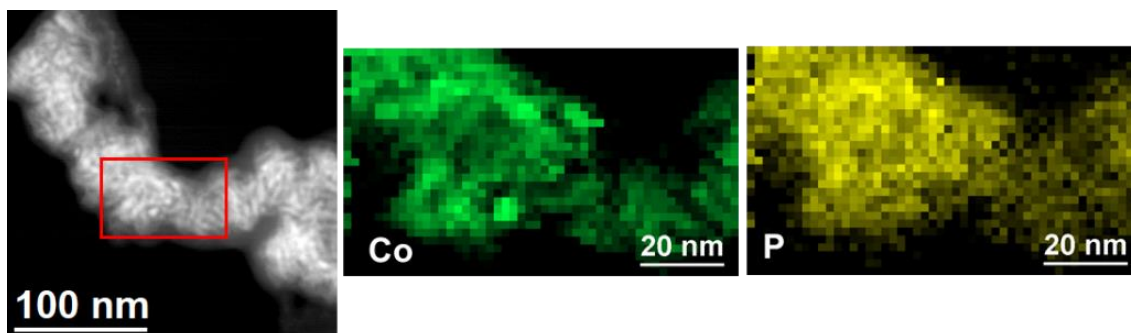


Figure 2.S5. EELS compositional maps of Co and P in the as prepared Co_2P nanorods and the corresponding STEM-ADF image on the left.

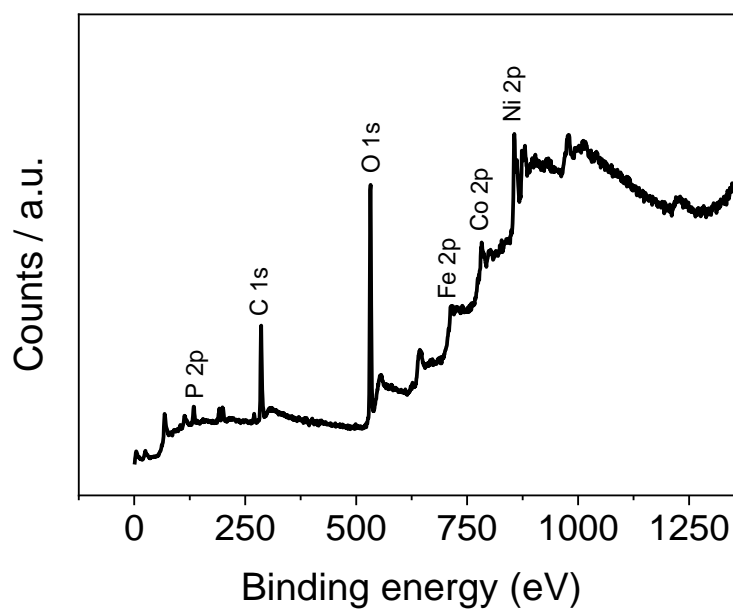


Figure 2.S6. XPS survey of CoFeP/NF before OER labelling the main signals.

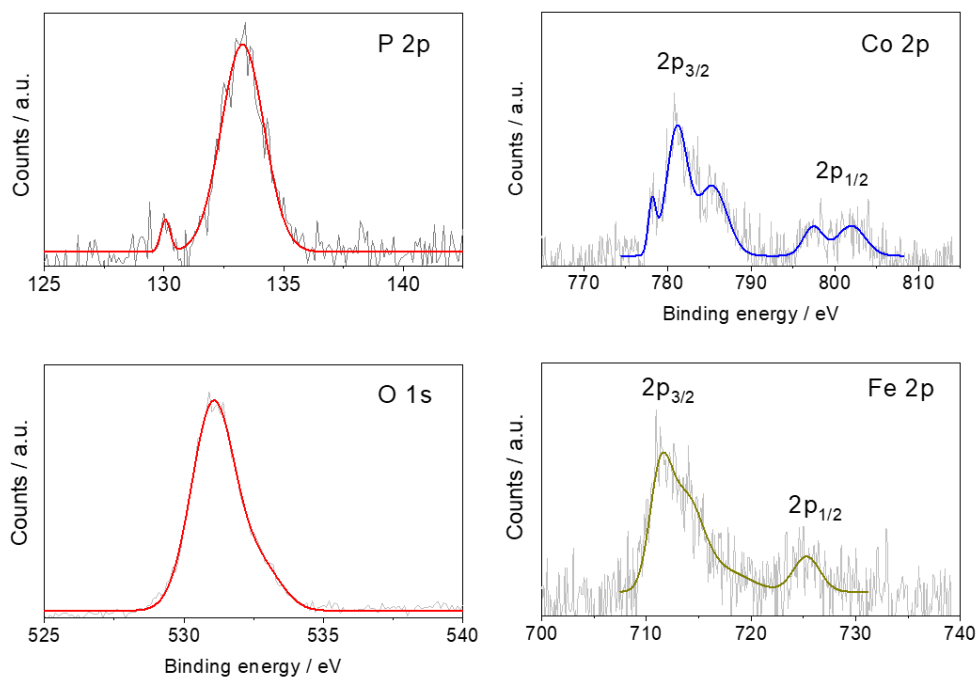


Figure 2.S7. XPS spectra in the P 2p, Co 2p, O 1s and Fe 2p regions for the CoFeP/NF electrode before OER (as-prepared).

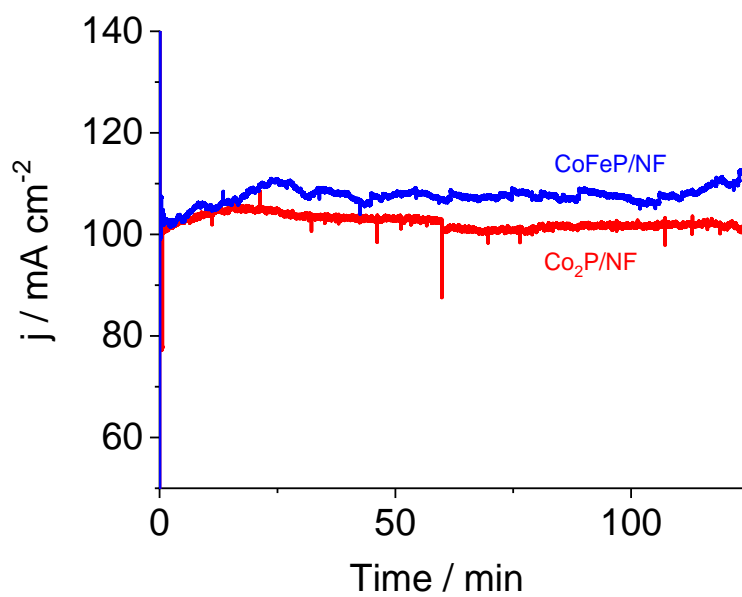


Figure 2.S8. Chronoamperograms starting from ca. 100 mA·cm⁻² for CoFeP/NF and Co₂P/NF electrodes.

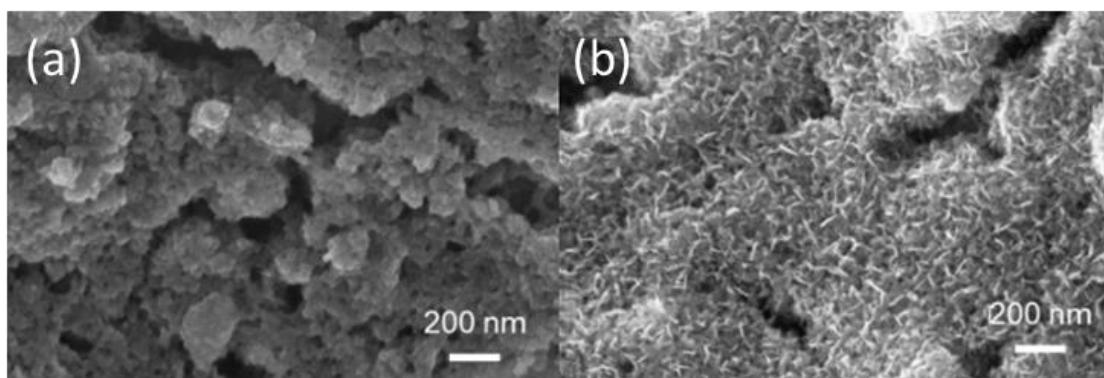


Figure 2.S9. SEM micrographs of Co₂P/NF electrodes: (a) as-prepared and (b) after 120 min of OER at 100 mA·cm⁻².

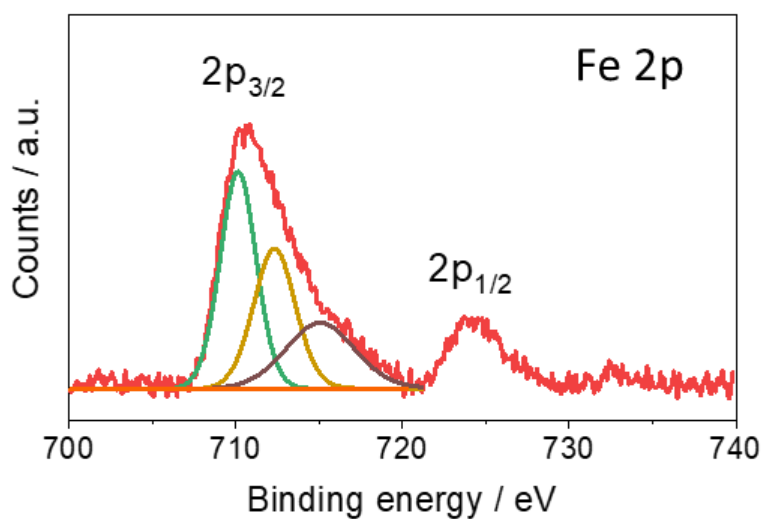


Figure 2.S10. XPS spectra in the Fe 2p region for a CoFeP/NF electrode (prepared by four immersion/drying steps) after OER.

Table 2.S1. Atomic percentages determined by XPS in the electrodes after OER.

Atomic concentrations / %	Co	Fe	P	O
Co ₂ P/NF	10.4	0	2.6	48.3
CoFeP/NF	8.8	5.6	1.5	47.2

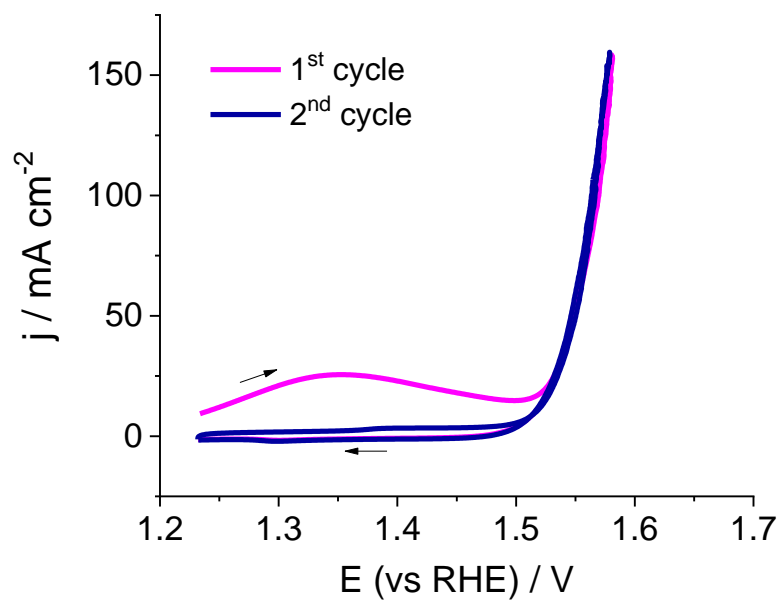


Figure 2.S11. First and second cyclic voltammograms at $5 \text{ mV}\cdot\text{s}^{-1}$ for a CoFeP/NF electrode in 1 M KOH.

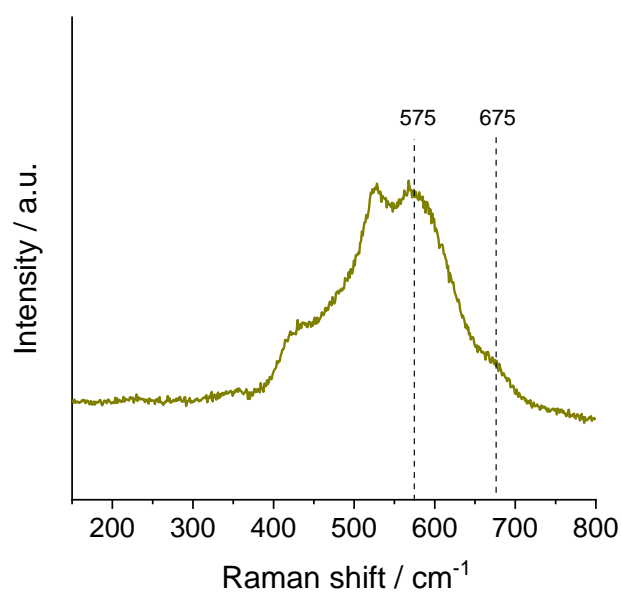


Figure 2.S12. Raman spectrum for a CoFeP/NF electrode after OER.

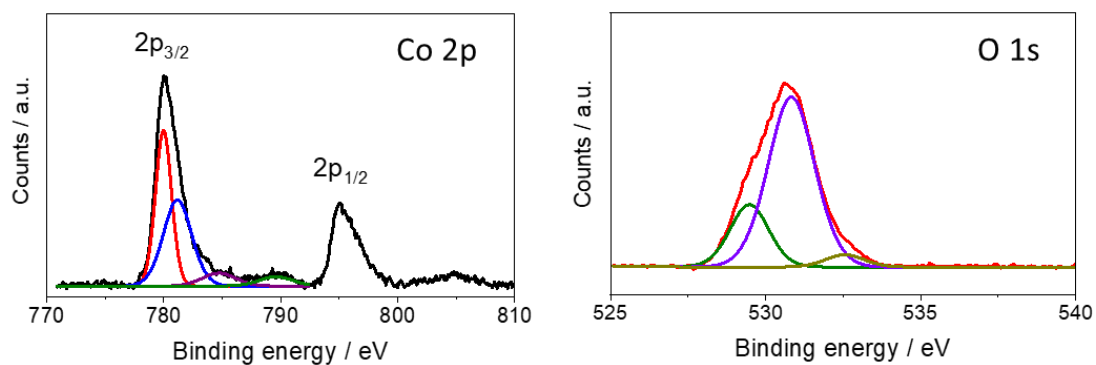


Figure 2.S13. XPS spectra in the Co 2p and O 1s regions for a Co₂P/NF electrode (prepared by four immersion/drying steps) after OER.

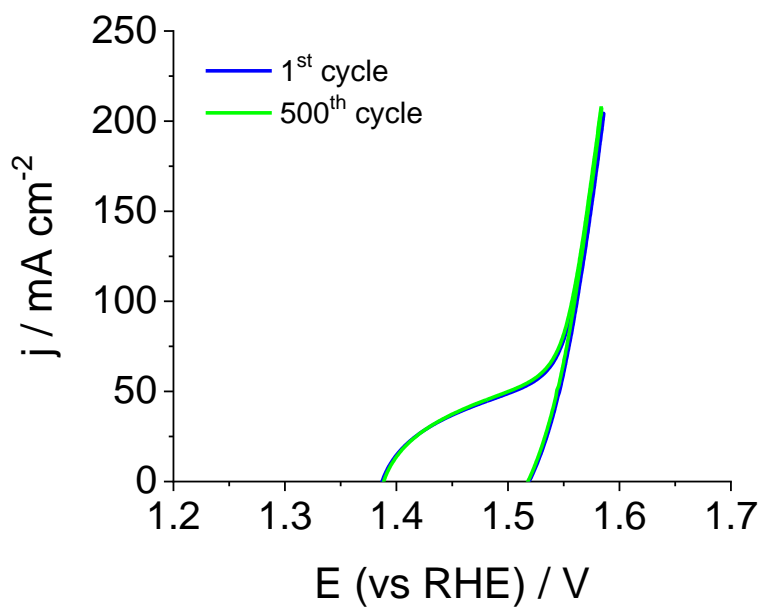


Figure 2.S14. Cyclic voltammograms corresponding to the 1st and 500th cycles at 200 mV·s⁻¹.

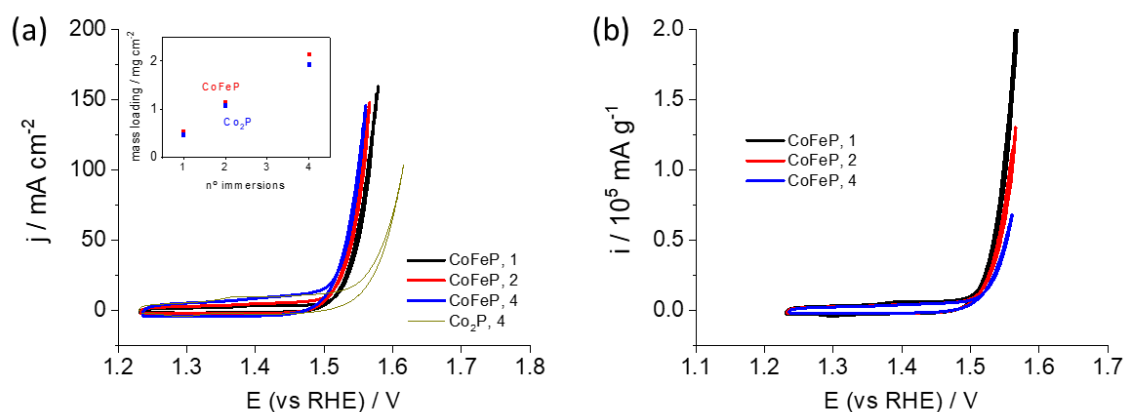


Figure 2.S15. Cyclic voltammograms for (a) current density and (b) current density normalized by the electrocatalyst mass loading vs E vs RHE recorded at $5 \text{ mV}\cdot\text{s}^{-1}$ for CoFeP/NF after 1, 2 and 4 immersions/drying steps. Co₂P/NF after 4 immersions was included in (a). Inset in (a) shows the electrocatalyst mass loading as a function of the number of immersions.

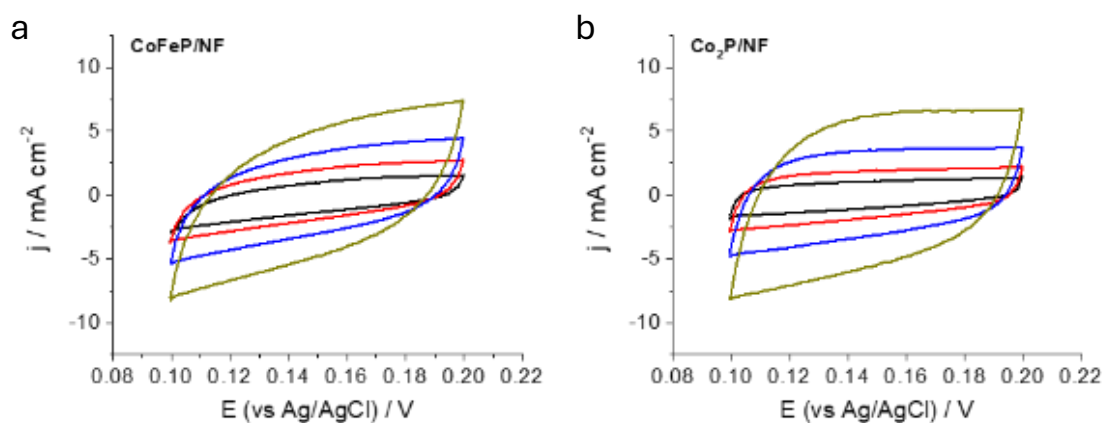


Figure 2.S16. Cyclic voltammograms of CoFeP/NF (a) and Co₂P/NF (b) electrodes at different scan rates ($5, 10, 20$ and $40 \text{ mV}\cdot\text{s}^{-1}$) in 1 M KOH .

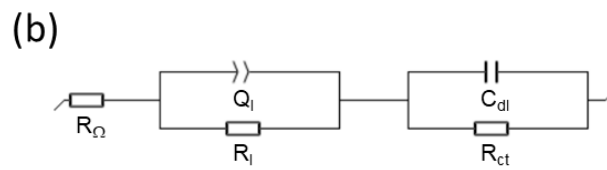
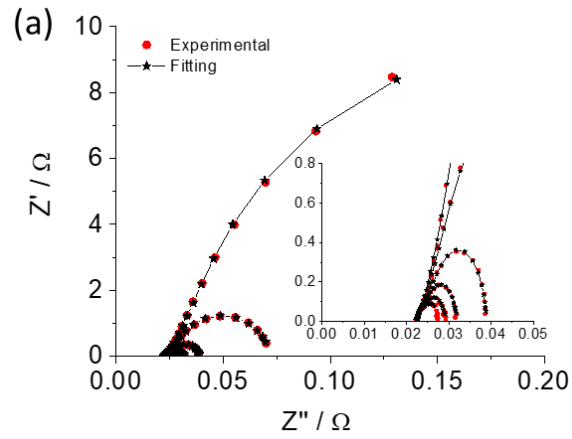


Figure 2.S17. (a) Nyquist plots of the CoFeP/NF electrode in 1 M KOH for different overpotentials (see Figure 2.4f) showing the experimental points and the theoretical curves adjusted by the equivalent circuit in (b).

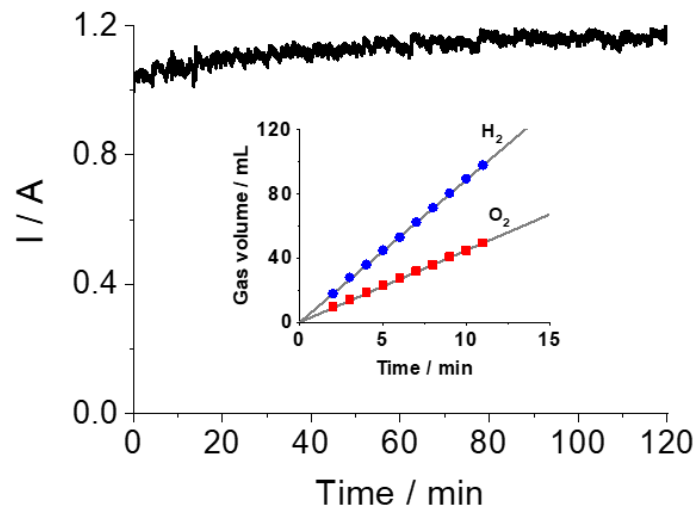


Figure 2.S18. Chronoamperogram in the full cell depicted in Figure 2.6a at a current density near 1 A at room temperature (without temperature control). Inset: experimental (points) and calculated (solid lines) accumulated volumes of H_2 and O_2 .

Table 2.S2. Comparison of the CoFeP-based electrodes for OER in 1 M KOH in chronological order.

Catalyst	Intermediate precursor material	Catalyst loading/ mg·cm ⁻²	η_{10} / mV	Tafel / mV·dec ⁻¹	Stability test	Ref.
(Co_{0.54}Fe_{0.46})₂P	Co-Fe-O nanocubes	N/A	280	N/A	N/A	1
(Co_{0.54}Fe_{0.46})₂P	Co-Fe-O nanocubes	0.2 ^a	370*	N/A	1000 cycles*	2
Co-Fe-P	CoFe- MOFs	1.0	244	58	30 h at 10 mA·cm ⁻²	3
Co_{0.7}Fe_{0.3}P/CNTs	Co _{1-x} Fe _x OOH	0.5	243	36	3 h at 10 mA·cm ⁻²	4
Fe₁Co₂P	Fe-Co MOFs	0.012 mg on a RDE ^a	362	50	8 h at ca. 4 mA·cm ⁻²	5
CoFeP	CoFe ₂ O ₄ , NaH ₂ PO ₂	0.05 mg on a GC ^a	350	59	12 h at 10 mA·cm ⁻²	6
CoFeP	CoFe-PBA nanocubes	0.015 mg on a GC	180	55	20 h at 10 mA·cm ⁻²	7
CoFeP-1.8	CoFe LDHs	3.41	242 (100 mA·cm ⁻²)	53	40 h at 100 mA·cm ⁻²	8
Co₂P-Fe₂P	FeOOH/ Co ₃ O ₄	3 (Co ₃ O ₄) + 4 (FeOOH) (precursors)	185	51	250 h from 10 to 100 mA·cm ⁻²	9

CoFeP	CoFe(OH) _x	15.1	193	73	50 h at 10 mA·cm ⁻²	10
Co₂P@NC-Fe₂P	FeHP-ZIF-67-2	1	260	41	35 h at 10 and 50 mA·cm ⁻²	11
p-CoFeP-0.35	Zn/Fe-Co PBA-x	0.283	280	48.8	12 h at 10 and 20 mA·cm ⁻²	12
CoFeP	Direct synthesis	ca. 0.5-2	285-270	42	1 h at 1 A·cm ⁻²	This work

^aCalculated from the reported experimental procedure

*in 0.1 M KOH

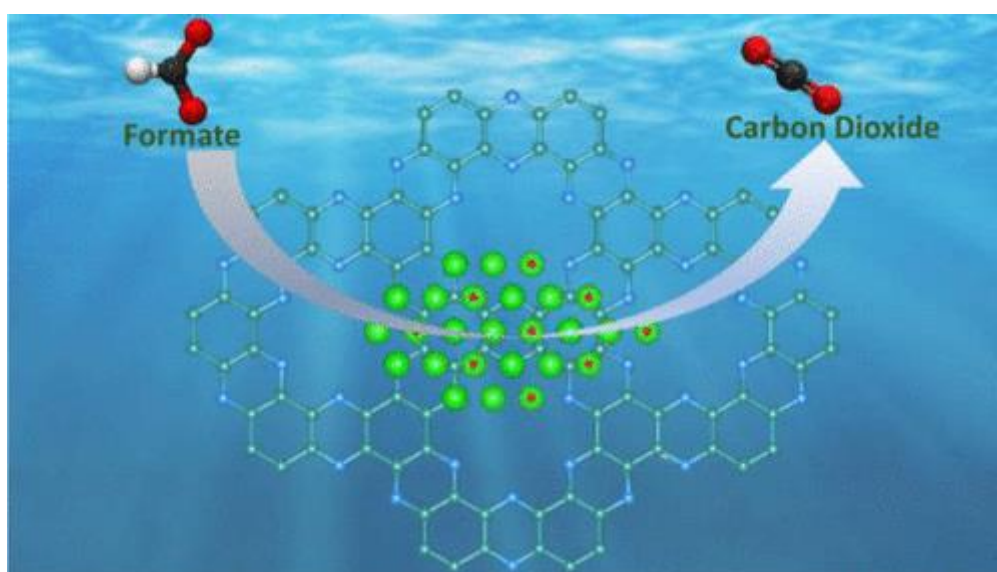
2.8. SI REFERENCES

1. Mendoza-Garcia, A.; Zhu, H.; Yu, Y.; Li, Q.; Zhou, L.; Su, D.; Kramer, M. J.; Sun, S. Controlled Anisotropic Growth of Co-Fe-P from Co-Fe-O Nanoparticles. *Angew. Chemie* **2015**, *127*, 9778–9781.
2. Mendoza-Garcia, A.; Su, D.; Sun, S. Sea Urchin-like Cobalt-Iron Phosphide as an Active Catalyst for Oxygen Evolution Reaction. *Nanoscale* **2016**, *8*, 3244–3247.
3. Zhang, T.; Du, J.; Xi, P.; Xu, C. Hybrids of Cobalt/Iron Phosphides Derived from Bimetal-Organic Frameworks as Highly Efficient Electrocatalysts for Oxygen Evolution Reaction. *ACS Appl. Mater. Interfaces* **2017**, *9*, 362–370.
4. Zhang, X.; Zhang, X.; Xu, H.; Wu, Z.; Wang, H.; Liang, Y. Iron-Doped Cobalt Monophosphide Nanosheet/Carbon Nanotube Hybrids as Active and Stable Electrocatalysts for Water Splitting. *Adv. Funct. Mater.* **2017**, *27*, 1606635.
5. Hong, W.; Kitta, M.; Xu, Q. Bimetallic MOF-Derived FeCo-P/C Nanocomposites as Efficient Catalysts for Oxygen Evolution Reaction. *Small Methods* **2018**, *2*, 1800214.
6. Du, Y.; Qu, H.; Liu, Y.; Han, Y.; Wang, L.; Dong, B. Bimetallic CoFeP Hollow Microspheres as

- Highly Efficient Bifunctional Electrocatalysts for Overall Water Splitting in Alkaline Media. *Appl. Surf. Sci.* **2019**, *465*, 816–823.
7. Zhang, X.; Wu, Y.; Sun, Y.; Liu, Q.; Tang, L.; Guo, J. CoFeP Hollow Cube as Advanced Electrocatalyst for Water Oxidation. *Inorg. Chem. Front.* **2019**, *6*, 604–611.
 8. Zhang, W.; Li, Y.; Zhou, L.; Zheng, Q.; Xie, F.; Ho Lam, K.; Lin, D. Ultrathin Amorphous CoFeP Nanosheets Derived from CoFe LDHs by Partial Phosphating as Excellent Bifunctional Catalysts for Overall Water Splitting. *Electrochim. Acta* **2019**, *323*, 134595.
 9. Liu, X.; Yao, Y.; Zhang, H.; Pan, L.; Shi, C.; Zhang, X.; Huang, Z. F.; Zou, J. J. In Situ-Grown Cobalt-Iron Phosphide-Based Integrated Electrode for Long-Term Water Splitting under a Large Current Density at the Industrial Electrolysis Temperature. *ACS Sustain. Chem. Eng.* **2020**, *8*, 17828–17838.
 10. Huang, X.; Gong, L.; Xu, H.; Qin, J.; Ma, P.; Yang, M.; Wang, K.; Ma, L.; Mu, X.; Li, R. Hierarchical Iron-Doped CoP Heterostructures Self-Assembled on Copper Foam as a Bifunctional Electrocatalyst for Efficient Overall Water Splitting. *J. Colloid Interface Sci.* **2020**, *569*, 140–149.
 11. Tang, Y. J.; You, L.; Zhou, K. Enhanced Oxygen Evolution Reaction Activity of a Co₂P@NC-Fe₂P Composite Boosted by Interfaces between a N-Doped Carbon Matrix and Fe₂P Microspheres. *ACS Appl. Mater. Interfaces* **2020**, *12*, 25884–25894.
 12. Peng, Z.; Qiu, X.; Cai, G.; Zhang, X.; Dong, Z. Simultaneous Tuning of the Cation Content and Pore Structure of Cobalt-Iron Bimetal Phosphide to Enhance the Electrochemical Oxygen Evolution. *J. Alloys Compd.* **2020**, *842*, 155784.

CHAPTER 3

Palladium hydride on C₂N to Boost Formate Oxidation



3.1. ABSTRACT

The lack of electrocatalysts for the FOR hampers the deployment of DFFC. To overcome this limitation, herein, we detail the production of palladium hydride particles supported on C₂N (PdH_{0.58}@C₂N) via a facile method. PdH_{0.58}@C₂N displays excellent FOR performance reaching current densities up to 5.6 A·mg_{Pd}⁻¹ and stable cycling and CA operation. The Pd lattice expands due to the hydrogen intercalation. Besides, an electronic redistribution associated with the distinct electronegativity of Pd and H is observed. Both phenomena modify the electron energy levels enhancing the activity and stability of the composite catalyst. More specifically, differential functional theory calculations show H intercalation to downshift the Pd d-band centre in Pd_{0.58}@C₂N, weakening adsorbate binding and accelerating the FOR rate-determining step.

3.2. INTRODUCTION

Fuel cells are an attractive alternative to conventional fossil fuel-based combustion technologies, offering high efficiencies of conversion from chemical to electrical energy. Among the possible liquid fuels, FA/formate offers a particularly simple oxidation reaction, involving the transfer of just two electrons.¹⁻⁵ In particular, FA is regarded as a safe, low-cost, and low-toxicity hydrogen carrier, with a large content of hydrogen, 4.4 wt %, excellent stability, low ignition point, and convenient transportation and storage.⁶⁻⁸ But it is the use of formate in alkaline cells the one that is attracting more recent attention. The use of a solid formate salt is beneficial in terms of storage and transportation over liquid FA.^{9, 10} Formate is also characterized by much lower toxicity and corrosiveness than FA, and therefore it can be used at higher concentrations.^{11, 12} Besides, the FOR presents faster reaction kinetics, lower over-potentials, faster reaction kinetics and reduced poisoning when compared with FA.¹³⁻¹⁵ Additionally, DFFC also present faster kinetics due to the rapid ORR kinetics in alkaline medium when compared with an acid environment.^{11, 16, 17} Moreover, formate is industrially used for the production of FA, thus having a reduced price. On top of all this, the synthesis of formate from CO₂RR has seen rapid progress recently and may reach industrialization in the foreseeable future, which could make DFFCs a net-zero CO₂ technology.¹⁸⁻²⁰

Pd is the most promising candidate to catalyse the FOR. However, the performance of Pd is still far from optimum in terms of stability and also activity.²¹ As a main drawback, Pd binds too strongly to hydrogen, limiting its desorption and thus blocking the adsorption sites available for additional reactants.^{22, 23} To improve the FOR performance, we need to develop effective strategies to tune the electronic properties of Pd and particularly to reduce the adsorption energy of the intermediates. Recently, the introduction of lighter and smaller elements to diffuse within the Pd lattice and expand it has awakened notorious attention. By changing the metal lattice parameters, the electronic properties of the metal can be modified and potentially optimized.²⁴⁻²⁶ Among possible light elements, H is particularly suitable to modify the Pd structure owing to the small atomic radius of H and the high affinity of Pd towards this element.²⁷⁻²⁹

To maximize its dispersion, electrocatalytic particles are generally supported on electrically conductive high surface area supports, such as carbon.³⁰ However, traditional carbon materials contain a uniformly distributed surface charge, which makes them catalytically inactive. To overcome this limitation, nitrogen-doped carbon and carbon nitrides can be used.³¹ In particular, C₂N has emerged as a new 2D graphene-like layered covalent organic material.³²⁻³⁴ The presence

of N atoms within the carbon lattice introduces polarity to interact with polar species and enhances thermal stability.³⁵⁻³⁷ Besides the electrical conductivity of C₂N is higher than that of other C-N materials. The unique porous structure of C₂N increases the electron density of the N atoms, which enables them to act as excellent sites for the nucleation and growth of metal.^{38, 39}

Taking into account all the above, we developed a strategy to produce palladium hydride (PdH_{0.58}) nanodendrites supported on C₂N. Such composite catalyst was tested towards FOR in alkaline media. To rationalize the obtained results, DFT calculations are used to identify the effect of H intercalation on the d-band centre of Pd within the composite Pd_{0.58}@C₂N and its influence on the binding of adsorbates.

3.3. RESULTS AND DISCUSSION

Palladium hydride NPs were produced in the presence of C₂N using Pd(acac)₂ as metal precursors and OAm as a solvent and hydrogen source (see details in the Experimental section, Figure 3.S1). In the presence of C₂N, Pd heterogeneously nucleates and grows at N sites on the C₂N surface which offer lone electron pairs and thus act as electron donors coordinating with the metal ions. Figure 3.S2 shows the nanosheet structure and composition of the initial C₂N support. Figures 1a-c and 3.S3 display representative SEM and TEM micrographs of the particles supported on C₂N. The final product consists of the C₂N covered with small hyperbranched NPs or nanodendrites. HRTEM micrographs reveal that the nanodendrites have a crystal phase in agreement with the Pd cubic phase (space group =Fm-3m) but with a significantly larger lattice parameter $a=b=c=4.0190 \text{ \AA}$, well above that of pure Pd $a=b=c=3.89 \text{ \AA}$. The larger lattice spacing measured confirms the presence of H within the Pd lattice.⁴⁰⁻⁴² Since the presence of H linearly affects the lattice parameter of PdH, from the HRTEM data we calculated a H/Pd atomic ratio of ca. 0.58. The XRD pattern of PdH_{0.58}@C₂N was consistent with that of the Pd face-centred cubic (fcc) structure (Pd-PDF#87-0641) but, consistently with HRTEM results, diffraction peaks were shifted to lower angles. A reference Pd@C₂N sample was produced by annealing PdH_{0.58}@C₂N under Ar at 450 °C for 2 h to remove the intercalated hydrogen. As shown in Figure 3.2a, after the annealing treatment, the shift of the XRD pattern disappeared. These results further confirm the expansion of the Pd lattice with the introduction of H.^{27, 28} HAADF-STEM micrographs (Figure 3.1d) and STEM-EELS elemental composition maps (Figure 3.1e) of PdH_{0.58}@C₂N show the presence of C, N, and Pd, being all the elements homogeneously distributed at the nm scale. Additional TEM, HRTEM, and STEM-EELS of the Pd@C₂N sample show a relatively similar architecture with a homogeneous distribution of the different elements (Figure 3.S4).

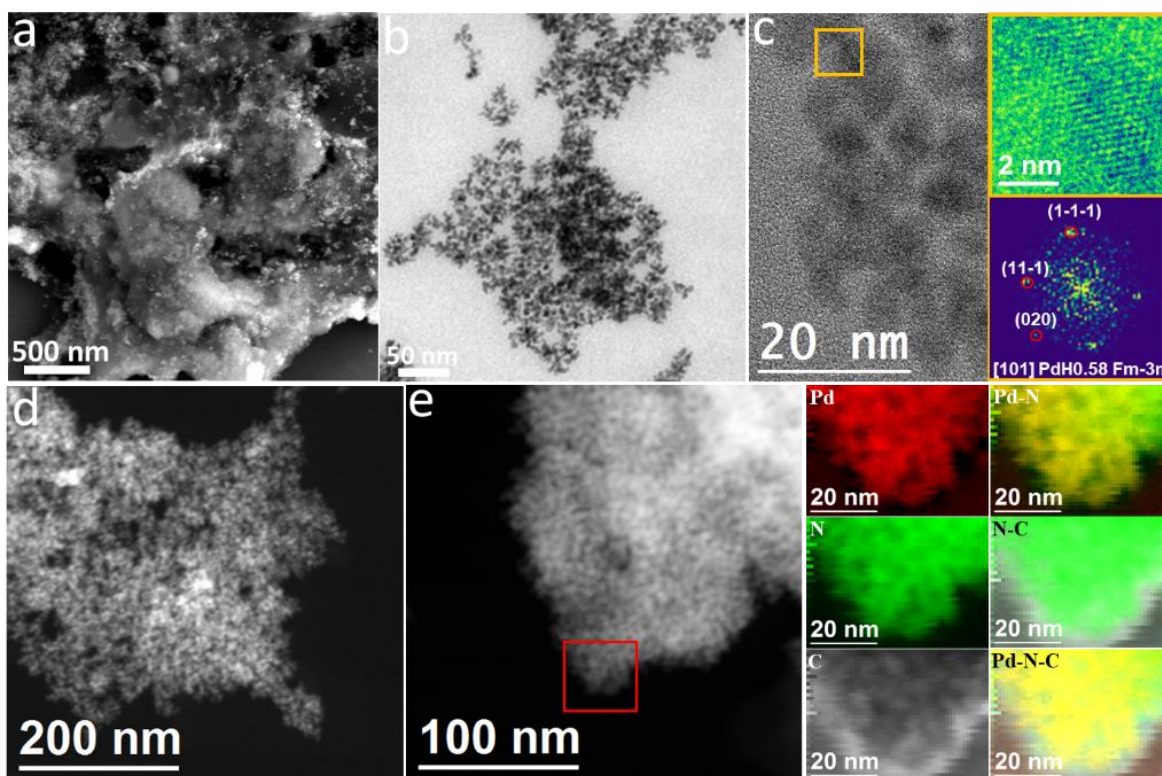


Figure 3.1. Structural and chemical characterization of PdH_{0.58}@C₂N. **a)** SEM image, **b)** TEM image, **c)** HRTEM and corresponding FFT spectrum of the PdH_{0.58}@C₂N, visualized along its [101] zone axis. **d, e)** HAADF-STEM and EELS chemical composition maps obtained from the red squared area of the STEM micrograph. Individual Pd M_{4,5}-edges at 335 eV (red), N K-edges at 401 eV (green) and C K-edges at 285 eV (grey) and composites of Pd-N, N-C and Pd-N-C.

As an additional reference material, self-standing PdH_{0.58} NPs were synthesized using the same procedure as for the synthesis of PdH_{0.58}@C₂N but in the absence of C₂N. Afterward, these NPs were physically mixed with C₂N to produce PdH_{0.58}/C₂N. TEM images of PdH_{0.58} and SEM images of PdH_{0.58}/C₂N samples show the PdH_{0.58} NPs to be highly agglomerated (Figures 3.S5 and 3.S6), which reveals the presence of C₂N during the Pd-based NP synthesis to decisively contribute to their dispersion. Besides, the XRD pattern of the PdH_{0.58}/C₂N sample displays an additional peak at ca. 35° associated with the presence of a small amount of the PdO phase (JCPDS 06-0515), which reveals that the coordination of PdH_{0.58} with C₂N during synthesis, through the N atoms, contributes to prevent its surface oxidation.

Figure 3.2b,c displays the XPS spectra of Pd@C₂N and PdH_{0.58}@C₂N. For both materials, the high-resolution Pd 3d XPS spectra presented two doublets. The majoritarian component, at 335.4 eV (Pd 3d_{3/2}) for PdH_{0.58}@C₂N, was associated with Pd⁰, and the minoritarian, at 336.5 eV (Pd 3d_{3/2}), with an oxidized Pd^{x+} chemical environment.^{25, 43} The Pd 3d spectra of PdH_{0.58}@C₂N was shifted

about 0.2 eV toward higher binding energies than Pd@C₂N, which indicates a charge redistribution within the palladium hydride, with Pd giving electrons to H. The presence of electron-deficient Pd in PdH_{0.58}@C₂N is consistent with previous reports.^{44, 45} Electron-poor Pd has been reported to reduce the electron exchange with CO 2π* orbitals, which translates into a weaker CO adsorption.⁴³ Thus, PdH_{0.58}@C₂N may present a higher resistance towards CO poisoning during FOR than Pd@C₂N.

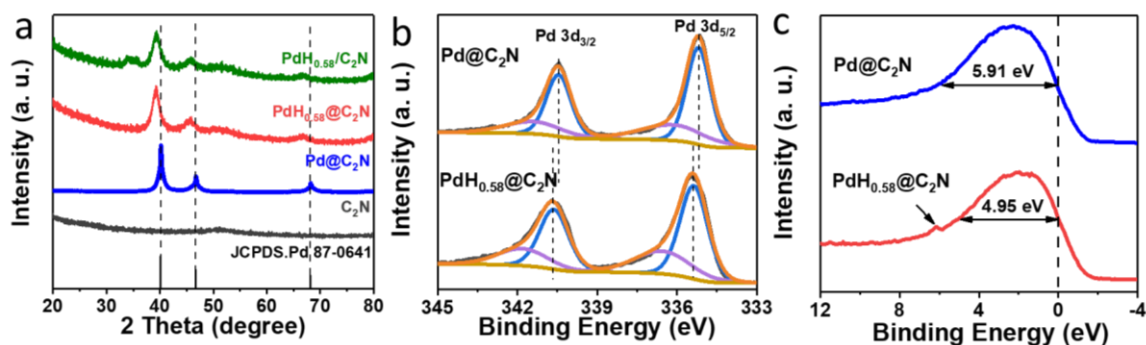


Figure 3.2. a) XRD patterns of C₂N, Pd@C₂N, PdH_{0.58}@C₂N, PdH_{0.58}/C₂N, b) High-resolution Pd 3d XPS spectra and c) valence band XPS spectra of Pd@C₂N and PdH_{0.58}@C₂N. The d-band widths are indicated by the double-headed arrows, and the black dash line highlights the Fermi level position.

The valence band XPS spectra of Pd@C₂N and PdH_{0.58}@C₂N are displayed in Figure 3.2c. A broad band of states, contributed by Pd 4d electronic states, is observed in both spectra.^{27, 28} PdH_{0.58}@C₂N shows a narrower bandwidth of *ca.* 4.95 eV as compared to 5.91 eV of Pd@C₂N, which indicates a modified electronic structure. Such narrower bandwidth results from the increase of distance between Pd atoms within the PdH.⁴⁶ Besides, a new peak in the band structure of PdH_{0.58} was observed at 6.17 eV and it was associated with the interaction between the H 1s and Pd 4d electronic states within the PdH.⁴⁷

The FOR performance of PdH_{0.58}@C₂N, Pd@C₂N, PdH_{0.58}/C₂N, and commercial Pd/C was studied in a conventional three-electrode system. First, CV curves were obtained in an Ar-saturated 0.5 M KOH solution (Figure 3.3a). In the cathodic scan, the current density peaks in the potential region -0.6 to -0.8 V vs. Hg/HgO are assigned to hydrogen adsorption. Besides, equivalent peaks in the anodic scan are associated with the desorption of hydrogen.⁴⁸ In the anodic scan, the increase of current density observed at about -0.2 V vs. Hg/HgO is assigned to the surface oxidation of palladium. Additionally, the current density peak associated with the PdO reduction is found at about -0.2 V versus Hg/HgO during the cathodic scan. The distinct hydrogen

adsorption/desorption features of hydrogen between PdH_{0.58}@C₂N and Pd@C₂N, indicate different surface atomic configurations.

The ECSA was estimated from the PdO reduction peak. CV curves showed the Pd oxide reduction peak area to be significantly larger on PdH_{0.58}@C₂N than on Pd@C₂N, PdH_{0.58}/C₂N and Pd/C, suggesting a larger ECSA. Quantitatively, ECSA was calculated from:

$$ECSA = \frac{Q (\mu C \cdot cm^{-2})}{Q_{PdO} (\mu C \cdot cm^{-2}) \times Pd_{loading} (mg \cdot cm^{-2}) \times 10} \quad (1)$$

where $Q_{PdO} = 405 \mu C \cdot cm^{-2}$ is the charge involved in the reduction of a PdO monolayer, Q is the charge obtained from the integration of the PdO reduction peak, and $Pd_{loading}$ is the Pd amount loaded on the working electrode.³⁰ From this equation, the ECSA values for Pd_{0.58}@C₂N, Pd@C₂N, PdH_{0.58}/C₂N and Pd@CB catalysts were 40.84 m² g⁻¹, 31.51 m² g⁻¹, 24.75 m² g⁻¹ and 18.78 m² g⁻¹, respectively. Thus, significantly larger ECSAs were obtained with the growth of PdH_{0.58} in the presence of C₂N.^{49, 50}

The electrocatalytic activity toward FOR was investigated by CV in a solution containing 0.5 M KOH and 0.5 M HCOOK (Figure 3.3b). The obtained current was normalized to the calculated ECSA. Even when normalizing to the ECSA, the PdH_{0.58}@C₂N catalyst exhibited a much higher specific activity when compared with the reference catalysts. PdH_{0.58}@C₂N delivered a peak current density of 27.44 mA cm⁻², well above that of Pd@C₂N (16.25 mA·cm⁻²), PdH_{0.58}/C₂N (14.37 mA·cm⁻²), and Pd/C (11.43 mA·cm⁻²). Even larger differences were obtained when normalizing to the mass of Pd. PdH_{0.58}@C₂N exhibited the highest mass activity at 5.60 A mg Pd⁻¹, which was 5.2-fold larger than that of Pd/C (1.07 A mg Pd⁻¹) and well above that of the other electrocatalysts. PdH_{0.58}@C₂N-based electrodes also provided the lowest onset potentials, as shown in Figure 3.3d. The onset potential of PdH_{0.58}@C₂N was -0.71 V, much smaller than that of Pd@C₂N (-0.64 V). Besides, as shown in Figure 3.3e, the lowest Tafel slope was also obtained for PdH_{0.58}@C₂N, at 90.4 mV dec⁻¹, significantly below that of Pd@C₂N, PdH_{0.58}/C₂N and Pd/C catalysts at 101.9, 168.6 and 208.1 mV dec⁻¹, respectively. The lowest Tafel slope of the PdH_{0.58}@C₂N catalyst indicates promoted FOR kinetics.

Figure 3.3f resumes the specific and mass activities of all catalysts in this work toward the FOR. Additionally, figure 3.3g and Table 3.S1 compare the results obtained in the present work with state-of-the-art Pd-based catalysts reported to date. Overall, PdH_{0.58}@C₂N shows outstanding specificity and mass activities, above most catalysts reported so far.

The electrocatalytic stability of PdH_{0.58}@C₂N was evaluated using CA measurements at -0.2 V in 0.5 M KOH + 0.5 M HCOOK electrolyte for 5000 s (Figure 3.3h). PdH_{0.58}@C₂N exhibited the

slowest current decay compared with the reference electrocatalysts. To remove the accumulated poisoning species, a rapid potential scan to oxidize and reduce the Pd surface was tested. Figure 3.3i shows the regeneration capacity of the tested catalysts. After every 1000 s of CA test, the catalysts were re-activated by cycling for 100 s in a clean 0.5 M KOH solution. This simple regeneration strategy allows cleaning the surface of the catalyst from adsorbed contaminants and thus recovering most of the catalytic activity. After 1000 cycles in the voltage range -0.9 to 0.3 V vs. Hg/HgO in 0.5 M KOH + 0.5 M HCOOK electrolyte, the catalyst was collected and analysed. As shown in TEM and HRTEM images in Figure 3.S7, the post-FOR product maintained the initial architecture, crystal phase and composition, without significant variations.

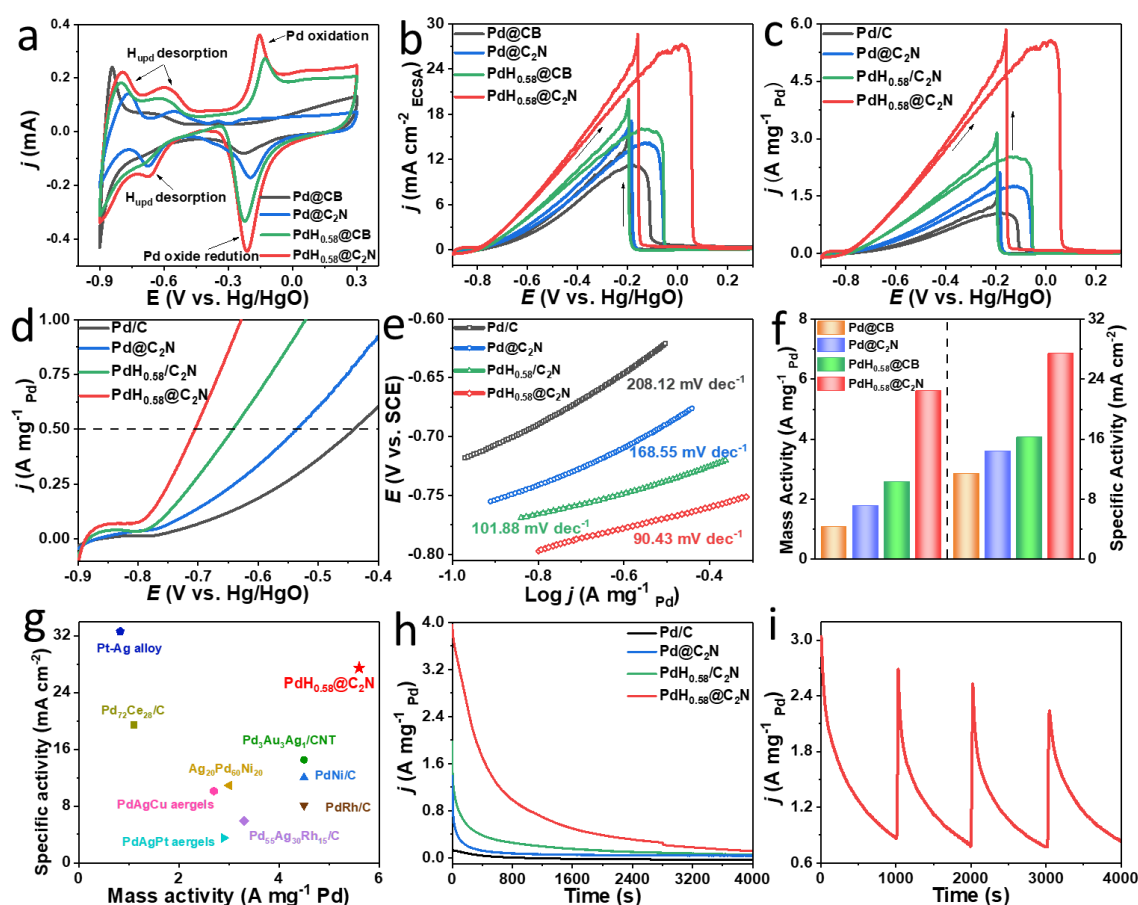
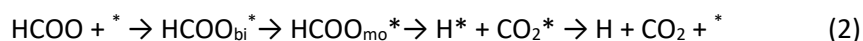


Figure 3.3. Electrochemical performance of PdH_{0.58}@C₂N, Pd@C₂N, PdH_{0.58}/C₂N, Pd/C catalysts for FOR. a) CV curves in Ar-saturated 0.5 M KOH solution and b, c) in a 0.5 M KOH + 0.5 M ethanol solution normalized by the geometric area (b) and the mass of Pd (c), d) enlarged CV curves at the onset potential, e) Tafel plot and calculated Tafel slopes, f) Comparison of mass activity and specific activity, g) Comparison of peak potentials between this work and previous reports, h) CA curves, i) CA curves with CV reactivation every 1000 s for PdH_{0.58}@C₂N.

To provide the theoretical basis for the experimental results, the thermochemical reaction energetics of the FOR on PdH_{0.58}@C₂N and Pd@C₂N were investigated by DFT calculations using the (111) surface of FCC Pd. The PDOSs of Pd@C₂N (111) and PdH_{0.58}@C₂N (111) surfaces is displayed in Figure 3.4a. The d-band of the PdH_{0.58}@C₂N surface is downshifted, with a centre farther away from the Fermi level (-2.02 eV) than that of the Pd@C₂N surfaces (-1.77 eV). We also calculated the d-band centre of the (111) surface, which gives the same result (Figure 3.S8, Supporting Information). The configurations of the adsorbed FOR intermediates (HCOO_{bi}^{*}, HCOO_{mo}^{*}, H^{*} and CO₂^{*}) on the surface of PdH_{0.58}@C₂N are displayed in Figure 3.4c. A priori, on Pd-based catalysts, the FOR direct path follows four steps:



where * denotes a surface site; and HCOO_{bi}^{*}, HCOO_{mo}^{*}, H^{*} and CO₂^{*} are the formate bidentate, formate monodentate, H and CO₂ adsorbed on the sites, respectively.^{51, 52} Figure 3.4b displays the free energy profiles of FOR steps. The results show an endothermic second step, HCOO_{bi}^{*} → HCOO_{mo}^{*}, having associated the highest energy barrier for both catalysts. DFT calculations show that the energy barrier for this RDS is 1.047 eV for PdH_{0.58}@C₂N surfaces and significantly higher for Pd@C₂N (1.151 eV) surfaces, which is consistent with the lower onset potential and higher activity of the former. Besides, the energy barrier for the desorption of the reaction products is also much lower for PdH_{0.58}@C₂N (0.738 eV) than for Pd@C₂N (0.986 eV), which is consistent with the higher activity and stability of the former.

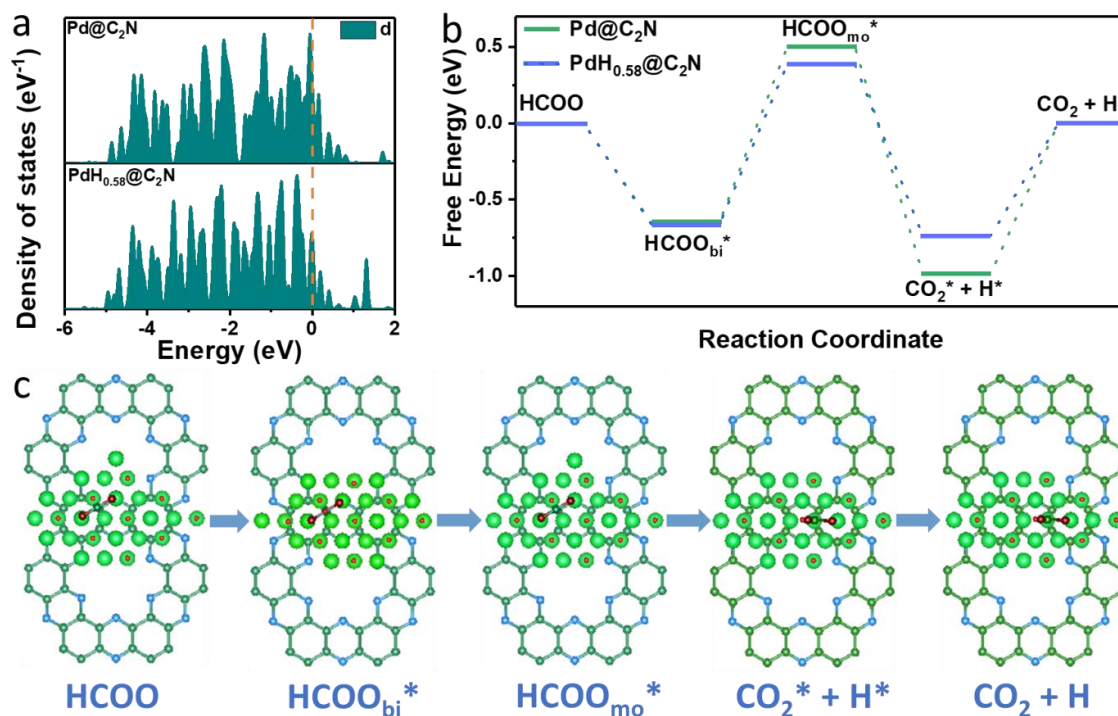


Figure 3.4. a) d-band centres of Pd 4d partial density of states, b) Gibbs free energy diagrams of FOR intermediates for PdH_{0.58}@C₂N and Pd@C₂N, c) Evolution of the local structural configurations illustrating FOR process of PdH_{0.58}@C₂N. (* represents the active site).

3.4. CONCLUSION

In summary, PdH_{0.58}@C₂N was prepared using a one-step *in situ* growth method based on the heterogeneous nucleation and growth of PdH_{0.58} on the surface of C₂N. The grown palladium hydride displays a favourable architecture with a high surface area. The presence of H provides several advantages, including an expansion of the Pd lattice and an electronic reconfiguration within the material that promotes the FOR catalytic performance, improving both activity and stability. DFT calculations show the presence of H to downshift the Pd d-band centre within Pd_{0.58}@C₂N, weakening the adsorbate binding and thus accelerating the rate-limiting step of the FOR. Overall, the presence of H allows tuning the Pd crystallographic and electronic structure to enhance electrocatalytic properties. Beyond FOR, the same strategy is susceptible to be applied to other electrocatalytic reactions.

3.5. REFERENCES

1. Mazumder, V.; Sun, S. Oleylamine-mediated synthesis of Pd nanoparticles for catalytic formic acid oxidation. *J. Am. Chem. Soc.* 2009, 131 (13), 4588-4589 DOI: 10.1021/ja9004915
2. Xiong, Y.; Dong, J.; Huang, Z.-Q.; Xin, P.; Chen, W.; Wang, Y.; Li, Z.; Jin, Z.; Xing, W.; Zhuang,

- Z.; Ye, J.; Wei, X.; Cao, R.; Gu, L.; Sun, S.; Zhuang, L.; Chen, X.; Yang, H.; Chen, C.; Peng, Q.; Chang, C.-R.; Wang, D.; Li, Y. Single-atom Rh/N-doped carbon electrocatalyst for formic acid oxidation. *Nat. Nanotechnol.* 2020, 15 (5), 390-397 DOI: 10.1038/s41565-020-0665-x
3. Luo, S.; Chen, W.; Cheng, Y.; Song, X.; Wu, Q.; Li, L.; Wu, X.; Wu, T.; Li, M.; Yang, Q.; Deng, K.; Quan, Z. Trimetallic synergy in intermetallic PtSnBi nanoplates boosts formic acid oxidation. *Adv. Mater.* 2019, 31 (40), 1903683 DOI: 10.1002/adma.201903683
 4. Zhou, Y.; Yang, Y.; Zhu, X.; Zhang, T.; Ye, D. d.; Chen, R.; Liao, Q. Novel Superaerophobic Anode with Fern-Shaped Pd Nanoarray for High-Performance Direct Formic Acid Fuel Cell. *Adv. Funct. Mater.* 2022, 2201872 DOI: 10.1002/adfm.202201872
 5. Montaña-Mora, G.; Qi, X.; Wang X.; Chacón-Borrero J.; Martínez-Alanis, P. R.; Yu, X.; Li, J.; Xue Q.; Arbiol, J.; Ibáñez, M.; Cabot, A.; Phosphorous incorporation into palladium tin nanoparticles for the electrocatalytic formate oxidation reaction. *J. Electroanal. Chem* 2023, 936, 117369 DOI: 10.1016/j.jelechem.2023.117369
 6. Yan, X.; Hu, X.; Fu, G.; Xu, L.; Lee, J. M.; Tang, Y. Facile synthesis of porous Pd₃Pt half-shells with rich “active sites” as efficient catalysts for formic acid oxidation. *Small* 2018, 14 (13), 1703940 DOI: 10.1002/smll.201703940
 7. Zhang, L.; Ding, L.-X.; Luo, Y.; Zeng, Y.; Wang, S.; Wang, H. PdO/Pd-CeO₂ hollow spheres with fresh Pd surface for enhancing formic acid oxidation. *Chem. Eng. J.* 2018, 347, 193-201 DOI: 10.1016/j.cej.2018.04.082
 8. Liang, W.; Wang, Y.; Zhao, L.; Guo, W.; Li, D.; Qin, W.; Wu, H.; Sun, Y.; Jiang, L. 3D Anisotropic Au@Pt-Pd Hemispherical Nanostructures as Efficient Electrocatalysts for Methanol, Ethanol, and Formic Acid Oxidation Reaction. *Adv. Mater.* 2021, 33 (30), 2100713 DOI: 10.1002/adma.202100713
 9. Luo, S.; Wang, Y.; Kong, T. C.; Pan, W.; Zhao, X.; Leung, D. Y. Flexible direct formate paper fuel cells with high performance and great durability. *J. Power Sources* 2021, 490, 229526 DOI: 10.1016/j.jpowsour.2021.229526
 10. Copenhaver, T. S.; Purohit, K. H.; Domalaon, K.; Pham, L.; Burgess, B. J.; Manorothkul, N.; Galvan, V.; Sotez, S.; Gomez, F. A.; Haan, J. L. A microfluidic direct formate fuel cell on paper. *Electrophoresis* 2015, 36 (16), 1825-1829 DOI: 10.1002/elps.201400554
 11. Hong, S.; Chung, S.; Park, J.; Hwang, J. P.; Lee, C. H.; Uhm, S.; Bong, S.; Lee, J. Contribution of Interstitial Boron in a Boron-Incorporated Palladium Catalyst Toward Formate Oxidation in an Alkaline Direct Formate Fuel Cell. *ACS Catal.* 2021, 11 (8), 4722-4729 DOI:

10.1021/acscatal.0c03555

12. Jiang, J.; Wieckowski, A. Prospective direct formate fuel cell. *Electrochem commun* 2012, 18, 41-43 DOI: 10.1016/j.elecom.2012.02.017
13. Ding, J.; Liu, Z.; Liu, X.; Liu, J.; Deng, Y.; Han, X.; Zhong, C.; Hu, W. Mesoporous decoration of freestanding palladium nanotube arrays boosts the electrocatalysis capabilities toward formic acid and formate oxidation. *Adv. Energy Mater.* 2019, 9 (25), 1900955 DOI: 10.1002/aenm.201900955
14. Li, Z.; Chen, F.; Bian, W.; Kou, B.; Wang, Q.; Guo, L.; Jin, T.; Tang, Q.; Pan, B. Surface Pourbaix diagram of AgPd nanoalloys and its application in formate oxidation reaction. *Electrochim. Acta* 2021, 386, 138465 DOI: 10.1016/j.electacta.2021.138465
15. Guo, L.; Jin, T.; Tang, Q.; Wang, J.; Pan, B.; Wang, Q.; Li, Z.; Wang, C.; Liu, J. Chen, Reconstruction of AgPd Nanoalloy with Oxidation for Formate Oxidation Electrocatalysis. *J. Mater. Chem. A* 2022. 10(26), 13998-14010 DOI: 10.1039/D2TA01890J
16. An, L.; Chen, R. Direct formate fuel cells: A review. *J. Power Sources* 2016, 320, 127-139 DOI: 10.1016/j.jpowsour.2016.04.082
17. Chang, J.; Feng, L.; Liu, C.; Xing, W.; Hu, X. An effective Pd–Ni₂P/C anode catalyst for direct formic acid fuel cells. *Angew. Chem. Int. Ed.* 2014, 53 (1), 122-126 DOI: 10.1002/anie.201308620
18. Yi, L.; Chen, J.; Shao, P.; Huang, J.; Peng, X.; Li, J.; Wang, G.; Zhang, C.; Wen, Z. Molten-salt-assisted synthesis of bismuth nanosheets for long-term continuous electrocatalytic conversion of CO₂ to formate. *Angew. Chem. Int. Ed.* 2020, 59 (45), 20112-20119 DOI: 10.1002/anie.202008316
19. Shang, H.; Wang, T.; Pei, J.; Jiang, Z.; Zhou, D.; Wang, Y.; Li, H.; Dong, J.; Zhuang, Z.; Chen, W.; Wang, D.; Zhang, J.; Li, Y. Design of a Single-Atom Indium^{δ+}–N₄ Interface for Efficient Electroreduction of CO₂ to Formate. *Angew. Chem. Int. Ed.* 2020, 59 (50), 22465-22469 DOI: 10.1002/anie.202010903
20. Li, J.; Kuang, Y.; Meng, Y.; Tian, X.; Hung, W.-H.; Zhang, X.; Li, A.; Xu, M.; Zhou, W.; Ku, C.-S.; Chiang, C.-Y.; Zhu, G.; Guo, J.; Sun, X.; Dai, H. Electroreduction of CO₂ to formate on a copper-based electrocatalyst at high pressures with high energy conversion efficiency. *J. Am. Chem. Soc.* 2020, 142 (16), 7276-7282 DOI: 10.1021/jacs.0c00122
21. Wang, Q.; Chen, F.; Guo, L.; Jin, T.; Liu, H.; Wang, X.; Gong, X.; Liu, Y. Nanoalloying effects on the catalytic activity of the formate oxidation reaction over AgPd and AgCuPd aerogels. *J.*

Mater. Chem. A 2019, 7 (27), 16122-16135 DOI: 10.1039/C9TA00664H

22. Guo, L.; Chen, F.; Jin, T.; Liu, H.; Zhang, N.; Jin, Y.; Wang, Q.; Tang, Q.; Pan, B. Surface reconstruction of AgPd nanoalloy particles during the electrocatalytic formate oxidation reaction. *Nanoscale* 2020, 12 (5), 3469-3481 DOI: 10.1039/C9NR09660D
23. Wang, Q.; Chen, F.; Tang, Q.; Guo, L.; Jin, T.; Pan, B.; Wang, J.; Li, Z.; Kou, B.; Bian, W. AgPdCo hollow nanospheres electrocatalyst with high activity and stability toward the formate electrooxidation. *Nano Res.* 2021, 14 (7), 2268-2276 DOI: 10.1007/s12274-020-3220-z
24. Chen, L.; Zhang, L.-R.; Yao, L.-Y.; Fang, Y.-H.; He, L.; Wei, G.-F.; Liu, Z.-P. Metal boride better than Pt: HCP Pd₂B as a superactive hydrogen evolution reaction catalyst. *Energy Environ. Sci.* 2019, 12 (10), 3099-3105 DOI: 10.1039/C9EE01564G
25. Xu, W.; Fan, G.; Chen, J.; Li, J.; Zhang, L.; Zhu, S.; Su, X.; Cheng, F.; Chen, J. Nanoporous palladium hydride for electrocatalytic N₂ reduction under ambient conditions. *Angew. Chem. Int. Ed.* 2020, 59 (9), 3511-3516 DOI: 10.1002/anie.201914335
26. Parker, S. F.; Walker, H. C.; Callear, S. K.; Grunewald, E.; Petzold, T.; Wolf, D.; Mobus, K.; Adam, J.; Wieland, S. D.; Jimenez-Ruiz, M.; Albers, P. W. The effect of particle size, morphology and support on the formation of palladium hydride in commercial catalysts. *Chem. Sci.* 2019, 10 (2), 480-489 DOI: 10.1039/C8SC03766C
27. Shi, Y.; Schimmenti, R.; Zhu, S.; Venkatraman, K.; Chen, R.; Chi, M.; Shao, M.; Mavrikakis, M.; Xia, Y. Solution-phase synthesis of PdH_{0.706} nanocubes with enhanced stability and activity toward formic acid oxidation. *J. Am. Chem. Soc.* 2022, 144 (6), 2556-2568 DOI: 10.1021/jacs.1c10199
28. Zhao, Z.; Huang, X.; Li, M.; Wang, G.; Lee, C.; Zhu, E.; Duan, X.; Huang, Y. Synthesis of stable shape-controlled catalytically active β -palladium hydride. *J. Am. Chem. Soc.* 2015, 137 (50), 15672-15675 DOI: 10.1021/jacs.5b11543
29. Chang, Q.; Kim, J.; Lee, J. H.; Kattel, S.; Chen, J. G.; Choi, S. I.; Chen, Z. Boosting activity and selectivity of CO₂ electroreduction by pre-hydridizing Pd nanocubes. *Small* 2020, 16 (49), 2005305 DOI: 10.1002/smll.202005305
30. Liu, J.; Luo, Z.; Li, J.; Yu, X.; Llorca, J.; Nasiou, D.; Arbiol, J.; Meyns, M.; Cabot, A. Graphene-supported palladium phosphide PdP₂ nanocrystals for ethanol electrooxidation. *Appl. Catal. B* 2019, 242, 258-266 DOI: 10.1016/j.apcatb.2018.09.105
31. Du, R.; Xiao, K.; Li, B.; Han, X.; Zhang, C.; Wang, X.; Zuo, Y.; Guardia, P.; Li, J.; Chen, J.; Arbiol, J.; Cabot, A.; Controlled oxygen doping in highly dispersed Ni-loaded g-C₃N₄ nanotubes for

- efficient photocatalytic H₂O₂ production. *Chem. Eng. J.* 2022, 441, 135999 DOI: 10.1016/j.cej.2022.135999
32. Tian, Z.; López-Salas, N.; Liu, C.; Liu, T.; Antonietti, M. C₂N: a class of covalent frameworks with unique properties. *Adv. Sci.* 2020, 7 (24), 2001767 DOI: 10.1002/advs.202001767
 33. Zhong, W.; Qiu, Y.; Shen, H.; Wang, X.; Yuan, J.; Jia, C.; Bi, S.; Jiang, J. Electronic spin moment as a catalytic descriptor for Fe single-atom catalysts supported on C₂N. *J. Am. Chem. Soc.* 2021, 143 (11), 4405-4413 DOI: 10.1021/jacs.1c00889
 34. Liang, Z.; Yang, D.; Tang, P.; Zhang, C.; Biendicho, J. J.; Zhang, Y.; Llorca, J.; Wang, X.; Li, J.; Heggen, M.; David, J.; Dunin-Borkowski, R. E.; Zhou, Y.; Morante, J. R.; Cabot, A.; Arbiol, J. Atomically dispersed Fe in a C₂N based catalyst as a sulfur host for efficient lithium–sulfur batteries. *Adv. Energy Mater.* 2021, 11 (5), 2003507 DOI: 10.1002/aenm.202003507
 35. Yang, D.; Liang, Z.; Zhang, C.; Biendicho, J. J.; Botifoll, M.; Spadaro, M. C.; Chen, Q.; Li, M.; Ramon, A.; Moghaddam, A. O.; Llorca, J.; Wang, J.; Morante, J. R.; Arbiol, J.; Chou, S.; Cabot, A. NbSe₂ Meets C₂N: A 2D-2D Heterostructure Catalysts as Multifunctional Polysulfide Mediator in Ultra-Long-Life Lithium–Sulfur Batteries. *Adv. Energy Mater.* 2021, 11 (36), 2101250 DOI: 10.1002/aenm.202101250
 36. Yang, D.; Liang, Z.; Tang, P.; Zhang, C.; Tang, M.; Li, Q.; Biendicho, J. J.; Li, J.; Heggen, M.; Dunin-Borkowski, R. E.; Xu, M.; Llorca, J.; Arbiol, J.; Morante, J. R.; Chou, S.-L.; Cabot, A.; A High Conductivity 1D π -d Conjugated Metal–Organic Framework with Efficient Polysulfide Trapping-Diffusion-Catalysis in Lithium–Sulfur Batteries. *Adv. Mater.* 2022, 34, 2108835 DOI: 10.1002/adma.202108835
 37. Zhang, C.; Du, R.; Martí-Sánchez, S.; Xiao, K.; Yang, D.; Zhang, C.; Li, C.; Zeng, G.; Chang, X.; He, R.; Arbiol, J.; Li, J.; Biendicho, J. J.; Cabot, A.; Tubular C₃N₄ Nanotubes as Metal-Free Sulfur Hosts toward Stable Lithium–Sulfur Batteries. *Energies*, 2023, 16(12):4545 DOI: 10.3390/en16124545
 38. He, M.; An, W.; Wang, Y.; Men, Y.; Liu, S. Hybrid Metal–Boron Diatomic Site Embedded in C₂N Monolayer Promotes C–C Coupling in CO₂ Electroreduction. *Small* 2021, 17 (42), 2104445 DOI: 10.1002/smll.202104445
 39. Shinde, S. S.; Lee, C. H.; Yu, J.-Y.; Kim, D.-H.; Lee, S. U.; Lee, J.-H. Hierarchically designed 3D holey C₂N aerogels as bifunctional oxygen electrodes for flexible and rechargeable Zn-air batteries. *ACS Nano* 2018, 12 (1), 596-608 DOI: 10.1021/acsnano.7b07473
 40. Kabiraz, M. K.; Kim, J.; Lee, W.-J.; Ruqia, B.; Kim, H. C.; Lee, S.-U.; Kim, J.-R.; Paek, S.-M.; Hong,

- J. W.; Choi, S.-I. Ligand Effect of Shape-Controlled β -Palladium Hydride Nanocrystals on Liquid-Fuel Oxidation Reactions. *Chem. Mater.* 2019, 31 (15), 5663-5673 DOI: 10.1021/acs.chemmater.9b01561
41. Zhao, Z.; Flores Espinosa, M. M.; Zhou, J.; Xue, W.; Duan, X.; Miao, J.; Huang, Y. Synthesis of surface controlled nickel/palladium hydride nanodendrites with high performance in benzyl alcohol oxidation. *Nano Res.* 2019, 12 (6), 1467-1472 DOI: 10.1007/s12274-019-2413-9
 42. Lin, B.; Wu, X.; Xie, L.; Kang, Y.; Du, H.; Kang, F.; Li, J.; Gan, L. Atomic imaging of subsurface interstitial hydrogen and insights into surface reactivity of palladium hydrides. *Angew. Chem. Int. Ed.* 2020, 59 (46), 20348-20352 DOI: 10.1002/anie.202006562
 43. Sun, H.-Y.; Ding, Y.; Yue, Y.-Q.; Xue, Q.; Li, F.-M.; Jiang, J.-X.; Chen, P.; Chen, Y. Bifunctional palladium hydride nanodendrite electrocatalysts for hydrogen evolution integrated with formate oxidation. *ACS Appl. Mater. Interfaces* 2021, 13 (11), 13149-13157 DOI: 10.1021/acscami.0c22106
 44. Dekura, S.; Kobayashi, H.; Ikeda, R.; Maesato, M.; Yoshino, H.; Ohba, M.; Ishimoto, T.; Kawaguchi, S.; Kubota, Y.; Yoshioka, S.; Matsumura, S.; Sugiyama, T.; Kitagawa H. The Electronic State of Hydrogen in the α Phase of the Hydrogen-Storage Material PdH(D)x: Does a Chemical Bond Between Palladium and Hydrogen Exist? *Angew. Chem. Int. Ed.* 2018, 130 (31), 9971-9975 DOI: 10.1002/ange.201805753
 45. Aboud, S.; Wilcox, J. A density functional theory study of the charge state of hydrogen in metal hydrides. *J. Phys. Chem. C* 2010, 114 (24), 10978-10985 DOI: 10.1021/jp911811r
 46. Wang, Z.; Dai, Z.; Wang, S.; Zhang, H.; Tian, W.; Xu, Y.; Li, X.; Wang, L.; Wang, H. J. Enhancing electrochemical ammonia synthesis on palladium nanorods through surface hydrogenation. *Chem. Eng. J.* 2021, 416, 129105 DOI: 10.1016/j.cej.2021.129105
 47. Zhang, J.; Chen, M.; Li, H.; Li, Y.; Ye, J.; Cao, Z.; Fang, M.; Kuang, Q.; Zheng, J.; Xie, Z. Stable palladium hydride as a superior anode electrocatalyst for direct formic acid fuel cells. *Nano energy* 2018, 44, 127-134 DOI: 10.1016/j.nanoen.2017.11.075
 48. Yu, X.; Liu, J.; Li, J.; Luo, Z.; Zuo, Y.; Xing, C.; Llorca, J.; Nasiou, D.; Arbiol, J.; Pan, K.; Kleinhanns, T.; Xie, Y.; Cabot, A. Phosphorous incorporation in Pd₂Sn alloys for electrocatalytic ethanol oxidation. *Nano Energy* 2020, 77, 105116 DOI: 10.1016/j.nanoen.2020.105116
 49. Zhou, M.; Liu, J.; Ling, C.; Ge, Y.; Chen, B.; Tan, C.; Fan, Z.; Huang, J.; Chen, J.; Liu, Z.; Huang, Z.; Ge, J.; Cheng, H.; Chen, Y.; Dai, L.; Yin, P.; Zhang, X.; Yun, Q.; Wang, J.; Zhang, H. Synthesis of Pd₃Sn and PdCuSn nanorods with L12 phase for highly efficient electrocatalytic ethanol

oxidation. *Adv. Mater* 2022, 34 (1), 2106115 DOI: 10.1002/adma.202106115

50. Zhou, X.; Ma, Y.; Ge, Y.; Zhu, S.; Cui, Y.; Chen, B.; Liao, L.; Yun, Q.; He, Z.; Long, H.; Li, L.; Huang, B.; Luo, Q.; Zhai L.; Wang, X.; Bai, L.; Wang, G.; Guan, Z.; Chen, Y.; Lee, C.-S.; Wang, J.; Ling, C.; Shao, M.; Fan, Z.; Zhang, H. Preparation of Au@Pd Core–Shell Nanorods with fcc-2H-fcc Heterophase for Highly Efficient Electrocatalytic Alcohol Oxidation. *J. Am. Chem. Soc.* 2021, 144 (1), 547-555 DOI: 10.1021/jacs.1c11313
51. Wang, Q.; Chen, F.; Tang, Q.; Guo, L.; Gebremariam, T. T.; Jin, T.; Liu, H.; Kou, B.; Li, Z.; Bian, W. Transition from core-shell to Janus segregation pattern in AgPd nanoalloy by Ni doping for the formate oxidation. *Appl. Catal. B* 2020, 270, 118861 DOI: 10.1016/j.apcatb.2020.118861
52. Tang, Q.; Chen, F.; Wang, Q.; Jin, T.; Guo, L.; Wu, Y.; Yu, S.; Li, Z. Surface reconstruction of AgPdF and AgPd nanoalloys under the formate oxidation reaction. *J. Mater. Chem. A* 2021, 9 (40), 23072-23084 DOI: 10.1039/D1TA05472D

SUPPORTING INFORMATION

3.6. SI EXPERIMENTAL SECTION

3.6.1. Chemicals

OAm (approximate C18 content 80–90%) was purchased from ACROS Organics. Palladium(II) acetylacetonate ($\text{Pd}(\text{acac})_2$, Pd 34.7 wt%), potassium hydroxide (KOH, 85%), sulfuric acid (95–98%), NMP (99.99%), diethyl ether (99.9%) and Nafion (5 wt% in a mixture of low aliphatic alcohols and water) were obtained from Sigma-Aldrich. EDA (99%), HACO (99%), CAA (98%), ODE (90%) and a reference Pd catalyst, 20% Pd on activated carbon powder, were purchased from Alfa Aesar. Hexane, ethanol and acetone were of analytical grade and obtained from various sources. MilliQ water was obtained from a Purelab flex from Elga. All chemicals were used as received, without further purification.

3.6.2. Synthesis of Hexaaminobenzene

CAA was added into a 15 mL glass vial placed in a 0 °C ice bath under vigorous stirring. Next, 5.64 mL EDA and a few drops of concentrated sulfuric acid were added. Then the ice bath was removed and the obtained solution was warmed up to room temperature. Afterwards, the solution was transferred to a 15 mL Teflon autoclave, where it was maintained at 80 °C for 12 h to complete the amination reactions. Then the solution was cooled to room temperature and the obtained mixture was vacuum filtrated using a PTFE membrane (0.47 μm), rinsed with diethyl ether and degassed ethanol three times, and finally vacuum dried overnight. The identity of the final product was confirmed by ^1H NMR. ^1H NMR (400 MHz, $\text{H}_2\text{O}-d_2$, δ): 3.39 (s, 2H, NH_2) (Figure 3.S1).

3.6.3. Synthesis of C_2N

An equal mol ratio of HAB and CAA, and degassed NMP were placed into a three-necked round bottom flask placed in an ice bath under argon gas. Under vigorous stirring, a few drops of concentrated sulfuric acid were added. Then the ice bath was removed and the mixture was warmed up to room temperature. The resulting solution was heated to 175 °C for 12 h. After cooling to room temperature, the mixture was vacuum filtrated, washed with ethanol and water three times, and finally freeze-dried for 24 h. The obtained black solid was annealed at 450 °C for 3 h under argon gas with a ramp rate of 5 °C min^{-1} .

3.6.4. Synthesis of PdH_{0.58}@C₂N, Pd@C₂N, PdH_{0.58} and PdH_{0.58}/C₂N

10 mL OAm, 5 mL ODE, and 5 mL of a C₂N ethanol solution (6 mg mL⁻¹) were added to a three-necked flask and heated to 120 °C for about 1h min under Ar atmosphere to remove water, ethanol, and oxygen. Afterwards, 0.5 mmol Pd(acac)₂ were added to the solution and the temperature of the mixture was slowly increased to 180 °C at a rate of 5 °C min⁻¹ and maintained for 30 min. After cooling, the obtained black product was washed with ethanol and hexane via centrifugation three times, dried in a vacuum oven at 60 °C overnight, and annealed at 350 °C in an Ar gas atmosphere for 2 h to remove the organic ligands. As a reference, Pd@C₂N was synthesized by annealing the PdH_{0.58}@C₂N in Ar gas at 450 °C for 2 h. Additionally, PdH_{0.58} NPs were also produced in the absence of C₂N and they were physically supported on C₂N by sonication in ethanol and hexane mixed solution to produce a third reference sample, PdH_{0.58}/C₂N.

3.6.5. Structural characterization

Powder XRD was performed on a Bruker AXS D8 Advance X-ray diffractometer with Cu-K α radiation ($\lambda = 1.5406 \text{ \AA}$). SEM analysis was conducted with a Zeiss Auriga microscope equipped with an EDS detector operating at 20 kV. TEM, HRTEM, HAADF-STEM and EELS analysis were obtained using a field emission gun FEI™ Tecnai F20 microscope with a Gatan Quantum filter at 200 kV. XPS measurements were conducted on a SPECS system equipped with an Al anode XR50 source operating at 150 W and a Phoibos 150 MCD-9 detector. ICP-MS was conducted with a Shimadzu simultaneous ICP atomic emission spectrometer ICPE-9820.

3.6.6. Electrochemical Measurements

Electrochemical measurements were conducted at room temperature with an electrochemical workstation (CHI 760E, CH Instruments) using a standard three-electrode system. A Hg/HgO (1 M KOH) and graphite rod were employed as reference and counter electrodes, respectively. The catalyst ink was produced by ultrasonically dispersing 2 mg of the catalyst powder in 750 μ L isopropanol, 230 μ L deionized water and 20 μ L of 5 wt% Nafion solution. The working electrode was prepared by drop-casting 5 μ L of the catalyst ink on a 5 mm diameter GC electrode and letting it dry naturally. CV curves were recorded at a scan rate of 50 mV s⁻¹ in Ar-saturated aqueous solutions that contained 0.5 M KOH or 0.5 M KOH + 0.5 M HCOOK. CA measurements were conducted at -0.2 V vs. Hg/HgO for 5000 s in a 0.5 M KOH + 0.5 M HCOOK electrolyte.

3.6.7. Computational method

We have employed VASP^{1,2} to perform all the DFT calculations within the GGA using the PBE formulation.³ We have chosen the PAW potentials^{4,5} to describe the ionic cores and take valence electrons into account using a plane wave basis set with a kinetic energy cutoff of 400 eV. Partial occupancies of the Kohn–Sham orbitals were allowed using the Gaussian smearing method and a width of 0.05 eV. The electronic energy was considered self-consistent when the energy change was smaller than 10^{-5} eV. A geometry optimization was considered convergent when the force change was smaller than 0.02 eV/Å. Grimme’s DFT-D3 methodology was used to describe the dispersion interactions.⁶

The equilibrium lattice constant of FCC Pd unit cell was optimized, when using a $10\times 10\times 10$ Monkhorst-Pack k-point grid for Brillouin zone sampling, to be $a=3.886$ Å. The equilibrium lattice constants of hexagonal C₂N monolayer unit cell were optimized, when put together with a vacuum layer in the depth of 15 Å and using a $3\times 3\times 1$ Monkhorst-Pack k-point grid for Brillouin zone sampling, to be $a=8.310$ Å. We then use it to construct a Pd(111)/C₂N heterojunction surface model (model 1). It should be noted that we also constructed the Pd(200)/C₂N model and calculated the formate adsorption energy on both Pd(111)/C₂N and Pd(200)/C₂N. Because the adsorption energy of formate on Pd(111)/C₂N was higher than on Pd(200)/C₂N, we used the former model for further calculations.

The Pd(111) part of model 1 has a $p(3\times 3)$ periodicity in the x and y directions and 3 atomic layers; the C₂N part has a unit cell of C₂N monolayer; the Pd(111)/C₂N slab was separated in the z direction by a vacuum layer in the depth of 15 Å in order to separate the surface slab from its periodic duplicates. Model 2 was built by adding one layer of H atoms between the topmost layer of Pd(111) part in model 1 and second layer of Pd(111). During structural optimizations, a $2\times 2\times 1$ k-point grid in the Brillouin zone was used for k-point sampling, and all atoms were allowed to relax.

The adsorption energy (E_{ads}) of adsorbate A was defined as: $E_{\text{ads}} = E_{\text{A/surf}} - E_{\text{surf}} - E_{\text{A(g)}}$, where $E_{\text{A/surf}}$, E_{surf} and $E_{\text{A(g)}}$ are the energy of adsorbate A adsorbed on the surface, the energy of clean surface, and the energy of isolated A molecule in a cubic periodic box with a side length of 20 Å and a $1\times 1\times 1$ Monkhorst-Pack k-point grid for Brillouin zone sampling, respectively.

The transition state of an elementary reaction step was located by the nudged elastic band (NEB) method.⁷ In the NEB method, the path between the reactant(s) and product(s) was discretized into a series of five structural images. The intermediate images were relaxed until the perpendicular forces were smaller than 0.02 eV/Å.

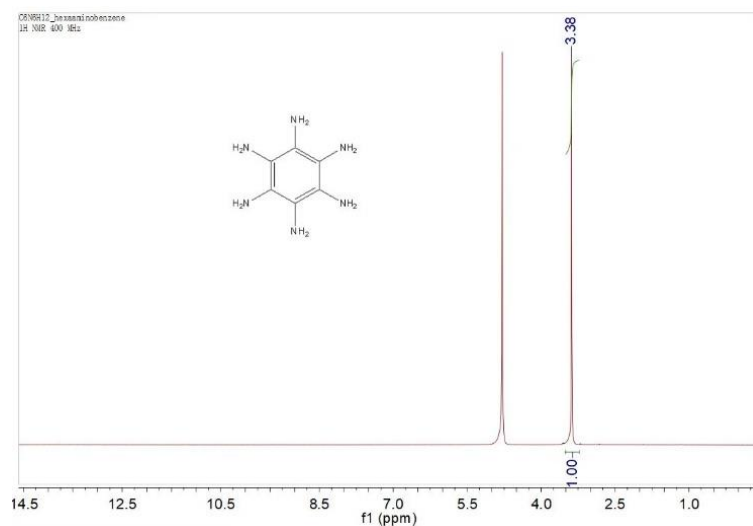


Figure 3.S1. ^1H NMR spectrum of HAB. (^1H NMR (400 MHz, $\text{H}_2\text{O}-d_2$, δ): 3.39 (s, 2H, NH_2))

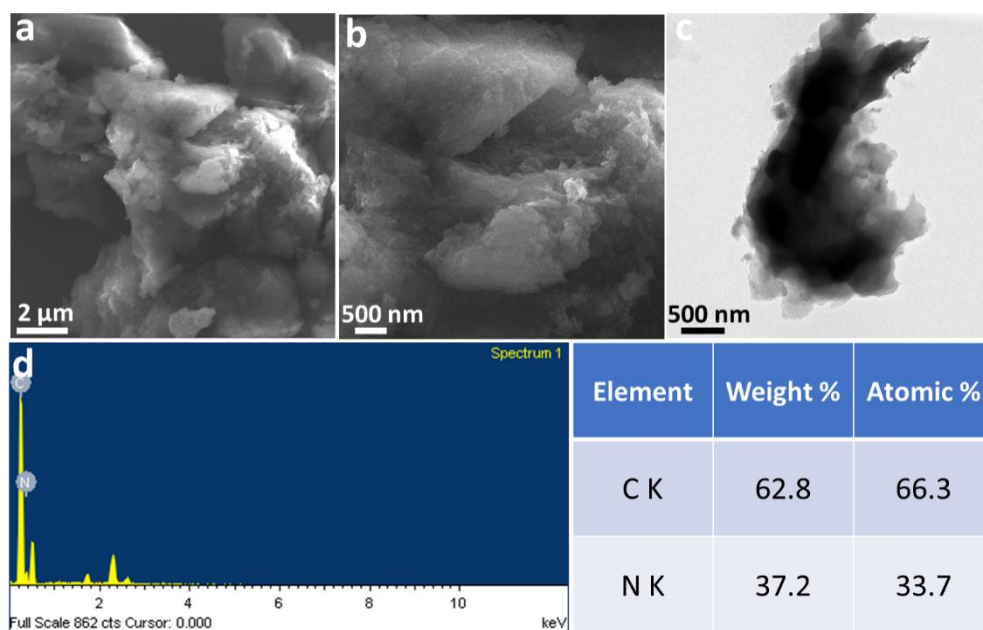


Figure 3.S2. a-b) SEM, c) TEM images and d) EDS result of C_2N .

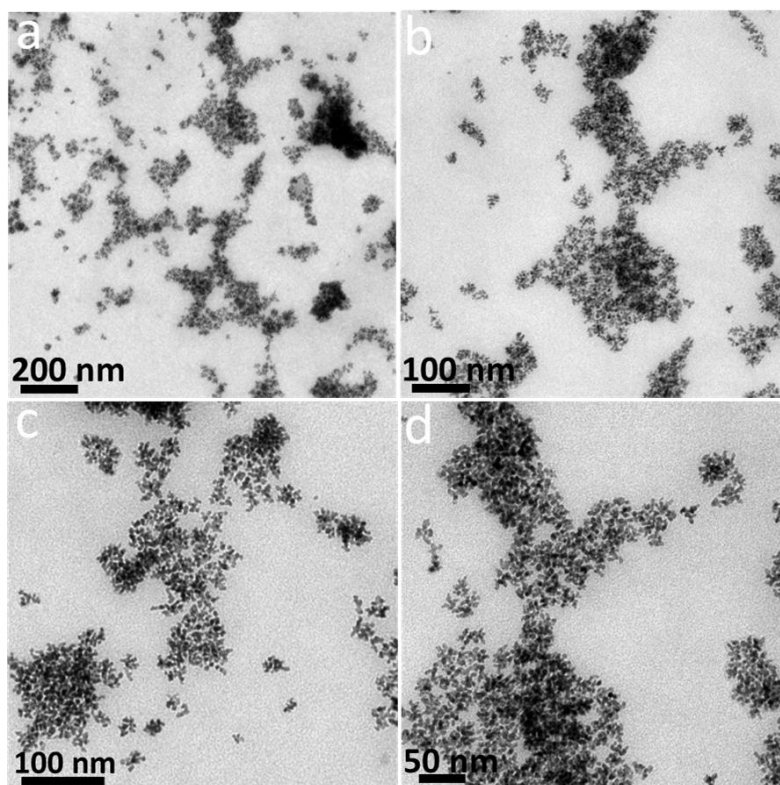


Figure 3.S3. a-d) TEM images of in situ PdH@C₂N

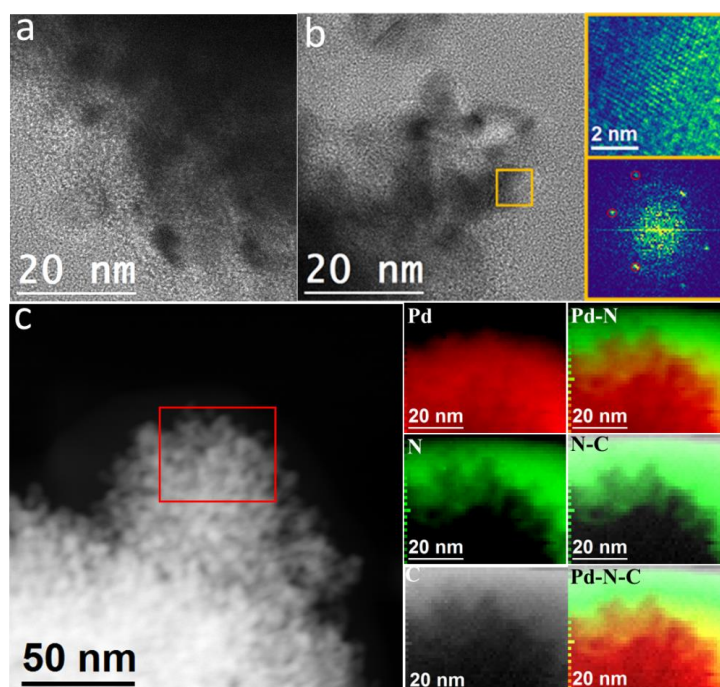


Figure 3.S4. a) TEM images of Pd@C₂N, **b)** HRTEM and corresponding FFT spectrum Pd@C₂N, **c)** HAADF-STEM and EELS chemical composition maps of Pd@C₂N obtained from the red squared area of the STEM micrograph. Individual Pd M_{4,5}-edges at 335 eV (red), N K-edges at 401 eV (green) and C K-edges at 285 eV (grey) and composites of Pd-N, N-C and Pd-N-C.

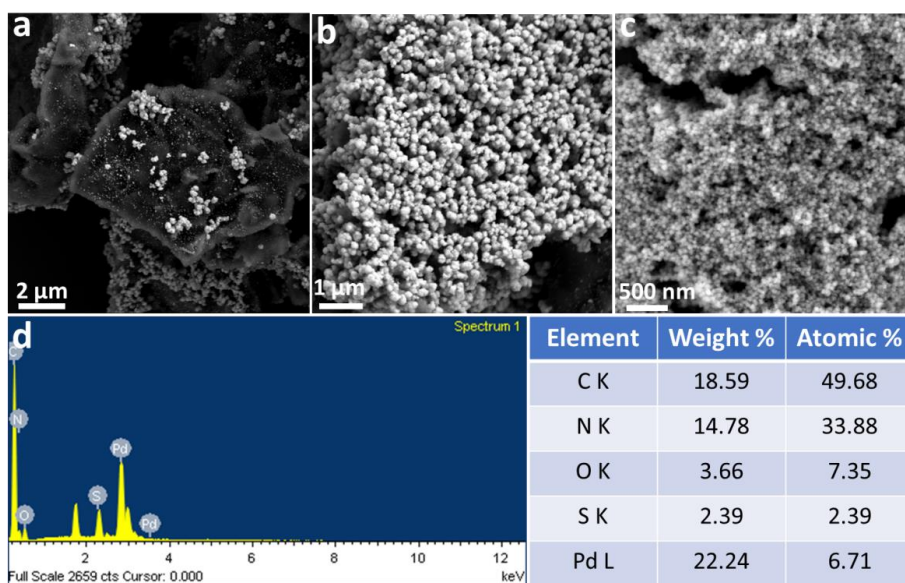


Figure 3.S5. a-c) SEM images and d) EDS result of PdH/C₂N.

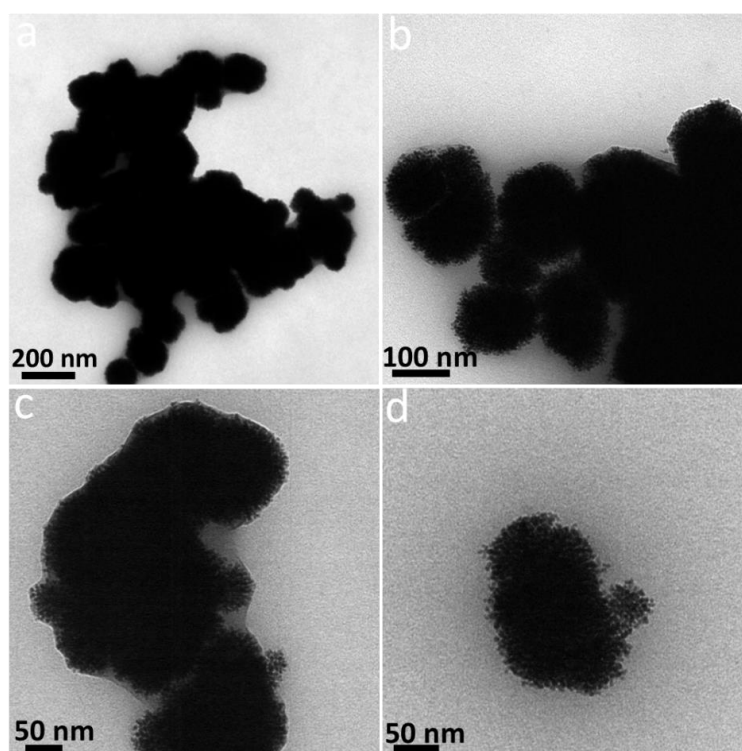


Figure 3.S6. a-d) TEM images of PdH_{0.58} NP without C₂N

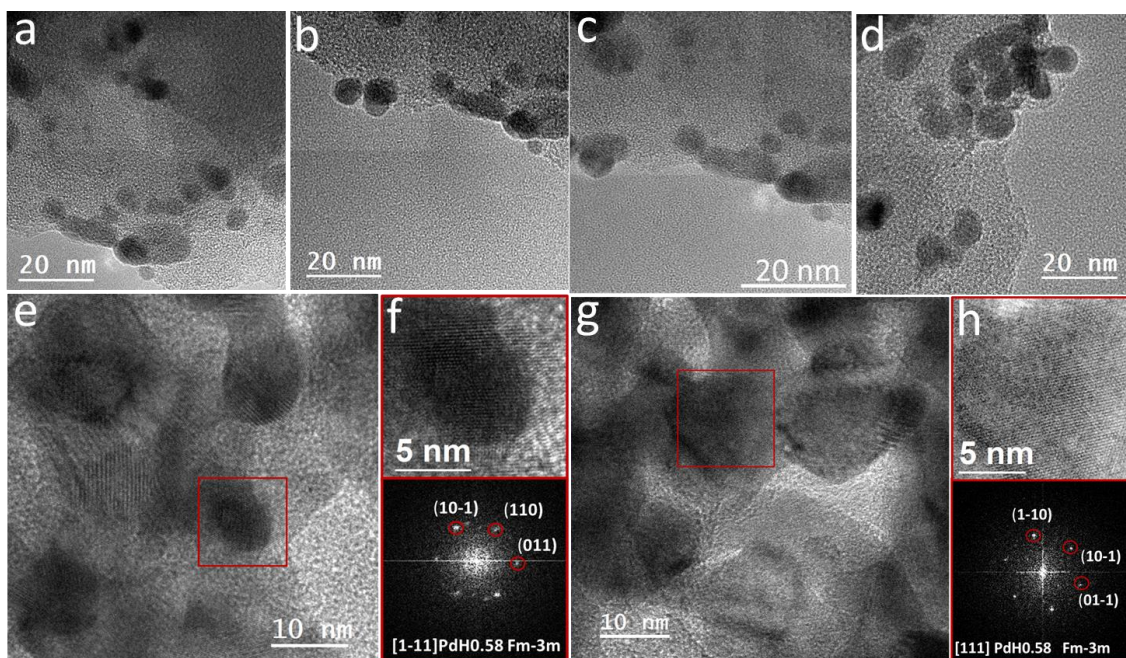


Figure 3.S7. a-d) TEM images; **e-h)** HRTEM images and corresponding FFT spectra of $\text{PdH}_{0.58}@C_2N$ after 1000 cycles in the range -0.9 to 0.3 V vs. Hg/HgO

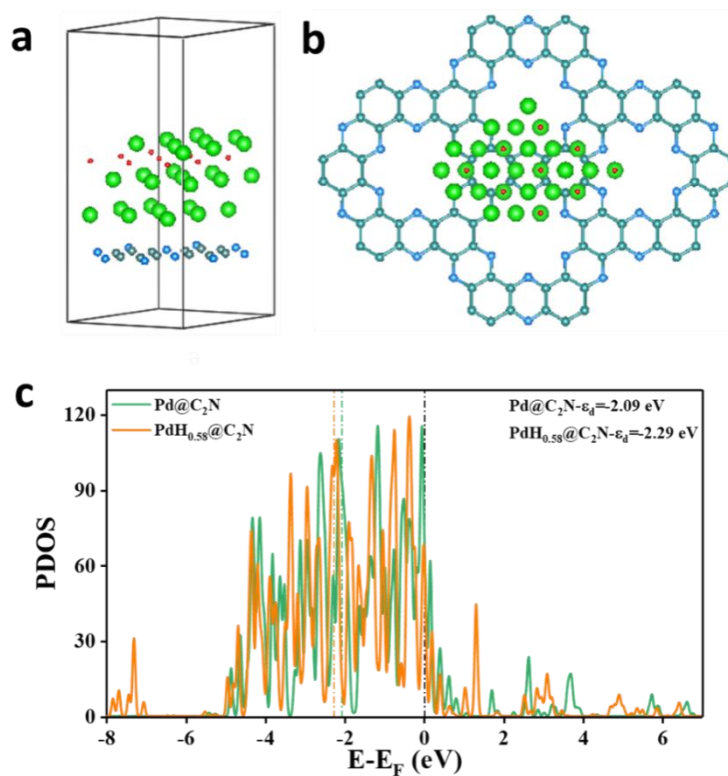


Figure 3.S8. a, b) Simulated $\text{PdH}_{0.58}@C_2N$ models and **c)** d-band centre of $\text{Pd}@C_2N$ and $\text{PdH}_{0.58}@C_2N$.

Table 3.S1. Summary of the FOR activity and stability of Pd-based nanoalloys.

Electrocatalyst	Mass activity (A mg _{Pd} ⁻¹)	Specific activity (mA cm ⁻²)	Electrolyte	Ref.
PdH_{0.58}@C₂N	5.6	27.4	0.5 M KOH + 0.5 M HCOOK	This work
Pd ₃ Au ₃ Ag ₁ /CNT	4.5	14.5	1.0 M KOH + 1.0 M HCOOK	8
PdNi/C	4.5	12.0	1.0 M KOH + 1.0 M HCOOK	9
PdRh/C	4.5	8.1	1.0 M KOH + 1.0 M HCOOK	10
Pd ₅₅ Ag ₃₀ Rh ₁₅ /C	3.3	5.9	1.0 M KOH + 1.0 M HCOOK	11
Ag ₂₀ Pd ₆₀ Ni ₂₀	3.0	10.9	2.0 M KOH + 2.0 M HCOOK	12
PdAgPt aerogels	2.9	3.5	0.5 M KOH + 0.5 M HCOOK	13
PdAgCu aerogels	2.7	10.1	1.0 M KOH + 1.0 M HCOOK	14
Pd ₇₂ Ce ₂₈ /C	1.1	19.4	1.0 M KOH + 1.0 M HCOOK	15
Pt-Ag alloy nanoballoon	0.8	32.6	1.0 M KOH + 1.0 M HCOOK	16
Pd ₁₀ /Ag-CNTs	4.7	0.9	1.0 M KOH + 1.0 M HCOOK	17

3.7. SI REFERENCES

- 1 Kresse, G.; Furthmüller, J.; Efficient iterative schemes for ab initio total-energy calculations using a plane-wave basis set, *Phys. Rev. B* **1996**, *54*, 11169 DOI: 10.1103/PhysRevB.54.11169
- 2 Kresse, G.; Furthmüller, J.; Efficiency of ab-initio total energy calculations for metals and semiconductors using a plane-wave basis set, *Comput. Mater. Sci.* **1996**, *6* (1) 15-50 DOI: 10.1016/0927-0256(96)00008-0
- 3 Perdew, J.-P.; Burke, K.; Ernzerhof, M.; Generalized gradient approximation made simple, *Phys. Rev. Lett.* **1996**, *77*(18), 3865 DOI: 10.1103/PhysRevLett.77.3865
- 4 Kresse, G.; Joubert, D.; From ultrasoft pseudopotentials to the projector augmented-wave method, *Phys. Rev. B* **1999**, *59* (3), 1758 DOI: 10.1103/PhysRevB.59.1758

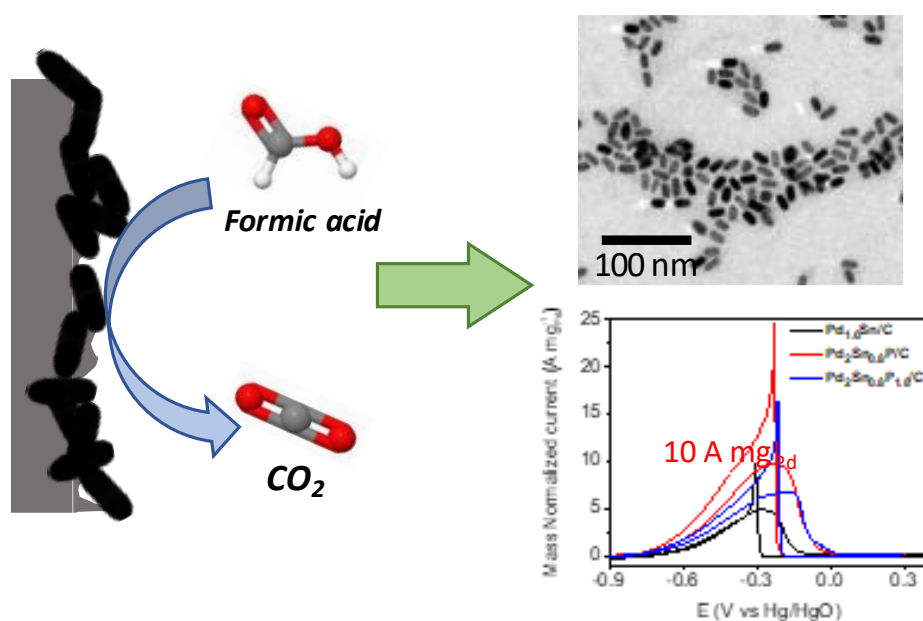
- 5 Blöchl, P.-E.; Projector augmented-wave method, *Phys. Rev. B* **1994**, *59* (24), 17953 DOI: 10.1103/PhysRevB.50.17953
- 6 Grimme, S.; Antony, J.; Ehrlich, S.; Krieg, H.; A consistent and accurate *ab initio* parametrization of density functional dispersion correction (DFT-D) for the 94 elements H-Pu, *J. Chem. Phys.* **2010**, *132*, 154104 DOI: 10.1063/1.3382344
- 7 Henkelman, G.; Uberuaga, B.-P.; Jónsson, H.; A climbing image nudged elastic band method for finding saddle points and minimum energy paths, *J. Chem. Phys.* **2000**, *113*, 9901–9904 DOI: 10.1063/1.1329672
- 8 Pan, B.; Chen, F.; Kou, B.; Wang, J.; Tang, Q.; Guo, L.; Wang, Q.; Li, Z.; Bian, W.; Wang, J.; Unexpectedly high stability and surface reconstruction of PdAuAg nanoparticles for formate oxidation electrocatalysis, *Nanoscale* **2020**, *12*, 11659-11671 DOI: 10.1039/D0NR01358G
- 9 Sankar, S.; Anilkumar, G.-M.; Tamaki, T.; Yamaguchi, T.; Binary Pd– Ni nanoalloy particles over carbon support with superior alkaline formate fuel electrooxidation performance, *ChemCatChem* **2019**, *11*(19), 4731-4737 DOI: 10.1002/cctc.201900960
- 10 Bai, J.; Xue, Q.; Zhao, Y.; Jiang, J.-X.; Zeng, J.-H.; Yin, S.-B.; Chen, Y.; Component-dependent electrocatalytic activity of ultrathin PdRh alloy nanocrystals for the formate oxidation reaction, *ACS Sustainable Chem. Eng.* **2019**, *7*(2), 2830–2836 DOI: 10.1021/acssuschemeng.8b06193
- 11 Jin, Y.; Chen, F.; Guo, L.; Wang, J.; Kou, B.; Jin, T.; Liu, H.; Engineering two-dimensional PdAgRh nanoalloys by surface reconstruction for highly active and stable formate oxidation electrocatalysis, *ACS Appl. Mater. Interfaces* **2020**, *12*(23), 26694–26703 DOI: 10.1021/acsaami.0c05929
- 12 Wang, Q.; Chen, F.; Tang, Q.; Guo, L.; Gebremariam, T.-T.; Jin, T.; Liu, H.; Kou, B.; Li, Z.; Bian, W.; Transition from core-shell to Janus segregation pattern in AgPd nanoalloy by Ni doping for the formate oxidation, *Appl. Catal. B*, **2020**, *270*, 118861 DOI: 10.1016/j.apcatb.2020.118861
- 13 Wang, J.; Chen, F.; Jin, Y.; Guo, L.; Gong, X.; Wang, X.; Johnston, R.; In situ high-potential-driven surface restructuring of ternary AgPd–Pt dilute aerogels with record-high performance improvement for formate oxidation electrocatalysis, *Nanoscale*, **2019**, *11*, 14174-14185 DOI: 10.1039/C9NR03266E
- 14 Wang, Q.; Chen, F.; Guo, L.; Jin, T.; Liu, H.; Wang, X.; Gong, X.; Liu, Y.; Nanoalloying effects on the catalytic activity of the formate oxidation reaction over AgPd and AgCuPd aerogels, *J.*

Mater. Chem. A, **2019**, *7*, 16122-16135 DOI: 10.1039/C9TA00664H

- 15 Tang, Q.; Chen, F.; Jin, T.; Guo, L.; Wang, Q.; Liu, H.; Alloying in inverse CeO₂/Pd nanoparticles to enhance the electrocatalytic activity for the formate oxidation reaction, *J. Mater. Chem. A*, **2019**, *7*, 22996-23007 DOI: 10.1039/C9TA07721A
- 16 Han, S.-H.; Liu, H.-M.; Bai, J.; Tian, X.L.; Xia, B.Y.; Zeng, J.-H.; Jiang, J.-X.; Chen, Y.; Platinum-silver alloy nanoballoon nanoassemblies with super catalytic activity for the formate electrooxidation, *ACS Appl. Energy Mater.* **2018**, *1* (3), 1252–1258 DOI: 10.1021/acsaem.8b00004
- 17 Wang, J.; Liu, C.; Lushington, A.; Cheng, N.; Banis, M.N.; Riese, A.; Sun, X.; Pd on carbon nanotubes-supported Ag for formate oxidation: the effect of Ag on anti-poisoning performance, *Electrochim. Acta*, **2016**, *210*, 285-292

CHAPTER 4

PHOSPHOROUS INCORPORATION INTO PALLADIUM TIN NANOPARTICLES FOR THE ELECTROCATALYTIC FORMATE OXIDATION REACTION



4.1. ABSTRACT

The deployment of DFFCs relies on the development of active and stable catalysts for the FOR. Palladium, providing effective full oxidation of formate to CO₂, has been widely used as FOR catalyst, but it suffers from low stability, moderate activity, and high cost. Herein, we detail a colloidal synthesis route for the incorporation of P on Pd₂Sn NPs. These NPs are dispersed on CB and the obtained composite is used as electrocatalytic material for the FOR. The Pd₂Sn_{0.8}P-based electrodes present outstanding catalytic activities with record mass current densities up to 10.0 A mg_{Pd}⁻¹, well above those of Pd_{1.6}Sn/C reference electrode. These high current densities are further enhanced by increasing the temperature from 25 °C to 40 °C. The Pd₂Sn_{0.8}P electrode also allows for slowing down the rapid current decay that generally happens during operation and can be rapidly re-activated through potential cycling. The excellent catalytic performance obtained is rationalized using DFT calculations.

4.2. INTRODUCTION

Fuel cells, characterized by high efficiencies of conversion from chemical to electrical energy, are an appealing alternative to conventional fossil fuel-based combustion technologies. Among the possible energy carriers, liquid and solid C_1 and C_2 fuels, such as ethanol, methanol, FA, or formate, are particularly attractive. Such fuels can be directly produced from CO₂RR, thus enabling a zero-CO₂ energy cycle, and offer advantages in terms of safety, storage, and transportation over carbon-free energy carriers such as hydrogen, hydrazine, or ammonia.¹

DFAFCs have received special attention due to their high energy density, low fuel crossover, and superior theoretical cell potential of 1.45 V, which is well above that of direct ethanol fuel cells, 1.14 V, and direct methanol fuel cells, 1.21 V. Despite these advantages, DFAFCs have not reached the market because of drawbacks associated with the use of an acid medium, including moderate stability related to the degradation of the electrodes and membrane, and the toxicity and corrosiveness of FA at high concentration.

As an alternative to DFAFCs, DFFCs have received much less attention despite their several key advantages.²⁻⁷ The use of a solid formate salt is beneficial in terms of storage and transportation over liquid FA. Formate is also characterized by much lower toxicity and corrosiveness than FA, and therefore it can be used at higher concentrations.^{3,6} Besides, DFFC present faster kinetics due to the rapid ORR kinetics in alkaline medium when compared with an acid environment.⁸

However, the performance and overall cost-effectiveness of DFFCs strongly depend on the performance of the catalyst activating the FOR. FOR can proceed through two main pathways.⁹ A first pathway is the direct formate oxidation to CO₂. This is the most convenient mechanism for electrochemical application because it is the fastest and most energetically efficient. The second pathway is the indirect reaction that involves the initial formation of intermediate CO_{ads} that is afterward oxidized to CO₂.

As a drawback of DFFCs, the demanding FOR requires the use of noble metal catalysts such as Pt and Pd. Among FOR electrocatalysts, Pt generally displays the highest initial activities, but it also suffers from poor stability.¹⁰⁻¹⁴ Pt-based catalysts generally drive FOR through the indirect path, producing CO_{ads} that strongly bind to the surface active sites, thus rapidly deactivating the catalyst.¹⁵ Besides being slightly more abundant and less expensive than Pt, Pd also shows higher long-term activity and durability, which has positioned Pd as the state-of-the-art FOR catalyst.^{2-4,16-20} However, pure Pd catalysts still suffer from too elevated cost, and unsatisfactory activity

and durability for the deployment of cost-effective commercial DFFC.²¹ While competition between the two FOR mechanisms exist in pure Pd catalysts, Pd oxidizes formate mainly through the direct pathway.²² During this process, formate decomposes into surface adsorbed H_{ads} and CO_{2ads}.²³ H_{ads} binds strongly to the Pd active sites, which is generally assumed to block the adsorption of unreacted formate molecules and, consequently, reduce the catalytic activity.^{24–26} Besides, the production of CO_{ads} through the minoritarian indirect reaction pathway also affects the catalyst's long-term activity.

Several strategies have been developed to overcome the limitations of Pd catalysts. The main approach is the alloying of palladium with other metallic or non-metallic elements. This alloying target three main objectives: i) to optimize the palladium electronic energy levels to tune the adsorption energy of precursors/intermediates/products; ii) to provide additional surface adsorption/reaction sites; and iii) to minimize the amount of Pd used. In this scenario, numerous noble metal Pd-based alloys have been tested, including Pd-Ag,^{27–29} Pd-Rh,³⁰ Pd-Au,^{31,32} Pd-Ag-Ir,³³ Pd-Ag-Ru,³⁴ Pd-Ag-Rh,³⁵ or Pd-Au-Ag³⁶. Besides, the alloying of Pd with abundant metals such as Sn, Cu, Ni, or Co is not only particularly interesting in terms of cost but also to promote the interaction with hydroxyl groups.^{24,37,38} The formation of M-OH weakens the adsorption of poisoning intermediates such as CO_{ads} and H_{ads}. As an example, J. Noborikawa et al. demonstrated Pd₈₇Cu₁₃/C to have 1.8 times higher activity than monometallic Pd/C.³⁹ Qiao Wang et al. showed that the incorporation of Cu into AgPd resulted in a factor 1.2 mass activity increment and improved stability compared to the binary compound.²⁴ Besides, Sankar et al. reported Pd_{2.3}Co/C with a mass activity of 2.5 A mg_{Pd}⁻¹ and PdNi/VC with 4.5 A mg_{Pd}⁻¹, well above that of Pd/C.^{38,40}

Among the different Pd alloys, PdSn is particularly interesting both in terms of cost and performance in oxidation reactions. We and others have demonstrated that the incorporation of Sn remarkably improves the Pd resistance towards poisoning and the electrooxidation catalytic activity by both electronic and geometrical effects.^{41–48} Several previous works have tested Pd-Sn alloys for the FA oxidation reaction (FAOR).^{49–53} Liu et al. showed Pd₂Sn as the most effective catalyst in comparison with other Pd_xSn_y alloys and pure Pd/C.⁵¹ Wang *et al.* obtained PdSn alloy NPs on carbon nanotubes with 1.81 times higher activity and superior stability towards FAOR than the palladium counterpart. Additionally, Hwang et al. deposited PdSn on Ti and demonstrated excellent performance in the interconversion between CO₂ and FA.^{52,53} Surprisingly, very few studies have focused on the application of Pd-Sn alloys as FOR electrocatalysts in DFFCs. Recently, Sasidharan *et al.* reported a Pd₈₅Sn₁₅ alloy with an excellent

FOR activity of 5.7 A mg^{-1} , which is more than 3.5 times that of Pd/C, and prominent stability.⁵⁴ Additionally, Hosseini-Benhangi developed a novel class of non-metal flow batteries using bifunctional CO_2 /formate electrocatalysis based on binary PdSn and ternary PdSnPb and PdSnIn alloys.⁵⁵

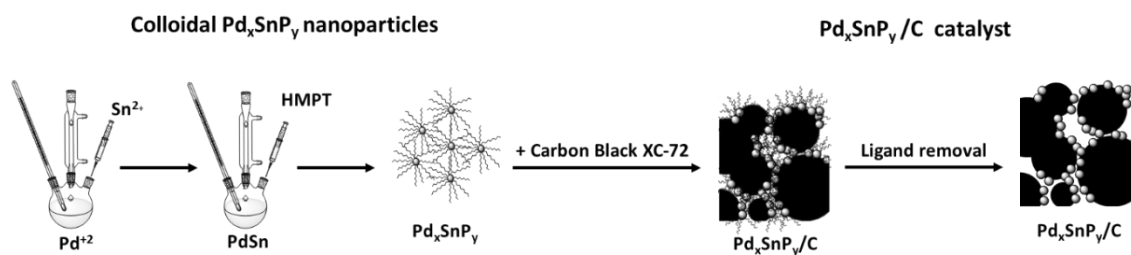
Phosphorus is an inexpensive non-metallic element with abundant valence electrons. Its alloying with metals modify the metal's electronic state, facilitating the adsorption of hydroxyl species and hampering the adsorption of poisoning compounds and the dissolution of metal ions from the catalyst surface. To the best of our knowledge, no studies have reported the use of palladium phosphides for FOR. However, Pd-P and Pd-M-P alloys have been demonstrated as efficient catalysts for the FAOR.⁵⁶⁻⁶¹ As an example, the ternary PdNiP exhibits a remarkable improvement in electrocatalytic activity towards FA, methanol, ethanol oxidation, and HER compared to the binary PdNi.⁶²⁻⁶⁵ Besides, we demonstrated the incorporation of P to PdSn alloys to significantly improve the catalyst performance towards the ethanol oxidation reaction.⁶⁶

In this work, we demonstrate that the incorporation of phosphorus into PdSn NPs results in a significant improvement of the FOR electrocatalytic performance. Using a colloidal synthesis method, Pd-Sn-P particles are prepared and afterward supported onto CB. The FOR activity and stability of the produced composite electrodes are experimentally analysed. Besides, the outstanding performances obtained are rationalized using DFT calculations.

4.3. RESULTS AND DISCUSSION

4.3.1. Catalyst physico-chemical properties.

As detailed in the experimental section (Supporting Information, SI), phosphorous-containing palladium tin-based catalysts were prepared through a four-step approach (Scheme 4.1). In the first step, colloidal Pd-Sn NPs were grown from the co-reduction of $\text{Pd}(\text{acac})_2$ and $\text{Sn}(\text{OAc})_2$ at $230 \text{ }^\circ\text{C}$ using OAm as both solvent and reducing agent, and TOP and MAC as stabilizers and shape-directing agents.⁶⁷ Afterwards, phosphorous was incorporated into the Pd-Sn NPs through reaction with HMPT at $300 \text{ }^\circ\text{C}$. In a third step, Pd-Sn-P NPs were supported onto CB Vulcan XC-72 to maximize the particle dispersion for electrochemical application. Once supported, the NP surface ligands were removed using an acid treatment and posterior annealing under an inert atmosphere to obtain a ligand-free electrocatalyst.⁶⁷⁻⁷⁴



Scheme 4.1. Schematic view of the process used to prepare the palladium tin phosphide-based catalyst.

TEM analysis of the produced Pd-Sn-P NPs shows them to be characterized by elongated geometries with an average length of 20 nm and an average thickness of 9 nm (Figure 4.1a). SEM-EDS and ICP-MS data confirmed the presence of the three elements with an atomic ratio of Pd/Sn/P = 2/0.8/1 (Figure 4.S1b). The powder XRD pattern of the Pd₂Sn_{0.8}P particles resembles that of an orthorhombic Pd₂Sn phase with space group Pnma (JCPDS 01-89-2057, Figure 4.1b). Figure 4.1c shows a representative HRTEM image of the Pd₂Sn_{0.8}P NPs. The FFT of the magnified detail matched that of the Pd₂Sn orthorhombic Pnma phase, consistent with XRD data. No additional phases, particularly the binary phosphides SnP (JCPDS 03-065-9787) and PdP (JCPDS 01-077-1421), were detected by HRTEM and XRD analyses (Figure 4.S5). Figure 4.1d displays a TEM image of the Pd₂Sn_{0.8}P particles homogeneously dispersed onto CB, after the purification and annealing process. HAADF-STEM and EELS analysis of the supported particles showed a uniform distribution of the three elements throughout each NP and between NPs (Figure 4.1e). To evaluate the electrocatalytic activity variation with the incorporation of phosphorous, binary Pd_{1.6}Sn and ternary Pd₂Sn_{0.8}P_{1.8} containing a larger amount of P were also prepared (Figure S1a and 4.S1c). Pd_{1.6}Sn and Pd₂Sn_{0.8}P_{1.8} also displayed elongated morphologies (Figure 4.S2 and 4.S3, respectively) and a structure similar to the orthorhombic Pd₂Sn phase (Figure 4.S4 and 4.S6, respectively).

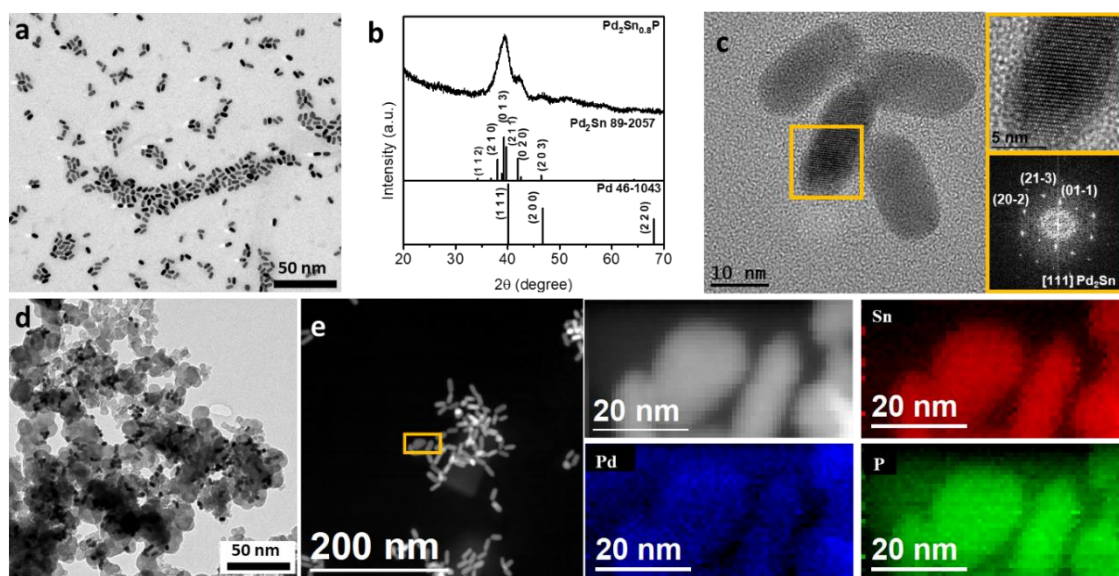


Figure 4.1. Structural and chemical characterization of Pd₂Sn_{0.8}P NPs. (a) TEM micrograph. (b) XRD pattern. (c) HRTEM micrograph, detail of the orange squared region and its corresponding indexed FFT. (d) TEM image of the Pd₂Sn_{0.8}P NPs supported onto CB. (e) HAADF-STEM general image of the Pd₂Sn_{0.8}P NPs (left) and HAADF-STEM magnified detail of the orange squared region on the left with the corresponding EELS elemental composition maps (right): Pd (blue), Sn (red) and P (green).

Figure 4.2 displays the XPS spectra of Pd₂Sn_{0.8}P NPs. The high-resolution Pd 3d XPS spectrum has the main doublet at 335.6 eV (3d_{5/2}) attributed to metallic Pd, and another less intense doublet at 337.2 eV (3d_{5/2}) assigned to Pd²⁺. The Sn 3d XPS spectrum also displays two doublets, at 484.8 eV (Sn 3d_{5/2}) and 487.0 eV (Sn 3d_{5/2}), that are assigned to a metallic Sn and an oxidized Sn^{x+} component, respectively. In this case, the oxidized Sn component is majoritarian. Figure 4.S7 shows a comparison of the XPS spectra of Pd-Sn alloys with and without phosphorous. We observe the introduction of P to have an electronic effect on Pd and Sn, shifting the Pd 3d and Sn 3d spectra to lower and higher binding energies, respectively. The P 2p XPS spectrum displays one doublet at 133.5 eV (P 2p_{3/2}) and 134.4 (P 2p_{1/2}) assigned to P within a phosphate environment. Thus, the surface of the deposited Pd₂Sn_{0.8}P particles was partially oxidized owing to its exposure to air, especially the Sn and P components.

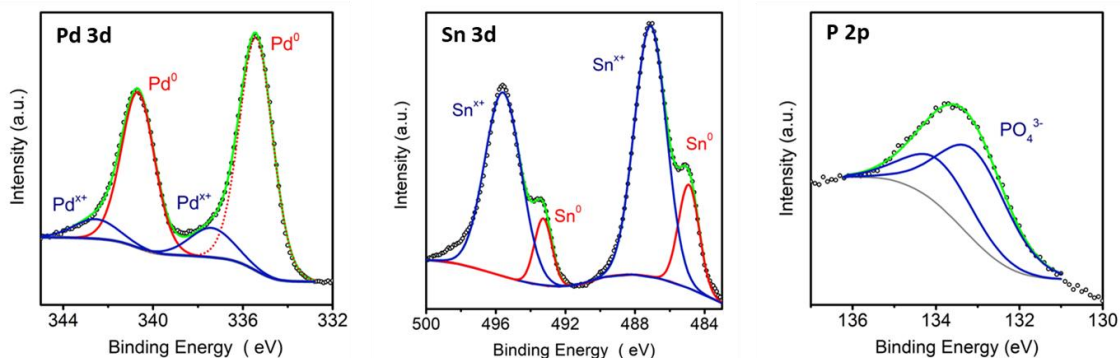


Figure 4.2. High-resolution Pd 3d, Sn 3d, and P 2p XPS spectra of the Pd₂Sn_{0.8}P catalyst.

4.3.2. Electrocatalytic formate oxidation.

The electrocatalytic properties of the carbon-supported Pd₂Sn_{0.8}P NPs toward FOR were assessed using a standard three-electrode system in a potential range of -0.9 to 0.4 V vs Hg/HgO. Initially, CV was performed at room temperature using a sweep rate of 50 mV s⁻¹ in an alkaline medium containing 1M KOH but no formate (Figure 4.3a). In these conditions, the CV curves obtained from Pd₂Sn_{0.8}P/C and Pd_{1.6}Sn/C catalysts displayed the characteristic Pd redox peaks in an alkaline medium. In the forward scan, the current density peaks in the region between -0.9 and -0.4 V are attributed to the oxidation of adsorbed hydrogen and the peaks in the region between 0.2 to 0.4 V are associated with the superficial Pd oxidation. The current density measured in the region between -0.5 and -0.4 is associated with OH⁻ adsorption³⁸ Notice this contribution is significantly larger for the samples containing P. In the reverse scan, the peak located at -0.5 V is associated with hydrogen adsorption and the peaks in the region between -0.2 to -0.4 V to Pd-O reduction. The ECSA was determined from the area of the Pd-O reduction peak (Q):

$$ECSA = \frac{Q (\mu\text{C}\cdot\text{cm}^{-2})}{Q_{PdO} (\mu\text{C}\cdot\text{cm}_{Pd}^{-2}) \cdot Pd_{loading} (\text{mg}\cdot\text{cm}^{-2})} \quad (3)$$

where Q_{PdO} corresponds to the charge associated with the reduction of a Pd-O monolayer (420 $\mu\text{C cm}^{-2}$). The ECSA obtained for Pd_{1.6}Sn/C, Pd₂Sn_{0.8}P/C and Pd₂Sn_{0.8}P_{1.8}/C are 44.38 m² g_{Pd}⁻¹, 197.1 m² g_{Pd}⁻¹ and 106.2 m² g_{Pd}⁻¹, respectively. Thus, despite introducing a third element, significantly larger ECSA values are obtained for Pd₂Sn_{0.8}P/C compared with Pd_{1.6}Sn/C.

Figure 4.3b shows the mass-normalized voltammograms obtained from binary Pd_{1.6}Sn/C and ternary Pd₂Sn_{0.8}P/C catalysts in an Ar-saturated 1 M KOH + 1 M HCOOK solution. During the anodic scan, a broad band at ca. -0.2 vs Hg/HgO is associated with the catalyst activity toward the FOR. In the high potential range, the current density decreases due to the oxidation of the

surface Pd. An extension of the FOR potential range is systematically obtained with the introduction of P, which we related to an increase in the resistance of the surface Pd towards oxidation. An additional extension is also systematically observed for the Pd₂Sn_{0.8}P_{1.8}/C electrode, which is associated with the presence of a P-related FOR site that evolves with cycling (Figure 4.S8). In the cathodic scan, the FOR activity is recovered at *ca.* -0.3 V vs Hg/HgO, when the Pd surface is reduced. As more clearly displayed in Figure 4.3c, the onset potential at 1 A mg_{Pd}⁻¹ of the Pd₂Sn_{0.8}P/C catalyst was significantly lower (-0.66) than that of the binary Pd_{1.6}Sn/C (-0.55 V) and ternary Pd₂Sn_{0.8}P_{1.8}/C (-0.62 V). The highest current densities were obtained with the Pd-Sn-P alloys. Pd₂Sn_{0.8}P/C was characterized by very high mass currents up to 10.0 A mg_{Pd}⁻¹ at *ca.* -0.2 V vs Hg/HgO, which is the highest value reported to date (Figure 4.3d). This value was more than twofold higher than that of binary Pd_{1.6}Sn/C (4.9 A mg_{Pd}⁻¹) and about 1.4 times higher than Pd₂Sn_{0.8}P_{1.8}/C (7.0 A mg_{Pd}⁻¹). The electrochemical impedance spectra at -0.6 V were used to investigate the influence of P on the charge transfer phenomena (Figure 4.S8). The lowest charge transfer resistance was obtained for the Pd₂Sn_{0.8}P, which agrees with the CV measurements.

The catalyst stability under FOR conditions was assessed by CA in an Ar-saturated 1M KOH + 1M HCOOK solution for 7200 s (Figure 4.3e). A relatively rapid current decay was obtained due to the double layer discharge and the progressive accumulation of adsorbed intermediate species (H_{ads} and/or CO_{ads}) that deactivate the catalyst active sites.^{22,25} Pd_{1.6}Sn/C was deactivated after 2000 s, while for both phosphide catalysts the mass current was still *ca.* 0.1 A mg_{Pd}⁻¹ after 5500 s and 4200 s for Pd₂Sn_{0.8}P/C and Pd₂Sn_{0.8}P_{1.8}/C, respectively. Thus, the incorporation of P not only increases the FOR activity but also the stability against the adsorption of poisoning species.

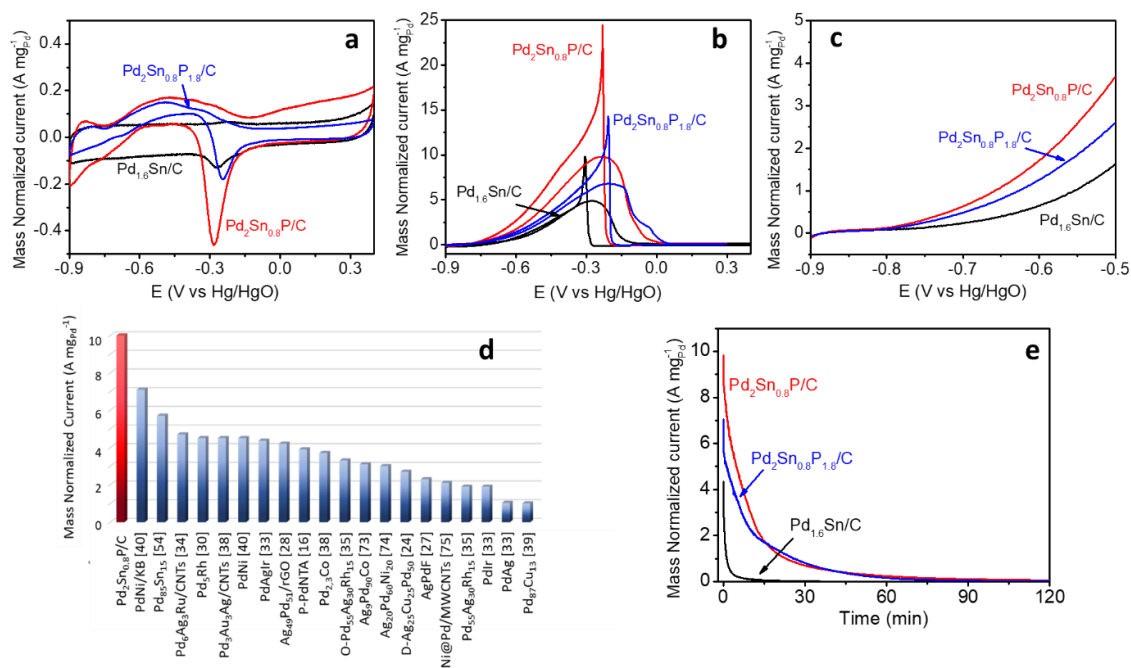


Figure 4.3. (a) CV voltammograms in 1 M of KOH aqueous solution, (b,c) CV voltammograms in 1 M KOH + 1 M HCOOK aqueous solution of Pd_{1.6}Sn/C (black line), Pd₂Sn_{0.8}P/C (red line) and Pd₂Sn_{0.8}P_{1.8}/C (blue line) catalysts, and (d) Comparison of prepared Pd₂Sn_{0.8}P/C mass current (red column) with Pd-based catalysts reported in the literature (blue columns). (e) CA test at the voltage of the maximum current response in 1 M KOH + 1 M HCOOK aqueous solution, of Pd_{1.6}Sn/C (black line), Pd₂Sn_{0.8}P/C (red line) and Pd₂Sn_{0.8}P_{1.8}/C (blue line) catalysts.

Figure 4.4 shows the dependence on temperature of the FOR electrochemical activity obtained from the three palladium-based catalysts. At 40 °C, the current density significantly increased and the onset potential diminished for the phosphorized catalysts. This improved performance is related to the fact that a higher temperature lowers the relative reaction energy barrier, decreasing the overpotential and facilitating the desorption of CO₂. The faster product desorption allows a higher rate of unreacted formate molecules to reach the catalyst's active sites, incrementing the current density.

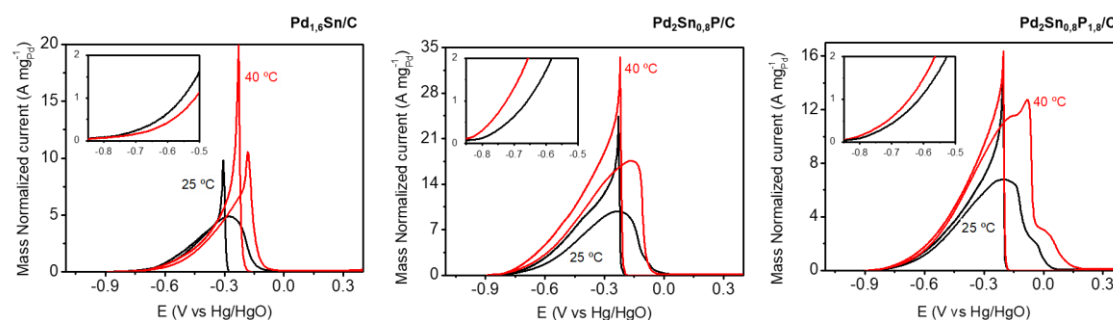


Figure 4.4. CV voltammograms of Pd_{1.6}Sn/C, Pd₂Sn_{0.8}P/C and Pd₂Sn_{0.8}P_{1.8}/C at 25 °C (black line) and 40 °C (red line).

To remove the accumulated poisoning species, a rapid potential scan to oxidize and reduce the Pd surface was tested. Figure 4.5 shows the regeneration capacity of the three tested catalysts. After every 30 minutes of CA test, the catalysts were re-activated by performing 2 CV cycles in the potential range -0.9 V to 0.4 V (vs Hg/HgO). All three catalysts demonstrate a high activity recovery and stability throughout the process.

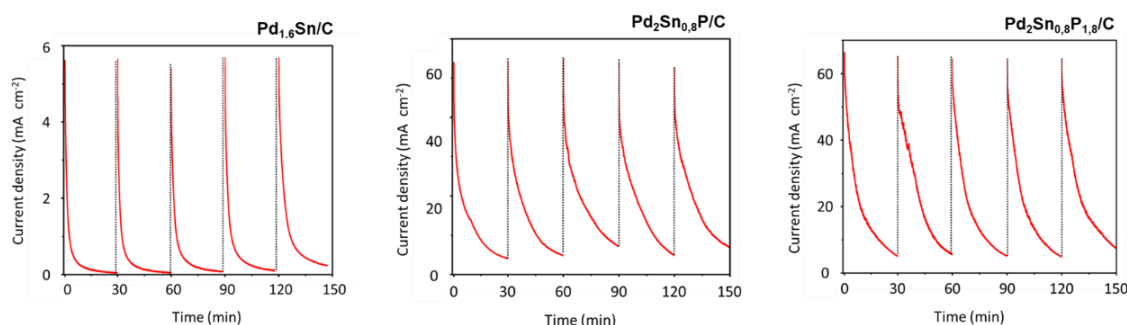


Figure 4.5. Successive CA curves of the Pd_{1.6}Sn/C, Pd₂Sn_{0.8}P/C and Pd₂Sn_{0.8}P_{1.8}/C catalysts regenerated every 30 min using two CV cycles (vertical lines).

4.3.3. DFT calculations

DFT calculations were used to gain insight into the mechanism behind the outstanding FOR performance experimentally measured from Pd₂Sn_{0.8}P catalysts. In aqueous conditions, the HCOO⁻ oxidation to CO₂ could occur through the following elementary steps:



The top-view and side-view structures of the optimized pristine Pd₂Sn and Pd₂Sn_{0.8}P and the corresponding adsorption structures of *HCOO and *CO₂ are shown in Figure 4.S9. The

computational Gibbs free energy of $^*\text{HCOO}$ oxidation to $^*\text{CO}_2$ was calculated comparatively on Pd_2Sn and $\text{Pd}_2\text{Sn}_{0.8}\text{P}$ (Figure 4.6a,b). It can be found that the free energy decreases in the first and second steps involving the $^*\text{HCOO}$ oxidation to adsorbed $^*\text{CO}_2$, thus they are energy-favourable exothermic reactions. However, the last step from adsorbed $^*\text{CO}_2$ to free CO_2 is an endothermic reaction, involving an energy barrier of 0.57 eV on Pd_2Sn (001) and just 0.33 eV on $\text{Pd}_2\text{Sn}_{0.8}\text{P}$ (001). Thus, it can be deemed that the $\text{Pd}_2\text{Sn}_{0.8}\text{P}$ (001) performs better activity than the Pd_2Sn (001) because of a significantly decreased adsorption energy of CO_2 after the incorporation of phosphorous into the Pd_2Sn system. That is, the adsorption energy of CO_2 on $\text{Pd}_2\text{Sn}_{0.8}\text{P}$ (001) surface is only about -0.33 eV, which is 0.24 eV above that on Pd_2Sn (001) surface (Figure 4.6b). The modulation of the electronic structure of $\text{Pd}_2\text{Sn}_{0.8}\text{P}$ through introducing P to the Pd-Sn system may play a dominant role during the reaction.^{75,76} In addition, the adsorption energy of HCOO on Pd_2Sn (001) is -1.23 eV, and -1.42 eV on $\text{Pd}_2\text{Sn}_{0.8}\text{P}$ (001). We need to point out that we further calculated the indirect FOR pathway, but this calculation yielded an energy barrier of the oxidation of HCOO to CO of more than 3 eV on $\text{Pd}_2\text{Sn}_{0.8}\text{P}$, pointing at a less favorable path.

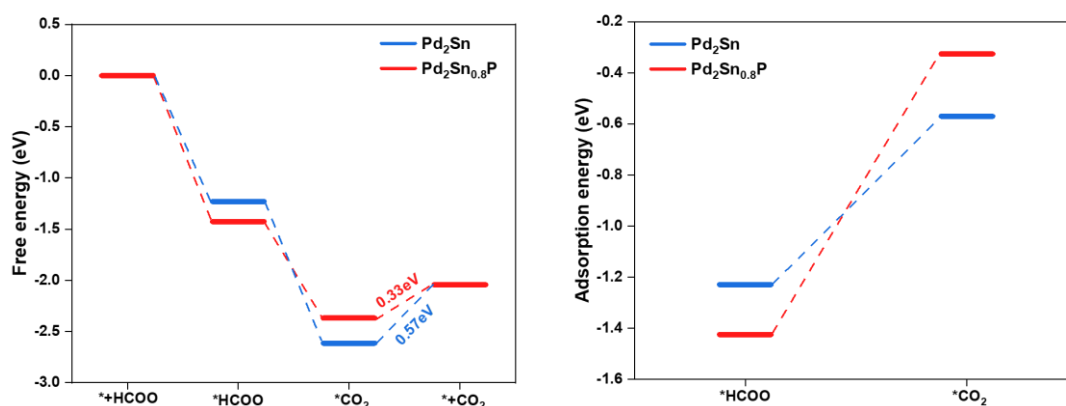


Figure 4.6. (a) Change of Gibbs free energy according to reactions of (4-6) on Pd_2Sn and $\text{Pd}_2\text{Sn}_{0.8}\text{P}$. (b) Adsorption energy of HCOO and CO_2 on Pd_2Sn and $\text{Pd}_2\text{Sn}_{0.8}\text{P}$.

The decreased interaction after P doping was further confirmed by the calculation of the charge density difference as shown in Figure 4.7. The moderate difference in HCOO adsorption energy is also reflected in the charge density difference in $\text{HCOO-Pd}_2\text{Sn}$ and $\text{HCOO-Pd}_2\text{Sn}_{0.8}\text{P}$ systems (Figure 4.7a,c). A significantly lower charge redistribution difference between CO_2 and $\text{Pd}_2\text{Sn}_{0.8}\text{P}$ (001) in Figure 4.7b was obtained compared with the system $\text{CO}_2\text{-Pd}_2\text{Sn}$ (001) in Figure 4.7d, implying a lower interaction. Thus, the desorption of CO_2 from $\text{Pd}_2\text{Sn}_{0.8}\text{P}$ (001) is much easier than from Pd_2Sn , which facilitates the re-exposure of active sites on the surface. The PDOS is shown in Figure 4.7e. The interaction of the p orbital of P and the d orbital of Pd can be found

around the Fermi level. The d band of Pd was expanded after the P doping. The d-band centre of Pd₂Sn is -2.82 eV, while it decreased to -3.34 eV in the Pd₂Sn_{0.8}P. This decrease in the d-band centre explains the decreased adsorption energy for the adsorbed species.

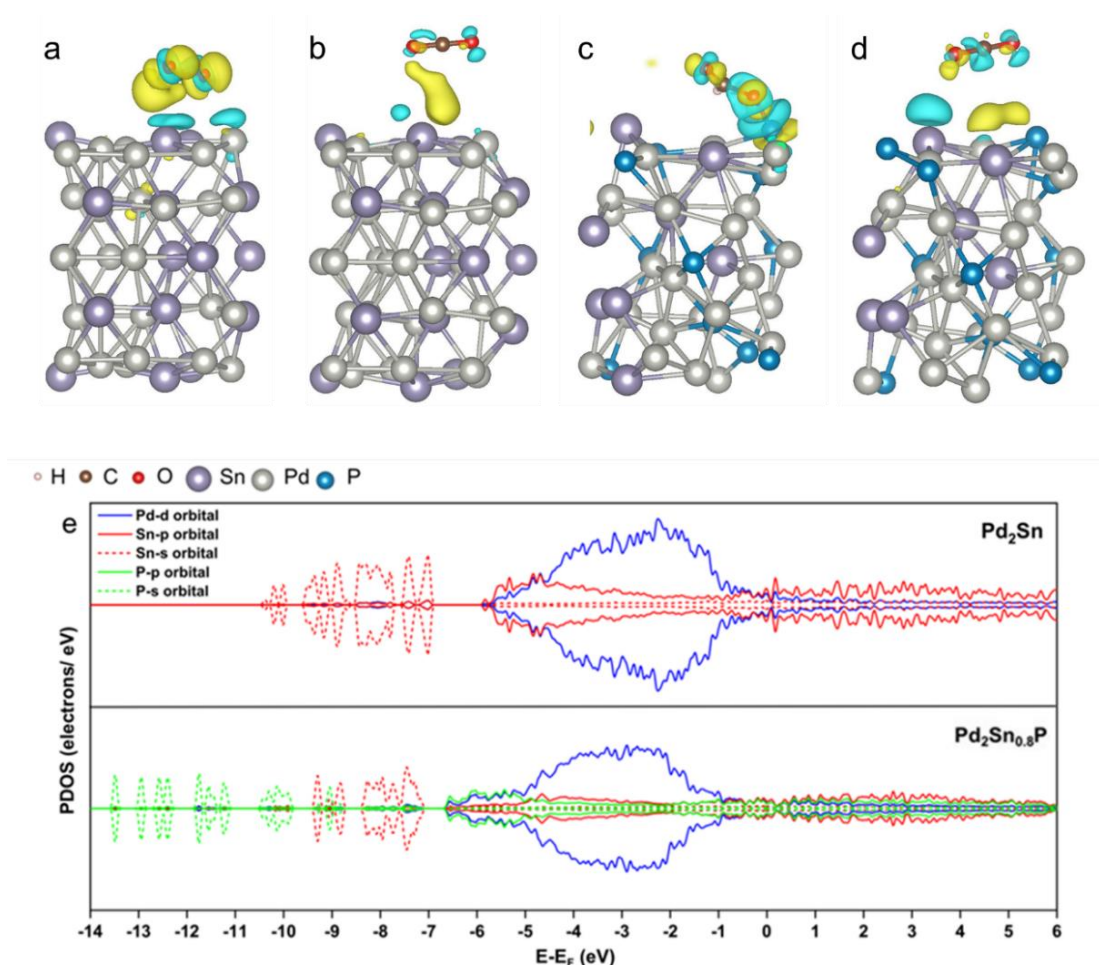


Figure 4.7. Charge density difference plots of (a) Pd₂Sn-HCOO, (b) Pd₂Sn-CO₂, (c) Pd₂Sn_{0.8}P-HCOO and (d) Pd₂Sn_{0.8}P-CO₂. The isosurface value is 0.00025 e Å⁻³. The blue region means charge depletion while the yellow region means charge accumulation. (e) PDOS of Pd₂Sn and Pd₂Sn_{0.8}P.

4.4. CONCLUSIONS

In summary, we demonstrated that through a phosphorization process, the electrocatalytic performance of Pd-Sn catalysts towards FOR can be strongly enhanced. Palladium tin phosphide catalysts were obtained by a colloidal process, in which the binary Pd-Sn was first obtained and, subsequently, phosphorized by HMPT at 300 °C. Pd₂Sn_{0.8}P/C catalysts exhibited not only higher activity and stability than Pd_{1.6}Sn/C and Pd/C catalysts but also the highest mass-specific current densities reported so far. Furthermore, activity can be boosted by increasing the temperature from 25 °C to 40 °C. While a rapid current decay throughout the CA test was obtained, especially for Pd/C and Pd_{1.6}Sn/C samples, the catalysts could be regenerated using two CV cycles. Finally,

DFT results confirmed that the presence of P favours the desorption of CO₂ thus reducing the energy barrier of the rate-limiting step.

4.5. REFERENCES

1. T. Vo, K. Purohit, C. Nguyen, B. Biggs, S. Mayoral, J.L. Haan, Formate: An Energy Storage and Transport Bridge between Carbon Dioxide and a Formate Fuel Cell in a Single Device, *ChemSusChem*. 8 (2015) 3853–3858.
2. X. Su, Z. Pan, L. An, Performance characteristics of a passive direct formate fuel cell, *Int. J. Energy Res.* 43 (2019) 7433–7443.
3. A.M. Bartrom, J. Ta, T.Q. Nguyen, J. Her, A. Donovan, J.L. Haan, Optimization of an anode fabrication method for the alkaline Direct Formate Fuel Cell, *J. Power Sources*. 229 (2013) 234–238.
4. L.Q. Wang, M. Bellini, J. Filippi, M. Folliero, A. Lavacchi, M. Innocenti, A. Marchionni, H.A. Miller, F. Vizza, Energy efficiency of platinum-free alkaline direct formate fuel cells, *Appl. Energy*. 175 (2016) 479–487.
5. K. Tran, T.Q. Nguyen, A.M. Bartrom, A. Sadiki, J.L. Haan, A fuel-flexible alkaline direct liquid fuel cell, *Fuel Cells*. 14 (2014) 834–841.
6. J. Jiang, A. Wieckowski, Prospective direct formate fuel cell, *Electrochem. Commun.* 18 (2012) 41–43.
7. A.M. Bartrom, J.L. Haan, The direct formate fuel cell with an alkaline anion exchange membrane, *J. Power Sources*. 214 (2012) 68–74.
8. X. Ge, A. Sumboja, D. Wu, T. An, B. Li, F.W.T. Goh, T.S.A. Hor, Y. Zong, Z. Liu, Oxygen reduction in alkaline media: From mechanisms to recent advances of catalysts, *ACS Catal.* 5 (2015) 4643–4667.
9. L. An, R. Chen, Direct formate fuel cells: A review, *J. Power Sources*. 320 (2016) 127–139.
10. M. Rosenbaum, U. Schröder, F. Scholz, Investigation of the electrocatalytic oxidation of formate and ethanol at platinum black under microbial fuel cell conditions, *J. Solid State Electrochem.* 10 (2006) 872–878.
11. S.H. Han, H.M. Liu, J. Bai, X.L. Tian, B.Y. Xia, J.H. Zeng, J.X. Jiang, Y. Chen, Platinum-Silver Alloy Nanoballoon Nanoassemblies with Super Catalytic Activity for the Formate Electrooxidation, *ACS Appl. Energy Mater.* 1 (2018) 1252–1258.
12. Sirlane G. da Silva, Julio César M. Silva, Guilherme S. Buzzo, Almir O. Neto, Mônica H.M.T. Assumpção, Use of PtAu/c electrocatalysts toward formate oxidation: Electrochemical and fuel cell considerations, *Mater. Renew. Sustain. Energy*. 5 (2016).
13. X. Yu, A. Manthiram, Catalyst-selective, scalable membraneless alkaline direct formate fuel

- cells, *Appl. Catal. B Environ.* 165 (2015) 63–67.
14. A. Nacys, V. Kovalevskij, E. Norkus, An Enhanced Oxidation of Formate on PtNi / Ni Foam Catalyst in an Alkaline Medium, (2022).
 15. J. John, H. Wang, E.D. Rus, H.D. Abruña, Mechanistic studies of formate oxidation on platinum in alkaline medium, *J. Phys. Chem. C.* 116 (2012) 5810–5820.
 16. J. Ding, Z. Liu, X. Liu, J. Liu, Y. Deng, X. Han, C. Zhong, W. Hu, Mesoporous Decoration of Freestanding Palladium Nanotube Arrays Boosts the Electrocatalysis Capabilities toward Formic Acid and Formate Oxidation, *Adv. Energy Mater.* 9 (2019) 1–8.
 17. V. Galvan, D.E. Glass, A.F. Baxter, G.K. Surya Prakash, Reduced Graphene Oxide Supported Palladium Nanoparticles for Enhanced Electrocatalytic Activity toward Formate Electrooxidation in an Alkaline Medium, *ACS Appl. Energy Mater.* 2 (2019) 7104–7111.
 18. M. V. Pagliaro, M. Bellini, J. Filippi, M.G. Folliero, A. Marchionni, H.A. Miller, W. Oberhauser, F. Vizza, Hydrogen production from the electrooxidation of methanol and potassium formate in alkaline media on carbon supported Rh and Pd nanoparticles, *Inorganica Chim. Acta.* 470 (2018) 263–269.
 19. X. Li, H. Hodson, C. Batchelor-Mcauley, L. Shao, R.G. Compton, Improving Formate and Methanol Fuels: Catalytic Activity of Single Pd Coated Carbon Nanotubes, *ACS Catal.* 6 (2016) 7118–7124.
 20. H. Hwang, S. Hong, J.W. Kim, J. Lee, Optimized electrode structure for performance and mechanical stability in a direct formate fuel cell using cation ionomer, *Sustain. Energy Fuels.* 4 (2020) 1899–1907.
 21. S. Zhang, Y. Shao, G. Yin, Y. Lin, Recent progress in nanostructured electrocatalysts for PEM fuel cells, *J. Mater. Chem. A.* 1 (2013) 4631–4641.
 22. Jin-Yi Wang, Han-Xuan Zhang, Kun Jiang, Wen-Bin Cai, From HCOOH to CO at Pd Electrodes: A Surface-Enhanced Infrared Spectroscopy Study, *J. Am. Chem. Soc.* 133 (2011) 14876–
 23. T. Takamura, F. Mochimaru, Adsorption and oxidation of formate on palladium in alkaline solution, 14 (1969) 111–119.
 24. Q. Wang, F. Chen, L. Guo, T. Jin, H. Liu, X. Wang, X. Gong, Y. Liu, Nanoalloying effects on the catalytic activity of the formate oxidation reaction over AgPd and AgCuPd aerogels, *J. Mater. Chem. A.* 7 (2019) 16122–16135.
 25. M. Choun, S. Hong, J. Lee, Adsorbed Hydrogen as a Site-Occupying Species in the Electrocatalytic Oxidation of Formate on Pd/C in Alkaline Medium, *J. Electrochem. Soc.* 165 (2018) J3266–J3270.
 26. Y. Zhou, J. Liu, J. Ye, Z. Zou, J. Ye, J. Gu, T. Yu, A. Yang, Poisoning and regeneration of Pd catalyst in direct formic acid fuel cell, *Electrochim. Acta.* 55 (2010) 5024–5027.

27. Q. Tang, F. Chen, Q. Wang, T. Jin, L. Guo, Y. Wu, S. Yu, Z. Li, Surface reconstruction of AgPdF and AgPd nanoalloys under the formate oxidation reaction, *J. Mater. Chem. A*. 9 (2021) 23072–23084.
28. L. Guo, F. Chen, T. Jin, H. Liu, N. Zhang, Y. Jin, Q. Wang, Q. Tang, B. Pan, Surface reconstruction of AgPd nanoalloy particles during the electrocatalytic formate oxidation reaction, *Nanoscale*. 12 (2020) 3469–3481.
29. J. Wang, C. Liu, A. Lushington, N. Cheng, M.N. Banis, A. Riese, X. Sun, Pd on carbon nanotubes-supported Ag for formate oxidation: The effect of Ag on anti-poisoning performance, *Electrochim. Acta*. 210 (2016) 285–292.
30. J. Bai, Q. Xue, Y. Zhao, J.X. Jiang, J.H. Zeng, S. Bin Yin, Y. Chen, Component-Dependent Electrocatalytic Activity of Ultrathin PdRh Alloy Nanocrystals for the Formate Oxidation Reaction, *ACS Sustain. Chem. Eng.* 7 (2019) 2830–2836.
31. Sirlane G. da Silva, Julio César M. Silva, Guilherme S. Buzzo, Estevam V. Spinacé, Almir O. Neto, Mônica H.M.T. Assumpção, PdAu/C Electrocatalysts as Anodes for Direct Formate Fuel Cell, *Electrocatalysis*. 6 (2015) 442–446.
32. Y. Li, Y. He, W. Yang, A high-performance direct formate-peroxide fuel cell with palladium-gold alloy coated foam electrodes, *J. Power Sources*. 278 (2015) 569–573.
33. Y. Jin, F. Chen, T. Jin, L. Guo, J. Wang, Mesoporous PdAgIr nanoalloys to catalyze formate oxidation with an unprecedentedly low onset potential, *J. Mater. Chem. A*. 8 (2020) 25780–25790.
34. T.T. Gebremariam, F. Chen, B. Kou, L. Guo, B. Pan, Q. Wang, Z. Li, W. Bian, PdAgRu nanoparticles on polybenzimidazole wrapped CNTs for electrocatalytic formate oxidation, *Electrochim. Acta*. 354 (2020) 136678.
35. Y. Jin, Y. Jin, F. Chen, F. Chen, L. Guo, L. Guo, J. Wang, J. Wang, B. Kou, B. Kou, T. Jin, T. Jin, H. Liu, H. Liu, Engineering Two-Dimensional PdAgRh Nanoalloys by Surface Reconstruction for Highly Active and Stable Formate Oxidation Electrocatalysis, *ACS Appl. Mater. Interfaces*. 12 (2020) 26694–26703.
36. B. Pan, F. Chen, B. Kou, J. Wang, Q. Tang, L. Guo, Q. Wang, Z. Li, W. Bian, J. Wang, Unexpectedly high stability and surface reconstruction of PdAuAg nanoparticles for formate oxidation electrocatalysis, *Nanoscale*. 12 (2020) 11659–11671.
37. L. Chen, L. Lu, H. Zhu, Y. Chen, Y. Huang, Y. Li, L. Wang, Improved ethanol electrooxidation performance by shortening Pd-Ni active site distance in Pd-Ni-P nanocatalysts, *Nat. Commun.* 8 (2017) 1–9.
38. S. Sankar, G.M. Anilkumar, T. Tamaki, T. Yamaguchi, Cobalt-Modified Palladium Bimetallic Catalyst: A Multifunctional Electrocatalyst with Enhanced Efficiency and Stability toward

- the Oxidation of Ethanol and Formate in Alkaline Medium, *ACS Appl. Energy Mater.* 1 (2018) 4140–4149.
39. J. Noborikawa, J. Lau, J. Ta, S. Hu, L. Scudiero, S. Derakhshan, S. Ha, J.L. Haan, Palladium-copper electrocatalyst for promotion of oxidation of formate and ethanol in alkaline media, *Electrochim. Acta.* 137 (2014) 654–660.
 40. S. Sankar, G.M. Anilkumar, T. Tamaki, T. Yamaguchi, Binary Pd–Ni Nanoalloy Particles over Carbon Support with Superior Alkaline Formate Fuel Electrooxidation Performance, *ChemCatChem.* 11 (2019) 4731–4737.
 41. A.N. Geraldes, D. Furtunato Da Silva, J.C. Martins Da Silva, O. Antonio De Sá, E.V. Spinacé, A.O. Neto, M. Coelho Dos Santos, Palladium and palladium-tin supported on multi wall carbon nanotubes or carbon for alkaline direct ethanol fuel cell, *J. Power Sources.* 275 (2015) 189–199.
 42. L.X. Ding, A.L. Wang, Y.N. Ou, Q. Li, R. Guo, W.X. Zhao, Y.X. Tong, G.R. Li, Hierarchical Pd–Sn alloy nanosheet dendrites: An economical and highly active catalyst for ethanol electrooxidation, *Sci. Rep.* 3 (2013) 1–7.
 43. W. Du, K.E. MacKenzie, D.F. Milano, N.A. Deskins, D. Su, X. Teng, Palladium-tin alloyed catalysts for the ethanol oxidation reaction in an alkaline medium, *ACS Catal.* 2 (2012) 287–297.
 44. C. Wang, Y. Wu, X. Wang, L. Zou, Z. Zou, H. Yang, Low temperature and surfactant-free synthesis of Pd₂Sn intermetallic nanoparticles for ethanol electro-oxidation, *Electrochim. Acta.* 220 (2016) 628–634.
 45. R. Saraswathy, R. Suman, P. Malin Bruntha, D. Khanna, V. Chellasamy, Mn-doped nickeltitanate (Ni_{1-x}Mn_xTiO₃) as a promising support material for PdSn electrocatalysts for methanol oxidation in alkaline media, *RSC Adv.* 11 (2021) 28829–28837.
 46. H. You, F. Gao, C. Wang, J. Li, K. Zhang, Y. Zhang, Y. Du, Rich grain boundaries endow networked PdSn nanowires with superior catalytic properties for alcohol oxidation, *Nanoscale.* 13 (2021) 17939–17944.
 47. J. Liang, S. Li, Y. Chen, X. Liu, T. Wang, J. Han, S. Jiao, R. Cao, Q. Li, Ultrathin and defect-rich intermetallic Pd₂Sn nanosheets for efficient oxygen reduction electrocatalysis, *J. Mater. Chem. A.* 8 (2020) 15665–15669.
 48. Z. Luo, J. Lu, C. Flox, R. Nafria, A. Genç, J. Arbiol, J. Llorca, M. Ibáñez, J.R. Morante, A. Cabot, Pd₂Sn [010] nanorods as a highly active and stable ethanol oxidation catalyst, *J. Mater. Chem. A.* 4 (2016) 16706–16713.
 49. DandanTu, B. Wu, B. Wang, C. Deng, Y. Gao, A highly active carbon-supported PdSn catalyst for formic acid electrooxidation, *Appl. Catal. B Environ.* 103 (2011) 163–168.

50. D. Chen, S. Pei, Z. He, H. Shao, J. Wang, K. Wang, Y. Wang, Y. Jin, High active PdSn binary alloyed catalysts supported on B and N codoped graphene for formic acid electro-oxidation, *Catalysts*. 10 (2020).
51. Z. Liu, X. Zhang, Carbon-supported PdSn nanoparticles as catalysts for formic acid oxidation, *Electrochem. Commun.* 11 (2009) 1667–1670.
52. R.X. Wang, Y.J. Fan, Z.R. Liang, J.M. Zhang, Z.Y. Zhou, S.G. Sun, PdSn nanocatalysts supported on carbon nanotubes synthesized in deep eutectic solvents with high activity for formic acid electrooxidation, *RSC Adv.* 6 (2016) 60400–60406.
53. E. Hwang, H. Kim, H. Park, T. Lim, Y.T. Kim, S.H. Ahn, S.K. Kim, Pd–Sn alloy electrocatalysts for interconversion between carbon dioxide and formate/formic acid, *J. Nanosci. Nanotechnol.* 17 (2017) 7547–7555.
54. S. Sasidharan, A.A. Sasikala Devi, R. Jose, T. Tamaki, A.M. Gopinathan, T. Yamaguchi, Alkaline Formate Oxidation with Colloidal Palladium-Tin Alloy Nanocrystals, *ACS Appl. Energy Mater.* 5 (2022) 266–277.
55. P. Hosseini-Benhangi, C.C. Gyenge, E.L. Gyenge, The carbon dioxide redox flow battery: Bifunctional CO₂ reduction/formate oxidation electrocatalysis on binary and ternary catalysts, *J. Power Sources*. 495 (2021) 229752.
56. J. Duan, Z. Xiang, H. Zhang, B. Zhang, X. Xiang, Pd-Co₂P nanoparticles supported on N-doped biomass-based carbon microsheet with excellent catalytic performance for hydrogen evolution from formic acid, *Appl. Surf. Sci.* 530 (2020) 147191.
57. Z. Yu, X.K. Wei, J. Xu, Y. Li, A. Araujo, J.L. Faria, R.E. Dunin-Borkowski, L. Liu, Multifunctional Noble Metal Phosphide Electrocatalysts for Organic Molecule Electro-Oxidation, *ACS Appl. Energy Mater.* 4 (2021) 1593–1600.
58. L. Feng, J. Chang, K. Jiang, H. Xue, C. Liu, W. Bin Cai, W. Xing, J. Zhang, Nanostructured palladium catalyst poisoning depressed by cobalt phosphide in the electro-oxidation of formic acid for fuel cells, *Nano Energy*. 30 (2016) 355–361.
59. Y. Bao, H. Liu, Z. Liu, F. Wang, L. Feng, Pd/FeP catalyst engineering via thermal annealing for improved formic acid electrochemical oxidation, *Appl. Catal. B Environ.* 274 (2020) 119106.
60. T.J. Wang, Y.C. Jiang, J.W. He, F.M. Li, Y. Ding, P. Chen, Y. Chen, Porous palladium phosphide nanotubes for formic acid electrooxidation, *Carbon Energy*. (2022) 1–11.
61. K.C. Poon, B. Khezri, Y. Li, R.D. Webster, H. Su, H. Sato, A highly active Pd-P nanoparticle electrocatalyst for enhanced formic acid oxidation synthesized via stepwise electroless deposition, *Chem. Commun.* 52 (2016) 3556–3559.
62. Z. Yu, J. Xu, I. Amorim, Y. Li, L. Liu, Easy preparation of multifunctional ternary PdNiP/C catalysts toward enhanced small organic molecule electro-oxidation and hydrogen

- evolution reactions, *J. Energy Chem.* 58 (2021) 256–263.
63. J. Chang, L. Feng, C. Liu, W. Xing, X. Hu, An effective Pd-Ni₂P/C anode catalyst for direct formic acid fuel cells, *Angew. Chemie - Int. Ed.* 53 (2014) 122–126.
 64. S. Wang, J. Chang, H. Xue, W. Xing, L. Feng, Catalytic Stability Study of a Pd-Ni₂P/C Catalyst for Formic Acid Electrooxidation, *ChemElectroChem.* 4 (2017) 1243–1249.
 65. X. Liang, B. Liu, J. Zhang, S. Lu, Z. Zhuang, Ternary Pd-Ni-P hybrid electrocatalysts derived from Pd-Ni core-shell nanoparticles with enhanced formic acid oxidation activity, *Chem. Commun.* 52 (2016) 11143–11146.
 66. X. Yu, J. Liu, J. Li, Z. Luo, Y. Zuo, C. Xing, J. Llorca, D. Nisiou, J. Arbiol, K. Pan, T. Kleinhanns, Y. Xie, A. Cabot, Phosphorous incorporation in Pd₂Sn alloys for electrocatalytic ethanol oxidation, *Nano Energy.* 77 (2020).
 67. D. Yang, Z. Liang, P. Tang, C. Zhang, M. Tang, Q. Li, J.J. Biendicho, J. Li, M. Heggen, R.E. Dunin-Borkowski, M. Xu, J. Llorca, J. Arbiol, J.R. Morante, S.L. Chou, A. Cabot, A High Conductivity 1D π -d Conjugated Metal–Organic Framework with Efficient Polysulfide Trapping-Diffusion-Catalysis in Lithium–Sulfur Batteries, *Adv. Mater.* 34 (2022) 1–11.
 68. C. Zhang, B. Fei, D. Yang, H. Zhan, J. Wang, J. Diao, J. Li, G. Henkelman, D. Cai, J.J. Biendicho, J.R. Morante, A. Cabot, Robust Lithium–Sulfur Batteries Enabled by Highly Conductive WSe₂-Based Superlattices with Tunable Interlayer Space, *Adv. Funct. Mater.* 32 (2022).
 69. M. Li, D. Yang, J.J. Biendicho, X. Han, C. Zhang, K. Liu, J. Diao, J. Li, J. Wang, M. Heggen, R.E. Dunin-Borkowski, J. Wang, G. Henkelman, J.R. Morante, J. Arbiol, S.L. Chou, A. Cabot, Enhanced Polysulfide Conversion with Highly Conductive and Electrocatalytic Iodine-Doped Bismuth Selenide Nanosheets in Lithium–Sulfur Batteries, *Adv. Funct. Mater.* 32 (2022).
 70. X. Wang, X. Han, R. Du, Z. Liang, Y. Zuo, P. Guardia, J. Li, J. Llorca, J. Arbiol, R. Zheng, A. Cabot, Unveiling the role of counter-anions in amorphous transition metal-based oxygen evolution electrocatalysts, *Appl. Catal. B Environ.* 320 (2023) 121988.
 71. R. Du, K. Xiao, B. Li, X. Han, C. Zhang, X. Wang, Y. Zuo, P. Guardia, J. Li, J. Chen, J. Arbiol, A. Cabot, Controlled oxygen doping in highly dispersed Ni-loaded g-C₃N₄ nanotubes for efficient photocatalytic H₂O₂ production, *Chem. Eng. J.* 441 (2022) 135999.
 72. X. Wang, X. Han, R. Du, C. Xing, X. Qi, Z. Liang, P. Guardia, J. Arbiol, A. Cabot, J. Li, Cobalt Molybdenum Nitride-Based Nanosheets for Seawater Splitting, *ACS Appl. Mater. Interfaces.* 14 (2022) 41924–41933. D. Yang, M. Li, X. Zheng, X. Han, C. Zhang, J. Jacas Biendicho, J. Llorca, J. Wang, H. Hao, J. Li, G. Henkelman, J. Arbiol, J.R. Morante, D. Mitlin, S. Chou, A. Cabot, Phase Engineering of Defective Copper Selenide toward Robust Lithium-Sulfur Batteries, *ACS Nano.* 16 (2022) 11102–11114.
 73. X. Wang, J. Li, Q. Xue, X. Han, C. Xing, Z. Liang, P. Guardia, Y. Zuo, R. Du, L. Balcells, J. Arbiol,

- J. Llorca, X. Qi, A. Cabot, Sulfate-Decorated Amorphous-Crystalline Cobalt-Iron Oxide Nanosheets to Enhance O-O Coupling in the Oxygen Evolution Reaction, *ACS Nano*. 17 (2023) 825–836.
74. Y. Zhou, Q. Wang, X. Tian, J. Chang, L. Feng, Electron-enriched Pt induced by CoSe₂ promoted bifunctional catalytic ability for low carbon alcohol fuel electro-reforming of hydrogen evolution, *J. Energy Chem.* 75 (2022) 46–54.
75. Y. Zhou, Y. Kuang, G. Hu, X. Wang, L. Feng, An effective Pt–CoTe/NC catalyst of bifunctional methanol electrolysis for hydrogen generation, *Mater. Today Phys.* 27 (2022).

SUPPORTING INFORMATION

4.6. SI EXPERIMENTAL AND THEORETICAL METHODS

4.6.1. Chemicals

OAm (98%) was purchased from Acros Organics. Palladium(II) acetylacetonate ($\text{Pd}(\text{acac})_2$, Pd 34.7 wt%), tin(II) acetate ($\text{Sn}(\text{OAc})_2$, 99%), HMPT (97%), TOP (97%), MAC (98%), potassium hydroxide (KOH, 85%) and Nafion (5 wt% in a mixture of low aliphatic alcohols and water) were obtained from Sigma-Aldrich. Potassium formate (HCOOK, 99%, water less than 2%) was purchased from Alfa Aesar. CB Vulcan XC-72 was acquired from Fuel Cell Earth. Hexane, ethanol and acetone were of analytical grade and purchased from various sources. MilliQ water was obtained from a Purelab flex from Elga. All reagents and solvents were used without further purification.

4.6.2. Synthesis of $\text{Pd}_{1.6}\text{Sn}$ and $\text{Pd}_2\text{Sn}_{0.8}\text{P}_x$ NPs

The synthesis of $\text{Pd}_2\text{Sn}_{0.8}\text{P}$ NPs was adapted from our previous work.[1] Briefly, 95 mg (0.31 mmol) of $\text{Pd}(\text{acac})_2$ and 100 mg (1.5 mmol) of MAC were mixed with 20 mL of OAm in a 50 mL three-neck flask and degassed under vacuum at 120 °C for 1 h. Under Ar atmosphere, 1 mL of TOP and 73 mg (0.3 mmol) of $\text{Sn}(\text{OAc})_2$, which were stored inside the glovebox, were introduced. Then the temperature was raised to 230 °C at a rate of 5 °C min^{-1} and maintained for 30 min. Subsequently, the sample was heated to 300 °C for 40 min. During this temperature increase, the solution gradually turned black, indicating the nucleation of Pd–Sn NCs. Once the solution reached 300 °C, 0.2 mL (1.1 mmol) of HMPT was injected and the solution was allowed to react for 1 h before it was cooled to ambient temperature with a water bath. Larger amounts of P could be introduced by increasing the amount of HMPT during the phosphorization process. We particularly tested the addition of 0.4 mL (2.2 mmol) of HMPT. On the other hand, $\text{Pd}_{1.6}\text{Sn}$ NPs were produced by skipping the phosphorization step, i.e. without adding HMPT. The product was precipitated with acetone, centrifugated at 7000 rpm for 3 min and re-dispersed with chloroform. This cleaning cycle was repeated 3 times and the final black product was kept in hexane.

4.6.3. Characterization

Powder XRD patterns were collected from the samples supported on a Si substrate on a Bruker-AXS D8 Advanced X-ray diffractometer with Ni-filtered (2 μm thickness) Cu K radiation ($\lambda = 1.5406 \text{ \AA}$) operating at 40 kV and 40 mA. The 2θ range was between 20-80°. SEM analysis was conducted with a Zeiss Auriga microscope equipped with an EDS detector and BSE contrast mode, operating at 20 kV. TEM images were carried out with a JEOL 2000 FX II working at 80 kV. HRTEM analysis was carried out using a field emission gun FEI™ Tecnai F20 microscope at 200 kV with a point-to-point resolution of 0.19 nm. HAADF-STEM was combined with EELS in the Tecnai F20 with a Gatan Quantum filter. XPS was analysed on a Specs system equipped with an Al anode XR50 source operating at 150 W and a Phoibos 150 MCD-9 detector. The CasaXPS program was employed for the data process. ICP-MS was conducted with a Shimadzu simultaneous ICP atomic emission spectrometer ICPE-9820.

4.6.4. Electrochemical tests

Electrocatalysts were prepared by supporting the particles onto CB Vulcan XC-72. Before incorporating the NPs, the CB was treated with HNO_3 at 80 °C for 3 hours. To prepare the catalyst, a dispersion of $\text{Pd}_2\text{Sn}_{0.8}\text{P}$ ($\text{Pd}_{1.6}\text{Sn}$ or $\text{Pd}_2\text{Sn}_{0.8}\text{P}_{1.8}$) in hexane was mixed with a dispersion of CB in ethanol. The mixture was sonicated for 1 h. Then the product was collected by centrifugation and then re-dispersed in a mixture of acetic acid/ethanol (10 % v/v) to remove surface organic ligands through sonication. Afterward, the catalyst was washed three times with ethanol, dried at 60 °C overnight and annealed at 300 °C in an Ar atmosphere for 1 h. A catalyst ink was prepared by ultrasonically dispersing 6 mg of electrocatalyst, 1 mL of isopropanol and 30 μL of Nafion. The working electrode was prepared by coating a GC electrode, with a surface area of 0.196 cm^2 , with 3 μL of the ink and dried under ambient conditions. The amount of Pd on the catalyst was determined ICP-MS. From the concentration of Pd on the catalyst obtained by ICP, we determined that 0.5, 1.4 and 2.4 μg of Pd were used to prepare the $\text{Pd}_{1.6}\text{Sn}$, $\text{Pd}_2\text{Sn}_{0.8}\text{P}$ and $\text{Pd}_2\text{Sn}_{0.8}\text{P}_{1.8}$ electrodes, respectively. Electrochemical measurements were conducted at room temperature with a VersaSTAT electrochemical workstation using a three-neck-type cell including a Pt gauze as a counter electrode and a Hg/HgO (1 M KOH) electrode as reference. The catalytic activity was determined using CV at a scan rate of 50 mV/s in Ar-saturated aqueous solutions containing 1 M KOH or 1 M KOH + 1 M HCOOK. EIS was carried out in the range from 0.1Hz to 100kHz with an amplitude of 10mV. Stability was explored using 7200 s CA tests at the potential in which the maximum mass current was obtained in Ar-saturated 1 M KOH + 1 M HCOOK electrolyte.

4.6.5. DFT calculations.

DFT calculations were performed using the VASP.^{2,3} The interaction between the electrons and ions was described using the PAW method.⁴ The PBE functional with GGA was utilized to treat the electronic exchange-correlation energies.⁵ For all the geometry optimizations, the cut-off energy was set at 500 eV. The 3×3×1 Monkhorst-Pack k-points were set to optimize the bulk structure of Pd₂Sn and Pd₂Sn_{0.8}P.⁶ A five-layer 3×3×1 Pd₂Sn (001) model which contains 30 Pd atoms and 15 Sn atoms, and a similar Pd₂Sn_{0.8}P model which contains 23 Pd atoms, 10 Sn and 12 P atoms were chosen to be studied comparatively. All atoms could relax until the electronic self-consistency and the ionic relaxation reached the convergence criteria of 10⁻⁵ eV and 0.02 eV/Å. The adsorption energies for COOH and CO₂ on the surfaces were calculated based on the following equation:

$$E_{\text{ads}} = E^*_{\text{adsorbate}} - (E^* + E_{\text{adsorbate}}) \quad (1)$$

where $E^*_{\text{adsorbate}}$, E^* and $E_{\text{adsorbate}}$ are the total energies for either COOH or CO₂ adsorbed on the substrate, pure substrate and the free COOH or CO₂ adsorbate.

The Gibbs free energy change, ΔG , of each reaction step is evaluated based on CHE model:

$$\Delta G = \Delta E + \Delta E_{\text{ZPE}} - T\Delta S \quad (2)$$

where ΔE is the reaction energy directly computed from the DFT calculations, ΔE_{ZPE} is the zero-point energy obtained from vibrational frequency calculations, and $T\Delta S$ is the corresponding entropy difference obtained from standard tables for gas-phase molecules.

4.7. SI RESULTS

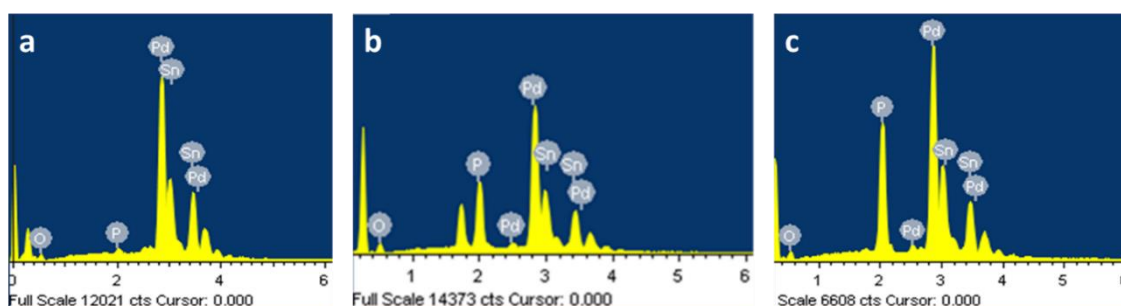


Figure 4.S1. SEM-EDS analysis of (a) Pd_{1.6}Sn, (b) Pd₂Sn_{0.8}P and (c) Pd₂Sn_{0.8}P_{1.8}.

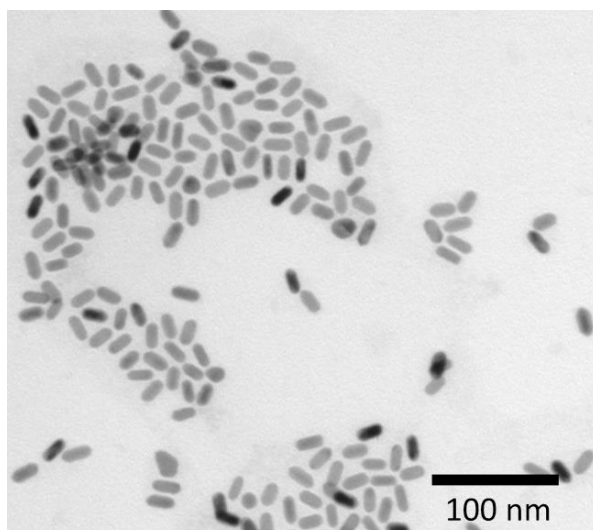


Figure 4.S2. TEM micrograph of Pd_{1.6}Sn nanorods.

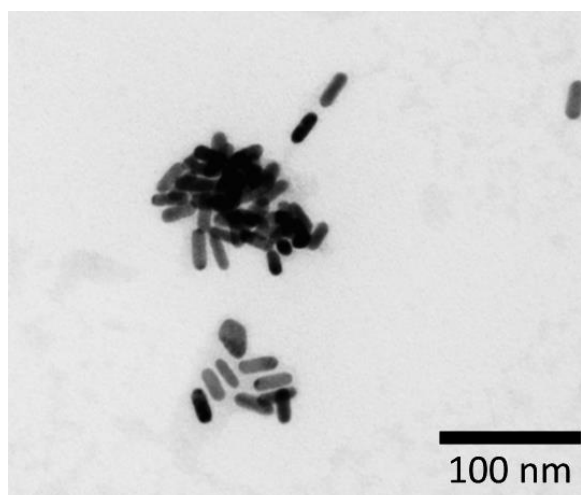


Figure 4.S3. TEM micrograph of Pd₂Sn_{0.8}P_{1.8} nanorods.

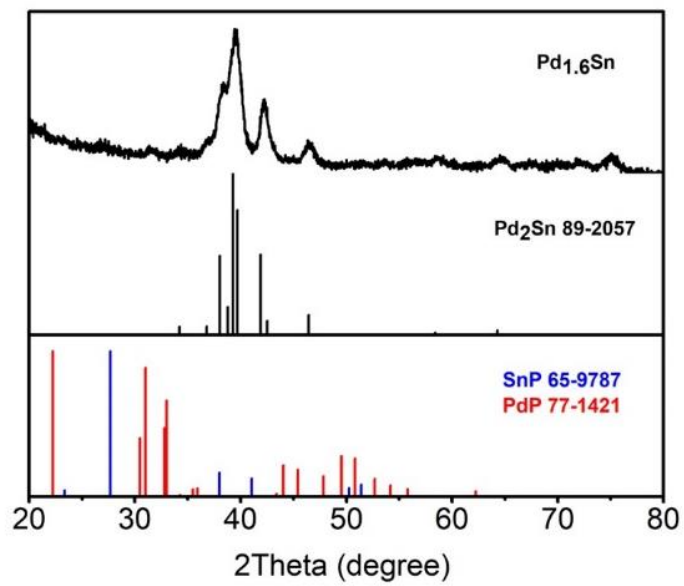


Figure 4.S4. XRD pattern of Pd_{1.6}Sn nanorods

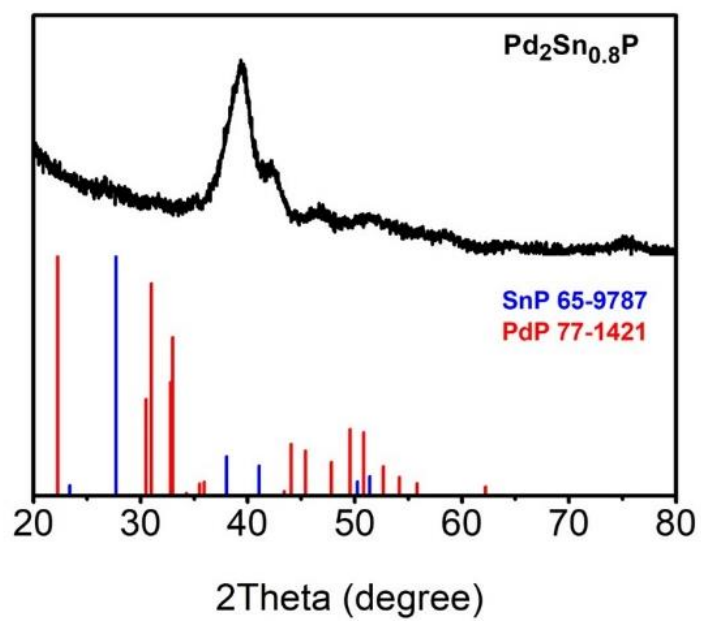


Figure 4.S5. XRD pattern of Pd₂Sn_{0.8}P nanorods

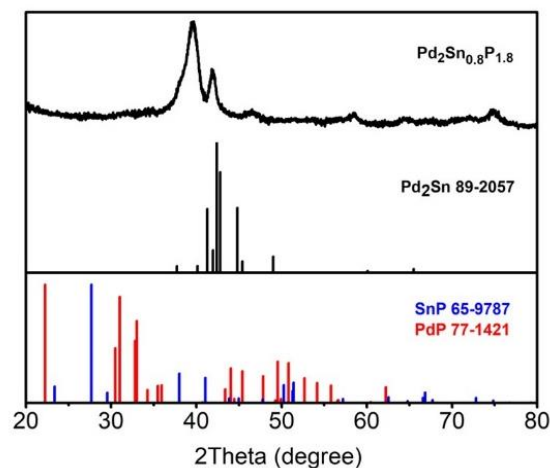


Figure 4.S6. XRD pattern of Pd₂Sn_{0.8}P_{1.8} nanorods

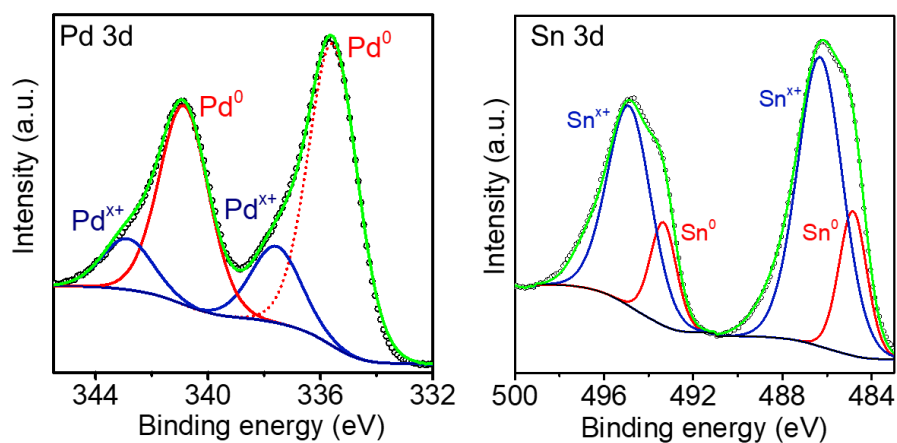


Figure 4.S7. High-resolution Pd 3d and Sn 3d XPS spectra of the Pd_{1.6}Sn catalyst.

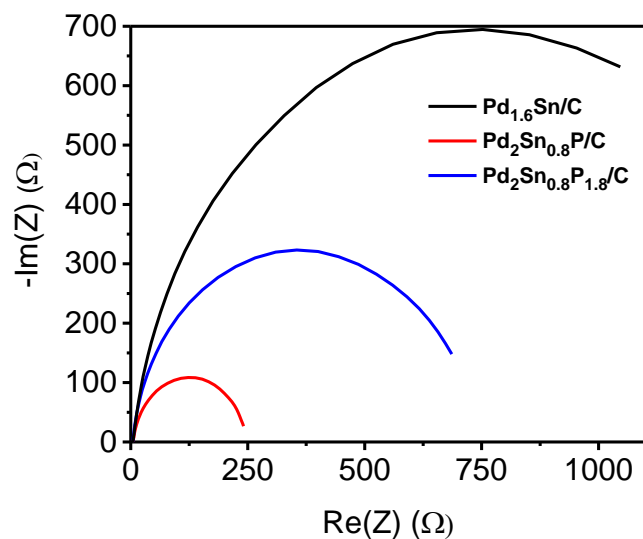


Figure 4.S8. Nyquist plots in 1 M KOH and 1 M HCOOK for the formate oxidation at -0.6 V of Pd_{1.6}Sn/C (black line), Pd₂Sn_{0.8}P/C (red line) and Pd₂Sn_{0.8}P_{1.8}/C (blue line) catalysts.

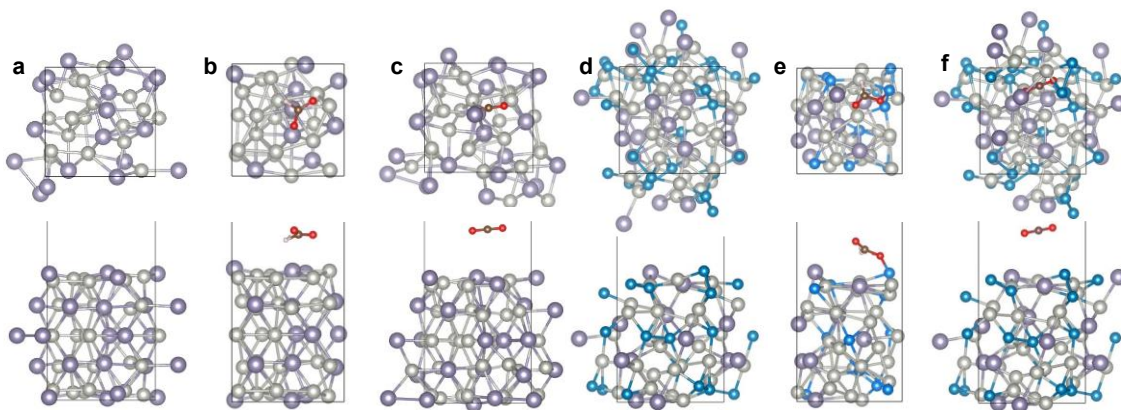


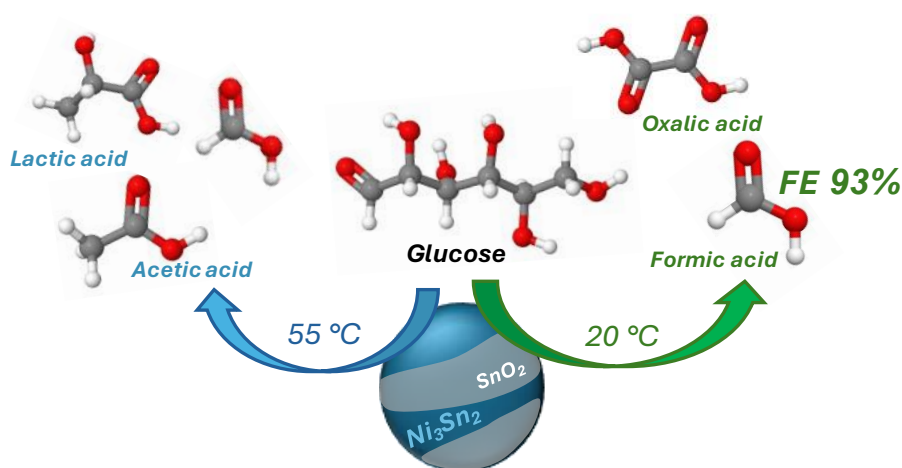
Figure 4.S9. Top and side views of the optimized structures before and after the adsorption of *COOH and *CO_2 on Pd_2Sn (a-c) and $Pd_2Sn_{0.8}P$ (d-f). H (small white), C (small purple), O (small red), Pd (big white), Sn (big purple) and P (big blue).

4.8. SI REFERENCES

1. X. Yu, J. Liu, J. Li, Z. Luo, Y. Zuo, C. Xing, J. Llorca, D. Nasiou, J. Arbiol, K. Pan, T. Kleinmanns, Y. Xie and A. Cabot, *Nano Energy*, 2020, **77**, 105116.
2. G. Kresse and J. Furthmüller, *Phys Rev B Condens Matter*, 1996, **54**, 11169–11186.
3. G. K. and J. Hafner, *Phys. Rev. B*, 1994, **49**, 14251--14269.
4. P. E. Blöchl, *Phys. Rev. B*, 1994, **50**, 17953–17979.
5. J. P. Perdew, K. Burke and M. Ernzerhof, *Phys. Rev. Lett.*, 1996, **77**, 3865–3868.
6. H. J. M. and J. D. Pack, *Phys. Rev. B*, 1976, **13**, 5188–5192.

CHAPTER 5

Oxophilic Sn to promote glucose oxidation to formic acid in Ni nanoparticles



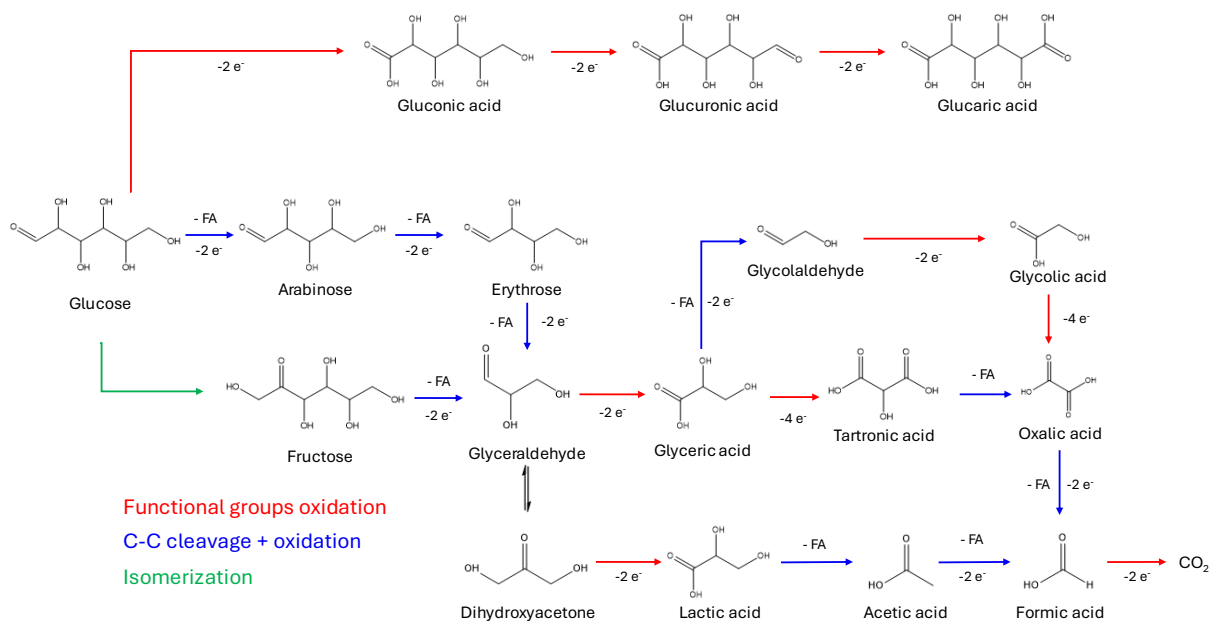
5.1. ABSTRACT

The electrochemical GOR presents an opportunity to produce hydrogen and high-value chemical products. Herein, we investigate the effect of Sn in Ni nanoparticles for the GOR to FA. Electrochemical results show that the maximum activity is related to the amount of Ni, as Ni sites are responsible for catalyzing the GOR via the NiOOH/Ni(OH)₂ pair. However, the GOR kinetics increases with the amount of Sn, associated with an enhancement of the OH⁻ supply to the catalyst surface for Ni(OH)₂ reoxidation to NiOOH. NiSn nanoparticles supported on carbon nanotubes (NiSn/CNT) exhibit excellent current densities and direct GOR via C-C cleavage mechanism, obtaining FA with a FE of 93% at 1.45 V vs. RHE. GOR selectivity is further studied by varying the applied potential, glucose concentration, reaction time, and temperature. FE toward FA production decreases due to formic overoxidation to carbonates at low glucose concentrations and high applied potentials, while AA and LA are obtained with high selectivity at high glucose concentrations and 55 °C. DFT calculations show that the SnO₂ facilitates the adsorption of glucose on the surface of Ni and promotes the formation of the catalytic active Ni³⁺ species.

5.2. INTRODUCTION

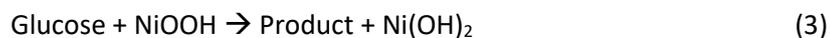
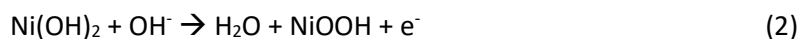
Glucose is one of the main biomass-derived compounds in terms of production volume, cost, safety, potential uses, and ease of transportation and storage. While primarily used in the food industry, it finds additional applications in the production of bioplastics and biofuels as well as in pharmaceutical and cosmetic manufacturing. Besides, the GOR can be also coupled with the HER for energy-efficient hydrogen production. As an alternative to the OER (1.23 V vs RHE), the GOR offers a much lower oxidation potential (0.05 V vs RHE). Additionally, within this coupled system, the GOR can be used to produce several value-added chemical compounds and fuels under mild synthesis conditions. Among others, the value-added glucose oxidation products range from 6C species such as gluconic acid and GRA down to OXA and FA. The relatively large number of carbons in the structure increases the complexity of the reaction mechanisms in action and the related challenge of maximizing product selectivity. Two main mechanisms with a complex interconnection have been proposed in the literature (Scheme 5.1). A first GOR pathway consists of the sequential oxidation of the aldehyde and alcohol functional groups located at the edges of the molecule generating gluconic acid followed by glucuronic acid, and eventually GRA.^[1] A second GOR mechanism involves the cleavage of one of the C-C bonds. This cleavage predominantly occurs at the glucose edge, shortening it by one carbon atom at each step, to enter the glyceraldehyde/dihydroxyacetone route to finally yield LA (3-C), OXA (2-C) and FA (1-C).^[2-4] The 5C, 4C, and 3C compounds can be generally produced with lower selectivity due to the difficulty in precisely stopping the C-C cleavage reaction at early stages. Glucose can additionally isomerize to fructose under basic conditions and also enter the glyceraldehyde/dihydroxyacetone route.^[5] Glyceraldehyde/dihydroxyacetone further oxidizes to form either glyceric acid or LA, respectively, that further oxidizes to TA or AA and FA, respectively.^{[3],[6]}

Among the possible GOR products, the selective production of FA is particularly interesting owing to its extensive use in various sectors such as agriculture, water treatment, medicines, and especially in the food, chemical, and textile industries. Besides, in the energy field, the development of direct FA/formate fuel cells is a topic of major interest due to their high potential energy density, safe fuel transportation and storage, and superior theoretical cell potential.^[7-9] In addition, the oxidation of each glucose molecule all the way down to FA provides 10 e⁻ that can be used to produce 5 H₂ molecules.



Scheme 5.1. Scheme of some of the possible GOR pathways.

The multiple GOR pathways and products underscore the importance of developing highly active but at the same time selective electrocatalysts. While noble metals such as Pt, Au, or Rh are commonly used for the electrooxidation of biomass-derived products, their scarcity and high price limit their industrial application. Among the alternative catalytic materials, Ni-based compounds are particularly attractive electrocatalysts in basic media due to their impressive activity, high abundance, low cost, and reduced toxicity. In an alkaline media cell, the GOR mechanism generally relies on the conversion of the surface of the Ni-based material to Ni(OH)₂. Then, under GOR operation conditions, when injecting electrons at the cathode and withdrawing them from the anode at a proper potential, the Ni(II) ions at the anode are further oxidized to Ni(III), in the form of nickel oxyhydroxide (NiOOH). The formation of this NiOOH triggers the GOR, thus Ni(III) is considered the catalytic active species. In the process of biomass electrooxidation, Ni(III) acts as an electron acceptor, receiving an electron from the glucose molecule, thus reducing back to Ni(II). Subsequently, the electrode re-oxidizes this Ni(II) to Ni(III) by withdrawing another electron, completing the cycle. This cyclic electron transfer, involving the reduction and subsequent re-oxidation of nickel ions, plays a pivotal role in the GOR mechanism and depends on the ability to exchange electrons with the electrode, the availability of OH⁻ groups on the catalyst surface, and the adsorption of the glucose and intermediate molecules: ^[10]



While nickel is widely acknowledged for its outstanding catalytic activity and versatility in facilitating a broad range of reactions, it is also commonly noted for its lack of selectivity and stability.^[4,11-14] Thus, several strategies have been developed to overcome these issues. One main approach is the formation of Ni alloys to adjust the surface electronic structure and introduce additional anchoring and catalytic sites. In this direction, Ni has been combined with several other transition metals such as Fe and Co within oxides, nitrides, and chalcogenides, among others.^[1,15-17] Yu et al. reported NiFeO_x and NiFeN_x compounds that convert glucose via the functional groups oxidation mechanism, achieving a maximum FE of 87% for GNA plus GRA.^[1] Lin et al. synthesized NiCoSe_x as a bifunctional catalyst for both GOR and HER, that directs the reaction through the C-C bond cleavage pathway, achieving a FE for formate of 70%.^[17] Moreover, Wei et al. catalyzed the GOR mainly to FA with a FE of 86 % using a Mn-doped nickel iron phosphate.^[18]

Alternatively, alloying noble metals such as Pd and Pt with p-block elements such as Sn, with higher oxophilicity, has been demonstrated as an excellent strategy to promote electrooxidation.^[19] As an example, Brouzgou et al. reported that Pd₃Sn₂/C and PdSn/C exhibited higher electrocatalytic activity and stability than Pd/C towards the GOR.^[20] Our group and others have also demonstrated the high activity and enhanced stability of PdSn and PtSn-based catalysts towards ethanol and formate oxidation.^[21-24] The presence of Sn within the alloy or SnO₂ forming a composite has two important effects. On the one hand, Sn can alter the interaction with reactants/products, stabilizing intermediates. This adjustment of adsorption energies between reactants and catalyst surface sites can significantly alter, and potentially even entirely redirect, the reaction pathway.^[25] In this direction, Tang et al. showed how within a Pt-Sn catalyst the charge transfer from Sn to Pt facilitates the C-O and C-C polarization, thus promoting complete ethanol oxidation to CO₂.^[26] On the other hand, the oxophilic character of Sn and readily formation of Sn(OH)_x species contributes to promoting water activation at low potentials, providing oxygen-containing species, OH_{ads}, to the surface. In this way, Sn promotes oxidation reactions by lowering the oxidation barriers through hydrogen-bond interactions.^[27] As an example in this direction, Du et al. showed that the addition of Sn to Pd promoted AA production through the ethanol oxidation reaction.^[24] Besides, Liu et al. demonstrated that Pt-

SnO₂ core-shell heterostructures facilitate C-C cleavage by the oxidation of CO_{ads} and CH_{x,ads} promoted in the presence of OH_{ads} formed at Sn sites.^[28] In the particular case of Ni, the presence of Sn could potentially provide the OH_{ads} needed for the re-oxidation of Ni(OH)₂ to the active oxyhydroxide sites (Equation 2).

Ni-Sn catalysts have been demonstrated effective in promoting the electrooxidation of methanol, ethanol, and urea, among others, the performance of NiSn towards the GOR is yet to be explored.^[29,30] In this work, we investigate the effect of Sn inclusion in Ni nanoparticles supported on CNTs as a catalyst for the GOR. We analyze how the amount of Sn influences the GOR kinetics and the oxidation products at different potentials and initial glucose concentrations. Furthermore, we explore the products generated over extended 24-hour reactions at both room temperature and 55 °C. Additionally, we assess the stability of the catalysts through consecutive one-hour electrochemical experiments with electrolyte regeneration between each cycle. Besides, to rationalize the obtained results, density functional theory (DFT) calculations are used to identify the effect of Sn on the Ni(OH)₂ structure.

5.3. EXPERIMENTAL SECTION

5.3.1. Chemicals

OAm (98%), H₂SO₄ (98 %), and AA (99.8%) were purchased from Acros Organics. LA (90%) was obtained from VWR, and GNA aqueous solution (50%) from ThermoFisher. Nickel(II) acetylacetonate (Ni(acac)₂, 95%), tin(II) acetate (Sn(OAc)₂, 95%), TOP (97%), TBAB (97%), KOH (85%), D-(+)-Glucose (99.5%), GRA (98%), D-(-)-Fructose (99%), OXA (98%), FA (97%) and Nafion (5 wt% in a mixture of low aliphatic alcohols and water) were obtained from Sigma-Aldrich. MWCNT were purchased from Carnd-China. Hexane, ethanol, and acetone were of analytical grade and purchased from various sources. MilliQ water was obtained from a Purelab flex from Elga. All reagents and solvents were used without further purification.

5.3.2. Synthesis of NiSn_{0.6}, NiSn_{1.8} and Ni nanoparticles

The synthesis of NiSn_{0.6} nanoparticles was adapted from our previous work.^[31] Briefly, 224 mg (0.9 mmol) of Ni(acac)₂ and 112 mg (0.5 mmol) of SnCl₂ were mixed with 20 mL of OAm in a 50 mL three-neck flask and degassed under vacuum at 120 °C for 1 h. Under Ar atmosphere, 5 mL of TOP was introduced. Then the temperature was raised to 230 °C at a rate of 5 °C min⁻¹. Once the solution reached 230 °C, a solution of 2.5 mmol of TBAB in 5 mL of purged OAm was injected. After the injection, the solution turned immediately black indicating the nucleation of Ni-Sn

nanocrystals. Then it was allowed to react for 2 h before it was cooled to ambient temperature with a water bath. The product was precipitated with acetone, centrifugated at 7000 rpm for 3 min, and re-dispersed with chloroform. This cleaning cycle was repeated 3 times and the final black product was kept in hexane. To produce the NiSn_{1.8}, the ratio Ni/Sn was varied increasing the amount of SnCl₂ to 202 mg and reducing the Ni(OAc)₂ to 124 mg. On the other hand, Ni nanoparticles were produced without adding SnCl₂.

5.3.3. Synthesis of NiSn_x/CNTs

NiSn_x/CNTs electrocatalysts were prepared by supporting the particles onto MWCNTs, with a loading amount of 20 %. To prepare the catalyst, a dispersion of NiSn_x (NiSn_{0.6}, NiSn_{1.8}, or Ni) nanoparticles in hexane was mixed with a dispersion of MWCNTs in ethanol. The mixture was sonicated for 1 h. Then the product was collected by centrifugation and then re-dispersed in a mixture of acetic acid/ethanol (10 % v/v) to remove surface organic ligands through sonication. Afterward, the catalyst was washed three times with ethanol, dried at 60 °C overnight, and annealed at 300 °C in an Ar atmosphere 1 h.

5.3.4. Characterization

XRD patterns were collected from the samples supported on a Si substrate on a Bruker-AXS D8 Advanced X-ray diffractometer with Ni-filtered (2 μm thickness) Cu K radiation ($\lambda = 1.5406 \text{ \AA}$) operating at 40 kV and 40 mA. The 2θ range was between 20-80°. SEM analysis was conducted with a Zeiss Auriga microscope equipped with an EDS detector and BSE contrast mode, operating at 20 kV. HRTEM images and STEM studies were conducted on an FEI Tecnai F20 field emission gun microscope operated at 200 kV with a point-to-point resolution of 0.19 nm, which was equipped with HAADF and a Gatan Quantum EELS detector. AC-HAADF-STEM was performed in a double aberration-corrected Thermo Fisher Spectra 300 STEM operated at 300 KeV. The Spectra 300 is equipped with a Super X EDS detector. XPS was analyzed on a SPECS system equipped with an Al anode XR50 source operating at 150 W and a Phoibos 150 MCD-9 detector. The Multipak data reduction software (Physical Electronic-PHI, Inc., EE. UU.) was employed for the data process (C 1s peak corrected at binding energy of 284.8 eV). ICP-OES was conducted using an Agilent system model 5100.

5.3.5. Electrochemical tests

A catalyst ink was prepared by ultrasonically dispersing 6 mg of electrocatalyst, 0.8 mL of isopropanol, 0.2 mL of H₂O, and 50 μL of Nafion. Electrochemical analyses were conducted in an

H-type electrochemical cell at room temperature with a BioLogic electrochemical workstation. A three-electrode system was utilized to perform all the tests with a Pt gauze as a counter electrode and a Hg/HgO (KOH saturated) electrode as a reference. The working electrode was prepared by coating a CP, with a surface area of 1 cm², with 0.5 mL of the ink using an aerograph to disperse the liquid. The amount of catalyst deposited onto the CP was 3 mg.

All the potentials were converted to RHE potential following equation (4):

$$E_{\text{RHE}} = E_{\text{Hg/HgO}} + 0.059 \cdot \text{pH} + 0.098 \quad (4)$$

A proton exchange membrane (Nafion 117) was used to separate anode and cathode compartments. The cathode was prepared using a 45 mL solution of 1M KOH, while 45 mL of a glucose solution in 1M KOH was used in the anode. CV and LSV curves were performed at a scan rate of 5 mV/s. EIS was carried out from 100 MHz to 0.1 Hz with an amplitude of 5 mV. The ECSA was established with the C_{dl} , obtained by CV cycles at OCV \pm 50 mV at different scan rates (from 5 - 100 mV s⁻¹). Generally, C_{dl} is determined from the linear fit of the current vs the scan rate, v :

$$I = C_{\text{dl}} \cdot v \quad (5)$$

Then, ECSA is calculated by dividing the double-layer capacitance by the C_s

$$ECSA = \frac{C_{\text{dl}}}{C_s} \quad (6)$$

which is 0.04 mF cm⁻² based on values reported in alkaline solution.^[32]

CA experiments were conducted for 1 hour at a potential range from 1.35 to 1.6V vs RHE at a concentration of 10 mM glucose in 1M KOH. The same conditions were used, but this time maintaining the applied potential constant at 1.45 V and 1.55 V, while increasing the glucose concentration from 10 mM to 100 mM

5.3.6. Product analysis

Liquid products generated from the glucose electrooxidation were quantified by HPLC equipped with a Rezex™ ROA-Organic Acid H⁺ (8%) column (LC column 300 x 7.8 mm), diode array detector operating at 210 nm and a refractive index detector. The mobile phase consists of a 0.005 N H₂SO₄ solution with a flow rate of 0.2 mL min⁻¹ and a temperature of 40 °C. For the HPLC determination, 1 mL of the sample is extracted and diluted with 0.5 mL of 2M H₂SO₄ aqueous solution. FE was calculated with the following equation (7):

$$FE (\%) = \frac{n_{e^-} \cdot F \cdot mol_{product}}{Q_{total}} \cdot 100 \quad (7)$$

where F is the faradaic constant (96500 C mol⁻¹), n is the number of transferred electrons based on the balanced half-cell reaction and Q is the total charge passed throughout the experiment.

Selectivity was calculated with the following equation (8):

$$Selectivity (\%) = \frac{mols_{product} \cdot C_{product}}{mols_{glucose} \cdot C_{glucose}} \cdot 100 \quad (8)$$

where C_{product} is the number of carbons of each product, C_{glucose} is the number of carbons that the molecule of glucose has (C_{glucose} = 6), mols_{product} are the mols obtained of each product, and mols_{glucose} are the mols of glucose consumed during the reaction.

5.3.7. DFT analysis

DFT calculations were carried out with the VASP.^[33,34] The PBE functional within GGA was chosen to describe the electronic exchange-correlation energies.^[35] The PAW method was utilized to describe the interaction between the electrons and the ions.^[36] For all the geometry optimizations, the cut-off energy was set at 600 eV. The 2×2×1 Monkhorst-Pack k-points were used to sample the Brillouin zone.^[37] A mono-layer 3×4×1 Ni(OH)₂ (001) model which contains 12 Ni atoms was used to represent the pristine Ni(OH)₂ catalysts, while a mono-layer Ni(OH)₂/SnO₂ which contains 6 Ni atoms and 6 Sn atoms was chosen to represent the oxidative NiSn alloy system. A vacuum with a 15 Å thickness along the z-axis was inserted to eliminate the periodic interaction of the catalysts. A Hubbard U was specified onto the d orbitals of Ni with an effective U value of 4.00. All atoms could relax until the electronic self-consistency and the ionic relaxation reached the convergence criteria of 10⁻⁶ eV and 0.01 eV/Å. The adsorption energies for glucose on the surfaces were calculated based on the following equation (9):

$$E_{ads} = E^*_{glucose} - (E^* + E_{glucose}) \quad (9)$$

where E*_{glucose}, E*, and E_{glucose} are the total energies for glucose adsorbed on the Ni(OH)₂ or Ni(OH)₂/SnO₂. A more negative E_{ads} means a stronger adsorption.

To determine the effect of SnO₂ on the O-H bond scission in both pristine Ni(OH)₂ and Ni(OH)₂/SnO₂. The formation energy of H vacancy, E_{f,H}, was calculated according to equation 10:

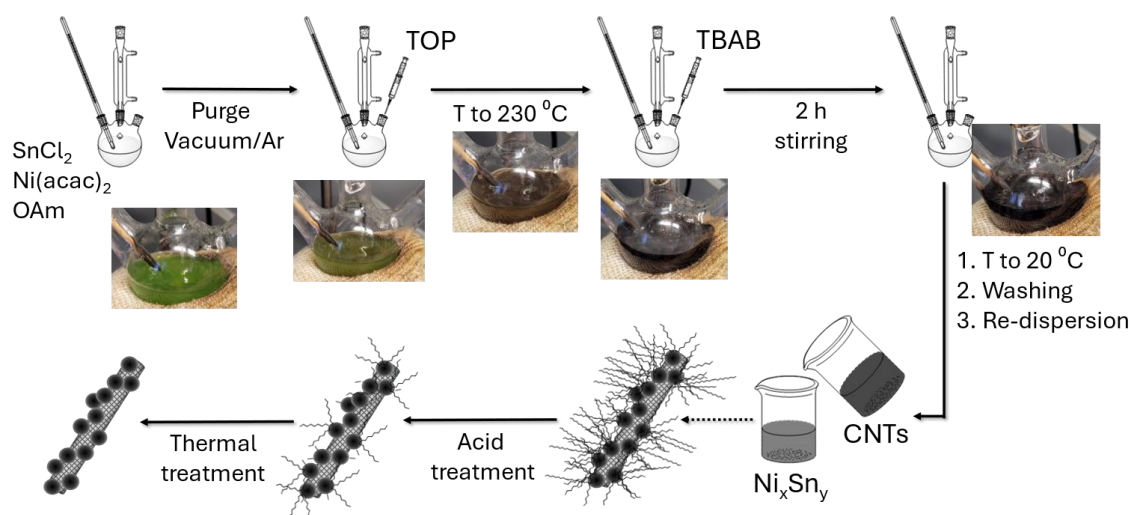
$$E_{f-Hv} = E_{slab-Hv} + 1/2 E_{H_2} - E_{slab} \quad (10)$$

where $E_{slab-Hv}$, E_{H_2} , and E_{slab} are the total energies of structure with an H vacancy, gaseous H_2 , and the catalysts without hydrogen vacancy, respectively. A more positive E_{f-Hv} means a more difficult O-H scission.

5.4. RESULTS AND DISCUSSION

5.4.1. Catalyst preparation and characterization

NiSn-based catalysts supported on carbon nanotubes (NiSn_y/CNT) were produced in four steps (Scheme 5.2, see details in the Experimental section). First, colloidal NiSn nanoparticles were synthesized from the simultaneous co-reduction at 230 °C of the two metal precursors, Sn(Oac)₂ and Ni(acac)₂, with borane TBAB within a mixture of OAm and TOP, used as solvents and stabilizers. NiSn particles with two Ni/Sn precursor ratios, NiSn_{1.8} and NiSn_{0.6}, were produced. Additionally, as a reference, a pure Ni sample was also produced in the same conditions. In a second step, to maximize the electrocatalyst electrical conductivity and minimize the aggregation of the NiSn particles, they were dispersed on the surface of multi-walled CNTs. Finally, in a third and fourth step, ligands were removed using a diluted AA solution and the material was annealed at 300 °C for 1 h under an inert atmosphere.



Scheme 5.2. Schematic diagram of the preparation of the NiSn-based catalyst

Figure 5.1a-f shows representative TEM and images of the different catalysts. The Ni particles in Ni/CNT appear very small and are distributed along the CNTs with an undefined geometry. With the introduction of Sn, the particle geometry becomes more regular. While NiSn_{0.6} particles have

a spheroidal shape with a large size and shape distribution, $\text{NiSn}_{1.8}$ particles are slightly smaller and show a more homogeneous spherical geometry. XRD pattern (Figure 5.1g) of Ni/CNTs shows no metal-related XRD peaks, which is consistent with an amorphous lattice. Only the XRD pattern of the carbon nanotubes with a main peak at about $2\theta \approx 25^\circ$ is observed. In contrast, the XRD patterns of the two NiSn_y/CNT catalysts produced show the presence of the orthorhombic Ni_3Sn_2 crystallographic phase. In both NiSn_y/CNT samples, bands around $2\theta \approx 28^\circ$ and $2\theta \approx 34^\circ$ can be appreciated, which coincide with the main peaks of the SnO_2 structure. The presence of both metals was confirmed through ICP-OES and SEM-EDS (Figure 5.S1). The Ni/Sn ratios of the two NiSn_y/CNT samples measured by ICP-OES were $\text{NiSn}_{0.8}$ and $\text{NiSn}_{1.5}$, which slightly differ from the nominal metal ratios used. Nevertheless, we will rely on the nominal metal ratio to refer to the two different materials.

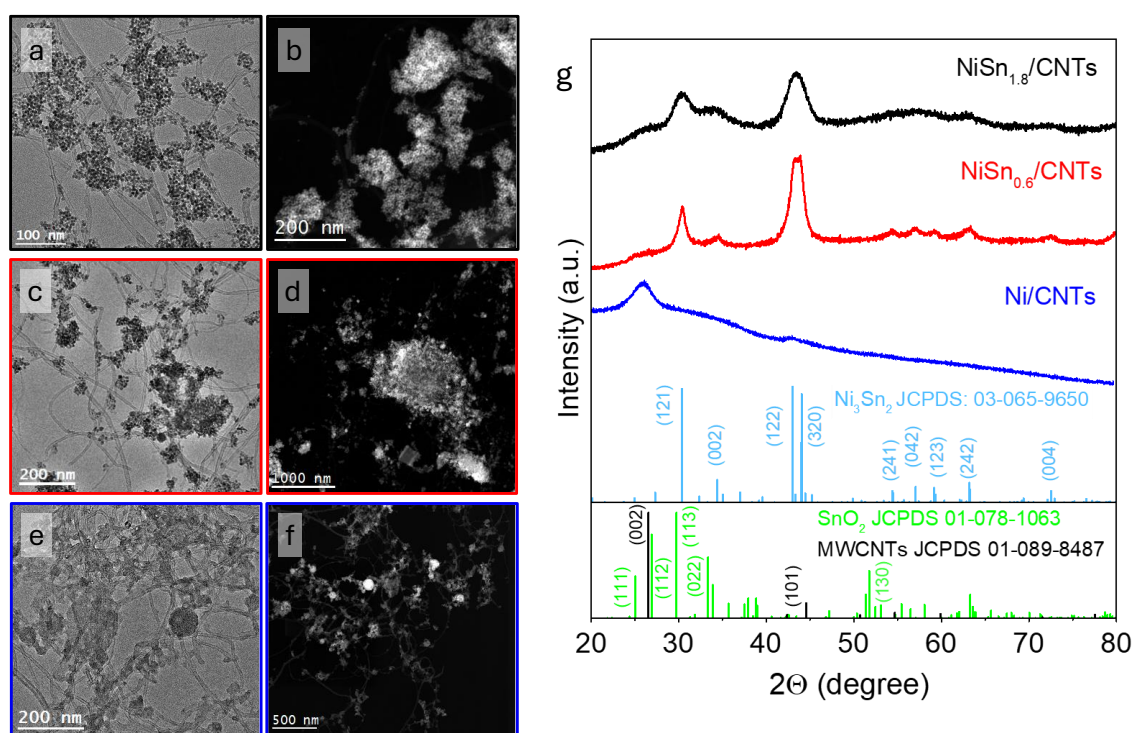


Figure 5.1. (a-f) Representative TEM (a, c, e) and STEM-HAADF (b, d, e) micrographs of $\text{NiSn}_{1.8}/\text{CNT}$ (a,b), $\text{NiSn}_{0.6}/\text{CNT}$ (c, d) and Ni/CNT (e, f) catalysts. (g) XRD patterns of $\text{NiSn}_{1.8}/\text{CNT}$ (black line), $\text{NiSn}_{0.6}/\text{CNT}$ (red line), and Ni/CNT (blue line) catalysts.

Figure 5.2a-b shows an AC STEM-HAADF image of the $\text{NiSn}_{0.6}/\text{CNT}$ sample. The power spectrum analysis confirms the presence of the Ni_3Sn_2 phase, characterized by an orthorhombic crystal structure within the Pnm space group. Moreover, atomic resolution AC STEM-HAADF images display a SnO_2 shell surrounding the Ni_3Sn_2 core, with an orthorhombic structure belonging to the Pbcn space group. Upon further examination of the atomic plane frequencies obtained from the FFT spectra calculated using STEM-HAADF images (specifically, the bottom right panel in

Figure 5.2a), we observed additional frequency spots corresponding to atomic planes associated with SnO_2 . After filtering out these frequencies related to SnO_2 and aligning them with the Ni_3Sn_2 core lattice fringes, we evidenced that the SnO_2 shell exhibits a discontinuous morphology, as clearly depicted in the frequency-filtered map shown in Figure 5.2b. The thickness of the SnO_2 shell is close to 2 nm. Frequency-filtered maps of a single nanoparticle (Figure 5.2b) and EDX maps of a particle's ensemble (Figure 5.2c) corroborate the core-shell structure. HRTEM analysis of the $\text{NiSn}_{1.8}$ nanoparticles displays a similar core-shell structure (Figure 5.S2), showing a core crystallizing in the Ni_3Sn_2 orthorhombic phase and a similarly thick SnO_2 shell. The similar shell thickness despite the higher Sn amount is consistent with the smaller size of the $\text{NiSn}_{1.8}$ cores. HAADF-STEM coupled with STEM-EELS analysis of the NiSn_y/CNT (Figures 5.S3 and 5.S4) shows that Sn is homogeneously distributed throughout the sample, while Ni is concentrated within the center of the particles (core) and the O is mainly found in the nanoparticles shell. In Ni/CNT , oxygen and nickel are equally distributed, showing full oxidation of the nickel nanostructures (Figure 5.S5).

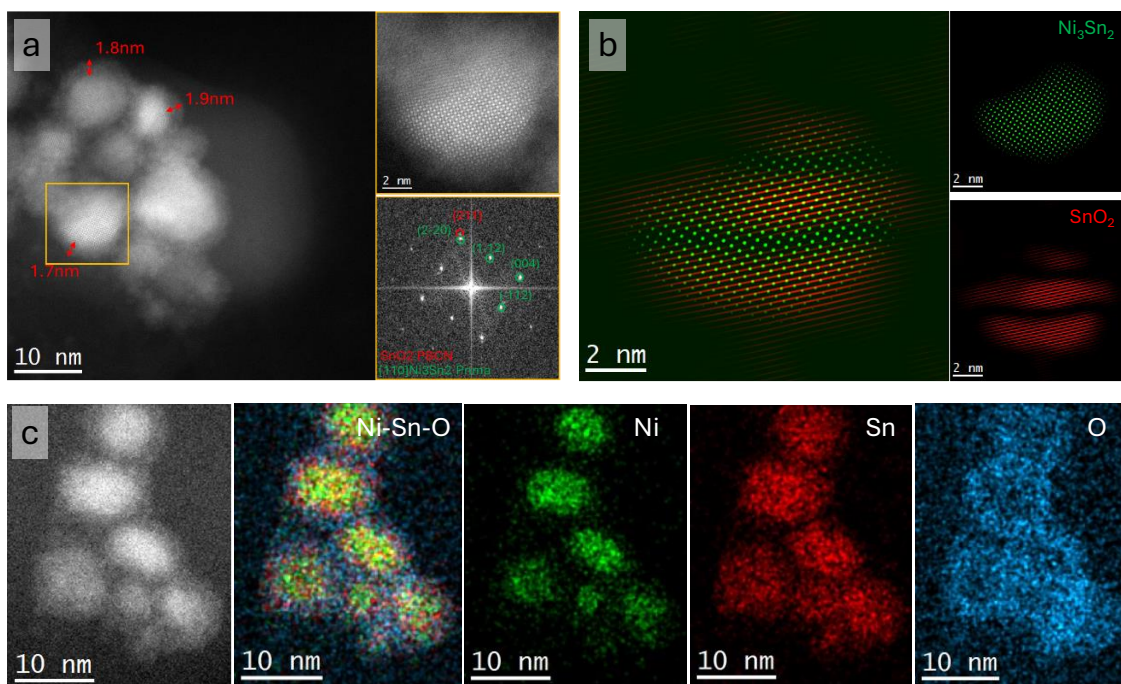


Figure 5.2. (a) Z-contrast AC STEM-HAADF micrograph of $\text{NiSn}_{0.6}$ nanoparticles and detail of the orange squared region and its corresponding FFT. (b) Frequency filtered map of the nanoparticle highlighted in (a) by the orange box showing the Ni_3Sn_2 core in green and SnO_2 shell in red. (c) EDX elemental maps of $\text{NiSn}_{0.6}$ particles showing the Ni (green), Sn (red), and O (blue) distributions.

The high-resolution Ni 2p XPS spectrum of NiSn_{0.6}/CNT shows two doublets at 853.0 eV (2p_{3/2}) and 856.7 eV (2p_{3/2}), corresponding to Ni(0) and Ni(II) oxidation states, respectively (Figure 5.S6a). The Ni(II) chemical environment, which accounts for about 56% of the total Ni detected on the NiSn_{0.6}/CNT surface, is generated during the acid treatment. Likewise, Sn exists in two chemical states, Sn(0) at 485 eV (3d_{5/2}) and Sn(IV) at 487 eV (3d_{5/2}). The Sn(IV) accounts for about 79% of the total Sn detected by XPS. The Ni/Sn atomic ratio provided by XPS is Ni/Sn \approx 0.1, which is consistent with the Sn surface segregation and the formation of the SnO₂ shell on the Ni₃Sn₂ particle surface, as observed by atomic resolution AC HAADF STEM, STEM-EDX, and STEM-EELS analyses. Similar results were obtained for the NiSn_{1.8}/CNT sample (Figure 5.S6b). In this case, Ni(0) and Ni(II) oxidation states account for about 47% and 53% of the total Ni, respectively. Besides, Sn(0) and Sn(IV) account for about 10% and 90% of the total Sn. The Ni/Sn atomic ratio provided by XPS in this sample is Ni/Sn \approx 0.05, consistent with the higher amount of Sn introduced in this material, the Sn surface segregation, and the formation of the SnO₂ shell on the Ni₃Sn₂ particle surface, as observed by HRTEM, STEM-EDX and STEM-EELS analyses. On the other hand, the Ni 2p XPS spectrum of the Ni/CNT sample (Figure 5.S7) confirms a unique oxidation state (Ni(II)) associated with the small size of the Ni particles in this sample.

5.4.2. Electrochemical characterization

The electrochemical properties of the Ni-based catalysts towards GOR were evaluated using a double-compartment H-cell, with a conventional three-electrode configuration (see details in the SI). Electrodes were fabricated onto a 1 x 1 cm CP substrate via airbrushing using an ink containing 3 mg of catalyst, 0.75 mL of ethanol, 0.2 mL of Milli-Q water, and 50 μ L of Nafion (Figure 5.S8). Despite its lower conductivity and smaller surface area compared to Ni foam, CP was selected as support to remove a potential role of the Ni support on the GOR reaction.

LSV in the potential range of 1.0 to 1.8 V vs RHE was first conducted in 1 M of KOH at a scan rate of 5 mV s⁻¹ (Figure 5.3a). LSV curves show a peak between 1.3 V and 1.5 V corresponding to the Ni⁰/Ni²⁺ oxidation to Ni³⁺ (NiOOH). At potentials higher than 1.6 V, LSV voltammograms display an increase in intensity associated with the OER. The larger Ni oxidation current obtained for Ni/CNTs and NiSn_{0.6}/CNT compared with NiSn_{1.8}/CNT is consistent with the lower Ni amount of the latter. The larger Ni oxidation current obtained with the NiSn_{0.6}/CNT electrode, compared to the Ni/CNT, can be attributed to two factors. First, in the bimetallic samples, nickel is found in both Ni⁰ and Ni²⁺ states, implying that part of the oxidation to Ni³⁺ involves three electrons (Ni⁰ to Ni³⁺). In contrast, all the Ni within Ni/CNTs is found as Ni²⁺, thus involving only one electron (Ni²⁺ to Ni³⁺). XPS analysis of the electrodes after the electrochemical experiment (Figure 5.S9)

reveals that the metallic Ni peaks in the bimetallic samples have disappeared, indicating complete oxidation of nickel during the LSV. Besides, the oxyhydroxide formation involves the reaction with OH⁻ molecules in solution, which is potentially enhanced by the oxophilic nature of Sn. In this direction, Tafel plots confirm the NiSn alloy to promote the kinetics of NiOOH formation (Figure 5.S10a).

The electrocatalytic GOR activity was evaluated by adding 10 mM of glucose to the 1 M KOH solution. LSV curves of the electrodes in the presence of glucose (Figure 5.3b) display three distinct regions: (1) a minor rise in current between 1.1 V and 1.35 V, associated with the formation of Ni³⁺ species, followed by (2) an abrupt boost at approximately 1.35 V, coinciding with the Ni oxidation to Ni³⁺, and (3) a subsequent current surge at potentials higher than 1.55 V, where the contribution of the OER becomes significant. As will be discussed later in the manuscript, glucose conversion at potentials below 1.35 V is almost negligible, which confirms NiOOH species are the truly active catalysts. XPS analysis of the material after the LSV curves confirms the presence of Ni³⁺ (Figure 5.S10). The current densities in the 1.1-1.35 V region match well the amount of Ni within each material, Ni/CNT > NiSn_{0.6}/CNT > NiSn_{1.8}/CNT. The current density in region 2 (1.35 V - 1.6 V) reflects the GOR electrocatalytic activity of the materials. Both the onset potential and the steepness of the slope improve with the tin content. The GOR Tafel plots (Figure 5.3c) in this second region confirm that the kinetics are faster in NiSn_{1.8}/CNT > NiSn_{0.6}/CNT > Ni/CNT. As the applied potentials increase, mass transport becomes the limiting step of the process. Desorbed products from the electrode surface hinder the arrival of new glucose molecules, leading to a saturation of the current displayed in the voltammogram. The saturation current of the NiSn_{1.8}/CNTs catalyst remains significantly lower than that of the other two materials owing to the lower amount of Ni. Meanwhile, in the Ni/CNT, given that the reaction proceeds at a slower rate compared to bimetallic compounds, it is necessary to apply higher potentials to augment the GOR rate and attain electrode surface saturation. Increasing the glucose concentration prevents current saturation by alleviating reactant diffusion limitations. Notably, NiSn_{0.6}/CNT exhibits its peak GOR activity in 100 mM of glucose, as observed by LSV (Figure 5.3d) and the Tafel plot (Figure 5.S10b).

CV in the range between 1.0 V and 1.8 V of the electrodes within a 1 M KOH solution shows the pair redox Ni²⁺/Ni³⁺ at oxidation potentials between 1.3-1.5 V and reduction potentials between 1.3-1.05 V (Figure 5.3e). When adding 100 mM glucose, a significant increase in current associated with the GOR is observed for all the samples, and no reduction peak is detected. As displayed in equation 3, the glucose oxidation induces the reduction of NiOOH to Ni(OH)₂. All

the NiOOH species formed are immediately reduced upon glucose interaction. Thus during the reduction process, all species are already reduced, which explains the absence of the reduction peak. Extending the potential window down to 0.1 V (Figure 5.S11), with and without glucose, no additional oxidative peaks are obtained. Nevertheless, during the reduction process in 1 M KOH, an extra peak is observed at 0.5 - 0.7 V, corresponding to the reduction of the oxygen generated during the OER at high potentials. Since, in the presence of glucose, the GOR activity predominates over OER for the as-prepared electrocatalysts within the measured potential range, hardly any current variation associated with the oxygen reduction reaction is observed. The EIS data in Figure 5.3f indicate that NiSn_{0.6}/CNT exhibited the lowest charge-transfer resistance, confirming it as the most efficient GOR catalyst among the three tested materials.

The relative ECSA was estimated by C_{dl} measurements (Equations 5 and 6). Capacitances for the as-prepared catalysts are compared in Figure 5.S12. Results show that the calculated capacitance follows a trend Ni/CNT > NiSn_{1.8}/CNT > NiSn_{0.6}/CNT. The calculated ECSA values indicate that Ni/CNT has the highest electrochemical surface area (205 cm²), followed by NiSn_{1.8} (122.5 cm²) and NiSn_{0.6} (60 cm²), which is consistent with the different sizes of the Ni-based particles, but it is inversely proportional to the kinetics of the GOR process. This suggests that the activity of the prepared materials is closely related not to the exposed active sites but to their intrinsic activity.

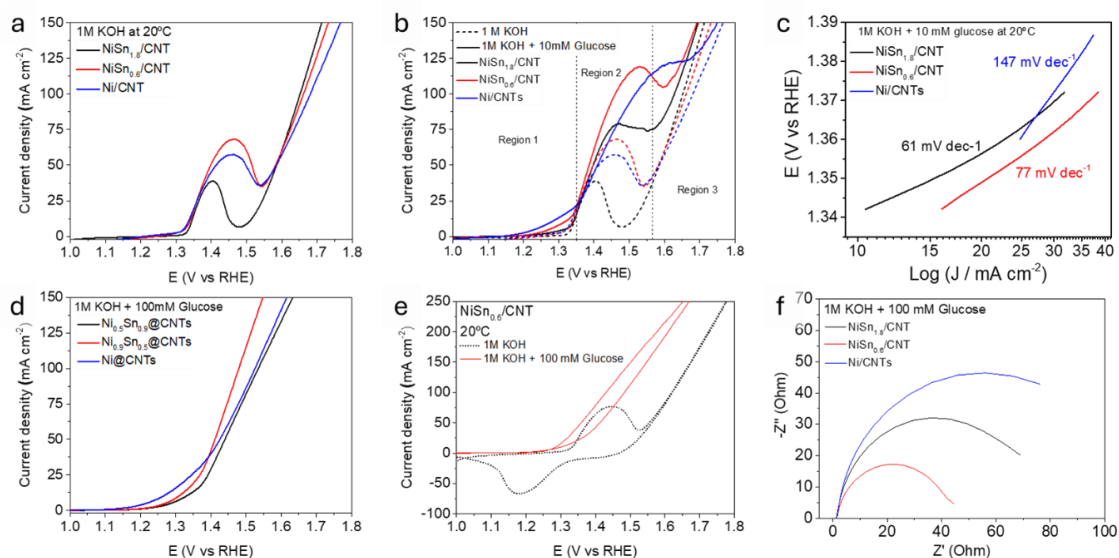


Figure 5.3. (a-d) LSV voltammograms in 1 M KOH aqueous solution (a), LSV voltammograms and Tafel slopes in 1 M KOH + 10 mM glucose aqueous solution (b, c) and LSV voltammograms in 1 M KOH + 100 mM glucose aqueous solution (d) using NiSn_{1.8}/CNT (black line), NiSn_{0.6}/CNT (red line) and Ni/CNT (blue line) catalysts. (e) CV voltammograms of NiSn_{0.6}/CNT in 1 M KOH (black

dotted line) and (red solid line) 1 M KOH + 100 mM glucose. (f) Nyquist plots in 1 M KOH + 100 mM glucose aqueous solution of NiSn_{1.8}/CNT (black line), NiSn_{0.6}/CNT (red line), and Ni/CNT (blue line) catalysts.

In the Faradaic region, the potential difference between the oxidation and reduction peaks of Ni(OH)₂ ↔ NiOOH is directly correlated with the electron transfer kinetics between the electrode surface and the active centers, which indicates whether the reaction is kinetically favorable.^[38] Comparing the value of 0.25 V, obtained for NiSn_{0.6}, with the values of 0.3 V and 0.18 V for Ni and NiSn_{1.8}, respectively (Figure 5.S13), it is evident that the incorporation of Sn improves the reaction kinetics of Ni(OH)₂ ↔ NiOOH.

The Γ* of Ni(OH)₂/NiOOH redox species is another key kinetic parameter for evaluating and comparing the performance of different materials. This parameter provides information about the amount of NiOOH active sites available on the surface, which are crucial for electrochemical reactions. The Γ* can be determined from the linear fit of the I_a with the scan rate from 10-80 mV s⁻¹ (Figures 5.S14)

$$I_a = \left(\frac{n^2 F^2}{4RT} \right) A \Gamma^* \nu \quad (11)$$

where F is the Faraday constant (96485 C mol⁻¹), n is the number of transferred electrons (n=1), T is the temperature (295 K), R is the gas constant (8.314 J K⁻¹ mol⁻¹) and A is the geometric surface area of the electrode (1 cm²). The Γ* value for NiSn_{0.6} electrodes, as obtained from the forward scans, was 2.9 × 10⁻⁶ mol cm⁻² (Figure 5.14e), which is slightly higher than the Γ* value for Ni at 2.7 × 10⁻⁶ mol cm⁻² and for NiSn_{1.8} at 1.9 × 10⁻⁶ mol cm⁻². A higher Γ* value indicates a greater density of active sites, which can translate to a higher charge storage capacity and improved efficiency in electron transfer.

Since proton diffusivity is generally the rate-limiting step controlling the Ni(OH)₂ ↔ NiOOH redox reaction for Ni-based electrodes,^[39] we decided to calculate the D within the electrodes using the simplified form of the Randles–Sevcik equation (12):

$$I_{ac} = 2,69 \cdot 10^5 n^{3/2} A D^{1/2} C \nu^{1/2} \quad (12)$$

n represents the number of electrons transferred in the redox reaction, while A denotes the electrode area. The diffusion coefficient of the redox species is indicated by D, the concentration of the redox species is given by C, and ν stands for the scan rate. The results for the proton

diffusion coefficient indicate that diffusion in the NiSn_{0.6} electrode ($3.81 \times 10^{-7} \text{ cm}^2 \text{ s}^{-1}$) is faster than in Ni/CNT ($3.12 \times 10^{-7} \text{ cm}^2 \text{ s}^{-1}$) and NiSn_{1.8}/CNT ($1.86 \times 10^{-7} \text{ cm}^2 \text{ s}^{-1}$).

The TOF values were deduced from the mass of the catalyst added to the electrode

$$\text{TOF} = \left(\frac{J A}{n F m} \right) \quad (13)$$

where F is the Faraday constant (96485 C mol^{-1}), n is the number of transferred electrons, m is the number of moles of catalyst involved in the reaction, J is the current density and A is the geometric surface area of the electrode (1 cm^2). A TOF value of 0.044 s^{-1} was obtained for NiSn_{0.6} at 1.45 V in the presence of glucose, while NiSn_{1.8} and Ni showed TOF values of 0.035 s^{-1} and 0.007 s^{-1} , respectively. This TOF value indicates that the active sites in NiSn catalysts are more efficient compared to the monometallic compound, as the reaction kinetics are faster despite a lower ECSA value.

The glucose electrochemical conversion was further studied using CA measurements conducted for 1 h at room temperature. The obtained products were identified and quantified using HPLC. The electrocatalysis was initially carried out with a constant glucose concentration of 10 mM, while varying the working potential within the range from 1.35 to 1.6 V. At potentials lower than 1.35 V, a very low glucose conversion (< 5%) was achieved. Beyond 1.60 V, there is strong competition with the OER, particularly as glucose is being consumed and its concentration decreases, thereby reducing the GOR FE. In the voltage range 1.35-1.6 V, FA, and OXA were the only GOR products, with FA being the predominant one for the three catalysts. This result points to glucose being mainly converted throughout the C-C bond cleavage pathway. Considering the two identified products, the total FE (calculated by Equation 7) is below 100% in the entire potential range tested (Figure 5.4a-c). We attribute this discrepancy to the overoxidation of the generated FA to CO₂ which was in turn converted to carbonate within the alkaline solution. This was confirmed when 2M sulfuric acid was added to the electrolyte solution after 1h GOR and a clear effervescence, due to the conversion of carbonates to CO₂, was observed. The FA oxidation was intensified as the applied potential was increased. Thus, the FE for FA gradually decreased with the working potential, even in the range where no competition with OER was expected. The NiSn_{0.6}/CNT electrode was the most active when considering LSV curves, but it provided the lowest glucose conversion and the lowest FA selectivities. This is attributed to the faster FA oxidation in this material, which reduces the overall GOR and the GOR-to-FA selectivity.

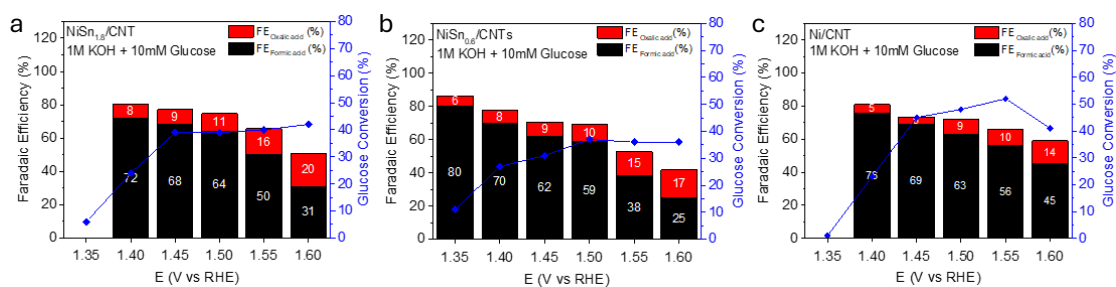


Figure 5.4. FE of the GOR to FA and OXA using NiSn_{1.8}/CNT (a), NiSn_{0.6}/CNT (b), and Ni/CNT (c) as electrodes at applied potentials from 1.40 to 1.60 V in 1M KOH and 10 mM glucose for 1h.

Figure 5a-b presents the characterization of the NiSn_{0.6}/CNT sample after GOR, conducted at a potential of 1.45 V vs. RHE in 1M KOH and 10 mM glucose. The power spectrum analysis and atomic-resolution AC STEM-HAADF images reveal the presence of both the Ni₃Sn₂ core phase and the SnO₂ shell, with their crystalline structures preserved post-reaction. Furthermore, STEM-EELS analysis (Figure 5.5c) shows that, following the reaction, Sn remains predominantly localized in the nanoparticle core and the thin oxide shell, consistent with its pre-reaction state. However, a faint signal is also detected throughout the material, suggesting the presence of dispersed Sn atoms across the entire sample. In contrast, nickel is found in large concentrations both at the core and also forming an oxide matrix surrounding the particles, along with small pure Ni precipitates, as indicated by the stronger Ni signal. This surface nickel oxide formation is attributed to the generation of NiOOH during the reaction, highlighting the material's transformation under catalytic conditions.

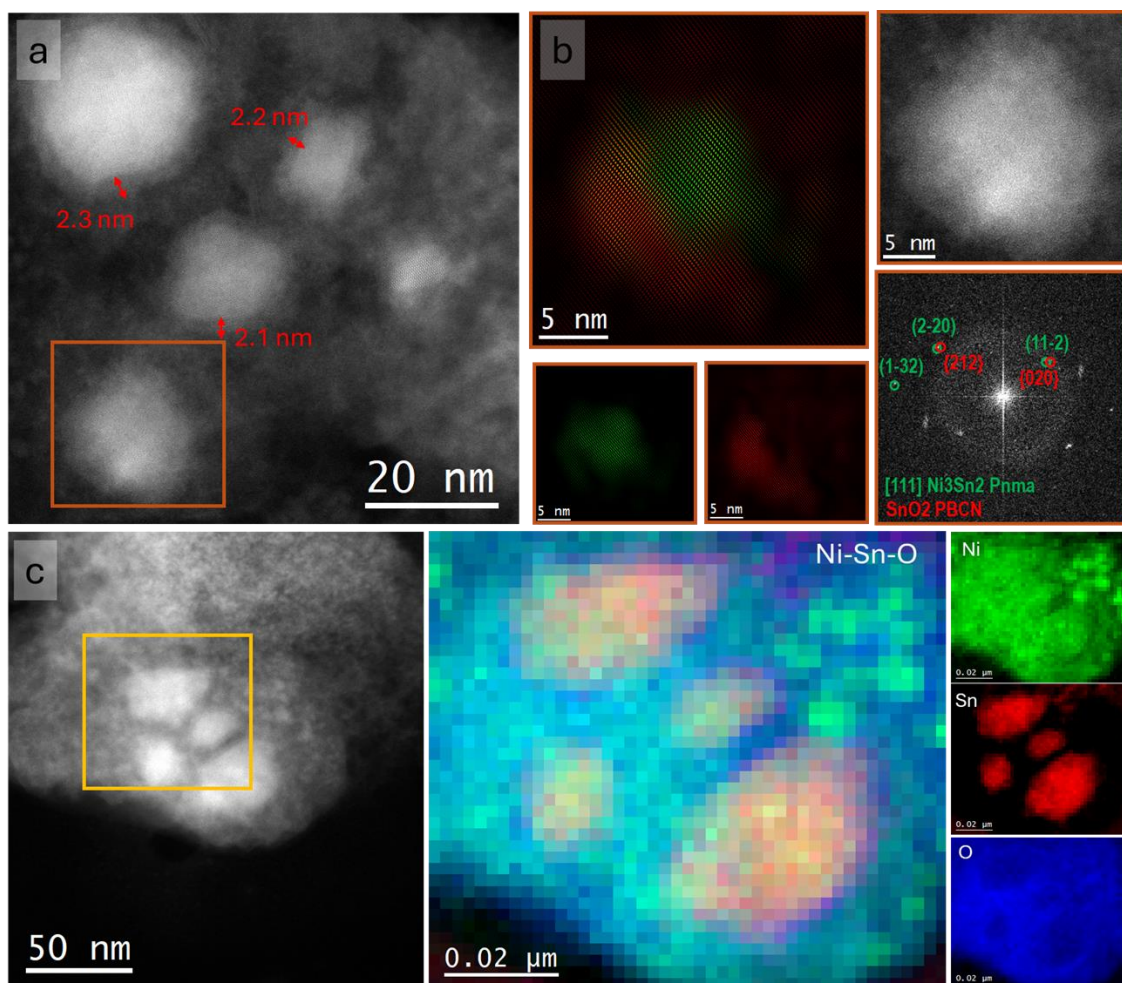


Figure 5.5. Characterization of $\text{NiSn}_{0.6}$ nanoparticles after being used as catalysts in the GOR applying a potential of 1.45 V vs. RHE for 1 h in 1M KOH and 10 mM glucose. (a) Z-contrast AC STEM-HAADF micrograph of the nanoparticles and detail of the orange squared region and its corresponding FFT. (b) Frequency filtered map of the nanoparticle highlighted in (a) by the orange box showing the Ni_3Sn_2 core in green and SnO_2 shell in red. (c) EDX elemental maps of $\text{NiSn}_{0.6}$ particles showing the Ni (green), Sn (red), and O (blue) distributions.

The GOR catalytic activity is strongly dependent on glucose concentration. To maximize GOR and minimize FA overoxidation, the potential was set at 1.45 V and the glucose concentration was increased from 10 mM to 100 mM. As depicted in Figure 5.6a, the FE for FA production increases with the amount of glucose in the solution. At a higher glucose concentration, pristine glucose molecules faster replace the generated FA, which is thus less susceptible to being overoxidated. The $\text{NiSn}_{0.6}/\text{CNT}$ reaches the maximum FA FE (93 %) at 100 mM of glucose and demonstrates to be more selective than $\text{NiSn}_{1.8}/\text{CNT}$ (83 %) and Ni/CNT (84 %) in the same reaction conditions (Figure 5.S15). This FE value for FA is one of the largest values reported and the highest for a Ni-based catalyst (Table 5.S1). At a higher applied potential of 1.55 V (Figure 5.6b), the FE for FA

also increases with the glucose concentrations, but it decreases in comparison to the results obtained at a lower applied potential due to FA overoxidation. Besides, although the activity for GOR is enhanced using the bimetallic NiSn_x/CNT catalysts, the FE at higher potentials for FA is Ni (83%) > NiSn_{1.8} (81%) > NiSn_{0.6} (76%).

As previously mentioned, the C-C cleavage oxidation process competes with the non-Faradaic degradation process. As seen in Scheme 5.1, under basic conditions, glucose can convert to fructose and subsequently form various compounds such as LA, TA, or AA. This degradation occurs within the bulk of the electrolyte, distinct from the oxidative process occurring at the electrode surface. The overall product selectivity was calculated based on a carbon balance (see details in the Experimental section, Equation 8), which accounts for the glucose consumed in the process and, therefore, includes the products obtained in both the gas and liquid phases. The results show that the non-Faradaic glucose degradation pathway is promoted when the glucose initial concentration is increased, as evidenced by the higher proportion of fructose detected. Additionally, AA is obtained, which has not been widely reported as a product of GOR. Increasing the applied potential, a minor overall selectivity is obtained (Figure 5.6b), particularly at lower concentrations, due to increased carbonate production. Furthermore, the observed proportion of fructose diminishes with the applied potential, which is attributed to the accelerated GOR, resulting in less remaining unreacted glucose.

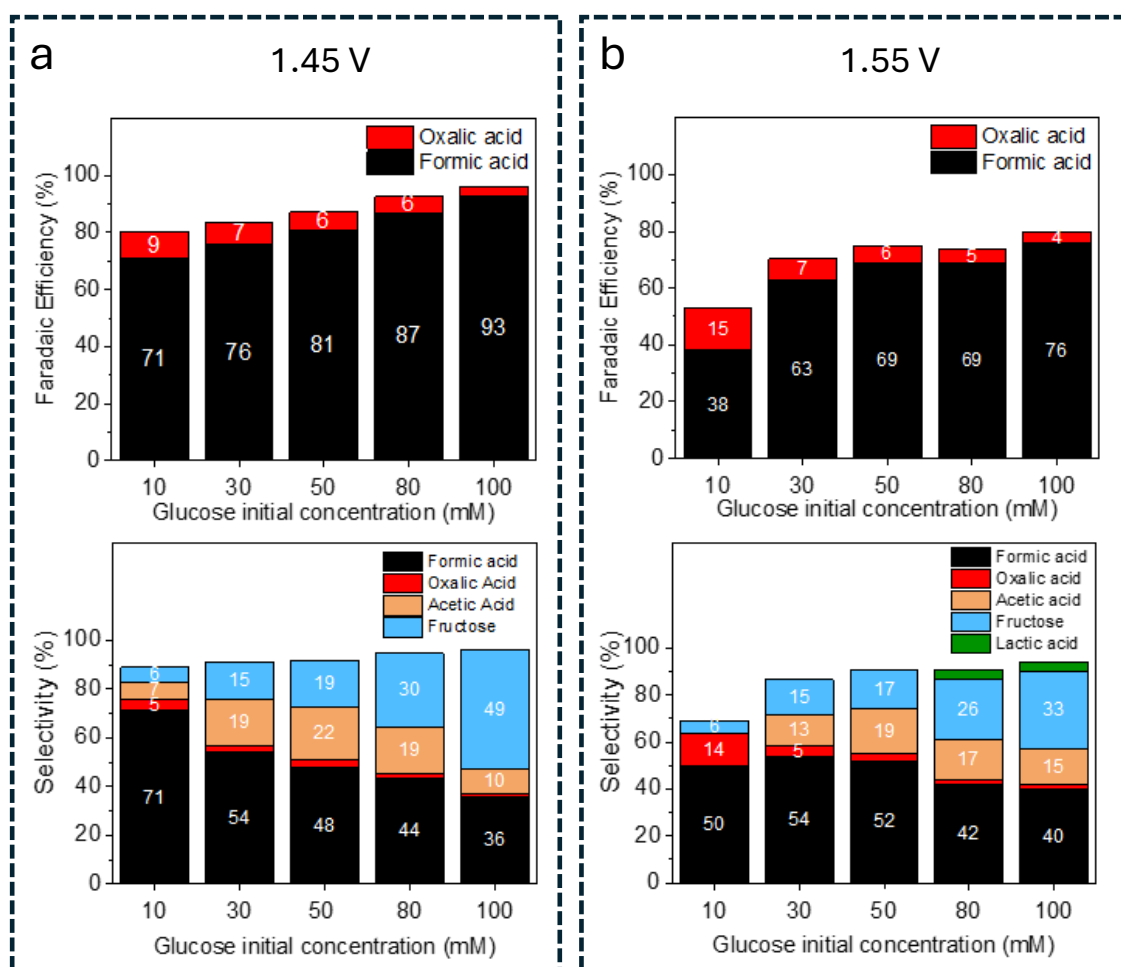


Figure 5.6. FE (top) and selectivity (bottom) of the products obtained during GOR at applied potentials of 1.45 V (a) and 1.55 V (b) using a NiSn_{0.6}/CNT electrode. GOR was performed for 1h at 20 °C in 1M KOH and increasing glucose concentration from 10 to 100 mM.

Most previous works show the results obtained after relatively short reaction times to minimize the glucose conversion by non-Faradaic processes. To evaluate this aspect, a long-term experiment was performed to study how glucose oxidation varies over time (Figure 5.7). The electrocatalytic reaction was carried out for 24 h at an applied potential of 1.45V and an initial glucose concentration of 30 mM to reduce the overoxidation of FA while also minimizing glucose degradation. At ambient temperature, the FE for FA decreases over time, as the declining glucose concentration leads to overoxidation of the generated FA (Figure 5.7a). Consequently, a decrease in the selectivity of FA is observed. On the other hand, the selectivity towards AA increases over time, eventually surpassing that of FA. The same experiments were conducted at a temperature of 55°C to enhance the reaction kinetics. Initially, the reaction was performed at a potential of 1.35 V (Figure 5.7b). At 55°C, unlike at room temperature, a significant consumption of glucose was observed. After 1 hour, the maximum FE value obtained was 94%, although a similar decrease over time was observed. At this potential, a higher selectivity for LA

was evident. Elevated temperatures accelerate the kinetics of glucose oxidation to FA but also promote the degradation process. Conversely, at a higher potential of 1.45 V and elevated temperature (55°C), the decrease in FA is more rapid, as is the oxidation of LA, resulting in a higher amount of AA (Figure 5.7c).

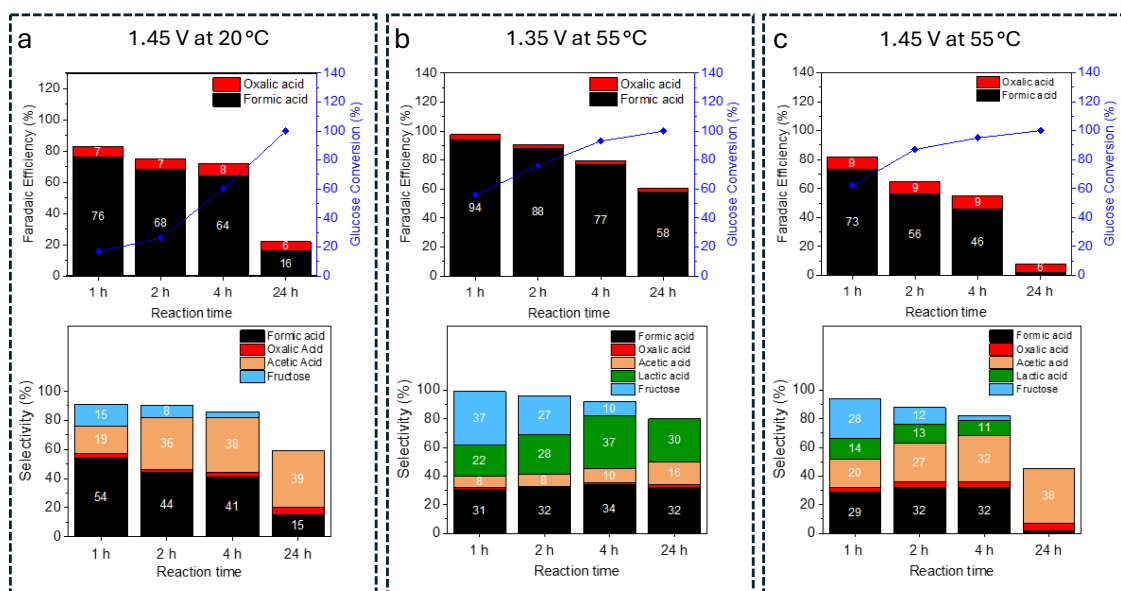


Figure 5.7. FE and glucose conversion (top) and selectivity (bottom) of products obtained during GOR using NiSn_{0.6}/CNT as the electrode in 1M KOH and 30 mM glucose for 24 h. The different experiments were carried out at 1.45 V at 20 °C (a), 1.35 V at 55 °C (b), and 1.45 V at 55 °C (c).

The stability of NiSn_{0.6}/CNT under GOR conditions was evaluated through 5 subsequent cycles of CA, each lasting 1 hour in a solution of 1M KOH and 10 mM glucose (Figure 5.S16). After each experiment, the electrolyte was replaced with the same amount of reactant. It is observed that the decrease in the CA curves is solely due to glucose consumption, as each new cycle starts with the same current value. If there were any deactivation of the material, a progressive or total decrease would be observed at the beginning of each cycle. The glucose consumption and formate production in each cycle were analyzed by HPLC (Figure 5.S17) and, at the end of each cycle, both remained constant, indicating that the activity of the catalyst did not decrease with each reaction. The observation is consistent with the post-catalysis characterization results, previously discussed, which show no loss of Ni or Sn after the GOR. This confirms that the NiSn alloy is stable under GOR operation.

5.4.3. DFT calculations

To gain insight into the role of Sn on the GOR over the Ni surface, DFT calculations were conducted. The adsorption energy of glucose on pure Ni(OH)₂ and on Ni(OH)₂ sites near a Sn

atom was first calculated. The top-view and side-view structures of the optimized pristine Ni(OH)_2 and the Sn-containing Ni(OH)_2 , along with the corresponding adsorption structures of glucose, are shown in Figure 5.8a,b. Calculations revealed that, in absolute value, the adsorption energy of glucose on Ni(OH)_2 , -0.22 eV increased with the introduction of Sn, up to -0.34 eV. As shown in Figure 5.8c, the spin density difference between spin-up and spin-down electrons decreased from 0.82 eV to 0.76 eV after introducing Sn to Ni(OH)_2 . The reduced antiferromagnetic spintronics indicates an improved electroconductivity in the oxidative Sn-containing Ni(OH)_2 alloy, which explains the variation in activation energy compared to pristine Ni(OH)_2 . Besides, to determine the effect of the SnO_2 shell on the catalytic activity of Ni(OH)_2 , the process of gaining effective oxidative NiOOH intermediate through Ni(OH)_2 was analyzed (Figure 5.8d,e). The E_{f-HV} of the pristine Ni(OH)_2 , which represents the transformation of Ni(OH)_2 to NiOOH , is as large as 2.03 eV. In contrast, in the $\text{Ni(OH)}_2/\text{SnO}_2$ composite, it decreases to 1.06 eV. A more positive E_{f-HV} implies the O-H scission is less favored. Thus, overall, the presence of Sn/ SnO_2 not only enhances glucose adsorption by modulating the antiferromagnetic spintronics of Ni but also promotes the formation of the active species NiOOH .

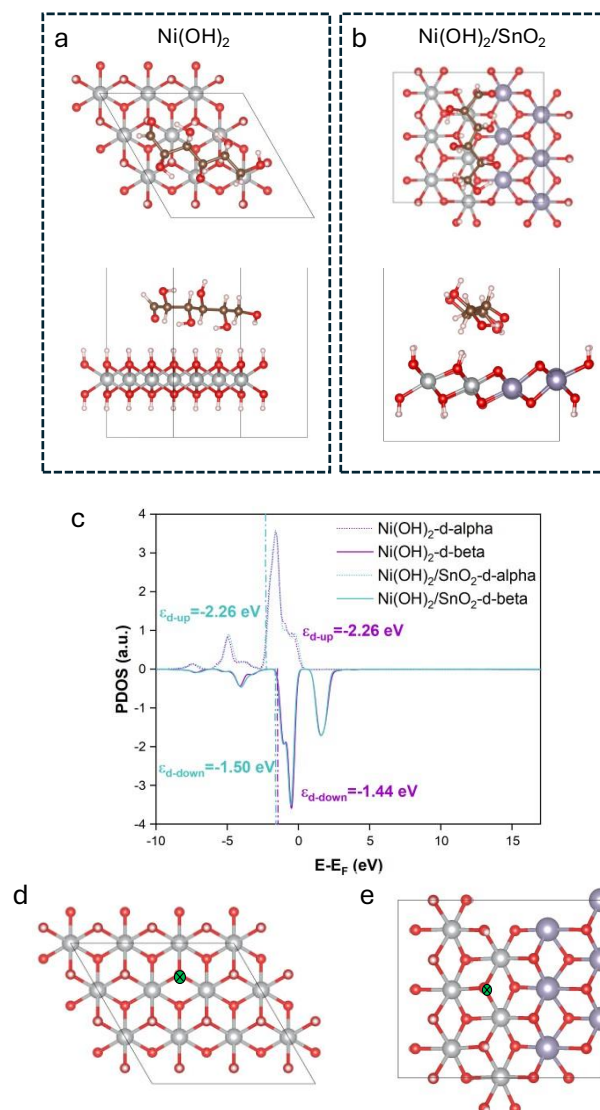


Figure 5.8. (a,b) Top and side views of the optimized structures of glucose adsorption on Ni(OH)₂ (a) and Sn-Ni(OH)₂ (b) surface. H (small white), C (small brown), O (small red), Ni (big white), and Sn (big purple). (c) Partial density of states (PDOS) curves of the d-orbital electrons of Ni in Ni(OH)₂ and oxidative Sn-Ni(OH)₂. (d,e) Top-view of the deprotonation process on Ni(OH)₂ surface (d) and oxidative Ni(OH)₂/SnO₂ composite (e).

5.5. CONCLUSIONS

In summary, we detailed the synthesis of NiSn_x nanoparticles via colloidal reduction and their subsequent support on CNTs. Characterization revealed the NiSn_x particles to display a core-shell Ni₃Sn₂@SnO₂ architecture, with a porous SnO₂ shell and smaller and more regularly shaped cores observed at higher Sn concentrations. NiSn_x/CNT catalysts exhibited enhanced GOR performance, displaying improved kinetics with increasing Sn concentration and higher activity with greater Ni content. Notably, NiSn_{0.6}/CNT demonstrated superior electrochemical

performance compared to both NiSn_{1.8}/CNT and Ni/CNT. Furthermore, the analysis of the oxidation products highlighted the excellent performance of the NiSn_{0.6}/CNT catalyst, achieving a maximum FE of 93% for FA at 1.45 V vs RHE. We observed that at higher potentials and lower concentrations, FA overoxidation to carbonates occurs, reducing the total FE. Higher glucose concentrations mitigate FA overoxidation but increase competition with glucose degradation in basic conditions. Consequently, at high concentrations, FA selectivity decreases, while AA and LA production increases. Enhanced selectivity for these compounds is also observed with longer reaction times and higher temperatures. Even though achieving high selectivity and efficiency in an H-type cell remains challenging due to the complexity of the GOR mechanisms, intermediate conditions of 50 mM and 1.5 V at temperatures below 50°C are proposed to maximize FA production while minimizing competition with the formation of other products. Finally, DFT results confirmed that the presence of Sn/SnO₂ promotes the Ni activity thus enhancing the adsorption of glucose and boosting the oxohydroxyde formation.

5.6. REFERENCES

1. W. J. Liu, Z. Xu, D. Zhao, X. Q. Pan, H. C. Li, X. Hu, Z. Y. Fan, W. K. Wang, G. H. Zhao, S. Jin, G. W. Huber, H. Q. Yu, *Nat. Commun.* 2020, 11, 1–11.
2. Y. Q. Zhu, H. Zhou, J. Dong, S. M. Xu, M. Xu, L. Zheng, Q. Xu, L. Ma, Z. Li, M. Shao, H. Duan, *Angew. Chemie - Int. Ed.* 2023, 62, DOI 10.1002/anie.202219048.
3. H. Zhou, Y. Ren, B. Yao, Z. Li, M. Xu, L. Ma, X. Kong, L. Zheng, M. Shao, H. Duan, *Nat. Commun.* 2023, 14, 1–12.
4. Y. Wang, M. Xu, X. Wang, R. Ge, Y. Q. Zhu, A. Z. Li, H. Zhou, F. Chen, L. Zheng, H. Duan, *Sci. Bull.* 2023, 68, 2982–2992.
5. L. Ostervold, S. I. Perez Bakovic, J. Hestekin, L. F. Greenlee, *RSC Adv.* 2021, 11, 31208–31218.
6. A. Anil, J. White, E. Campos dos Santos, I. Terekhina, M. Johnsson, L. G. M. Pettersson, A. Cornell, G. Salazar-Alvarez, *J. Mater. Chem. A* 2023, 11, 16570–16577.
7. X. Su, Z. Pan, L. An, *Int. J. Energy Res.* 2019, 43, 7433–7443.
8. A. M. Bartrom, J. Ta, T. Q. Nguyen, J. Her, A. Donovan, J. L. Haan, *J. Power Sources* 2013, 229, 234–238.
9. L. Q. Wang, M. Bellini, J. Filippi, M. Folliero, A. Lavacchi, M. Innocenti, A. Marchionni, H. A. Miller, F. Vizza, *Appl. Energy* 2016, 175, 479–487.
10. M. Fleischmann, K. Korinek, D. Pletcher, *J. Electroanal. Chem.* 1971, 31, 39–49.
11. Z. Liu, Y. Shen, *ACS Appl. Energy Mater.* 2022, 5, 11723–11731.
12. A. M. Abdelrahim, M. G. Abd El-Moghny, M. E. El-Shakre, M. S. El-Deab, *RSC Adv.* 2023, 13, 1811–1822.

13. V. P. Ananikov, *ACS Catal.* 2015, 5, 1964–1971.
14. P. Sabatier, *Catalysis in Organic Chemistry*, 1922.
15. S. Jiao, N. Kang, M. Liu, Y. Zhang, Y. Li, B. Maryam, P. Zhang, X. Liu, *Catalysts* 2016, 14, 1–23.
16. C. Lin, P. Zhang, S. Wang, Q. Zhou, B. Na, H. Li, J. Tian, Y. Zhang, C. Deng, L. Meng, J. Wu, C. Liu, J. Hu, L. Zhang, *J. Alloys Compd.* 2020, 823, 153784.
17. X. Lin, H. Zhong, W. Hu, J. Du, *Inorg. Chem.* 2023, 62, 10513–10521.
18. N. Wei, S. Zhang, X. Yao, Y. Feng, V. Nica, J. Yang, Q. Zhou, *Sep. Purif. Technol.* 2024, 343, 127178.
19. D. Chai, W. Wang, F. Wang, Y. Kang, Y. Yang, Z. Lei, *Electrochim. Acta* 2016, 189, 295–302.
20. Dandan Tu, B. Wu, B. Wang, C. Deng, Y. Gao, *Appl. Catal. B Environ.* 2011, 103, 163–168.
21. R. M. Abdel Hameed, A. E. Fahim, N. K. Allam, *J. Mol. Liq.* 2020, 297, 111816.
22. X. Yu, J. Liu, J. Li, Z. Luo, Y. Zuo, C. Xing, J. Llorca, D. Nasiou, J. Arbiol, K. Pan, T. Kleinmanns, Y. Xie, A. Cabot, *Nano Energy* 2020, 77, DOI 10.1016/j.nanoen.2020.105116.
23. Z. Luo, J. Lu, C. Flox, R. Nafria, A. Genç, J. Arbiol, J. Llorca, M. Ibáñez, J. R. Morante, A. Cabot, *J. Mater. Chem. A* 2016, 4, 16706–16713.
24. W. Du, K. E. MacKenzie, D. F. Milano, N. A. Deskins, D. Su, X. Teng, *ACS Catal.* 2012, 2, 287–297.
25. D. W. Boukhvalov, G. D'Olimpio, J. Liu, C. Ghica, M. C. Istrate, C. N. Kuo, G. G. Politano, C. S. Lue, P. Torelli, L. Zhang, A. Politano, *Chem. Commun.* 2023, 6040–6043.
26. X. Tang, B. Zhang, Y. Li, Y. Xu, Q. Xin, W. Shen, *J. Mol. Catal. A Chem.* 2005, 235, 122–129.
27. T. H. Huang, H. S. Zheng, Y. M. Cheng, C. W. Liu, S. W. Lee, J. H. Wang, K. W. Wang, *Sustain. Energy Fuels* 2019, 3, 3352–3362.
28. C. W. Liu, Y. W. Chang, Y. C. Wei, K. W. Wang, *Electrochim. Acta* 2011, 56, 2574–2581.
29. N. A. M. Barakat, F. S. Al-Mubaddel, M. Rezual Karim, M. Alrashed, H. Yong Kim, *Int. J. Hydrogen Energy* 2018, 43, 21333–21344.
30. J. Li, Z. Luo, Y. Zuo, J. Liu, T. Zhang, P. Tang, J. Arbiol, J. Llorca, A. Cabot, *Appl. Catal. B Environ.* 2018, 234, 10–18.
31. J. Li, X. Xu, X. Yu, X. Han, T. Zhang, Y. Zuo, C. Zhang, D. Yang, X. Wang, Z. Luo, J. Arbiol, J. Llorca, J. Liu, A. Cabot, *ACS Appl. Mater. Interfaces* 2020, 12, 4414–4422.
32. C. C. L. McCrory, S. Jung, J. C. Peters, T. F. Jaramillo, *J. Am. Chem. Soc.* 2013, 135, 16977–16987.
33. G. Kresse and J. Furthüller, *Phys Rev B Condens Matter* 1996, 54, 11169–11186.
34. G. Kresse, J. Hafner, *Phys. Rev. B* 1994, 49, 14251–14269.
35. J. P. Perdew, K. Burke, M. Ernzerhof, *Phys. Rev. Lett.* 1996, 77, 3865–3868.
36. P. E. Blöchl, *Phys. Rev. B* 1994, 50, 17953–17979.

37. H. J. M. and J. D. Pack, *Phys. Rev. B* 1976, 13, 5188–5192.
38. J. Li, C. Xing, Y. Zhang, T. Zhang, M. C. Spadaro, Q. Wu, Y. Yi, S. He, J. Llorca, J. Arbiol, A. Cabot, C. Cui, *Small* 2021, 17, DOI 10.1002/smll.202006623.
39. L. Xiao, J. T. Lu, P. F. Liu, L. Zhuang, J. W. Yan, R. G. Hu, H. W. Mao, C. J. Lin, *Chinese Chem. Lett.* 2005, 16, 419–422.
40. R. Ciancio, R. E. Dunin-Borkowski, E. Snoeck, M. Kociak, R. Holmestad, J. Verbeeck, A. I. Kirkland, G. Kothleitner, J. Arbiol, *Microsc. Microanal.* 2022, 28, 2900–2902.

SUPPORTING INFORMATION

5.7. SI RESULTS

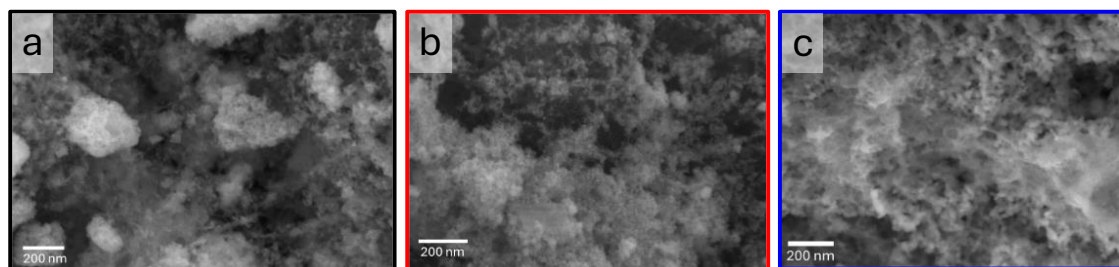


Figure 5.S1. Representative SEM images of the as-prepared NiSn_{1.8}/CNT (a), NiSn_{0.6}/CNT (b) and Ni/CNT(c) catalyst.

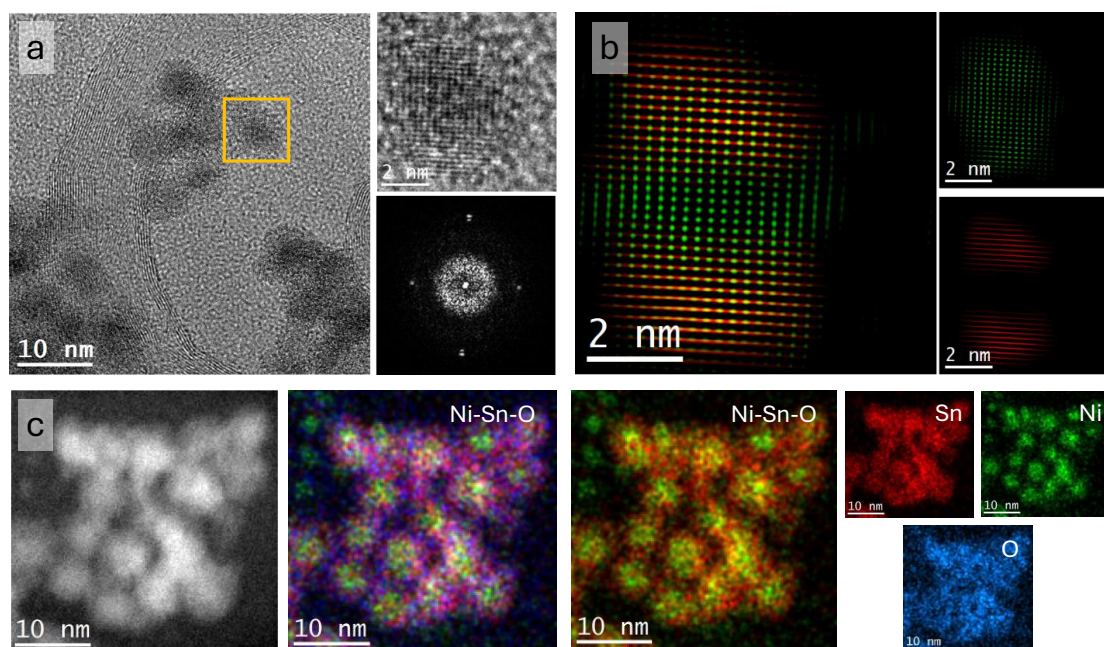


Figure 5.S2. (a) HRTEM micrograph of NiSn_{1.8} nanoparticles and detail of the orange squared region and its corresponding FFT analysis. (b) Frequency filtered map of the nanoparticle highlighted in (a) by the orange box showing the Ni₃Sn₂ core in green and SnO₂ shell in red. (c) EDX elemental maps of NiSn_{0.6} particles showing Ni (green), Sn (red), and O (blue) distribution.

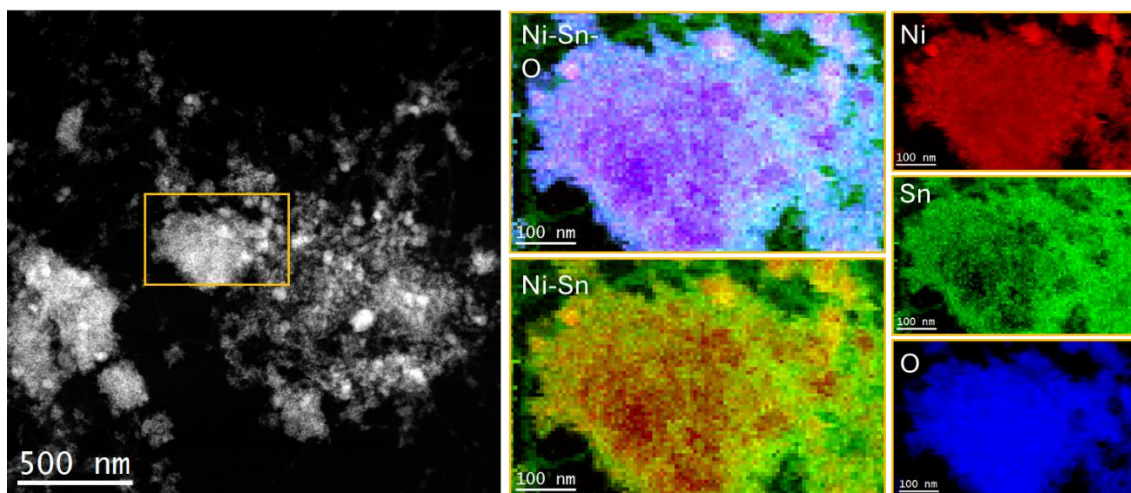


Figure 5.S3. STEM-EELS elemental maps of NiSn_{0.6}/CNT NPs showing a Ni (green), Sn (red) and O (blue) distribution.

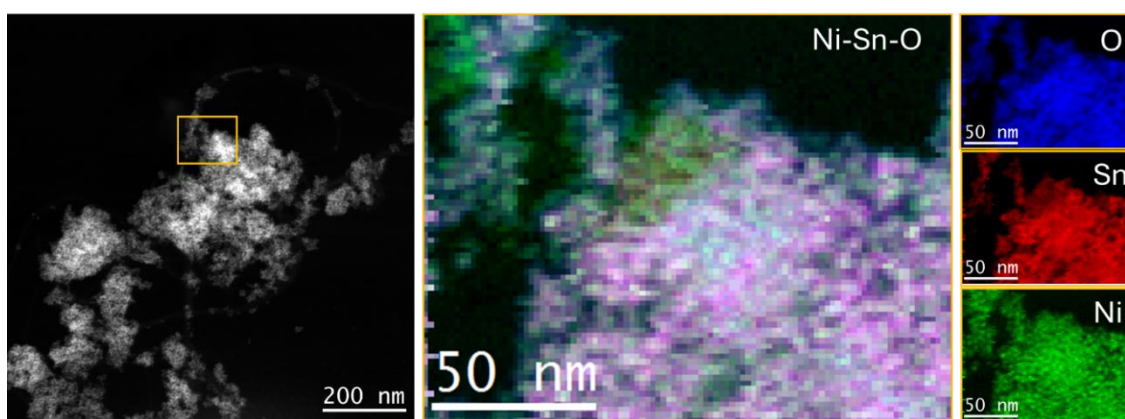


Figure 5.S4. STEM-EELS elemental maps of NiSn_{1.8}/CNT NPs showing a Ni (green), Sn (red) and O (blue) distribution.

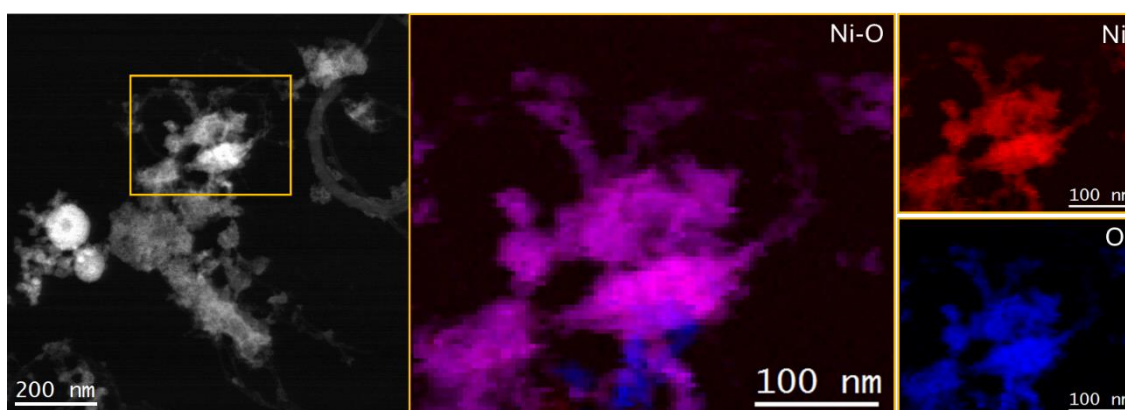


Figure 5.S5. STEM-EELS elemental maps of Ni/CNT NPs showing a Ni (red) and O (blue) distribution.

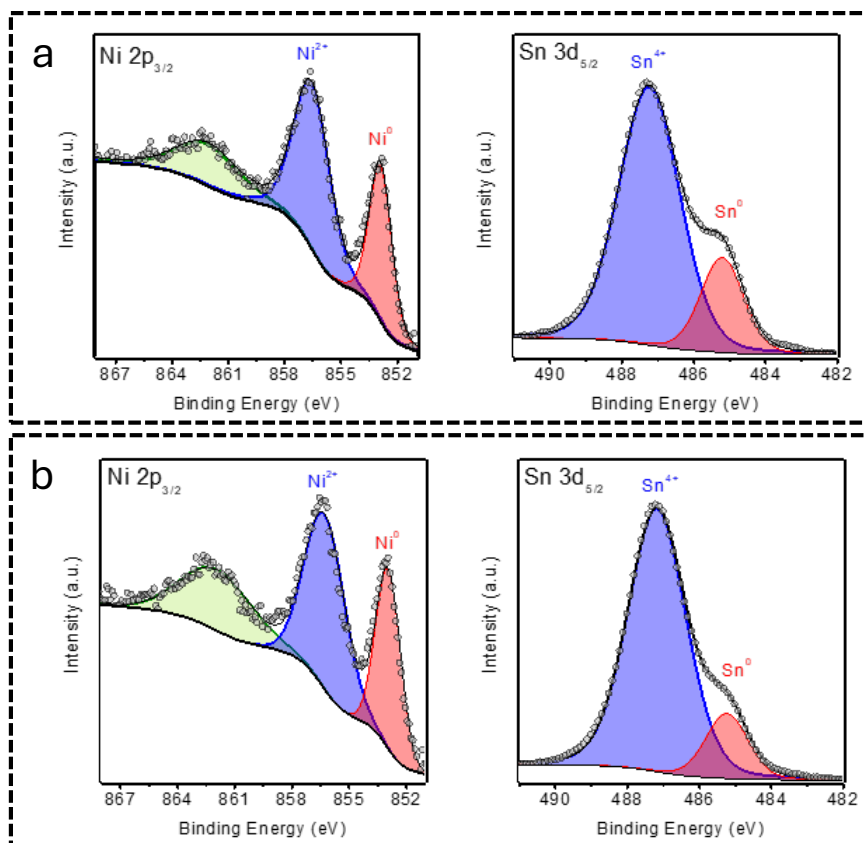


Figure 5.S6. High-resolution Ni 2p_{3/2} and Sn 3d_{5/2} XPS spectra of the NiSn_{0.6}/CNT (a) and NiSn_{1.8}/CNT (b) catalysts.

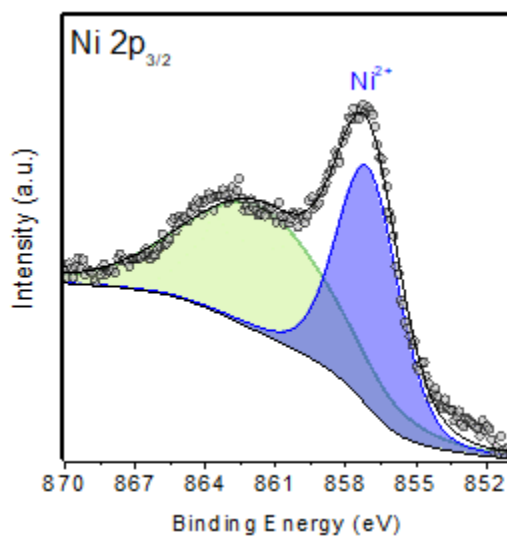


Figure 5.S7. High-resolution Ni 2p_{3/2} XPS spectra of the Ni/CNT catalyst.

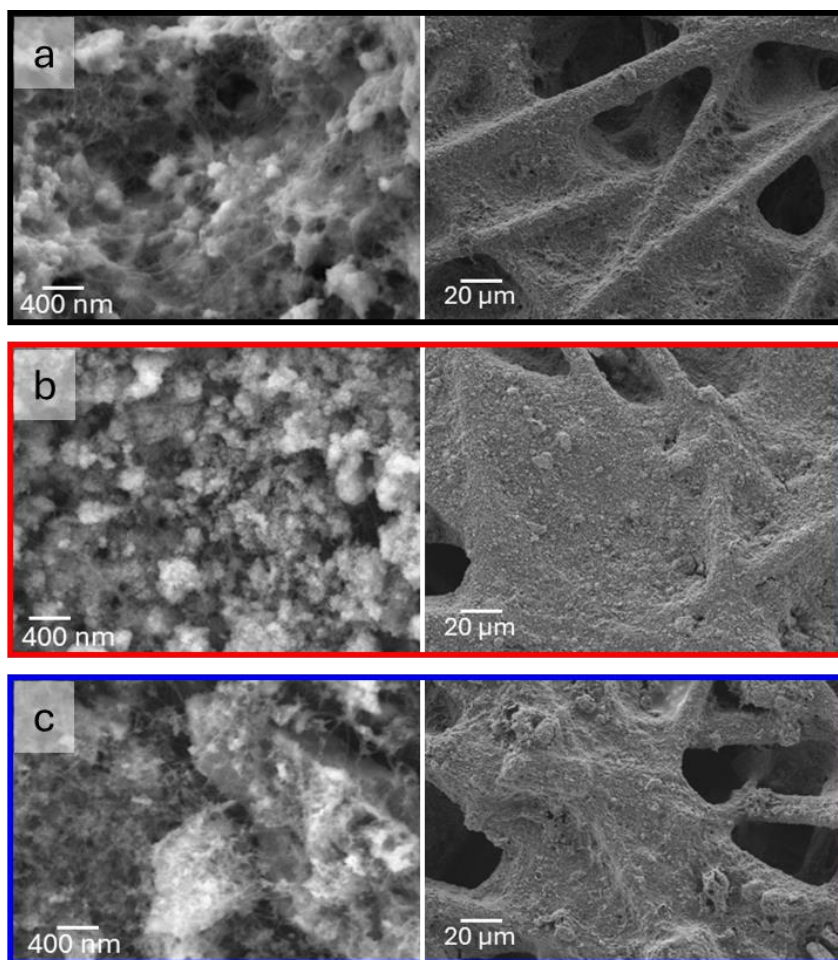


Figure 5.58. Representative SEM images of NiSn_{1.8}/CNT (a), NiSn_{0.6}/CNT (b) and Ni/CNT (c) catalyst.

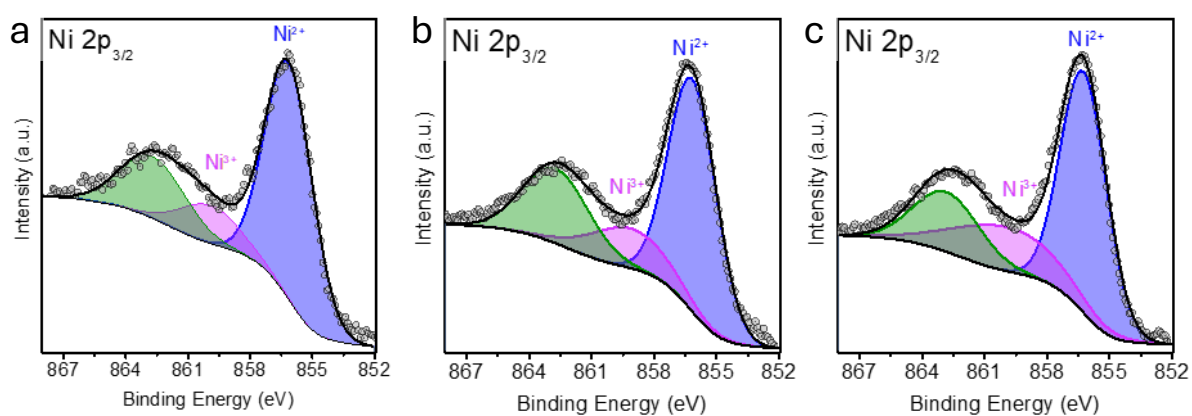


Figure 5.59. High-resolution Ni 2p_{3/2} of NiSn_{1.8}/CNT (a), NiSn_{0.6}/CNT (b) and Ni/CNT (c) catalyst performed after electro-characterization.

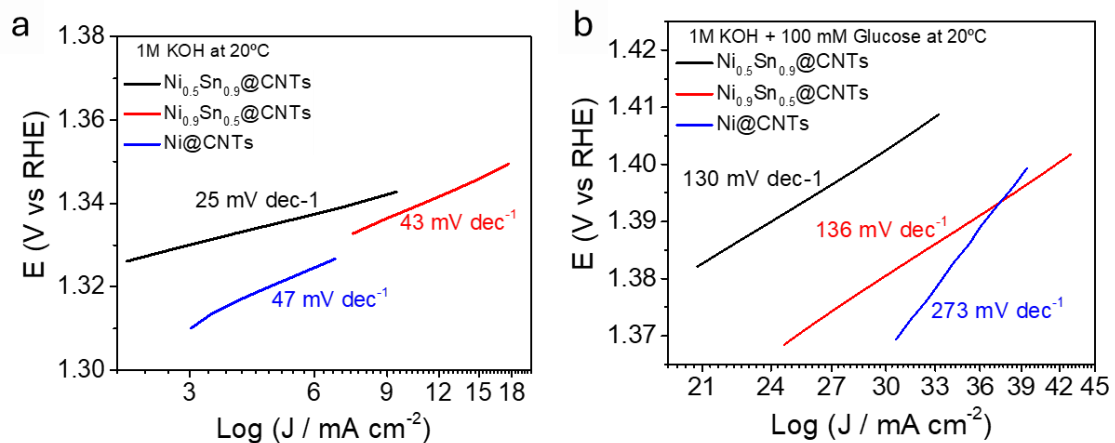


Figure 5.S10. Tafel plots in 1M KOH (a) and 1M KOH +100 mM glucose (b) of NiSn_{1.8}/CNT (black line), NiSn_{0.6}/CNT (red line), and Ni/CNT (blue line) catalysts.

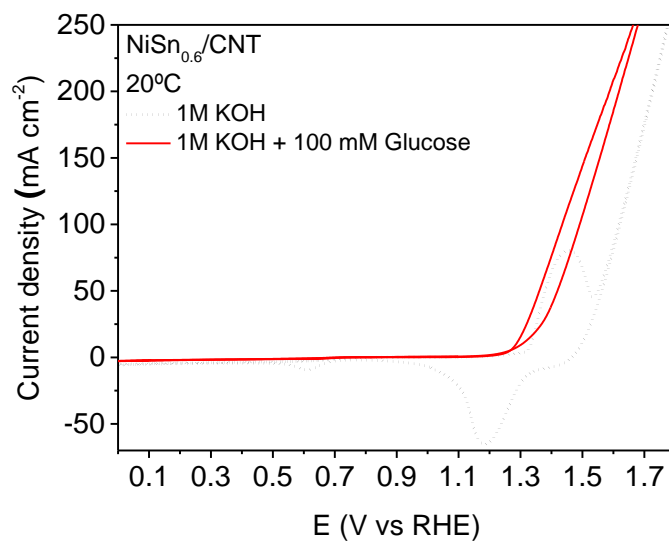


Figure 5.S11. CV voltammogram of NiSn_{0.6}/CNT in 1 M KOH (Black dotted line) and 1 M KOH + 100 mM glucose (red solid line).

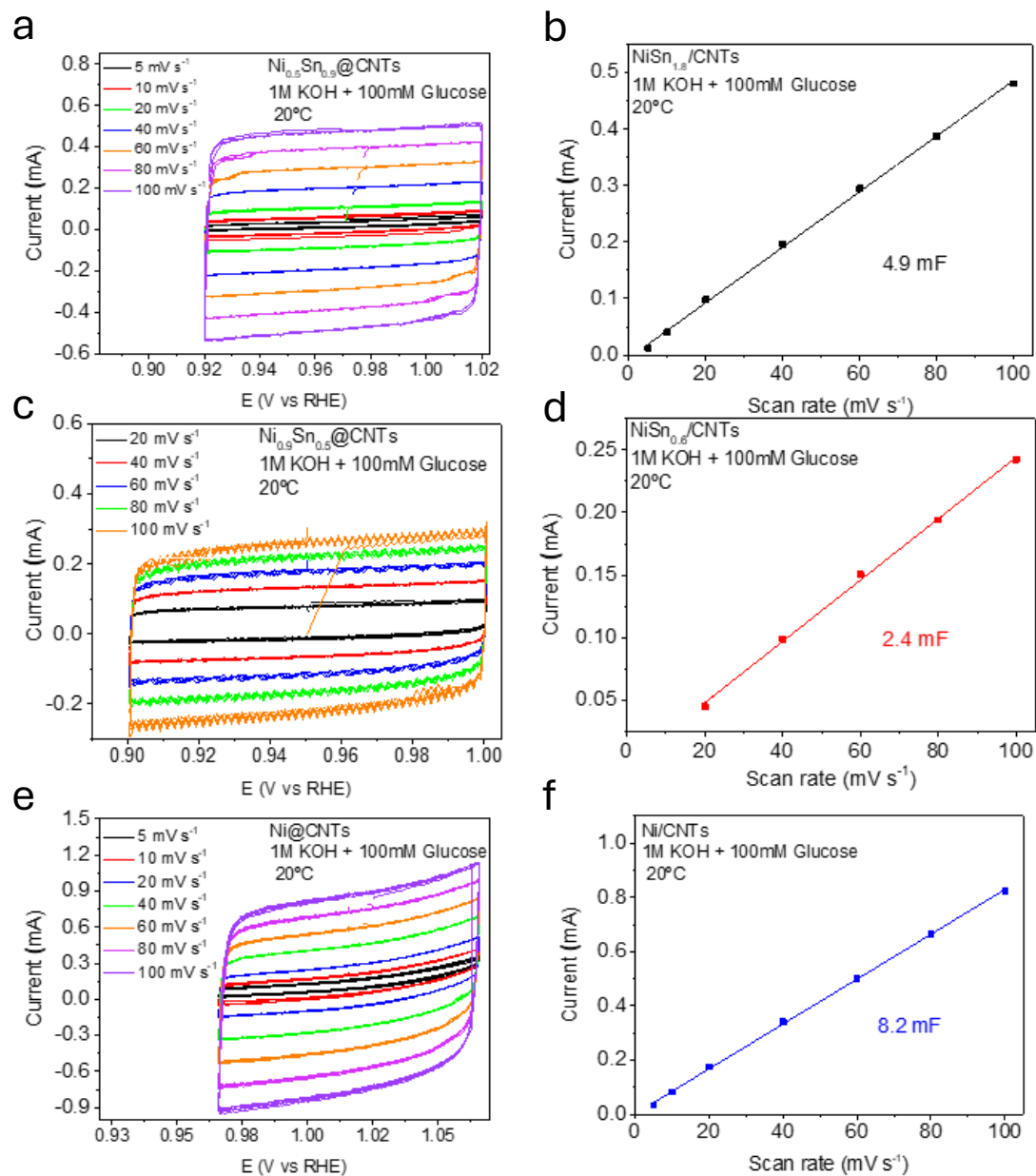


Figure 5.S12. ECSA determination of $\text{NiSn}_{1.8}/\text{CNT}$ (a, b), $\text{NiSn}_{0.6}/\text{CNT}$ (c, d), and Ni/CNT (e, f) catalysts. (a, c, e) CV voltammograms at $\text{OCP} \pm 50 \text{ mV}$ at different scan rates ($100 - 5 \text{ mV s}^{-1}$). (b, d, f) Capacitive current as a function of scan rate.

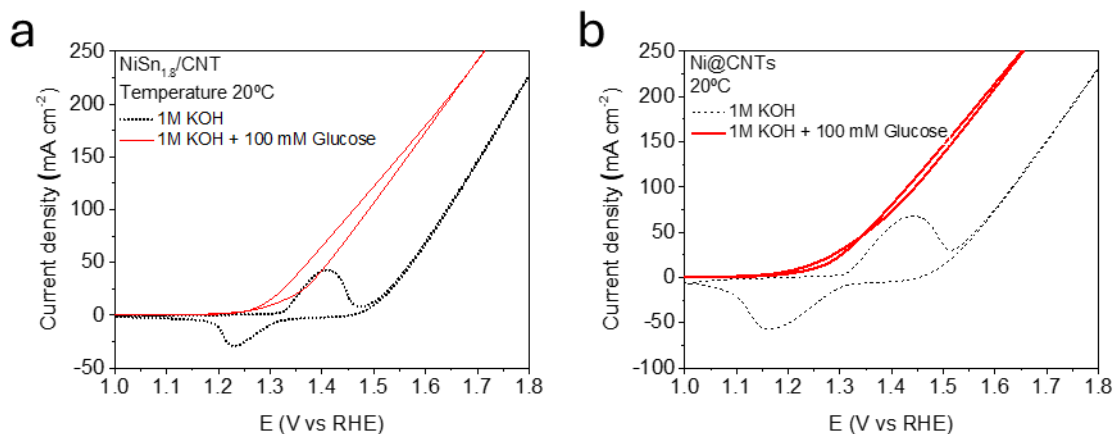


Figure 5.S13. CV voltammograms of NiSn_{1.8}/CNT (a) and Ni/CNT (b) in 1 M KOH (black dotted line) and (red solid line) 1 M KOH + 100 mM glucose.

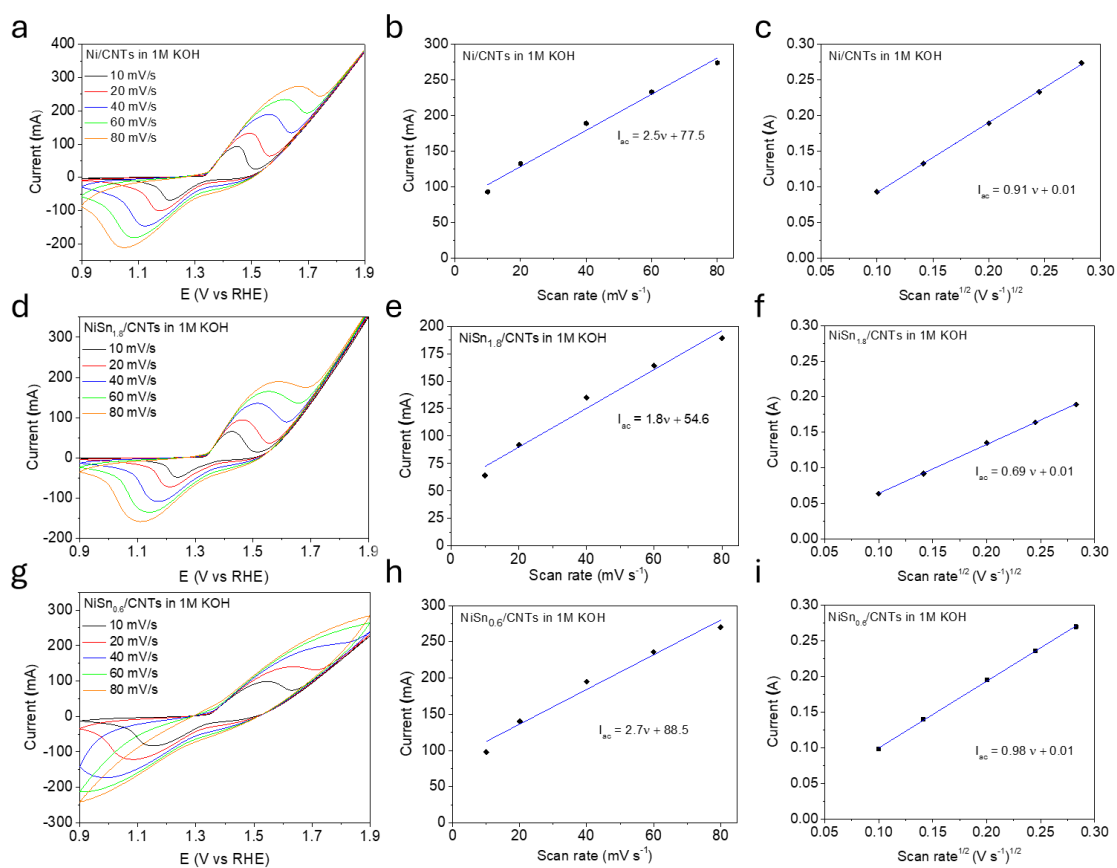


Figure 5.S14. Electrochemical kinetics of Ni/CNT (a, b, c), NiSn_{1.8}/CNT (d, e, f), and NiSn_{0.6}/CNT (g, h, i) catalysts in 1.0 m KOH. (a,d,c) CV curves in the potential range from 0.9 to 1.9 V with variable scan rate of 10–80 mV s⁻¹. (b,e,f) Linear fitting of the peak current as a function of the scan rate. (c, f, i) Linear fitting of the peak current as a function of the square root of scan rate.

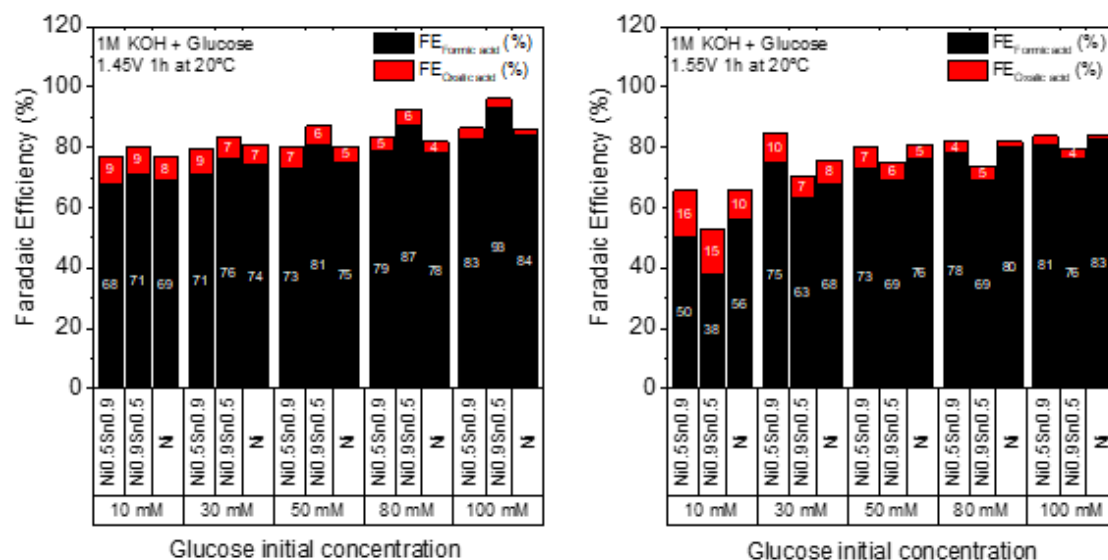


Figure 5.S15. FE comparison graph of the GOR to FA and OXA using the as-prepared NiSn_{1.8}/CNT, NiSn_{0.6}/CNT, and Ni/CNT catalysts with an applied potential of 1.45 V (a) and 1.55 V (b). The GOR experiment was carried out for 1h in 1M KOH increasing the glucose initial concentration from 10 mM to 100 mM.

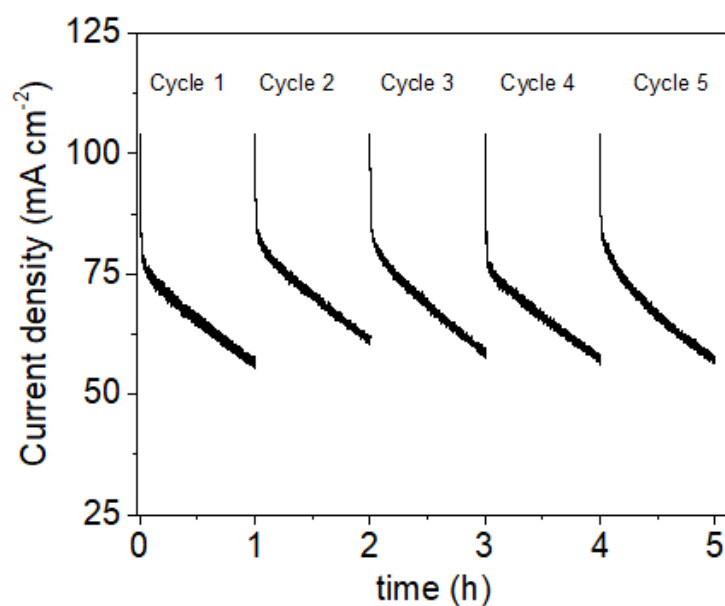


Figure 5.S16. Five subsequent CA curves of NiSn_{0.6}/CNT at 1.45V in 1M KOH and 10 mM of glucose at room temperature. The electrolyte was replaced after each cycle.

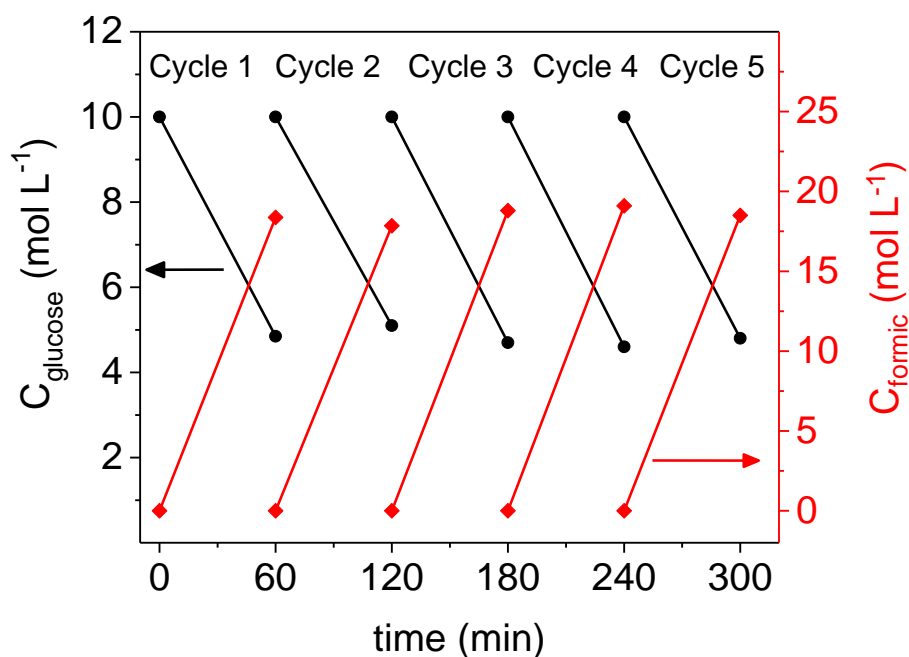


Figure 5.S17. Variation in the concentration of glucose and formic acid present in the electrolyte during the electrooxidation of glucose reaction, applying a potential of 1.45V vs RHE using the as-prepared NiSn_{0.6}/CNTs catalyst. The electrolyte was replaced after each cycle.

Table 5.S1. Bibliographic reported results using different catalysts toward GOR.

Catalyst	Main product	Selectivity (%)	FE (%)	Potencial	Ref.
Au	GNA	86		0.55 V _{RHE}	1
Cu	FA	54		1.80 V _{RHE}	
Pt	GNA	68		0.70 V _{RHE}	
Fe _{0.1} -CoSe ₂ /CC	GNA		87	0.72V _{RHE}	2
NiFeO _x /NiFoam	GRA		87	1.39 V _{RHE}	3
Cu ²⁺	FA	50		1.5 V _{RHE}	4
NiO/CNT	FA	~ 90		1.46-1.66 V _{RHE}	5
CuO/CNT		~95			
Co ₃ O ₄ /CNT		86			

CoOOH	FA	84	90	1.5 V _{RHE}	6
CoOOH	FA		69	1.6 V _{RHE}	7
CuO	FA	70	95	1.4 V _{RHE}	8
NiOOH			~ 65		
CoOOH			70		
NiO	FA	6	39	1.91 V _{RHE}	9
NiCoSe _x	FA		70	1.40 V _{RHE}	10
Mn-doped nickel iron phosphate embedded in a P, N codoped carbon substrate	FA		86	1.45 V _{RHE}	11
NiO + TEMPO	GRA	83	83	1.45 V _{RHE}	12
NiSn _{0.6} /CNT	FA	36	93	1.45 V _{RHE}	This work

5.8. SI REFERENCES

1. G. Moggia, T. Kenis, N. Daems and T. Breugelmans, *ChemElectroChem*, 2020, **7**, 86–95.
2. D. Zheng, J. Li, S. Ci, P. Cai, Y. Ding, M. Zhang and Z. Wen, *Appl. Catal. B Environ.*, 2020, **277**, 119178.
3. W. J. Liu, Z. Xu, D. Zhao, X. Q. Pan, H. C. Li, X. Hu, Z. Y. Fan, W. K. Wang, G. H. Zhao, S. Jin, G. W. Huber and H. Q. Yu, *Nat. Commun.*, 2020, **11**, 1–11.
4. L. Ostervold, S. I. Perez Bakovic, J. Hestekin and L. F. Greenlee, *RSC Adv.*, 2021, **11**, 31208–31218.
5. Z. Liu and Y. Shen, *ACS Appl. Energy Mater.*, 2022, **5**, 11723–11731.
6. H. Zhou, Y. Ren, B. Yao, Z. Li, M. Xu, L. Ma, X. Kong, L. Zheng, M. Shao and H. Duan, *Nat. Commun.*, 2023, **14**, 1–12.
7. Y. Q. Zhu, H. Zhou, J. Dong, S. M. Xu, M. Xu, L. Zheng, Q. Xu, L. Ma, Z. Li, M. Shao and H. Duan, *Angew. Chemie - Int. Ed.*, DOI:10.1002/anie.202219048.
8. Y. Wang, M. Xu, X. Wang, R. Ge, Y. Q. Zhu, A. Z. Li, H. Zhou, F. Chen, L. Zheng and H. Duan,

- Sci. Bull.*, 2023, **68**, 2982–2992.
9. G. Sanghez de Luna, T. Tabanelli, J. J. Velasco-Vélez, E. Monti, F. Ospitali, S. Albonetti, F. Cavani, G. Fornasari and P. Benito, *Sustain. Energy Fuels*, 2023, 4474–4477.
 10. X. Lin, H. Zhong, W. Hu and J. Du, *Inorg. Chem.*, 2023, **62**, 10513–10521.
 11. N. Wei, S. Zhang, X. Yao, Y. Feng, V. Nica, J. Yang and Q. Zhou, *Sep. Purif. Technol.*, 2024, **343**, 127178.
 12. K. Zhang, Z. X. Zhan, M. Zhu, H. Lai, X. He, W. Deng, Q. Zhang and Y. Wang, *J. Energy Chem.*, 2023, **80**, 58–67.

CHAPTER 6

GENERAL DISCUSSION

Colloidal NPs were fabricated using the thermal decomposition method, which requires relatively moderate temperature and pressure conditions and yields particles with homogeneous structure, morphology, and composition. As introduced earlier in the first chapter, precursors decompose with increasing temperature, leading to the formation of monomers. Then, these monomers assemble to form small nuclei, which subsequently grow generating the NCs. The nucleation and growth process for the metallic alloys occurs within the range of 180 to 230°C, whereas a temperature of around 300°C is required to decompose phosphide precursors.

Besides temperature, these methods need four main components: (1) a solvent, (2) precursors, (3) capping agents/surfactants, and (4) reducing agents.

Alkylamines, specifically HAD (C16) and OAm (C18), were used as solvents due to their compatibility with a wide range of precursors, their high boiling points (above 320°C), and their roles as reducing and capping agents. HDA was initially employed in the synthesis of CoFeP but was later replaced by OAm in subsequent materials. Using OAM resulted in an improvement in particle monodispersity, and a more efficient washing step, as HDA solidifies at room temperature, causing aggregation of the final material.

ODE (a C18 alkene) was used as a solvent alongside alkylamines in the synthesis of CoFeP and PdH_{0.58}. It does not act as a reducing agent, thus minimizing this effect from the alkylamines. As a non-polar solvent, it helps in stabilizing hydrophobic ligands. Moreover, ODE can act as a surface passivating agent and stabilizing medium. However, ODE polymerizes at high temperatures, producing significant amounts of polymer on the surface of the NC, making it difficult to remove and potentially hindering the electrochemical reaction. For this reason, in the synthesis of Pd₂Sn_{0.8}P and NiSn_{0.6}, only OAm was used as the solvent.

Both organometallic complexes and inorganic salts have been utilized as metal precursors. In the synthesis of CoFeP, Fe and Co carbonyls were selected, resulting in the formation of

homogeneous and active particles for the OER. However, due to their high reactivity and sensitivity, they require highly careful handling and storage. For this reason, and because $\text{Ni}(\text{CO})_4$ is highly flammable and extremely toxic, the carbonyl was replaced by the $\text{Ni}(\text{acac})_2$ complex in the synthesis of Ni-Sn. For the Pd-based compounds, the acetylacetonate was also used as Pd precursor, as it has been reported to provide better control over the NCs morphology compared to the chloride or acetate salts. In contrast, both acetate and chloride were used as Sn precursors. While $\text{Sn}(\text{OAc})_2$ was added in the $\text{Pd}_2\text{Sn}_{0.8}\text{P}$ synthetic route, the SnCl_2 was used for the preparation of $\text{NiSn}_{0.6}$. The acetate, in the Ni-based synthesis, produces a dense SnO_2 shell surrounding the Ni-Sn core that hinders the active sites. As a phosphorus precursor, two compounds were employed. Firstly, TPOP was used for the CoFeP nanocrystals due to its stability under ambient conditions, which facilitates its manipulation and storage. However, in the synthesis of $\text{Pd}_2\text{Sn}_{0.8}\text{P}$, the P precursor was changed to HMPT. Although it must be stored under inert conditions due to its susceptibility to oxidation, HMPT offers greater reactivity and versatility than TPOP.

The capping agents provide control primarily over both the morphology and structure of the nanoparticles, as well as stabilize them preventing their aggregation. The particle size and shape can not only be regulated by changing the concentration of these reagents but also by varying the affinity of these complexes with the particle surface. For example, although the C_2N support influences $\text{PdH}_{0.58}$ growth, alkylamines act as capping agents in the production of both CoFeP and $\text{PdH}_{0.58}$ nanostructures. As a result, while nanorod-like shapes are obtained in the synthesis of CoFeP, nanodendrites are produced in the synthesis of $\text{PdH}_{0.58}$. On the other hand, TOP is added as a capping agent in the synthesis of $\text{Pd}_2\text{Sn}_{0.8}\text{P}$ and $\text{NiSn}_{0.6}$ particles due to its excellent ability to stabilize the particles. Various tests omitting TOP were carried out and large aggregates or highly heterogeneous particles were obtained. Furthermore, the introduction of various surfactants has been shown to influence morphology by preferentially binding to specific crystallographic faces. For instance, the addition of MAC in the $\text{Pd}_2\text{Sn}_{0.8}\text{P}$ synthesis produces NRs, due to chlorine ions inducing TOP desorption at the nanoparticle tip facets.

As previously mentioned, alkylamines are often playing the role of reducing agents, as in CoFeP, $\text{PdH}_{0.58}$ and $\text{Pd}_2\text{Sn}_{0.8}\text{P}$ synthetic routes. However, for the synthesis of $\text{NiSn}_{0.6}$, TBAB was introduced to accelerate the reduction of both Ni and Sn, facilitating the production of the alloy.

Once NCs were obtained, they were deposited on different supports. CoFeP NPs were deposited onto an NF support, offering high conductivity, high stability and large surface area. The main drawback of this support is that it requires careful coating because, unlike carbon supports,

nickel exhibits reactivity with certain compounds, including biomass derivatives. To avoid any potential effects from the NF, different carbon-based supports were used in the FOR and GOR. The PdH was supported, during synthesis, onto a 2D graphene-like C₂N. This material not only exhibits higher electrical conductivity compared to other C-N compounds, but the pores in the C₂N structure also have a higher electron density, making them excellent nucleation sites. The Pd₂Sn_{0.8}P NPs were deposited on CB offering low cost, high commercial availability, chemical stability, large surface area, and good conductivity. However, when preparing the NiSn_{0.6} catalyst for the GOR, it was decided to substitute CB with CNTs. CNTs possess a larger surface area, higher electrical conductivity, and a greater ability to provide anchoring sites compared to CB.

The electrochemical experiments were conducted under alkaline conditions, of 1M KOH, because at this pH the studied reactions are kinetically improved. The electrocatalysis of both the OER and the FOR was carried out in a three-electrode cell since the generated products, O₂ and CO₂, do not cause crossover. Although the FOR reaction may proceed via the indirect pathway, using Pd-based catalysts the CO is likely to be produced in very small amounts and mostly remain adsorbed on the electrode surface. In contrast, an H-type electrochemical cell was used for the GOR performance. As extensively discussed, as a result of the complex GOR process a wide range of soluble products can be generated, which can undergo reduction again onto the Pt surface.

The prepared catalysts have been applied in different reactions with two distinct objectives. Firstly, both CoFeP and PdH, as well as Pd₂Sn_{0.8}P, were studied in the OER and FOR reactions, respectively, aiming to achieve high catalytic activity for potential application in fuel cells. The modifications introduced in each compound resulted in an increase in current density in the voltammograms compared to analogous materials reported in the literature. Additionally, chronoamperometric studies revealed enhanced stability over time. In the FOR and GOR reactions, a noticeable decrease in activity was observed over time, attributed not necessarily to catalyst deactivation but rather to a reduction in formate concentration in solution. Hence, stability was evaluated in two ways: (1) through consecutive CV cycles and (2) through CA cycles, with the electrolyte replaced to monitor any progressive decrease in activity compared to the initial chronoamperogram.

The second main application of my work was the conversion of biomass derivatives into other high-value products. During the electrocatalysis of glucose, it has been important to not only assess the activity and stability of the catalysts but also to analyse the products obtained at various potentials. HPLC analysis has been employed to identify and quantify the different

compounds formed during the electrochemical reactions. This comprehensive analysis allowed us to gain insights into the selectivity and efficiency of the catalysts in promoting the desired transformations of biomass derivatives.

Transition metal-based compounds have demonstrated high activity for both the OER and GOR, with a FE exceeding 90% for formic acid in the latter reaction. However, it is noteworthy that Pd-based compounds still exhibit a significantly lower reaction potential. Therefore, it is essential to evaluate both the properties exhibited by the materials and the economic investment required for their applications and working conditions.

CONCLUSIONS

Throughout the thesis, various nanostructured materials with well-defined morphology and composition have been synthesized and applied to the OER and the oxidation of biomass derivatives such as formate and glucose. These catalysts have shown high activity and long-term stability, outperforming analogous materials. The development of these materials opens new avenues for innovation, enabling the exploitation of renewable and sustainable resources and reducing dependence on fossil fuels.

NPs with various morphologies and structures have been prepared using the thermal decomposition methods. By adjusting parameters such as temperature, reactants, and reaction times, optimal conditions have been established to produce highly active catalysts with minimal or no noble metal content. Specifically, using this colloidal method, it has been possible to introduce light elements (such as P and H) or alloy with other oxophilic metals (such as Sn), thereby modifying the performance and activity of the catalysts.

It has been determined the introduction of P increases the activity and stability of the catalysts through two mechanisms.

CoFeP particles have been synthesized, exhibiting a nanorod-like shape, and have been studied for the OER reaction. During the electrochemical study, it has been established that P acts as a sacrificial element for homogeneous metal oxyhydroxide distribution, which allows a high density of active sites.

On the other hand, using colloidal synthesis, palladium-tin phosphide particles have also been prepared, featuring a nanorod-like shape. In contrast to CoFeP, electrochemical studies using Pd₂Sn_{0.8}P for the FOR reaction show that phosphorus favours the desorption of CO₂, thereby reducing the energy barrier of the rate-limiting step

By tuning the experimental conditions, it has also been possible to introduce H into the Pd structure, improving the electrocatalytic properties of the noble metal. The results demonstrate that H causes an expansion of the Pd lattice and an electronic reconfiguration within the material, enhancing both activity and stability. Similarly to phosphorus in Pd₂Sn_{0.8}P, H weakens the adsorbate binding, thus accelerating the rate-limiting step.

On the other hand, it has been established that the incorporation of oxophilic metals is another appropriate strategy to increase the electrocatalytic efficiency of Ni-based compounds. The

kinetics of the GOR reaction are favoured once Sn is introduced, although the activity is related to the amount of nickel present in the NPs.

FUTURE WORK

After the thesis has been completed, it is considered that the objectives set at the beginning have been achieved. However, it is important to recognize that these were specific objectives, established based on the time, knowledge, and resources available throughout the project. Science, in this sense, is a continuous effort that extends beyond individual work, encompassing collaboration within the community.

As discussed in the different sections, the initial objective was to contribute to the research and development of materials for the exploitation of biomass derivatives, to use more environmentally sustainable compounds and technologies. In this regard, compounds such as $\text{Pd}_2\text{Sn}_{0.8}\text{P}$ and $\text{PdH}_{0.58}$ have been produced, optimizing the use of noble metals. Additionally, compounds like $\text{NiSn}_{0.6}$ and CoFeP have been developed, utilizing abundant and inexpensive materials, and improving the performance of multiple compounds based on more expensive or toxic elements.

Nonetheless, this work also aims to serve as a starting point and a modest inspiration for future projects, as there are still aspects left to be further developed or investigated more extensively.

Various materials have been applied to these three reactions OER, FOR, and GOR, due to their advantages and the demonstrated importance in both energy production and the generation of key compounds for industry. However, as shown in the first chapter, numerous biomass-derived compounds can be transformed into others with higher value or used as electron sources. For this reason, one of the upcoming objectives should be to apply the developed catalysts to other biomass-derived compounds such as furans, amino acids, or even other sugars and carboxylic acids, and observe the activity towards the oxidation reaction along with the efficiency of the obtained products.

Secondly, closely linked to the projects conducted in this thesis, some aspects should be further pursued in the future:

- Firstly, continuing the study of Pd-based materials for the FOR, these materials should be applied in flow cells, which are more suitable for subsequent scale-up and application. In flow cells, there are other factors to consider, such as flow rate or whether the flow passes through the sample or not, but it is interesting to examine due to higher current density values are usually obtained due to more efficient contact between the catalyst and the electrolyte.

- Another aspect to consider is the application of the materials in flow cells. As discussed in various chapters, the produced materials have improved current densities compared to analogous catalysts reported in the literature. However, the study conducted thus far has been in a standard three-electrode electrochemical cell. Therefore, it is intriguing to observe the electrical energy produced in fuel cells and determine if these materials can truly be competitive.
- In the third place, an in-situ study of the various materials during the electrochemical reaction should be considered. These studies can be particularly interesting for phosphides. On one hand, it has been observed that during the OER, CoFeP reacts in a controlled manner to form the active oxyhydroxide species. On the other hand, phosphides significantly enhance the activity of the FOR compared to their phosphorus-free analogues, and it would be valuable to study the exact reaction mechanism to better understand and further optimize the various parameters. Additionally, as discussed, the GOR is a complex reaction that can follow different pathways. In situ characterization can help discern the mechanism by which NiSn_{0.6} oxidizes glucose in this reaction, allowing for a better understanding of the process.

Finally, another aspect to consider for future work is the reduction of CO₂. The consumption of biomass for energy production is considered carbon-neutral because the CO₂ generated is equivalent to the amount captured during the growth of the biomass precursor species. However, in recent years, research has been focusing on the electrochemical reduction of CO₂ to transform it into species such as formic acid, methanol, or ethanol, which can be used in fuel cells. To this end, we are researching the application of single metal atom materials as cathodes for the transformation of CO₂ into formic acid, to recycle the CO₂ produced in liquid fuel cells. Nevertheless, optimizing the electrochemical results and achieving a more comprehensive characterization of the materials are necessary. Moreover, we are also currently working on using NiSn_{0.6} and Cu_xSn NPs for this reaction, with FA being obtained as the product with higher faradaic efficiency.

CURRICULUM VITAE



Passionate, competitive, reflexive, persistent and constant. Person with teamwork skills, organized and with a huge desire to learn and to grow up personally and professionally.

Personal Information

Guillem Montaña Mora

Sant Joan Despí (Barcelona)

+34 671 64 95 07

guillemmonmora@gmail.com

03-1994

Education

2020 - 2024: PhD in Nanoscience and Nanotechnology - Institut de Recerca en Energia de Catalunya (IREC) and Institute of Science and Technology Austria (IST Austria). Synthesis of new materials applied in electrochemical systems for the biomass conversion.

2020 – 2021: Postgraduate Course in Technology transfer: from scientific knowledge to the markets at the University Pompeu Fabra Barcelona School of Management

2017 – 2018: Master of Materials Applied Chemistry at the Universitat de Barcelona – Department of Chemistry and Physics.

2016: Chemical degree at the Universitat de Barcelona - Department of Chemistry and Physics.

Languages

Catalan: Native or bilingual proficiency.

Spanish: Native or bilingual proficiency.

English: Advance (CAE)

2017: C1 level studies at Merit School.

First Certificated (FCE).

2016: Optional subjects cursred in English in the Chemical degree.

English studies in Dublin

Experience

2024: Technical consultant at Zabala innovations

2019 and 2021: Researcher at IST Austria (Klosterneuburg, Austria) working on the electrocatalytic reduction of CO₂.

2019: Researcher at the Universitat de Barcelona specializing in the synthesis and characterization of metal and semiconductor nanomaterials.

2018 - 2019: Research and development technician at *Industrias Químicas del Vallés, S.A.* (R&D department), executing projects focused on scaling up, optimizing, and developing industrial processes for copper salts at pilot plant scale, followed by their subsequent study

2017: Researcher at the Universitat de Barcelona synthesizing and studying binary, ternary, and complex nanoheterostructures of noble metal chalcogenides in solution .

2016 - 2017: Research assistant at *Industrias Químicas del Vallés, S.A.* (IQV) working on an R&D project aimed at optimizing and developing industrial processes for copper salts.

2016: Final degree project at the Organic Department (Universitat de Barcelona), focusing on the synthesis and characterization of luminescent compounds.

2013 - 2016: 600 hours of practical laboratory (Universitat de Barcelona) throughout the degree at the Department of Chemistry and Physics.

2015: Internship at the Department of Inorganic Chemistry (Universitat de Barcelona).

2011: Internship at the Department of Inorganic Chemistry (Universitat Autònoma de Barcelona) - Programa Argó.

Articles participation

2024: Oxophilic Sn to promote glucose oxidation to formic acid in Ni nanoparticles

2024: Improved Mn⁴⁺/Mn²⁺ Contribution in High-Voltage Zn–MnO₂ Batteries Enabled by an Al³⁺-Ion Electrolyte

2024: Enhanced electrochemical hydrogenation of benzaldehyde to benzyl alcohol on Pd@ Ni-MOF by modifying the adsorption configuration.

2023: Palladium hydride on C₂N to boost formate oxidation.

2023: Cobalt–Iron oxyhydroxide obtained from the metal phosphide: A highly effective electrocatalyst for the Oxygen Evolution Reaction at high current densities.

2023: Phosphorous incorporation into palladium tin nanoparticles for the electrocatalytic formate oxidation reaction.

2022: Spontaneous hetero-attachment of single-Component colloidal precursors for the synthesis of asymmetric Au–Ag₂X (X = S, Se) heterodimers.

Project Participation

Carboformic: Atmospheric CO₂ transformation into clean and renewable energy carrier

Uncorrelated: Solid-liquid thermoelectric systems development with uncorrelated properties to improve heat-to-electricity conversion efficiency.

Technical Skills

Pack Microsoft office

Transmission electron microscopy, Scanning Electron Microscopy and Energy-dispersive X-ray spectroscopy. X-ray diffraction.

Gas and Liquid chromatography.

UV-Vis and Fourier-transform infrared Spectroscopy

Electrochemical skills

COLLECTION OF PUBLICATIONS PRESENTED IN THIS
THESIS

Cobalt–Iron Oxyhydroxide Obtained from the Metal Phosphide: A Highly Effective Electrocatalyst for the Oxygen Evolution Reaction at High Current Densities

María Isabel Díez-García,* Guillem Montaña-Mora, Marc Botifoll, Andreu Cabot, Jordi Arbiol, Mohammad Qamar, and Joan Ramon Morante

Cite This: *ACS Appl. Energy Mater.* 2023, 6, 5690–5699

Read Online

ACCESS |

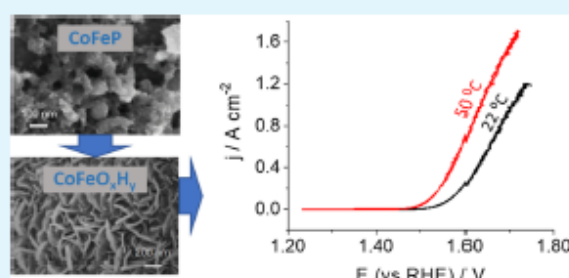
Metrics & More

Article Recommendations

Supporting Information

ABSTRACT: The development of high current density anodes for the oxygen evolution reaction (OER) is fundamental to manufacturing practical and reliable electrochemical cells. In this work, we have developed a bimetallic electrocatalyst based on cobalt–iron oxyhydroxide that shows outstanding performance for water oxidation. Such a catalyst is obtained from cobalt–iron phosphide nanorods that serve as sacrificial structures for the formation of a bimetallic oxyhydroxide through phosphorous loss concomitantly to oxygen/hydroxide incorporation. CoFeP nanorods are synthesized using a scalable method using triphenyl phosphite as a phosphorous precursor. They are deposited without the use of binders on nickel foam to enable fast electron transport, a highly effective surface area, and a high density of active sites. The morphological and chemical transformation of the CoFeP nanoparticles is analyzed and compared with the monometallic cobalt phosphide in alkaline media and under anodic potentials. The resulting bimetallic electrode presents a Tafel slope as low as 42 mV dec⁻¹ and low overpotentials for OER. For the first time, an anion exchange membrane electrolysis device with an integrated CoFeP-based anode was tested at a high current density of 1 A cm⁻², demonstrating excellent stability and Faradaic efficiency near 100%. This work opens up a way for using metal phosphide-based anodes for practical fuel electrosynthesis devices.

KEYWORDS: cobalt iron phosphide, nanorods, anode, nickel foam, oxyhydroxide, anion exchange membrane



INTRODUCTION

The production of fuels by electroconversion coupled with renewable sources is one of the backbones of a sustainable energy future. In most of these systems, such as the electrosynthesis of H₂, NH₃, or CO₂ reduction products, the corresponding cathodic reaction is usually coupled to the oxygen evolution reaction (OER). Nevertheless, OER is the most sluggish reaction in the overall process, and its complexity derives from the four reaction steps associated with this reaction. Consequently, a rational design of the anode requires strategies for overcoming this drawback. The use of multi-metallic catalysts is advantageous as they can provide appropriate metallic sites for achieving a more effective reduction of the energy barriers associated with each reaction step.^{1,2} To this end, a dispersion of metallic atoms with adjacent locations in the electrode frame and skeleton should be ensured to achieve an adequate density of active sites to reach high production rates. Furthermore, this rational design of the anode must take into account its electrical conductivity to guarantee adequate electron transport, the mass transport to or from the active sites to prevent diffusion limitations, and

also the kinetics associated with the reactions taking place in the active site.

The use of metal oxides as electrocatalysts generally has the limitation of their low conductivity. Among the alternative compounds reported, transition metal phosphides (TMPs) are excellent candidates as some of them present metallic-like properties and exhibit much higher conductivities³ than the corresponding metal oxides. TMPs have attracted much interest as electrocatalysts for water splitting for both half-reactions, hydrogen evolution reaction (HER) and OER.^{1,4–7} In this context, cobalt, iron, and the corresponding bimetallic phosphides have been reported as electrocatalysts for the OER, displaying low overpotentials.^{1,7,8} So far, most of these studies have been focused on the electrocatalytic activity at low and

Received: January 5, 2023

Accepted: April 17, 2023

Published: May 25, 2023



medium currents ($10\text{--}50\text{ mA cm}^{-2}$), while working at high current densities, $>1\text{ A cm}^{-2}$, has barely been studied despite its relevance concerning the demonstration of industrial feasibility. For achieving such high production rates, more attention must be paid to different features such as high active site density, high turnover frequency (TOF), and efficient mass transport of the chemical species from and toward the electrocatalysts to optimize the reaction overpotentials.

However, most transition metal compounds are not stable under the oxidizing conditions of OER, and the influence of the chemical transformation of these materials in the catalytic reaction should be considered.^{8–11} Usually, metal (oxy)-hydroxides are generated in situ at the surface of oxides, selenides, or even phosphides.^{3,9,10,12–14} In some cases, the transformation is not only limited to the surface and also affects the electrocatalyst bulk, which could be detrimental if the new material possesses low conductivity. A detailed analysis of the material conversion and the role of the non-metallic element need to be faced for a complete rational design of the anode. Metal (oxy)hydroxides are well known to have a high electrocatalytic performance, providing highly active sites for OER,^{9,15–17} especially those containing Fe, Co, or Ni.^{18–20} In fact, for these materials, the combination of Fe with Ni or Co has led to improved activity.²¹ The enhancement of the electrochemical activity for OER in bimetallic CoFe-based electrocatalysts compared with the corresponding monometallic compounds has also been corroborated by observing a decrease in the overpotentials.^{9,22–24} This is a critical aspect in the design of the anodes for achieving commercially viable electrolyzers for fuel production.

In this work, we report on a detailed investigation of CoFe bimetallic phosphide and the transformation mechanism in alkaline electrolyte leading to high-performance anodes for OER at high current densities, $>1\text{ A cm}^{-2}$. The rational procedure to prepare the electrodes involves as the first step the synthesis of tiny nanorods mainly composed of CoFeP. They are obtained by a “heating up” process using triphenyl phosphite (TPOP) which is advantageous against other phosphorous precursors because it is air-stable and inexpensive.²⁵ A nickel foam (NF) substrate has been selected as a 3D scaffold of the electroactive material because of its high conductivity and porous structure. The simplicity of the method employed for loading the electrocatalyst should be highlighted because of its potential scalability and the fact that no additives or heat treatments are used. The CoFeP/NF electrodes were characterized from a morphological, structural, physicochemical, and functional point of view before and after OER in alkaline electrolyte. The most significant results concern the depletion of phosphorus (linked to the formation of CoFe oxyhydroxide) and the radically different morphology between the initial nanorod-like shape found in the CoFeP powder and the nanoplate-like shape of the oxyhydroxide after OER. All of these characteristics allow a rational design of the anode for working at high current densities. Then, the effectivity of the proposed strategy for the anode design is tested for reaching 1 A cm^{-2} for OER. The significance of the transformation of the bimetallic phosphide into a bimetal oxyhydroxide and the role played by phosphorus have been analyzed.

EXPERIMENTAL SECTION

Synthesis of Colloidal CoFeP Nanoparticles. For the synthesis of the CoFeP nanoparticles,²⁶ 2.4 g (10 mmol) of 1-hexadecylamine (HDA, 90%, Acros Organics) was mixed with 10.0 mL of 1-octadecene (ODE, 90%, ACROS Organics) and 2.6 mL (10 mmol) of TPOP (99%, ACROS Organics) in a 50 mL flask. The system was degassed, heated to $130\text{ }^{\circ}\text{C}$, and kept at this temperature for 1 h to remove low boiling point impurities, moisture, and oxygen. Then, the mixture was cooled down to $60\text{ }^{\circ}\text{C}$, and 4 mL of ODE containing 380 mg (1 mmol) $\text{Co}_2(\text{CO})_8$ (95%, ACROS Organics) and 0.3 mL of (2 mmol) $\text{Fe}(\text{CO})_5$ (Sigma-Aldrich) were added. First, the temperature was increased to $230\text{ }^{\circ}\text{C}$, and then, the mixture was stirred for 30 min. Second, the mixture was heated to $300\text{ }^{\circ}\text{C}$ for 40 min and kept at this temperature for 1 h. Finally, the system was allowed to cool down to $200\text{ }^{\circ}\text{C}$ by removing the heating mantle and subsequently cooled rapidly down to room temperature with a water bath. The product was precipitated using acetone and centrifuged for 3 min at 7500 rpm. To remove organics, three dispersion and precipitation cycles using chloroform and acetone were additionally carried out to obtain a cleaner CoFeP precipitate. To synthesize the Co_2P nanoparticles used as the reference material, an identical procedure was followed but without adding the iron precursor.

Ligand Removal. 10 mL of a dispersion CoFeP or Co_2P in hexane (10 mg mL^{-1}) was mixed with 10 mL of acetonitrile to form a two-phase mixture. Afterward, 1 mL of HBF_4 solution (48%) was added. The resulting solution was sonicated until the nanoparticles transferred from the upper to the bottom layer. Finally, these nanoparticles were washed with ethanol three times and dispersed in 10 mL of ethanol with around 0.5 mL of *N,N*-dimethylformamide for further use.

Electrode Preparation. NF substrates were cleaned in an ultrasonic bath in 1 M HCl, water, and ethanol for 10 min in each one. A suspension of 10 mg mL^{-1} of the CoFeP nanoparticles in ethanol was sonicated for 30 min. The cleaned NF substrates were dipped into this suspension for 30 s, and subsequently, the excess dispersion was removed. Finally, the electrode was dried at ambient temperature. The deposited amount of catalyst used for the objective of this work was estimated to be enough to guarantee enough active site density $>10^{18}\text{ cm}^{-2}$ to facilitate reaching a current density higher than 1 A cm^{-2} . Electrodes with a higher amount of electrocatalyst have been prepared by repeating the immersion and drying steps up to four times. Unless otherwise stated, the electrodes were prepared with a single immersion, and the samples named “after OER” were previously subjected to a current density of ca. 120 mA cm^{-2} for 2 h.

Morphological, Structural, and Physicochemical Characterization. Structural characterization was performed by X-ray diffraction (XRD) using a Bruker D8 Advance diffractometer equipped with a $\text{Cu K}\alpha$ (1.5406 \AA) radiation source, LYNXEYE super speed detector, and Ni filter. A Bragg–Brentano (θ – 2θ) configuration was used with a step size of 0.025° . The morphology of the electrodes was analyzed by a Zeiss Auriga 60 field emission scanning electron microscope (FESEM). Both the high-resolution transmission electron microscopy (HRTEM) and scanning transmission electron microscopy (STEM)–electron energy-loss spectroscopy (EELS) are obtained in an FEI F20 at 200 kV. The HRTEM was acquired with a condenser aperture of $100\text{ }\mu\text{m}$, no objective aperture, spot size 3, and a BM-UltraScan CCD camera. The STEM–EELS was acquired with a condenser aperture of $70\text{ }\mu\text{m}$, no objective aperture, nominal camera length 30 mm , spot size 6, and Gatan EF-CCD camera. The same conditions apply for STEM–energy dispersive X-ray (EDX), with a detector EDAX super ultra-thin window X-ray detector, 136 eV resolution ($Z > Z(\text{Be})$), and a detector area of 30 mm^2 . The EELS and EDX supporting STEM images are obtained using an annular dark field detector (DF4). For analyzing the samples, the initial CoFeP or Co_2P samples were diluted in hexane before deposition on the grid. For the analysis of the electrode after OER, the electrocatalyst was scraped from the NF substrate, and the resulting powder was dispersed in hexane by sonication before the deposition on the grid. For the X-ray photoelectron spectroscopy

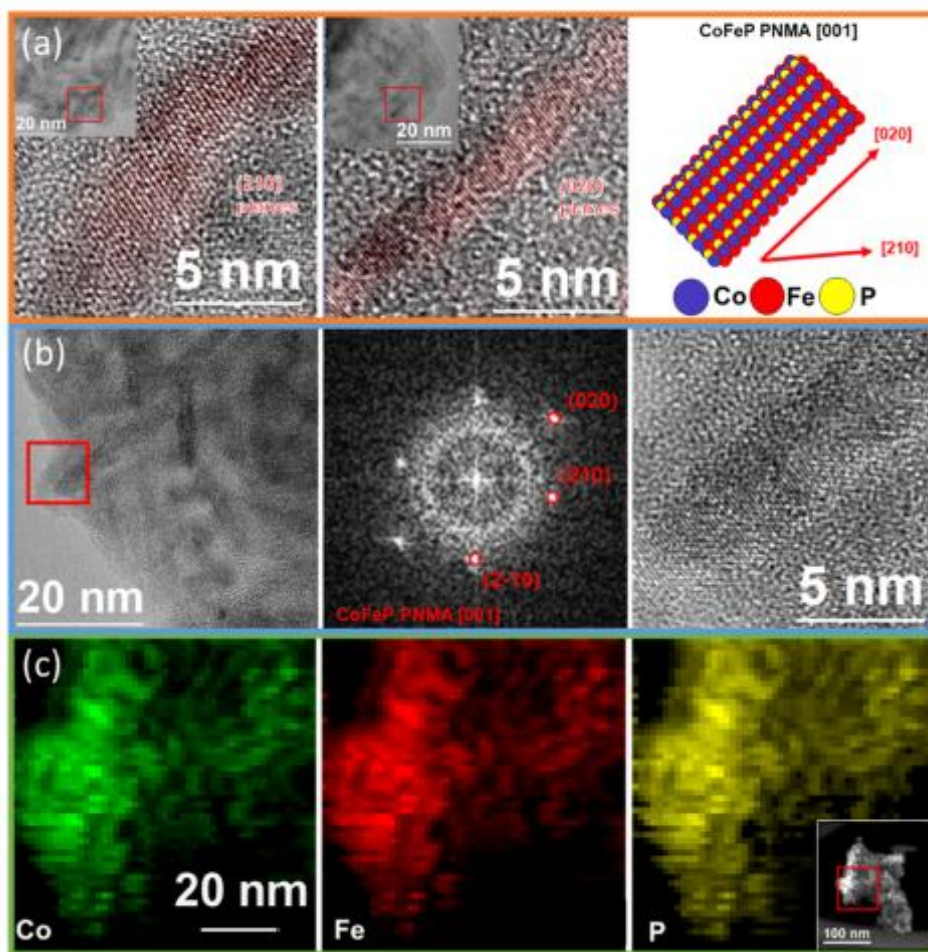


Figure 1. (a) HRTEM images showing individual nanorods (from the red squared region in the lower magnification images in the inset) and the schematic illustration of the orientation of the nanorods on the right side. (b) FFT spectrum corresponding to the HRTEM image of a CoFeP nanorod on the right that corresponds to the red squared region of the image on the left. (c) EELS compositional maps of Co, Fe, and P in CoFeP nanorods. The inset shows the corresponding STEM-ADF image.

(XPS) analysis, a monochromatic X-ray source Al $K\alpha$ line was used in both a PHI 5500 Multitechnique System (Physical Electronics) for the electrodes before OER and a NEXSA X-ray photoelectron spectrometer (Thermo-Scientific) for the electrodes after OER.

Electrochemical Measurements. The electrochemical performance of the CoFeP-based electrodes was analyzed with a Biologic VMP-300 potentiostat using a three-electrode cell. All the potentials were measured against an Ag/AgCl reference electrode. The potentials in the RHE scale are calculated according to $E(\text{vs RHE}) = E(\text{vs Ag/AgCl}) + 0.205 \text{ V} + 0.059 \cdot \text{pH}$. To evaluate the OER activity, linear sweep and cyclic voltammeteries were performed at a scan rate of 5 mV s^{-1} in 1 M KOH. All the potentials were corrected with the IR drop, and the corresponding resistance (R) was determined by electrochemical impedance spectroscopy (EIS). The overpotentials were calculated in all cases as $\eta = E - 1.23 \text{ V}$, where E is the applied potential vs RHE. The determination of double-layer capacitance (C_{dl}) by cyclic voltammeteries was performed between 0.1 and 0.2 V vs Ag/AgCl, a potential region with no faradaic processes, at different scan rates. The electrochemically active surface area (ECSA) was calculated as C_{dl}/C_{ref} , where C_{ref} is a reference capacitance for a planar surface taken as $40 \mu\text{F cm}^{-2}$.^{27,28} Nyquist plots were obtained by EIS in the frequency range of 50 kHz to 100 mHz and employing a signal amplitude of 10 mV. The fitting of the experimental EIS curves to the equivalent circuit was performed

with the Biologic software. The calculation of the TOF can differ from study to study.²⁷ In this work, TOF is calculated as the number of product molecules (O_2) per second and active site: $\text{TOF} = jA/(4Ne)$, where j is the current density, A is the area, N is the number of active sites, and e is the elementary charge constant ($1.6 \times 10^{-19} \text{ C}$). The calculated number of active sites is 3.2×10^{18} and 2.3×10^{18} for CoFeP and Co_2P , respectively. They are estimated considering that both Co and Fe metallic atoms act as active sites. The metallic content was calculated by the difference of the electrode mass after and before the electrocatalyst loading and the elemental ratios obtained by EDX in the as-prepared electrodes. In the full cell assembly, water splitting was performed in a two-electrode configuration with the two compartments separated by a Sustainion (Dioxide Materials) alkaline exchange membrane. The gas outlets from the anodic and cathodic compartments were connected to two inverted graduated cylinders filled with water to measure accumulated O_2 and H_2 , respectively. For the theoretical calculation of the volumes, they are considered ideal gases. The presence of H_2 was corroborated by gas chromatography using He as a carrier gas.

RESULTS AND DISCUSSION

Characterization of the CoFeP Nanoparticles and the Fabricated CoFeP/NF Electrode. The bimetallic CoFeP

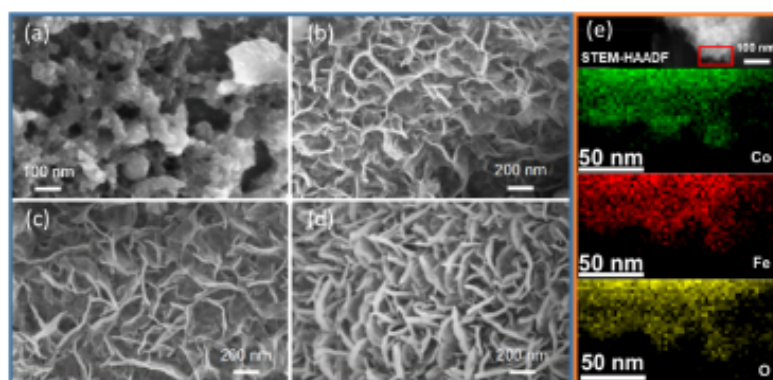


Figure 2. SEM micrographs showing the morphology of the (a) as-prepared and after (b) 5, (c) 30, and (d) 120 min of OER for a CoFeP/NF electrode. (e) EELS compositional maps of the powder obtained by scraping the electrocatalyst from the electrode surface of the CoFeP/NF electrode after 120 min of OER.

nanoparticles obtained by the TPOP route were characterized in terms of morphology, crystallinity, and composition. HRTEM images were recorded to obtain information about the nanostructure morphology. Figures 1a,b and S1 show the synthesized CoFeP nanoparticles exhibiting a nanorod-like shape with a length up to about 18 nm and a diameter of 2–4 nm. FFT (fast Fourier transform) in Figure 1b reveals the presence of the CoFeP PNMA 62 phase that is according to the XRD analysis in Figure S2. Importantly, the planes observed in isolated nanorods (Figure 1a) can be ascribed to the (020) and (210) planes of CoFeP PNMA. Figure 1a shows a sketch of the nanorod crystallographic arrangement. It was observed that these rods present a growth direction [010] (and its corresponding (020) observed planes), which coincides with the longitudinal axis of the nanorods, which is further supported by its relative orientation with the resolved (210) planes of CoFeP. Additionally, EELS compositional maps of Co, Fe, and P were also performed to get insights into the nanostructure composition. Figure 1c shows a particle composed of the coalescence of different nanorods. A similar spatial distribution of the three elements along all the particles was found, coherent with the expected stoichiometry of the CoFeP. Nevertheless, EELS quantification reveals a slightly higher concentration of Co against Fe, Co/Fe \approx 1.5. Monometallic Co₂P nanoparticles were also analyzed by HRTEM. They also exhibit rod-like shapes (Figure S3), having similar sizes to the bimetallic nanorods. The planes found have similar interplanar distances to that of CoFeP and are according to the Co₂P PNMA, which was further corroborated by FFT (Figure S4). As in the case of CoFeP, Co and P are homogeneously distributed through the Co₂P nanorods as revealed by EELS (Figure S5). In both CoFeP and Co₂P nanoparticles, the metal to phosphorous ratio, based on the atomic concentration obtained by EDX, was near 1.3, which is lower than the stoichiometric. This can be partly due to the presence of oxygenated species such as metal phosphates or the presence of CoP as a secondary phase.

XPS is used to gather information about the first fourth or sixth atomic monolayers (2–3 nm) at the sample surface. This has been employed to characterize the surface composition and chemical nature of the synthesized electrocatalyst, although it can be altered by the interaction with the ambient air after its deposition on the NF. The full survey spectrum of a bare CoFeP/NF electrode shown in Figure S6 reveals the presence of Co, Fe, P, O, and C. In the P 2p spectra (Figure S7), the

largest peak is located near 133.3 eV and can be correlated with the presence of phosphate species.^{9,10} This confirms that the surface of the electrocatalyst is composed of a metal phosphate rather than a phosphide after air exposure, which usually occurs in metal phosphides.^{15,23} The Co 2p spectrum in Figure S7 exhibits the 2p_{3/2} and 2p_{1/2} signals with the overlapping of different contributions including satellite peaks. The fact that the position of the strongest peak in the Co 2p_{3/2} region (781.2 eV) was higher than the typical peak positions of metal oxides, together with the predominant peak in the O 1s region at 531.1 eV (Figure S7), is in agreement with the presence of metal phosphate.^{29,30} The small peak located at 778.1 eV in Co 2p_{3/2} could be assigned according to some authors to the presence of metal phosphides, although the corresponding Co 2p_{1/2} signal is challenging to be identified probably because of the small amount of phosphide detected at the surface.^{9,24} Accordingly, a very small peak at 130.1 eV in the P 2p spectrum can be attributed to metal phosphide. The Fe 2p_{3/2} signal (Figure S7) revealed the presence of oxidized iron species.⁹ Therefore, the results from the XPS characterization indicate that the outer layer of the electrocatalyst surface shows a transformation from metal phosphide to phosphate, even when the samples were stored in a protective atmosphere before the analysis.

Characterization of the CoFeP-Based Electrodes as Anodes for OER. Metal phosphides can be unstable in alkaline media (1 M KOH) under anodic conditions, and then a detailed physicochemical characterization was performed before and after OER to study the material transformation and especially the role of phosphorous. Despite the transformation, the electrodes were stable for OER, and any significant decay of the current was observed at about 100 mA cm⁻² (Figure S8). Figure 2a–d shows the morphology of the CoFeP nanostructures on the NF surface before and after OER by FESEM images. The small particle size of the CoFeP nanorods favors a good dispersion of the electrocatalyst on the NF surface. In the as-prepared electrodes, a porous network of interconnected nanoparticles with spherical shape is observed (Figure 2a), probably derived from the coalescence of the initial CoFeP nanorods observed in Figure 1a and the oxidation of the surface leading to an outer metal phosphate layer. The CoFeP/NF electrodes were analyzed after chronoamperometries at different times selecting a potential in the OER region with a current density near 100 mA cm⁻². A radical change of the overall morphology was observed (Figure

2b–d) after OER, now displaying nanostructures with a plate-like shape resembling 2D units and thus conferring high effective area to the electrode. However, there was no significant evolution of the morphology from 5 to 120 min of OER. The approximate dimensions of the nanoplates are 200–400 and 10–40 nm in length and thickness, respectively. For comparison purposes, the Co₂P/NF electrodes were also analyzed by SEM before and after OER (Figure S9). A similar morphological change was observed after 120 min of OER, although in this case, the nanoplates were smaller with an approximate length of 60 nm and a thickness of 10 nm.

Despite the huge transformation of the material, a homogeneous distribution of Co and Fe is observed in the EELS maps as shown in Figure 2e. Remarkably, we could not observe any presence of crystalline planes in the HRTEM images neither in the corresponding FFT patterns obtained in the samples after OER, pointing out the amorphous nature of the transformed material. Furthermore, the high oxygen signal together with the absence of phosphorous suggests that oxygenated phases as oxygen and hydroxyl groups have replaced the initial phosphide/phosphate species forming oxyhydroxide structures. To further investigate these assumptions, high-resolution XPS spectra shown in Figures 3 and S10

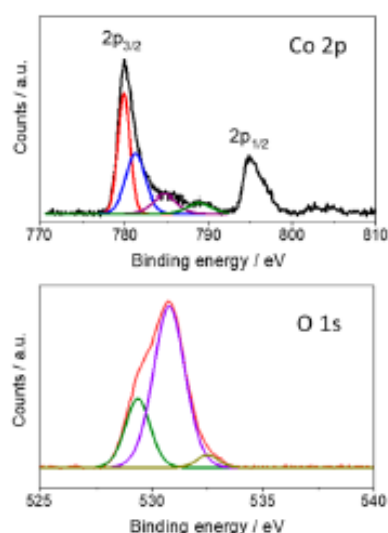


Figure 3. XPS spectra in the Co 2p and O 1s regions for the CoFeP/NF electrodes after OER.

in the electrodes after OER are compared with the previous results using fresh samples (Figure S7). To increase the intensity of the XPS signal, the analysis was performed in a sample synthesized by four immersions in the iron precursor dispersion. We must stand out on several significant features. On one hand, there is a low concentration of residual phosphorous at the surface (see Table S1). On the other hand, a significant change in the O 1s spectrum is noticeable after OER (Figure 3). Apart from the peak around 532.5 eV that can be attributed to absorbed H₂O, the main signal can be deconvoluted into two peaks. The one at 529.4 eV is according to M–O and the largest peak at 530.8 eV would correspond to M–OH species supporting the presence of metal oxyhydroxides.¹⁵ These characteristics are endorsed for the measured spectra of Co 2p and Fe 2p shown in Figures 3, S7, and S10, in which the most intense peaks in the 2p_{3/2} signals are shifted to lower energies in agreement with the

expected values of oxyhydroxides compared to the initial phosphates. Therefore, after the electrochemical measurements in alkaline media, the material is transformed in terms of morphology and composition from the initial CoFeP to CoFeO_xH_y. After immersing in the 1 M KOH solution, a morphological change occurs; afterward, the cyclic voltammogram of the CoFeP (Figure S11) shows an anodic irreversible peak appearing at 1.35 V vs RHE that is only present in the first cycle. This peak has been attributed to the irreversible evolution of CoOOH.^{19,31,32} Accordingly, a peak near the same potential region was also observed in the Co₂P/NF electrodes. After this anodic peak, the current densities for OER remain constant, as evidenced by the overlapping of the first and second voltammetric curves shown in Figure S11. The complete morphological transformation of the CoFeP structure together with the phosphorous loss leading to CoFeO_xH_y is favored by the small size of the initial nanoparticles and the interconnected porous network formed by these nanoparticles that facilitate the permeability of the alkaline electrolyte. Raman analysis shown in Figure S12 supports the presence of metal oxyhydroxide. Concretely, the bands at 575 and 675 cm⁻¹ can be correlated with cobalt and iron oxyhydroxides,^{33–35} although the presence of oxides/hydroxides as secondary phases cannot be discarded. On the other hand, Co₂P/NF electrodes were also analyzed by XPS after OER (Figure S13). No differences in the oxidation states of cobalt with respect to the bimetallic material are observed, as the Co 2p region presents the same characteristics.

Electrochemical Analysis of the Electrodes Fabricated Using CoFeP as the Electrocatalyst. The electrochemical activity of the initial bimetallic CoFeP/NF transformed to CoFeO_xH_y/NF has been investigated in a 1 M KOH electrolyte. Figure 4a shows the cyclic voltammograms after IR correction for the CoFeP/NF electrode, compared with both the Co₂P/NF electrode and the bare NF scaffold. The bimetallic CoFeP/NF electrode presents the best catalytic activity for OER, outperforming the monometallic Co₂P/NF. The overpotentials for OER at 10 and 100 mA cm⁻² are 285 and 335 mV for CoFeP/NF and 345 and 410 mV for Co₂P/NF, respectively. The bare NF also presents electrochemical activity for OER in alkaline media^{36–38} but significantly lower than the bimetallic phosphide-loaded electrodes. The Tafel representation depicted in Figure 4b further confirms the favorable OER kinetics in the bimetallic electrocatalyst. The Tafel slope for Co₂P/NF is 53 mV dec⁻¹, while for CoFeP/NF, it is as low as 42 mV dec⁻¹. To the best of our knowledge, the latter value is the lowest reported for cobalt iron phosphide-based anodes without using a hybrid material (as compared in Table S2). Additionally, the behavior of the CoFeP/NF electrodes was tested during cycling for OER displaying good stability after 500 cycles (Figure S14).

Electrodes with different deposited amount of electrocatalysts were prepared by repeating different cycles of immersion in the CoFeP dispersion and drying up to four times, leading to different catalyst loading (see the inset of Figure S15a). The applied potentials for a given current density are reduced as the catalyst loading increases as expected. For 10 mA cm⁻², the overpotential is 270 mV for four immersions, 15 mV lower than for the one of a single immersion (Figure S15a). However, as the catalyst loading increases, the current density normalized by the mass loading decreases (Figure S15b). Then, for the lowest loaded amount of catalyst, there is an optimum dispersion of the CoFeP on

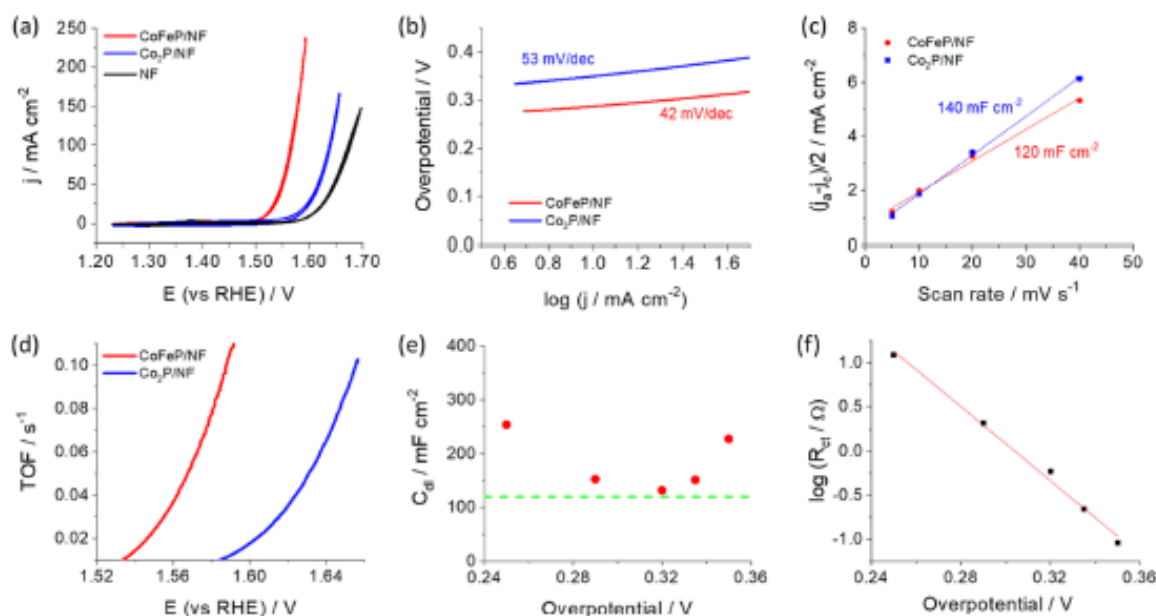


Figure 4. (a) Cyclic voltammogram recorded at 5 mV s^{-1} , (b) Tafel plots, (c) $(j_a - j_c)/2$ vs scan rate plot, and (d) calculated TOF values as a function of the potential for CoFeP/NF and Co₂P/NF in 1 M KOH. (e) C_{dl} and (f) $\log(R_{ct}/\Omega)$ vs overpotential from the Nyquist plots for CoFeP/NF in 1 M KOH. The green line in (e) indicates the C_{dl} value obtained from cyclic voltammograms in (c) and the red line in (f) the linear fitting.

the NF maximizing the number of reactive sites available per overall amount of catalyst. The overpotentials achieved in this work, considering the loaded amount of electrocatalyst, are one of the lowest reported for CoFeP-based anodes for OER (see Table S2).

To get more insights into the origin of the catalytic activity of CoFeO_xH_y obtained from the bimetallic phosphide, the double-layer capacitances were calculated from $(j_a - j_c)/2$ vs the scan rate plot obtained from Figure S16. The calculated C_{dl} values are similar for the CoFeP/NF and Co₂P/NF and are estimated as 120 and 140 mF cm^{-2} , respectively, as shown in Figure 4c. Then, the ECSA values of 3000 and 3500 cm^2 are obtained for CoFeP/NF and Co₂P/NF, respectively, referred to a planar surface. The huge ECSA values can be correlated with a high density of active sites due to good dispersion of the material favored by its low particle size and the porous structure of the electrode scaffold that allow the full penetration of the electrolyte.

Figure 4d displays TOF values deduced from the calculated number of active sites based on the loaded amounts of electrocatalysts. A TOF value of 0.1 s^{-1} is reached at 358 mV for the CoFeP/NF, while for Co₂P/NF, 425 mV is required. This demonstrates that despite both electrodes possessing similar ECSA and estimated number of active sites, the bimetallic phosphide exhibits a faster kinetic toward OER. This may be caused by the catalytic effects of the metallic Co and Fe adjacent sites cooperating on the four steps of the water oxidation reaction. This is supported by the lower value of Tafel slope in the CoFeP/NF electrode. In this regard, some decrease in the concentration of iron in the fabricated CoFeP nanoparticles is not critical in the OER activity, as when it decreases by 40%, the bimetallic electrode produces similar overpotentials. This is in agreement with a previous work using comparable Co/Fe ratios.¹⁵ A contribution derived from the

nickel substrate cannot be discarded as active nickel species for OER can be generated in the alkaline electrolyte.

Nyquist plots obtained from EIS are useful to better understand the electrocatalyst kinetics for OER. Then, they were recorded at different applied potentials (Figure S17a), and the obtained spectra were fitted according to the model circuit displayed in Figure S17b. R_{Ω} is the electrolyte resistance and the R_t and Q_t (a constant phase element) at high frequencies can be tentatively associated with the Ni/electrocatalyst interface or to the presence of a passive film.³⁹ C_{dl} and R_{ct} are related to the charge transfer to the electrolyte, and they can provide information about the OER kinetic parameters. Concretely, the exchange current density (j_0) and the Tafel slope (b) can be estimated from the Nyquist plots using the following expression^{40–42}

$$\log\left(\frac{1}{R_{ct}}\right) = \log\left(\frac{dj}{d\eta}\right) = \frac{1}{b}\eta + \log\left(\frac{2.3j_0}{b}\right) \quad (1)$$

where $b = 2.3RT/\alpha_s F$ in mV dec^{-1} , being α_s the overall transfer coefficient given by $\alpha_s = (n_f/\nu + n_s\beta_s)$, where n_f is the number of electrons transferred before the rate-determining step (rds), ν is the stoichiometric number with a typical value of one, n_s is the number of electrons transferred in each occurrence of the rds, and β_s is correlated with the symmetry factor.^{43,44} On one hand, C_{dl} values calculated from Figure S17 are represented in Figure 4e as a function of the overpotential. Although they are in the same order of magnitude as that obtained by cyclic voltammograms in the region without faradaic currents (Figure 4c), there exist some dispersion of the values in the considered range of potentials. On the other hand, according to eq 1, Figure 4f shows a linear relationship between $\log(R_{ct})$ and η . The points in Figure 4f can be fitted to a straight line with good fitting ($R^2 = 0.996$). The Tafel slope (b) can be calculated as 48 mV dec^{-1} , while a value of 42 mV dec^{-1} was determined from the voltammogram shown in Figure 4b.

Then, the overall charge transfer coefficient (α_a) can be calculated as 1.24–1.41. Such values suggest that a step subsequent to the first electron transfer is the rds with $\nu = 1$, $n_t = 1$ and $n_r = 1$.⁴⁴ According to eq 1, from the intercept with the y-axis, the exchange current density is calculated to be $1.1 \times 10^{-5} \text{ mA cm}^{-2}$.

The excellent characteristics based on the kinetics and the active site density suggest that the synthesized CoFe-based anodes are good candidates for working at high current densities as feasible and reliable electrodes. Thus, the electrochemical activity of these anodes was evaluated at higher applied potentials, and the effect of the temperature was studied. Figure 5a shows the potential region of current

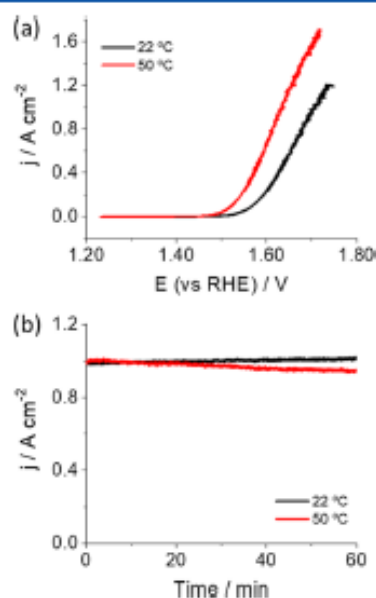


Figure 5. (a) Cyclic voltammogram and (b) chronoamperogram at a current density of ca. 1 A cm^{-2} at 22 and $50 \text{ }^\circ\text{C}$ for the CoFeP/NF electrode in 1 M KOH .

densities $>1 \text{ A cm}^{-2}$ at 22 and $50 \text{ }^\circ\text{C}$. For reaching 1 A cm^{-2} , the overpotential is only 475 mV, and they decrease by 70 mV when the temperature rises to $50 \text{ }^\circ\text{C}$. Furthermore, the stability tests at 1 A cm^{-2} in Figure 5b show that the current density remains constant at $22 \text{ }^\circ\text{C}$, while at $50 \text{ }^\circ\text{C}$, there is a slight decrease with time, which may be due to a lack of thermal stability of the experimental setup. Table 1 summarizes the approximate overpotential values achieved for 10, 100, and 1000 mA cm^{-2} based on Figure 5a.

Anion Exchange Membrane Water Electrolysis Performance. The stability of the electrocatalysts is a critical issue in fuel production and should be tested under more realistic conditions of continuous electrolyte flow to better evaluate its commercial viability. For this goal, the developed

Table 1. Overpotentials for OER at Selected Current Density Values at 22 and $50 \text{ }^\circ\text{C}$

j / mA cm ⁻²	η / mV	
	22 °C	50 °C
10	285	240
100	335	290
1000	475	405

cobalt iron oxyhydroxide anode was integrated into an electrolyzer schematized in Figure 6a for H_2 and O_2

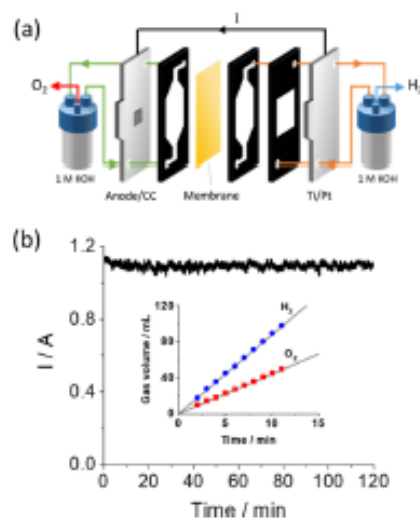


Figure 6. (a) Sketch of the alkaline exchange membrane electrolyzer using geometric electrode areas of 1 cm^2 in the anode and 10 cm^2 for the Ti/Pt cathode. CC = current collector. (b) Chronoamperogram in the full cell depicted in (a) at a current density near 1 A and heating the electrolytes to $50 \text{ }^\circ\text{C}$. Inset: experimental (points) and calculated (solid lines) accumulated volumes of H_2 and O_2 .

production, which is a relevant configuration for an industrial application. The cell comprises two compartments separated by an alkaline anion membrane, with the anolyte and catholyte recirculating at a high flow rate through the respective compartments. Consequently, this configuration allows for the separation and collection of both produced gases, where hydrogen evolves in the Ti/Pt plate (10 cm^2) and oxygen evolves in the CoFeO_xH_y/NF anode with a geometric area of 1 cm^2 .

The stability of the full cell was examined at a high current density of nearly 1 A by heating the electrolytes at $50 \text{ }^\circ\text{C}$. Figure 6b shows good stability of the current during 2 h, without any significant decay. Additionally, the volumes of H_2 and O_2 were measured for 10 min after 2 h at 1 A in the same conditions. The inset of Figure 6b displays the points corresponding to the measured gas volumes, while the straight lines correspond to the calculated values. An excellent agreement between the experimental and theoretical values was found, which means that the faradaic efficiency for OER and HER in both processes is near 100%. The outlet gas stream from the cathode was analyzed by gas chromatography confirming the presence of hydrogen gas. Similar results were obtained at room temperature (Figure S18) displaying also good stability. In that case, because of the lack of temperature control, an initial increase in the current was observed before thermal equilibration.

CONCLUSIONS

In this work, an efficient anode for OER obtained by the in situ generation of amorphous cobalt iron oxyhydroxide from the corresponding bimetallic phosphide on NF is reported. In the chemical conversion, phosphorous acts as a sacrificial element for homogeneous metal oxyhydroxide formation facilitated by the electrolyte permeation within the nanoporous structure. The initial CoFeP/NF electrode is synthesized from tiny rod-

like nanoparticles of bimetallic phosphide obtained by a feasible and scalable synthesis. These nanorods were dispersed in a 3D framework of a highly conductive nickel foam as a key element in the anode design. It ensures a high density of active sites as well as an appropriate pore size to guarantee the release of oxygen gas. Under alkaline media and anodic polarization, apart from the phosphorous depletion, the morphology radically changes from the initial nanorods to CoFe-oxyhydroxide nanoplates with a high ECSA. Remarkably, this procedure guarantees maintaining a homogeneous distribution of metal atoms on the nickel foam that allows for a rational design of the anodes to achieve a high density of active sites. The presence of Co and Fe atoms promotes favorable catalytic effects on the four-step reaction of water oxidation. Then, this rational anode design allows achieving working conditions of high current densities (higher than 1 A cm^{-2}) at optimized overpotentials lower than 500 mV for 1 A and Tafel slope as low as 42 mV dec^{-1} . Remarkably, apart from the feasible and scalable manufacturing route of the CoFeO_xH_y/NF electrode, its stability was excellent in an alkaline exchange membrane flow cell at 1 A, which makes this electrode a robust and promising anode in high production rate devices for fuel electrosynthesis.

■ ASSOCIATED CONTENT

Supporting Information

The Supporting Information is available free of charge at <https://pubs.acs.org/doi/10.1021/acsaem.3c00032>.

Supplementary HRTEM images, XRD pattern, EELS compositional maps, XPS spectra, chronoamperograms (stability tests), SEM images, atomic percentages determined by XPS, consecutive cyclic voltammograms (CVs) (stability test), CVs for different loading amounts of electrocatalyst, CVs at different scan rates for ECSA determination, Raman spectrum, Nyquist plots, volumes of H₂ and O₂ generated in full cell and table for the comparison of CoFeP-based electrodes (PDF)

■ AUTHOR INFORMATION

Corresponding Author

María Isabel Díez-García – Catalonia Institute for Energy Research (IREC), 08930 Barcelona, Spain; orcid.org/0000-0001-9939-8642; Email: midiez@irec.cat

Authors

Guillem Montaña-Mora – Catalonia Institute for Energy Research (IREC), 08930 Barcelona, Spain

Marc Botifoll – Catalan Institute of Nanoscience and Nanotechnology (ICN2), CSIC and BIST, Barcelona, Catalonia 08193, Spain

Andreu Cabot – Catalonia Institute for Energy Research (IREC), 08930 Barcelona, Spain; ICREA, Barcelona, Catalonia 08010, Spain; orcid.org/0000-0002-7533-3251

Jordi Arbiol – Catalan Institute of Nanoscience and Nanotechnology (ICN2), CSIC and BIST, Barcelona, Catalonia 08193, Spain; ICREA, Barcelona, Catalonia 08010, Spain; orcid.org/0000-0002-0695-1726

Mohammad Qamar – Interdisciplinary Research Center for Hydrogen and Energy Storage, King Fahd University of Petroleum and Minerals, 31261 Dhahran, Saudi Arabia; orcid.org/0000-0002-5351-9872

Joan Ramon Morante – Catalonia Institute for Energy Research (IREC), 08930 Barcelona, Spain

Complete contact information is available at: <https://pubs.acs.org/doi/10.1021/acsaem.3c00032>

Notes

The authors declare no competing financial interest.

■ ACKNOWLEDGMENTS

The project on which these results are based has received funding from the European Union's Horizon 2020 research and innovation programme under Marie Skłodowska-Curie grant agreement no. 801342 (Tecniospring INDUSTRY) and the Government of Catalonia's Agency for Business Competitiveness (ACCIÓ). The authors extend their overall appreciation to the Deputyship for Research & Innovation, Ministry of Education in Saudi Arabia for funding this research work through the project number DRI 598. M.I.D.-G. acknowledges the support from Ministerio de Ciencia e Innovación in Spain through the Juan de la Cierva fellowship (FJC2018-036229-I). M.I.D.-G. acknowledges M. Biset-Peiró (IREC) and S. Murcia (IREC) for their help in this work. M.B. acknowledges funding from the Catalan Agency for Management of University and Research Grants (AGAUR) Generalitat de Catalunya formation of investigators (FI) PhD grant. ICN2 and IREC receive support from the CERCA Programme/Generalitat de Catalunya and program 2021 SGR 00457 and 2021 SGR 01581. The authors thank support from the projects NANOGEN (PID2020-116093RB-C43) and CERES (PID2020-116093RB-C42), funded by MCIN/AEI/10.13039/501100011033/. ICN2 is supported by the Severo Ochoa program from Spanish MCIN / AEI (Grant No.: CEX2021-001214-S).

■ REFERENCES

- (1) Li, Y.; Dong, Z.; Jiao, L. Multifunctional Transition Metal-Based Phosphides in Energy-Related Electrocatalysis. *Adv. Energy Mater.* **2020**, *10*, 1902104.
- (2) Zhang, T.; Han, X.; Liu, H.; Biset-Peiró, M.; Zhang, X.; Tan, P.; Tang, P.; Yang, B.; Zheng, L.; Morante, J. R.; Arbiol, J. Quasi-Double-Star Nickel and Iron Active Sites for High-Efficiency Carbon Dioxide Electroreduction. *Energy Environ. Sci.* **2021**, *14*, 4847–4857.
- (3) Jin, Z.; Li, P.; Xiao, D. Metallic Co₂P Ultrathin Nanowires Distinguished from CoP as Robust Electrocatalysts for Overall Water-Splitting. *Green Chem.* **2016**, *18*, 1459–1464.
- (4) Xiao, P.; Chen, W.; Wang, X. A Review of Phosphide-Based Materials for Electrocatalytic Hydrogen Evolution. *Adv. Energy Mater.* **2015**, *5*, 1500985.
- (5) Pei, Y.; Cheng, Y.; Chen, J.; Smith, W.; Dong, P.; Ajayan, P. M.; Ye, M.; Shen, J. Recent Developments of Transition Metal Phosphides as Catalysts in the Energy Conversion Field. *J. Mater. Chem.* **2018**, *6*, 23220–23243.
- (6) Xu, S.; Zhao, H.; Li, T.; Liang, J.; Lu, S.; Chen, G.; Gao, S.; Asiri, A. M.; Wu, Q.; Sun, X. Iron-Based Phosphides as Electrocatalysts for the Hydrogen Evolution Reaction: Recent Advances and Future Prospects. *J. Mater. Chem. A* **2020**, *8*, 19729–19745.
- (7) Dutta, A.; Pradhan, N. Developments of Metal Phosphides as Efficient OER Precatalysts. *J. Phys. Chem. Lett.* **2017**, *8*, 144–152.
- (8) Zhang, H.; Majenburgh, A. W.; Li, X.; Schweizer, S. L.; Wehrspohn, R. B. Bifunctional Heterostructured Transition Metal Phosphides for Efficient Electrochemical Water Splitting. *Adv. Funct. Mater.* **2020**, *30*, 2003261.
- (9) Liu, X.; Yao, Y.; Zhang, H.; Pan, L.; Shi, C.; Zhang, X.; Huang, Z. F.; Zou, J. In Situ-Grown Cobalt–Iron Phosphide-Based Integrated Electrode for Long-Term Water Splitting under a Large Current

Density at the Industrial Electrolysis Temperature. *ACS Sustain. Chem. Eng.* **2020**, *8*, 17828–17838.

(10) Peng, Z.; Qiu, X.; Cai, G.; Zhang, X.; Dong, Z. Simultaneous Tuning of the Cation Content and Pore Structure of Cobalt-Iron Bimetal Phosphide to Enhance the Electrochemical Oxygen Evolution. *J. Alloys Compd.* **2020**, *842*, 155784.

(11) Wang, G. B.; Hsu, C. S.; Chen, H. M. The Individual Role of Active Sites in Bimetallic Oxygen Evolution Reaction Catalysts. *Dalton Trans.* **2020**, *49*, 17505–17510.

(12) Burke, M. S.; Enman, L. J.; Batchellor, A. S.; Zou, S.; Boettcher, S. W. Oxygen Evolution Reaction Electrocatalysis on Transition Metal Oxides and (Oxy)Hydroxides: Activity Trends and Design Principles. *Chem. Mater.* **2015**, *27*, 7549–7558.

(13) Wu, Z. P.; Lu, X. F.; Zang, S. Q.; Lou, X. W. Non-Noble-Metal-Based Electrocatalysts toward the Oxygen Evolution Reaction. *Adv. Funct. Mater.* **2020**, *30*, 1910274.

(14) Abed, J.; Ahmadi, S.; Laverdure, L.; Abdellah, A.; O'Brien, C. P.; Cole, K.; Sobrinho, P.; Sinton, D.; Higgins, D.; Mosey, N. J.; Thorpe, S. J.; Sargent, E. H. In Situ Formation of Nano Ni–Co Oxyhydroxide Enables Water Oxidation Electrocatalysts Durable at High Current Densities. *Adv. Mater.* **2021**, *33*, 2103812.

(15) Zhang, X.; Zhang, X.; Xu, H.; Wu, Z.; Wang, H.; Liang, Y. Iron-Doped Cobalt Monophosphide Nanosheet/Carbon Nanotube Hybrids as Active and Stable Electrocatalysts for Water Splitting. *Adv. Funct. Mater.* **2017**, *27*, 1606635.

(16) Wang, Y.; Kong, B.; Zhao, D.; Wang, H.; Selomulya, C. Strategies for Developing Transition Metal Phosphides as Heterogeneous Electrocatalysts for Water Splitting. *Nano Today* **2017**, *15*, 26–55.

(17) Hung, S. F.; Zhu, Y.; Tzeng, G. Q.; Chen, H. C.; Hsu, C. S.; Liao, Y. F.; Ishii, H.; Hiraoka, N.; Chen, H. M. In Situ Spatially Coherent Identification of Phosphide-Based Catalysts: Crystallographic Latching for Highly Efficient Overall Water Electrolysis. *ACS Energy Lett.* **2019**, *4*, 2813–2820.

(18) Trotochaud, L.; Young, S. L.; Ranney, J. K.; Boettcher, S. W. Nickel-Iron Oxyhydroxide Oxygen-Evolution Electrocatalysts: The Role of Intentional and Incidental Iron Incorporation. *J. Am. Chem. Soc.* **2014**, *136*, 6744–6753.

(19) Burke, M. S.; Kast, M. G.; Trotochaud, L.; Smith, A. M.; Boettcher, S. W. Cobalt-Iron (Oxy)Hydroxide Oxygen Evolution Electrocatalysts: The Role of Structure and Composition on Activity, Stability, and Mechanism. *J. Am. Chem. Soc.* **2015**, *137*, 3638–3648.

(20) Pei, Y.; Ge, Y.; Chu, H.; Smith, W.; Dong, P.; Ajayan, P. M.; Ye, M.; Shen, J. Controlled Synthesis of 3D Porous Structured Cobalt-Iron Based Nanosheets by Electrodeposition as Asymmetric Electrodes for Ultra-Efficient Water Splitting. *Appl. Catal., B* **2019**, *244*, 583–593.

(21) Chung, D. Y.; Lopes, P. P.; Farinazzo Bergamo Dias Martins, P.; He, H.; Kawaguchi, T.; Zapol, P.; You, H.; Tripkovic, D.; Strmcnik, D.; Zhu, Y.; Seifert, S.; Lee, S.; Stamenkovic, V. R.; Markovic, N. M. Dynamic Stability of Active Sites in Hydr(Oxy)-Oxides for the Oxygen Evolution Reaction. *Nat. Energy* **2020**, *5*, 222–230.

(22) Inohara, D.; Maruyama, H.; Kakihara, Y.; Kurokawa, H.; Nakayama, M. Cobalt-Doped Goethite-Type Iron Oxyhydroxide (α -FeOOH) for Highly Efficient Oxygen Evolution Catalysis. *ACS Omega* **2018**, *3*, 7840–7845.

(23) Zhang, W.; Li, Y.; Zhou, L.; Zheng, Q.; Xie, F.; Lam, K. H.; Lin, D. Ultrathin Amorphous CoFeP Nanosheets Derived from CoFe LDHs by Partial Phosphating as Excellent Bifunctional Catalysts for Overall Water Splitting. *Electrochim. Acta* **2019**, *323*, 134595.

(24) Tang, Y. J.; You, L.; Zhou, K. Enhanced Oxygen Evolution Reaction Activity of a $\text{Co}_2\text{P}@NC\text{-Fe}_2\text{P}$ Composite Boosted by Interfaces between a N-Doped Carbon Matrix and Fe_2P Microspheres. *ACS Appl. Mater. Interfaces* **2020**, *12*, 25884–25894.

(25) Liu, J.; Meyns, M.; Zhang, T.; Arbiol, J.; Cabot, A.; Shavel, A. Triphenyl Phosphite as the Phosphorus Source for the Scalable and Cost-Effective Production of Transition Metal Phosphides. *Chem. Mater.* **2018**, *30*, 1799–1807.

(26) Zhang, C.; Du, R.; Biendicho, J. J.; Yi, M.; Xiao, K.; Yang, D.; Zhang, T.; Wang, X.; Arbiol, J.; Llorca, J.; Zhou, Y.; Morante, J. R.; Cabot, A. Tubular CoFeP@CN as a Mott–Schottky Catalyst with Multiple Adsorption Sites for Robust Lithium–Sulfur Batteries. *Adv. Energy Mater.* **2021**, *11*, 2100432.

(27) McCrory, C. C. L.; Jung, S.; Peters, J. C.; Jaramillo, T. F. Benchmarking Heterogeneous Electrocatalysts for the Oxygen Evolution Reaction. *J. Am. Chem. Soc.* **2013**, *135*, 16977–16987.

(28) Xue, Y.; Hui, L.; Yu, H.; Liu, Y.; Fang, Y.; Huang, B.; Zhao, Y.; Li, Z.; Li, Y. Rationally Engineered Active Sites for Efficient and Durable Hydrogen Generation. *Nat. Commun.* **2019**, *10*, 2281.

(29) Sankar, S. S.; Rathishkumar, A.; Geetha, K.; Kundu, S. A Simple Route for the Synthesis of Cobalt Phosphate Nanoparticles for Electrocatalytic Water Oxidation in Alkaline Medium. *Energy Fuels* **2020**, *34*, 12891–12899.

(30) Yuan, C. Z.; Jiang, Y. F.; Wang, Z.; Xie, X.; Yang, Z. K.; Yousaf, A. B.; Xu, A. W. Cobalt Phosphate Nanoparticles Decorated with Nitrogen-Doped Carbon Layers as Highly Active and Stable Electrocatalysts for the Oxygen Evolution Reaction. *J. Mater. Chem. A* **2016**, *4*, 8155–8160.

(31) Koza, J. A.; Hull, C. M.; Liu, Y. C.; Switzer, J. A. Deposition of $\beta\text{-Co(OH)}_2$ Films by Electrochemical Reduction of Tris-(Ethylenediamine)Cobalt(III) in Alkaline Solution. *Chem. Mater.* **2013**, *25*, 1922–1926.

(32) Smith, R. D. L.; Prévot, M. S.; Fagan, R. D.; Trudel, S.; Berlinguette, C. P. Water Oxidation Catalysis: Electrocatalytic Response to Metal Stoichiometry in Amorphous Metal Oxide Films Containing Iron, Cobalt, and Nickel. *J. Am. Chem. Soc.* **2013**, *135*, 11580–11586.

(33) Zhou, J.; Yu, L.; Zhou, Q.; Huang, C.; Zhang, Y.; Yu, B.; Yu, Y. Ultrafast Fabrication of Porous Transition Metal Foams for Efficient Electrocatalytic Water Splitting. *Appl. Catal., B* **2021**, *288*, 120002.

(34) Liu, Y. C.; Koza, J. A.; Switzer, J. A. Conversion of Electrodeposited Co(OH)_2 to CoOOH and Co_3O_4 , and Comparison of Their Catalytic Activity for the Oxygen Evolution Reaction. *Electrochim. Acta* **2014**, *140*, 359–365.

(35) Hu, J.; Li, S.; Chu, J.; Niu, S.; Wang, J.; Du, Y.; Li, Z.; Han, X.; Xu, P. Understanding the Phase-Induced Electrocatalytic Oxygen Evolution Reaction Activity on FeOOH Nanostructures. *ACS Catal.* **2019**, *9*, 10705–10711.

(36) Dong, G.; Fang, M.; Zhang, J.; Wei, R.; Shu, L.; Liang, X.; Yip, S.; Wang, F.; Guan, L.; Zheng, Z.; Ho, J. C. In Situ Formation of Highly Active Ni-Fe Based Oxygen-Evolving Electrocatalysts via Simple Reactive Dip-Coating. *J. Mater. Chem. A* **2017**, *5*, 11009–11015.

(37) Urbain, F.; Du, R.; Tang, P.; Smirnov, V.; Andreu, T.; Finger, F.; Jimenez Divins, N.; Llorca, J.; Arbiol, J.; Cabot, A.; Morante, J. R. Upscaling high activity oxygen evolution catalysts based on CoFe_2O_4 nanoparticles supported on nickel foam for power-to-gas electrochemical conversion with energy efficiencies above 80%. *Appl. Catal., B* **2019**, *259*, 118055.

(38) Nie, J.; Hong, M.; Zhang, X.; Huang, J.; Meng, Q.; Du, C.; Chen, J. 3D Amorphous NiFe LDH Nanosheets Electrodeposited on: In Situ Grown NiCoP@NC on Nickel Foam for Remarkably Enhanced OER Electrocatalytic Performance. *Dalton Trans.* **2020**, *49*, 4896–4903.

(39) Lyons, M. E. G.; Brandon, M. P. The Oxygen Evolution Reaction on Passive Oxide Covered Transition Metal Electrodes in Alkaline Solution. Part III - Iron. *Int. J. Electrochem. Sci.* **2008**, *3*, 1463–1503.

(40) Doyle, R. L.; Lyons, M. E. G. An Electrochemical Impedance Study of the Oxygen Evolution Reaction at Hydrous Iron Oxide in Base. *Phys. Chem. Chem. Phys.* **2013**, *15*, S224–S237.

(41) Lyons, M. E. G.; Brandon, M. P. The Oxygen Evolution Reaction on Passive Oxide Covered Transition Metal Electrodes in Aqueous Alkaline Solution. Part 1-Nickel. *Int. J. Electrochem. Sci.* **2008**, *3*, 1386–1424.

(42) Han, L.; Tang, P.; Reyes-Carmona, Á.; Rodríguez-García, B.; Torrén, M.; Morante, J. R.; Arbiol, J.; Galan-Mascaros, J. R.

Enhanced Activity and Acid pH Stability of Prussian Blue-Type Oxygen Evolution Electrocatalysts Processed by Chemical Etching. *J. Am. Chem. Soc.* **2016**, *138*, 16037–16045.

(43) Exner, K. S.; Over, H. Beyond the Rate-Determining Step in the Oxygen Evolution Reaction over a Single-Crystalline IrO₂(110) Model Electrode: Kinetic Scaling Relations. *ACS Catal.* **2019**, *9*, 6755–6765.

(44) Negahdar, L.; Zeng, F.; Palkovits, S.; Broicher, C.; Palkovits, R. Mechanistic Aspects of the Electrocatalytic Oxygen Evolution Reaction over Ni–Co Oxides. *ChemElectroChem* **2019**, *6*, 5588–5595.

Palladium Hydride on C₂N to Boost Formate Oxidation

Xiang Wang,* Guillem Montaña-Mora, Xu Han, Jing Yu, Xueqiang Qi, Jordi Arbiol, Zhifu Liang,* Andreu Cabot,* and Junshan Li*

Cite This: *ACS Sustainable Chem. Eng.* 2023, 11, 11399–11405

Read Online

ACCESS |

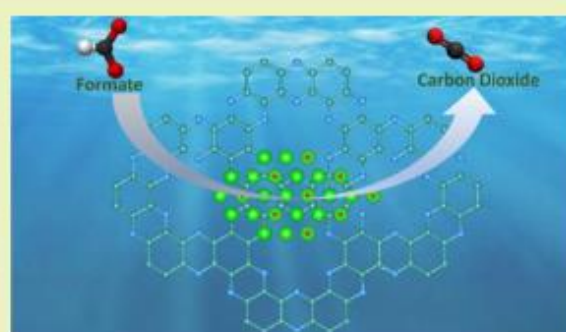
Metrics & More

Article Recommendations

Supporting Information

ABSTRACT: The lack of electrocatalysts for the formate oxidation reaction (FOR) hampers the deployment of direct formate fuel cells (DFFCs). To overcome this limitation, herein, we detail the production of palladium hydride particles supported on C₂N (PdH_{0.58}@C₂N) via a facile method. PdH_{0.58}@C₂N displays excellent FOR performance, reaching current densities up to 5.6 A·mgPd⁻¹ and stable cycling and chronoamperometric operation. The Pd lattice expands due to the hydrogen intercalation. Besides, an electronic redistribution associated with the distinct electronegativity of Pd and H is observed. Both phenomena modify the electron energy levels, enhancing the activity and stability of the composite catalyst. More specifically, differential functional theory calculations show H intercalation to downshift the Pd d-band center in Pd_{0.58}@C₂N, weakening adsorbate binding and accelerating the FOR rate-determining step.

KEYWORDS: electrocatalysis, direct formate fuel cell, palladium hydride, C₂N, formate oxidation reaction, fuel cell



INTRODUCTION

Fuel cells are an attractive alternative to conventional fossil fuel-based combustion technologies, offering high efficiencies of conversion from chemical to electrical energy. Among the possible liquid fuels, formic acid/formate offers a particularly simple oxidation reaction, involving the transfer of just two electrons.^{1–5} In particular, formic acid is regarded as a safe, low-cost, and low-toxicity hydrogen carrier, with a large content of hydrogen, 4.4 wt %, excellent stability, low ignition point, and convenient transportation and storage.^{6–8} However, it is the use of formate in alkaline cells that is attracting more recent attention. The use of a solid formate salt is beneficial in terms of storage and transportation over liquid formic acid.^{9,10} Formate is also characterized by much lower toxicity and corrosiveness than formic acid, and therefore it can be used at higher concentrations.^{11,12} Besides, the formate oxidation reaction (FOR) presents faster reaction kinetics, lower overpotentials, and reduced poisoning when compared with that of formic acid.^{13–15} Additionally, direct formate fuel cells (DFFCs) also present faster kinetics due to the rapid O₂ reduction reaction (ORR) kinetics in alkaline medium when compared with an acid environment.^{11,16,17} Moreover, formate is industrially used for the production of formic acid, thus available at a reduced price. On top of all these, the synthesis of formate from CO₂ reduction has seen rapid progress recently and may reach industrialization in the foreseeable future, which could make DFFCs a net-zero CO₂ technology.^{18–20}

Palladium (Pd) is the most promising candidate to catalyze the FOR. However, the performance of Pd is still far from optimum in terms of stability and also activity.²¹ As a main drawback, Pd binds too strongly to hydrogen, limiting its desorption and thus blocking the adsorption sites available for additional reactants.^{22,23} To improve the FOR performance, we need to develop effective strategies to tune the electronic properties of Pd and particularly to reduce the adsorption energy of the intermediates. Recently, the introduction of lighter and smaller elements to diffuse within the Pd lattice and expand it has awakened notorious attention. By changing the metal lattice parameters, the electronic properties of the metal can be modified and potentially optimized.^{24–26} Among the possible light elements, hydrogen (H) is particularly suitable to modify the Pd structure owing to the small atomic radius of H and the high affinity of Pd toward this element.^{27–29}

To maximize its dispersion, electrocatalytic particles are generally supported on electrically conductive high surface area supports, such as carbon.³⁰ However, traditional carbon materials contain uniformly distributed surface charges, making

Received: February 12, 2023

Revised: July 14, 2023

Published: July 25, 2023



them catalytically inactive. To overcome this limitation, nitrogen-doped carbon and carbon nitrides can be used.³¹ In particular, C₂N has emerged as a new 2D graphene-like layered covalent organic material.^{32–34} The presence of N atoms within the carbon lattice introduces polarity to interact with the polar species and enhances thermal stability.^{35–37} Besides, the electrical conductivity of C₂N is higher than that of other C–N materials. The unique porous structure of C₂N increases the electron density of the N atoms, which enables them to act as excellent sites for the nucleation and growth of metals.^{38,39}

Taking into account all the above, we developed a strategy to produce palladium hydride (PdH_{0.58}) nanodendrite supported on C₂N. Such a composite catalyst was tested toward FOR in alkaline media. To rationalize the obtained results, density functional theory (DFT) calculations were used to identify the effect of H intercalation on the d-band center of Pd within the composite Pd_{0.58}@C₂N and its influence on the binding of adsorbates.

RESULTS AND DISCUSSION

Palladium hydride nanoparticles were produced in the presence of C₂N using Pd(acac)₂ as the metal precursor and OAm as the solvent and hydrogen source (see details in the Experimental Section, Figure S1). In the presence of C₂N, Pd heterogeneously nucleates and grows at N sites on the C₂N surface which offer lone electron pairs and thus act as electron donors coordinating with the metal ions. Figure S2 shows the nanosheet structure and the composition of the initial C₂N support. Figures 1a–c and S3 display the representative SEM

pattern of PdH_{0.58}@C₂N was consistent with that of the Pd face-centered cubic (fcc) structure (Pd-PDF#87-0641), but, consistent with HRTEM results, diffraction peaks were shifted to lower angles. A reference Pd@C₂N sample was produced by annealing PdH_{0.58}@C₂N under Ar at 450 °C for 2 h to remove the intercalated hydrogen. As shown in Figure 2a, after the annealing treatment, the shift of the XRD pattern disappeared. These results further confirm the expansion of the Pd lattice with the introduction of H.^{27,28} The HAADF-STEM micrographs (Figure 1d) and STEM-EELS elemental composition maps (Figure 1e) of PdH_{0.58}@C₂N show the presence of C, N, and Pd, all the elements being homogeneously distributed at the nanometer scale. Additional TEM, HRTEM, and STEM-EELS of the Pd@C₂N sample show a relatively similar architecture with a homogeneous distribution of the different elements (Figure S4).

As an additional reference material, self-standing PdH_{0.58} nanoparticles were synthesized using the same procedure as that for the synthesis of PdH_{0.58}@C₂N but in the absence of C₂N. Afterward, these nanoparticles were physically mixed with C₂N to produce PdH_{0.58}/C₂N. The TEM images of PdH_{0.58} and SEM images of PdH_{0.58}/C₂N samples show the PdH_{0.58} nanoparticles to be highly agglomerated (Figures S5 and S6), which reveal the presence of C₂N during the Pd-based nanoparticle synthesis to decisively contribute to their dispersion. Besides, the XRD pattern of the PdH_{0.58}/C₂N sample displays an additional peak at ca. 35° associated with the presence of a small amount of the PdO phase (JCPDS 06-0515), which reveals that the coordination of PdH_{0.58} with C₂N during the synthesis, through the N atoms, contributes to prevent its surface oxidation.

Figure 2b,c displays the XPS spectra of Pd@C₂N and PdH_{0.58}@C₂N. For both materials, the high-resolution Pd 3d XPS spectra presented two doublets. The major component, at 335.4 eV (Pd 3d_{3/2}), for PdH_{0.58}@C₂N, was associated with Pd⁰, and the minor, at 336.5 eV (Pd 3d_{3/2}), with an oxidized Pd²⁺ chemical environment.^{25,43} The Pd 3d spectra of PdH_{0.58}@C₂N were shifted to about 0.2 eV toward higher binding energies than Pd@C₂N, which indicates a charge redistribution within palladium hydride, with Pd giving electrons to H. The presence of electron-deficient Pd in PdH_{0.58}@C₂N is consistent with previous reports.^{44,45} Electron-poor Pd has been reported to reduce the electron exchange with CO 2π* orbitals, which translates into a weaker CO adsorption.⁴³ Thus, PdH_{0.58}@C₂N may present a higher resistance toward CO poisoning during FOR than Pd@C₂N.

The valence band XPS spectra of Pd@C₂N and PdH_{0.58}@C₂N are displayed in Figure 2c. A broad band of states, contributed by Pd 4d electronic states, is observed in both spectra.^{27,28} PdH_{0.58}@C₂N shows a narrower bandwidth of ca. 4.95 eV as compared to 5.91 eV of Pd@C₂N, which indicates a modified electronic structure. Such narrower bandwidth results from the increase of distance between Pd atoms within PdH.⁴⁶ Besides, a new peak in the band structure of PdH_{0.58} was observed at 6.17 eV, and it was associated with the interaction between the H 1s and Pd 4d electronic states within PdH.⁴⁷

The FOR performance of PdH_{0.58}@C₂N, Pd@C₂N, PdH_{0.58}/C₂N, and commercial Pd/C was studied in a conventional three-electrode system. First, CV curves were obtained in an Ar-saturated 0.5 M KOH solution (Figure 3a). In the cathodic scan, the current density peaks in the potential region –0.6 to –0.8 V vs Hg/HgO are assigned to hydrogen adsorption. Besides, equivalent peaks in the anodic scan are

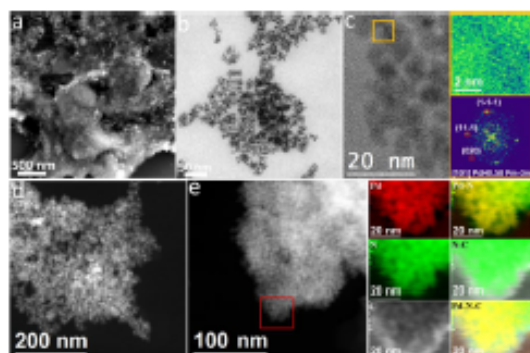


Figure 1. Structural and chemical characterization of PdH_{0.58}@C₂N. (a) SEM image, (b) TEM image, (c) HRTEM and the corresponding FFT spectrum of PdH_{0.58}@C₂N, visualized along its [101] zone axis. (d, e) HAADF-STEM and EELS chemical composition maps obtained from the red-squared area of the STEM micrograph. Individual Pd M_{4,5}-edges at 335 eV (red), N K-edges at 401 eV (green), and C K-edges at 285 eV (gray) and the composites of Pd–N, N–C, and Pd–N–C.

and TEM micrographs of the particles supported on C₂N. The final product consists of C₂N covered with small hyperbranched nanoparticles or nanodendrites. HRTEM micrographs reveal that the nanodendrites have a crystal phase in agreement with the Pd cubic phase (space group = *Fm-3m*) but with a significantly larger lattice parameter $a = b = c = 4.0190$ Å, well above that of pure Pd $a = b = c = 3.89$ Å. The larger lattice spacing measured confirms the presence of H within the Pd lattice.^{40–42} Since the presence of H linearly affects the lattice parameter of PdH, from the HRTEM data, we calculated a H/Pd atomic ratio of ca. 0.58. The XRD

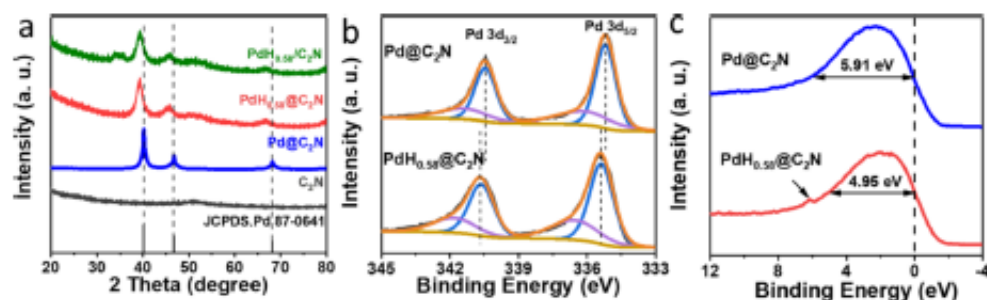


Figure 2. (a) XRD patterns of C₂N, Pd@C₂N, PdH_{0.58}@C₂N, and PdH_{0.58}/C₂N. (b) High-resolution Pd 3d XPS spectra and (c) valence band XPS spectra of Pd@C₂N and PdH_{0.58}@C₂N. The d-band widths are indicated by the double-headed arrows, and the black dashed line highlights the Fermi-level position.

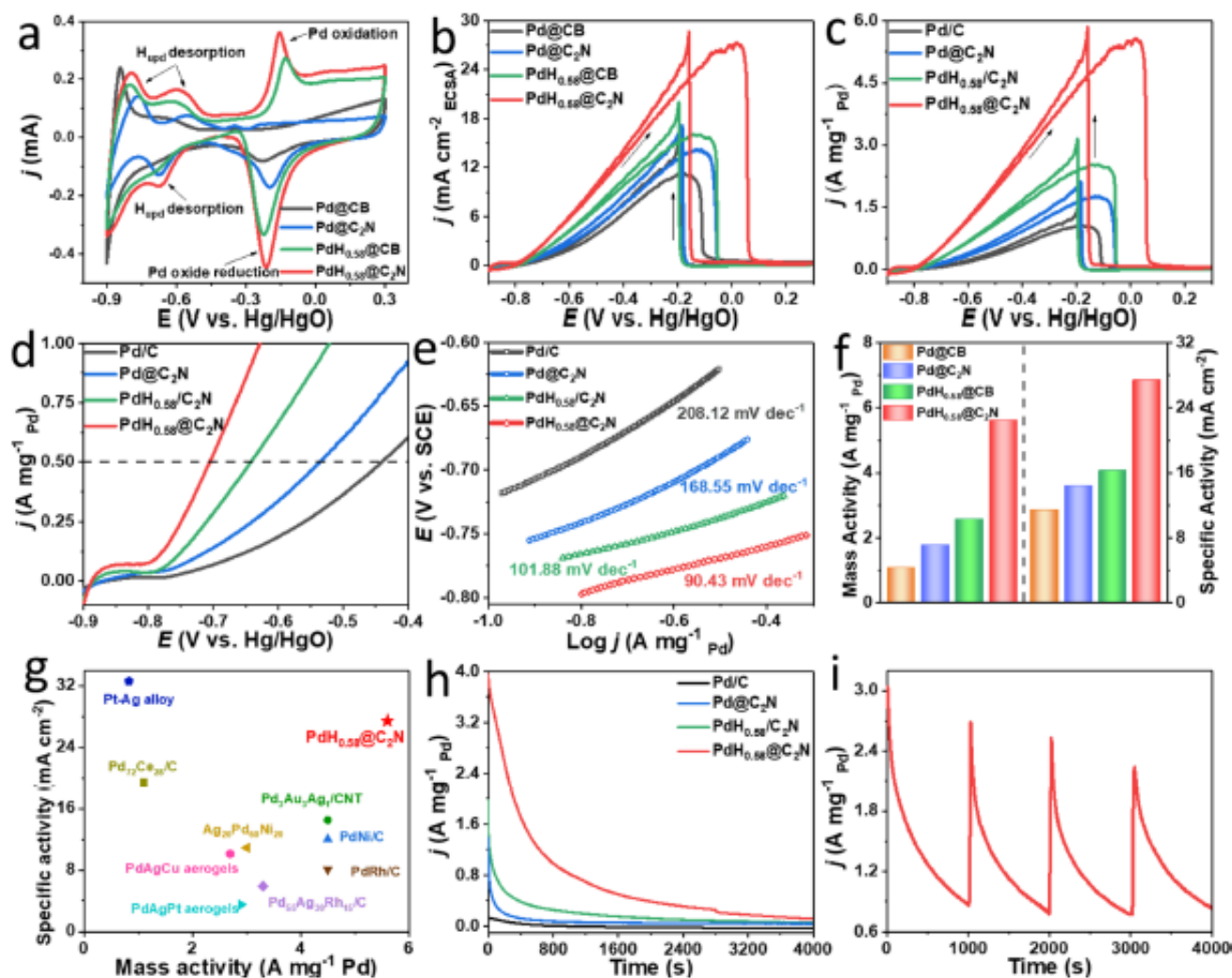


Figure 3. Electrochemical performance of PdH_{0.58}@C₂N, Pd@C₂N, PdH_{0.58}/C₂N, and Pd/C catalysts for FOR. (a) Cyclic voltammetry curves in Ar-saturated 0.5 M KOH solution and (b, c) in a 0.5 M KOH + 0.5 M ethanol solution normalized by the geometric area (b) and the mass of Pd (c). (d) Enlarged CV curves at the onset potential. (e) Tafel plot and the calculated Tafel slopes. (f) Comparison of mass activity and specific activity. (g) Comparison of peak potentials between this work and previous reports. (h) Chronoamperometric (CA) curves. (i) CA curves with CV re-activation every 1000 s for PdH_{0.58}@C₂N.

associated with the desorption of hydrogen.⁴⁸ In the anodic scan, the increase of current density observed at about -0.2 V vs Hg/HgO is assigned to the surface oxidation of palladium. Additionally, the current density peak associated with the PdO reduction is found at about -0.2 V versus Hg/HgO during the

cathodic scan. The distinct hydrogen adsorption/desorption features of hydrogen between PdH_{0.58}@C₂N and Pd@C₂N indicate different surface atomic configurations.

The electrochemical active surface area (ECSA) was estimated from the PdO reduction peak. CV curves showed

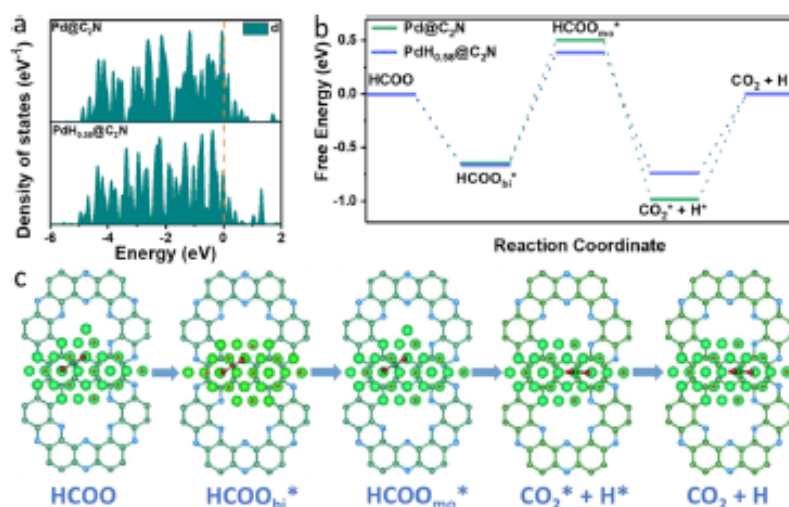


Figure 4. (a) d-band centers of Pd 4d partial density of states. (b) Gibbs free-energy diagrams of FOR intermediates for PdH_{0.58}@C₂N and Pd@C₂N. (c) Evolution of the local structural configurations illustrating the FOR process of PdH_{0.58}@C₂N (* represents the active site).

the Pd oxide reduction peak area to be significantly larger on PdH_{0.58}@C₂N than on Pd@C₂N, PdH_{0.58}/C₂N, and Pd/C, suggesting a larger ECSA. Quantitatively, ECSA was calculated from:

$$\text{ECSA} = \frac{Q \ (\mu\text{C}\cdot\text{cm}^{-2})}{Q_{\text{PdO}}(\mu\text{C}\cdot\text{cm}^{-2}_{\text{Pd}}) \times \text{Pd}_{\text{loading}}(\text{mg}\cdot\text{cm}^{-2}) \times 10} \quad (1)$$

where $Q_{\text{PdO}} = 405 \mu\text{C cm}^{-2}$ is the charge involved in the reduction of a PdO monolayer, Q is the charge obtained from the integration of the PdO reduction peak, and $\text{Pd}_{\text{loading}}$ is the Pd amount loaded on the working electrode.³⁰ From this equation, the ECSA values for Pd_{0.58}@C₂N, Pd@C₂N, PdH_{0.58}/C₂N, and Pd@CB catalysts were observed to be 40.84, 31.51, 24.75, and 18.78 m² g⁻¹, respectively. Thus, significantly larger ECSAs were obtained with the growth of PdH_{0.58} in the presence of C₂N.^{49,50}

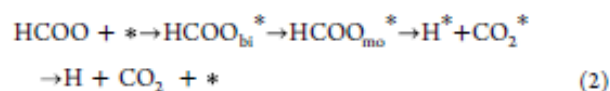
The electrocatalytic activity toward FOR was investigated by CV in a solution containing 0.5 M KOH and 0.5 M HCOOK (Figure 3b). The obtained current was normalized to the calculated ECSA. Even when normalizing to the ECSA, the PdH_{0.58}@C₂N catalyst exhibited a much higher specific activity when compared with the reference catalysts. PdH_{0.58}@C₂N delivered a peak current density of 27.44 mA cm⁻², well above that of Pd@C₂N (16.25 mA·cm⁻²), PdH_{0.58}/C₂N (14.37 mA·cm⁻²), and Pd/C (11.43 mA·cm⁻²). Even larger differences were obtained when normalizing to the mass of Pd. PdH_{0.58}@C₂N exhibited the highest mass activity at 5.60 A mg Pd⁻¹, which was 5.2-fold larger than that of Pd/C (1.07 A mg Pd⁻¹) and well above that of the other electrocatalysts. PdH_{0.58}@C₂N-based electrodes also provided the lowest onset potentials, as shown in Figure 3d. The onset potential of PdH_{0.58}@C₂N was -0.71 V, much smaller than that of Pd@C₂N (-0.64 V). Besides, as shown in Figure 3e, the lowest Tafel slope was also obtained for PdH_{0.58}@C₂N, at 90.4 mV dec⁻¹, significantly below that of Pd@C₂N, PdH_{0.58}/C₂N, and Pd/C catalysts at 101.9, 168.6, and 208.1 mV dec⁻¹, respectively. The lowest Tafel slope of the PdH_{0.58}@C₂N catalyst indicates promoted FOR kinetics.

Figure 3f resumes the specific and mass activities of all catalysts in this work toward the FOR. Additionally, Figure 3g

and Table S2 compare the results obtained in the present work with the state-of-the-art Pd-based catalysts reported to date. Overall, PdH_{0.58}@C₂N shows outstanding specificity and mass activities, above most catalysts reported so far.

The electrocatalytic stability of PdH_{0.58}@C₂N was evaluated using CA measurements at -0.2 V in 0.5 M KOH + 0.5 M HCOOK electrolyte for 5000 s (Figure 3h). PdH_{0.58}@C₂N exhibited the slowest current decay compared with the reference electrocatalysts. To remove the accumulated poisoning species, a rapid potential scan to oxidize and reduce the Pd surface was performed. Figure 3i shows the regeneration capacity of the tested catalysts. After every 1000 s of CA test, the catalysts were re-activated by cycling for 100 s in a clean 0.5 M KOH solution. This simple regeneration strategy allows cleaning the surface of the catalyst from the adsorbed contaminants and thus recovering most of the catalytic activity. After 1000 cycles in the voltage range -0.9 to 0.3 V vs Hg/HgO in the 0.5 M KOH + 0.5 M HCOOK electrolyte, the catalyst was collected and analyzed. As shown in TEM and HRTEM images in Figure S7, the post-FOR product maintained the initial architecture, crystal phase, and composition, without significant variations.

To provide the theoretical basis for the experimental results, the thermochemical reaction energetics of the FOR on PdH_{0.58}@C₂N and Pd@C₂N were investigated by DFT calculations using the (111) surface of fcc Pd. The projected density of states (PDOSs) of Pd@C₂N (111) and PdH_{0.58}@C₂N (111) surfaces are displayed in Figure 4a. The d-band of the PdH_{0.58}@C₂N surface is downshifted, with the center farther away from the Fermi level (-2.02 eV) than that of the Pd@C₂N surfaces (-1.77 eV). We also calculated the d-band center of the (111) surface, which gives the same result (Figure S8, Supporting Information). The configurations of the adsorbed FOR intermediates (HCOO_{bi}^{*}, HCOO_{mo}^{*}, H^{*} and CO₂^{*}) on the surface of PdH_{0.58}@C₂N are displayed in Figure 4c. A priori, on Pd-based catalysts, the FOR direct path follows four steps:



where * denotes a surface site, and $\text{HCOO}_{\text{bt}}^*$, $\text{HCOO}_{\text{mo}}^*$, H^* , and CO_2^* are the formate bidentate, formate monodentate, H, and CO_2 adsorbed on the sites, respectively.^{51,52} Figure 4b displays the free-energy profiles of the FOR steps. The results show an endothermic second step, $\text{HCOO}_{\text{bt}}^* \rightarrow \text{HCOO}_{\text{mo}}^*$, having the highest energy barrier associated for both catalysts. DFT calculations show that the energy barrier for this rate-determining step (RDS) is 1.047 eV for $\text{PdH}_{0.58}@\text{C}_2\text{N}$ surfaces and significantly higher for $\text{Pd}@\text{C}_2\text{N}$ (1.151 eV) surfaces, which is consistent with the lower onset potential and higher activity of the former. Besides, the energy barrier for the desorption of the reaction products is also much lower for $\text{PdH}_{0.58}@\text{C}_2\text{N}$ (0.738 eV) than for $\text{Pd}@\text{C}_2\text{N}$ (0.986 eV), which is consistent with the higher activity and stability of the former.

CONCLUSIONS

In summary, $\text{PdH}_{0.58}@\text{C}_2\text{N}$ was prepared using a one-step in situ growth method based on the heterogeneous nucleation and growth of $\text{PdH}_{0.58}$ on the surface of C_2N . The grown palladium hydride displays a favorable architecture with a high surface area. The presence of H provides several advantages, including an expansion of the Pd lattice and an electronic reconfiguration within the material that promotes the FOR catalytic performance, improving both activity and stability. DFT calculations show the presence of H to downshift the Pd d-band center within $\text{Pd}_{0.58}@\text{C}_2\text{N}$, weakening the adsorbate binding and thus accelerating the rate-limiting step of the FOR. Overall, the presence of H allows tuning the Pd crystallographic and electronic structures to enhance the electrocatalytic properties. Beyond FOR, the same strategy is susceptible to be applied to other electrocatalytic reactions.

ASSOCIATED CONTENT

Supporting Information

The Supporting Information is available free of charge at <https://pubs.acs.org/doi/10.1021/acssuschemeng.3c00852>.

Description of materials and methods; experimental procedure; computational methods; ^1H NMR spectrum of hexa-aminobenzene; SEM/TEM images and EDS results of C_2N ; TEM images of in situ $\text{PdH}@\text{C}_2\text{N}$; TEM/HRTEM and HAADF-STEM images, the corresponding FFT spectrum, EELS, and chemical composition maps of $\text{Pd}@\text{C}_2\text{N}$; SEM images and EDS results of $\text{PdH}@\text{C}_2\text{N}$; TEM images of $\text{PdH}_{0.58}$ nanoparticles without C_2N ; TEM/HRTEM images and the corresponding FFT spectra of $\text{PdH}_{0.58}@\text{C}_2\text{N}$ after 1000 cycles; and simulated $\text{PdH}_{0.58}@\text{C}_2\text{N}$ models and d-band center of $\text{Pd}@\text{C}_2\text{N}$ and $\text{PdH}_{0.58}@\text{C}_2\text{N}$ (PDF)

AUTHOR INFORMATION

Corresponding Authors

Xiang Wang – School of Chemical Engineering and Pharmacy, Wuhan Institute of Technology, Wuhan 430205, China; Catalonia Institute for Energy Research (IREC), 08930 Barcelona, Spain; Email: wangxiang@wit.edu.cn

Zhifu Liang – Catalonia Institute for Energy Research (IREC), 08930 Barcelona, Spain; Catalan Institute of Nanoscience and Nanotechnology (ICN2), CSIC and BIST, Barcelona 08193 Catalonia, Spain; College of Ocean Science and Engineering, Shanghai Maritime University, Shanghai 201306, China; Email: zhfliang@mail.usstc.edu.cn

Andreu Cabot – Catalonia Institute for Energy Research (IREC), 08930 Barcelona, Spain; ICREA Pg. Lluís Companys, Barcelona 08010 Catalonia, Spain; orcid.org/0000-0002-7533-3251; Email: acabot@irec.cat

Junshan Li – Catalonia Institute for Energy Research (IREC), 08930 Barcelona, Spain; Institute of Advanced Study, Chengdu University, Chengdu 610106, China; Email: lijunshan@cdu.edu.cn

Authors

Guillem Montaña-Mora – Catalonia Institute for Energy Research (IREC), 08930 Barcelona, Spain

Xu Han – Catalonia Institute for Energy Research (IREC), 08930 Barcelona, Spain; Catalan Institute of Nanoscience and Nanotechnology (ICN2), CSIC and BIST, Barcelona 08193 Catalonia, Spain

Jing Yu – Catalonia Institute for Energy Research (IREC), 08930 Barcelona, Spain; Catalan Institute of Nanoscience and Nanotechnology (ICN2), CSIC and BIST, Barcelona 08193 Catalonia, Spain

Xueqiang Qi – Catalonia Institute for Energy Research (IREC), 08930 Barcelona, Spain; College of Chemistry and Chemical Engineering, Chongqing University, Chongqing 400044, China; orcid.org/0000-0003-4566-9552

Jordi Arbiol – Catalan Institute of Nanoscience and Nanotechnology (ICN2), CSIC and BIST, Barcelona 08193 Catalonia, Spain; ICREA Pg. Lluís Companys, Barcelona 08010 Catalonia, Spain; orcid.org/0000-0002-0695-1726

Complete contact information is available at: <https://pubs.acs.org/10.1021/acssuschemeng.3c00852>

Notes

The authors declare no competing financial interest.

ACKNOWLEDGMENTS

The authors acknowledge funding from Generalitat de Catalunya 2021 SGR 01581 and the projects COMBENERGY (PID2019-105490RB-C32) from the Spanish Ministerio de Ciencia e Innovación, ENE2016-77798-C4-3-R, and NANOGEN (PID2020-116093RB-C43) funded by MCIN/AEI/10.13039/501100011033/ and by "ERDF A way of making Europe," by the "European Union." X.W., X.H., and R.D. thank the China Scholarship Council (CSC) for the scholarship support. The authors acknowledge funding from Generalitat de Catalunya 2017 SGR 327 and 2017 SGR 1246. ICN2 acknowledges the Severo Ochoa program from Spanish MINECO (grant no. SEV-2017-0706). IREC and ICN2 are funded by the CERCA Programme/Generalitat de Catalunya. Z.L. acknowledges funding from MINECO SO-FPT PhD grant (SEV-2013-0295-17-1). Li is grateful to project No. 22NSFSC0966 provided by the Science and Technology Department of Sichuan Province. J.L. is a Serra Hünter Fellow and is grateful to MICINN/FEDER RTI2018-093996-B-C31, GC 2017 SGR 128, and ICREA Academia program. Part of the present work has been performed in the frameworks of the Universitat de Barcelona Nanoscience PhD program and the Universitat Autònoma de Barcelona Materials Science PhD program.

REFERENCES

- (1) Mazumder, V.; Sun, S. Oleylamine-mediated synthesis of Pd nanoparticles for catalytic formic acid oxidation. *J. Am. Chem. Soc.* **2009**, *131*, 4588–4589.
- (2) Xiong, Y.; Dong, J.; Huang, Z.-Q.; Xin, P.; Chen, W.; Wang, Y.; Li, Z.; Jin, Z.; Xing, W.; Zhuang, Z.; Ye, J.; Wei, X.; Cao, R.; Gu, L.; Sun, S.; Zhuang, L.; Chen, X.; Yang, H.; Chen, C.; Peng, Q.; Chang, C.-R.; Wang, D.; Li, Y. Single-atom Rh/N-doped carbon electrocatalyst for formic acid oxidation. *Nat. Nanotechnol.* **2020**, *15*, 390–397.
- (3) Luo, S.; Chen, W.; Cheng, Y.; Song, X.; Wu, Q.; Li, L.; Wu, X.; Wu, T.; Li, M.; Yang, Q.; Deng, K.; Quan, Z. Trimetallic synergy in intermetallic PtSnBi nanoplates boosts formic acid oxidation. *Adv. Mater.* **2019**, *31*, No. 1903683.
- (4) Zhou, Y.; Yang, Y.; Zhu, X.; Zhang, T.; Ye, D.; Chen, R.; Liao, Q. Novel Superaerophobic Anode with Fern-Shaped Pd Nanoarray for High-Performance Direct Formic Acid Fuel Cell. *Adv. Funct. Mater.* **2022**, *32*, No. 2201872.
- (5) Montaña-Mora, G.; Qi, X.; Wang, X.; Chacón-Borrero, J.; Martínez-Alanis, P. R.; Yu, X.; Li, J.; Xue, Q.; Arbiol, J.; Ibáñez, M.; Cabot, A. Phosphorous incorporation into palladium tin nanoparticles for the electrocatalytic formate oxidation reaction. *J. Electroanal. Chem.* **2023**, *936*, No. 117369.
- (6) Yan, X.; Hu, X.; Fu, G.; Xu, L.; Lee, J. M.; Tang, Y. Facile synthesis of porous Pd₃Pt half-shells with rich "active sites" as efficient catalysts for formic acid oxidation. *Small* **2018**, *14*, No. 1703940.
- (7) Zhang, L.; Ding, L.-X.; Luo, Y.; Zeng, Y.; Wang, S.; Wang, H. PdO/Pd-CeO₂ hollow spheres with fresh Pd surface for enhancing formic acid oxidation. *Chem. Eng. J.* **2018**, *347*, 193–201.
- (8) Liang, W.; Wang, Y.; Zhao, L.; Guo, W.; Li, D.; Qin, W.; Wu, H.; Sun, Y.; Jiang, L. 3D Anisotropic Au@Pt–Pd Hemispherical Nanostructures as Efficient Electrocatalysts for Methanol, Ethanol, and Formic Acid Oxidation Reaction. *Adv. Mater.* **2021**, *33*, No. 2100713.
- (9) Luo, S.; Wang, Y.; Kong, T. C.; Pan, W.; Zhao, X.; Leung, D. Y. Flexible direct formate paper fuel cells with high performance and great durability. *J. Power Sources* **2021**, *490*, No. 229526.
- (10) Copenhaver, T. S.; Purohit, K. H.; Domalaon, K.; Pham, L.; Burgess, B. J.; Manorohtkul, N.; Galvan, V.; Sotex, S.; Gomez, F. A.; Haan, J. L. A microfluidic direct formate fuel cell on paper. *Electrophoresis* **2015**, *36*, 1825–1829.
- (11) Hong, S.; Chung, S.; Park, J.; Hwang, J. P.; Lee, C. H.; Uhm, S.; Bong, S.; Lee, J. Contribution of Interstitial Boron in a Boron-Incorporated Palladium Catalyst Toward Formate Oxidation in an Alkaline Direct Formate Fuel Cell. *ACS Catal.* **2021**, *11*, 4722–4729.
- (12) Jiang, J.; Wieckowski, A. Prospective direct formate fuel cell. *Electrochem. Commun.* **2012**, *18*, 41–43.
- (13) Ding, J.; Liu, Z.; Liu, X.; Liu, J.; Deng, Y.; Han, X.; Zhong, C.; Hu, W. Mesoporous decoration of freestanding palladium nanotube arrays boosts the electrocatalysis capabilities toward formic acid and formate oxidation. *Adv. Energy Mater.* **2019**, *9*, No. 1900955.
- (14) Li, Z.; Chen, F.; Bian, W.; Kou, B.; Wang, Q.; Guo, L.; Jin, T.; Tang, Q.; Pan, B. Surface Pourbaix diagram of AgPd nanoalloys and its application in formate oxidation reaction. *Electrochim. Acta* **2021**, *386*, No. 138465.
- (15) Guo, L.; Jin, T.; Tang, Q.; Wang, J.; Pan, B.; Wang, Q.; Li, Z.; Wang, C.; Liu, J.; Chen, F. Chen, Reconstruction of AgPd Nanoalloy with Oxidation for Formate Oxidation Electrocatalysis. *J. Mater. Chem. A* **2022**, *10*, 13998–14010.
- (16) An, L.; Chen, R. Direct formate fuel cells: A review. *J. Power Sources* **2016**, *320*, 127.
- (17) Chang, J.; Feng, L.; Liu, C.; Xing, W.; Hu, X. An effective Pd–Ni₂P/C anode catalyst for direct formic acid fuel cells. *Angew. Chem., Int. Ed.* **2014**, *53*, 122–126.
- (18) Yi, L.; Chen, J.; Shao, P.; Huang, J.; Peng, X.; Li, J.; Wang, G.; Zhang, C.; Wen, Z. Molten-salt-assisted synthesis of bismuth nanosheets for long-term continuous electrocatalytic conversion of CO₂ to formate. *Angew. Chem., Int. Ed.* **2020**, *59*, 20112–20119.
- (19) Shang, H.; Wang, T.; Pei, J.; Jiang, Z.; Zhou, D.; Wang, Y.; Li, H.; Dong, J.; Zhuang, Z.; Chen, W.; Wang, D.; Zhang, J.; Li, Y. Design of a Single-Atom Indium^{δ+}–N₄ Interface for Efficient Electroreduction of CO₂ to Formate. *Angew. Chem., Int. Ed.* **2020**, *59*, 22465–22469.
- (20) Li, J.; Kuang, Y.; Meng, Y.; Tian, X.; Hung, W.-H.; Zhang, X.; Li, A.; Xu, M.; Zhou, W.; Ku, C.-S.; Chiang, C.-Y.; Zhu, G.; Guo, J.; Sun, X.; Dai, H. Electroreduction of CO₂ to formate on a copper-based electrocatalyst at high pressures with high energy conversion efficiency. *J. Am. Chem. Soc.* **2020**, *142*, 7276–7282.
- (21) Wang, Q.; Chen, F.; Guo, L.; Jin, T.; Liu, H.; Wang, X.; Gong, X.; Liu, Y. Nanoalloying effects on the catalytic activity of the formate oxidation reaction over AgPd and AgCuPd aerogels. *J. Mater. Chem. A* **2019**, *7*, 16122–16135.
- (22) Guo, L.; Chen, F.; Jin, T.; Liu, H.; Zhang, N.; Jin, Y.; Wang, Q.; Tang, Q.; Pan, B. Surface reconstruction of AgPd nanoalloy particles during the electrocatalytic formate oxidation reaction. *Nanoscale* **2020**, *12*, 3469–3481.
- (23) Wang, Q.; Chen, F.; Tang, Q.; Guo, L.; Jin, T.; Pan, B.; Wang, J.; Li, Z.; Kou, B.; Bian, W. AgPdCo hollow nanospheres electrocatalyst with high activity and stability toward the formate electrooxidation. *Nano Res.* **2021**, *14*, 2268–2276.
- (24) Chen, L.; Zhang, L.-R.; Yao, L.-Y.; Fang, Y.-H.; He, L.; Wei, G.-F.; Liu, Z.-P. Metal boride better than Pt: HCP Pd₂B as a superactive hydrogen evolution reaction catalyst. *Energy Environ. Sci.* **2019**, *12*, 3099–3105.
- (25) Xu, W.; Fan, G.; Chen, J.; Li, J.; Zhang, L.; Zhu, S.; Su, X.; Cheng, F.; Chen, J. Nanoporous palladium hydride for electrocatalytic N₂ reduction under ambient conditions. *Angew. Chem., Int. Ed.* **2020**, *59*, 3511–3516.
- (26) Parker, S. F.; Walker, H. C.; Callear, S. K.; Grunewald, E.; Petzold, T.; Wolf, D.; Mobus, K.; Adam, J.; Wieland, S. D.; Jimenez-Ruiz, M.; Albers, P. W. The effect of particle size, morphology and support on the formation of palladium hydride in commercial catalysts. *Chem. Sci.* **2019**, *10*, 480–489.
- (27) Shi, Y.; Schimmenti, R.; Zhu, S.; Venkatraman, K.; Chen, R.; Chi, M.; Shao, M.; Mavrikakis, M.; Xia, Y. Solution-phase synthesis of PdH_{0.706} nanocubes with enhanced stability and activity toward formic acid oxidation. *J. Am. Chem. Soc.* **2022**, *144*, 2556–2568.
- (28) Zhao, Z.; Huang, X.; Li, M.; Wang, G.; Lee, C.; Zhu, E.; Duan, X.; Huang, Y. Synthesis of stable shape-controlled catalytically active β-palladium hydride. *J. Am. Chem. Soc.* **2015**, *137*, 15672–15675.
- (29) Chang, Q.; Kim, J.; Lee, J. H.; Kattel, S.; Chen, J. G.; Choi, S. I.; Chen, Z. Boosting activity and selectivity of CO₂ electroreduction by pre-hydridizing Pd nanocubes. *Small* **2020**, *16*, No. 2005305.
- (30) Liu, J.; Luo, Z.; Li, J.; Yu, X.; Llorca, J.; Nasiou, D.; Arbiol, J.; Meyns, M.; Cabot, A. Graphene-supported palladium phosphide PdP₂ nanocrystals for ethanol electrooxidation. *Appl. Catal., B* **2019**, *242*, 258–266.
- (31) Du, R.; Xiao, K.; Li, B.; Han, X.; Zhang, C.; Wang, X.; Zuo, Y.; Guardia, P.; Li, J.; Chen, J.; Arbiol, J.; Cabot, A. Controlled oxygen doping in highly dispersed Ni-loaded g-C₃N₄ nanotubes for efficient photocatalytic H₂O₂ production. *Chem. Eng. J.* **2022**, *441*, No. 135999.
- (32) Tian, Z.; López-Salas, N.; Liu, C.; Liu, T.; Antonietti, M. C₂N: a class of covalent frameworks with unique properties. *Adv. Sci.* **2020**, *7*, No. 2001767.
- (33) Zhong, W.; Qiu, Y.; Shen, H.; Wang, X.; Yuan, J.; Jia, C.; Bi, S.; Jiang, J. Electronic spin moment as a catalytic descriptor for Fe single-atom catalysts supported on C₂N. *J. Am. Chem. Soc.* **2021**, *143*, 4405–4413.
- (34) Liang, Z.; Yang, D.; Tang, P.; Zhang, C.; Biendicho, J. J.; Zhang, Y.; Llorca, J.; Wang, X.; Li, J.; Heggen, M.; David, J.; Dunin-Borkowski, R. E.; Zhou, Y.; Morante, J. R.; Cabot, A.; Arbiol, J. Atomically dispersed Fe in a C₂N based catalyst as a sulfur host for efficient lithium–sulfur batteries. *Adv. Energy Mater.* **2021**, *11*, No. 2003507.
- (35) Yang, D.; Liang, Z.; Zhang, C.; Biendicho, J. J.; Botifoll, M.; Spadaro, M. C.; Chen, Q.; Li, M.; Ramon, A.; Moghaddam, A. O.;

Llorca, J.; Wang, J.; Morante, J. R.; Arbiol, J.; Chou, S.; Cabot, A. NbSe₂ Meets C₂N: A 2D-2D Heterostructure Catalysts as Multifunctional Polysulfide Mediator in Ultra-Long-Life Lithium–Sulfur Batteries. *Adv. Energy Mater.* **2021**, *11*, No. 2101250.

(36) Yang, D.; Liang, Z.; Tang, P.; Zhang, C.; Tang, M.; Li, Q.; Biendicho, J. J.; Li, J.; Heggen, M.; Dunin-Borkowski, R. E.; Xu, M.; Llorca, J.; Arbiol, J.; Morante, J. R.; Chou, S.-L.; Cabot, A. A High Conductivity 1D π -d Conjugated Metal–Organic Framework with Efficient Polysulfide Trapping-Diffusion-Catalysis in Lithium–Sulfur Batteries. *Adv. Mater.* **2022**, *34*, No. 2108835.

(37) Zhang, C.; Du, R.; Martí-Sánchez, S.; Xiao, K.; Yang, D.; Zhang, C.; Li, C.; Zeng, G.; Chang, X.; He, R.; Arbiol, J.; Li, J.; Biendicho, J. J.; Cabot, A. Tubular C₃N₄ Nanotubes as Metal-Free Sulfur Hosts toward Stable Lithium–Sulfur Batteries. *Energies* **2023**, *16*, 4545.

(38) He, M.; An, W.; Wang, Y.; Men, Y.; Liu, S. Hybrid Metal–Boron Diatomic Site Embedded in C₂N Monolayer Promotes C–C Coupling in CO₂ Electroreduction. *Small* **2021**, *17*, No. 2104445.

(39) Shinde, S. S.; Lee, C. H.; Yu, J.-Y.; Kim, D.-H.; Lee, S. U.; Lee, J.-H. Hierarchically designed 3D holey C₂N aerogels as bifunctional oxygen electrodes for flexible and rechargeable Zn-air batteries. *ACS Nano* **2018**, *12*, 596–608.

(40) Kabiraz, M. K.; Kim, J.; Lee, W.-J.; Ruqia, B.; Kim, H. C.; Lee, S.-U.; Kim, J.-R.; Paek, S.-M.; Hong, J. W.; Choi, S.-I. Ligand Effect of Shape-Controlled β -Palladium Hydride Nanocrystals on Liquid-Fuel Oxidation Reactions. *Chem. Mater.* **2019**, *31*, 5663–5673.

(41) Zhao, Z.; Flores Espinosa, M. M.; Zhou, J.; Xue, W.; Duan, X.; Miao, J.; Huang, Y. Synthesis of surface controlled nickel/palladium hydride nanodendrites with high performance in benzyl alcohol oxidation. *Nano Res.* **2019**, *12*, 1467–1472.

(42) Lin, B.; Wu, X.; Xie, L.; Kang, Y.; Du, H.; Kang, F.; Li, J.; Gan, L. Atomic imaging of subsurface interstitial hydrogen and insights into surface reactivity of palladium hydrides. *Angew. Chem., Int. Ed.* **2020**, *59*, 20348–20352.

(43) Sun, H.-Y.; Ding, Y.; Yue, Y.-Q.; Xue, Q.; Li, F.-M.; Jiang, J.-X.; Chen, P.; Chen, Y. Bifunctional palladium hydride nanodendrite electrocatalysts for hydrogen evolution integrated with formate oxidation. *ACS Appl. Mater. Interfaces* **2021**, *13*, 13149–13157.

(44) Dekura, S.; Kobayashi, H.; Ikeda, R.; Maesato, M.; Yoshino, H.; Ohba, M.; Ishimoto, T.; Kawaguchi, S.; Kubota, Y.; Yoshioka, S.; Matsumura, S.; Sugiyama, T.; Kitagawa, H. The Electronic State of Hydrogen in the α Phase of the Hydrogen-Storage Material PdH(D)₂: Does a Chemical Bond Between Palladium and Hydrogen Exist? *Angew. Chem., Int. Ed.* **2018**, *130*, 9971–9975.

(45) Aboud, S.; Wilcox, J. A density functional theory study of the charge state of hydrogen in metal hydrides. *J. Phys. Chem. C* **2010**, *114*, 10978–10985.

(46) Wang, Z.; Dai, Z.; Wang, S.; Zhang, H.; Tian, W.; Xu, Y.; Li, X.; Wang, L.; Wang, H. J. Enhancing electrochemical ammonia synthesis on palladium nanorods through surface hydrogenation. *Chem. Eng. J.* **2021**, *416*, No. 129105.

(47) Zhang, J.; Chen, M.; Li, H.; Li, Y.; Ye, J.; Cao, Z.; Fang, M.; Kuang, Q.; Zheng, J.; Xie, Z. Stable palladium hydride as a superior anode electrocatalyst for direct formic acid fuel cells. *Nano Energy* **2018**, *44*, 127–134.

(48) Yu, X.; Liu, J.; Li, J.; Luo, Z.; Zuo, Y.; Xing, C.; Llorca, J.; Natsiou, D.; Arbiol, J.; Pan, K.; Kleinhanns, T.; Xie, Y.; Cabot, A. Phosphorous incorporation in Pd₂Sn alloys for electrocatalytic ethanol oxidation. *Nano Energy* **2020**, *77*, No. 105116.

(49) Zhou, M.; Liu, J.; Ling, C.; Ge, Y.; Chen, B.; Tan, C.; Fan, Z.; Huang, J.; Chen, J.; Liu, Z.; Huang, Z.; Ge, J.; Cheng, H.; Chen, Y.; Dai, L.; Yin, P.; Zhang, X.; Yun, Q.; Wang, J.; Zhang, H. Synthesis of Pd₃Sn and PdCuSn nanorods with L1₂ phase for highly efficient electrocatalytic ethanol oxidation. *Adv. Mater.* **2022**, *34*, No. 2106115.

(50) Zhou, X.; Ma, Y.; Ge, Y.; Zhu, S.; Cui, Y.; Chen, B.; Liao, L.; Yun, Q.; He, Z.; Long, H.; Li, L.; Huang, B.; Luo, Q.; Zhai, L.; Wang, X.; Bai, L.; Wang, G.; Guan, Z.; Chen, Y.; Lee, C.-S.; Wang, J.; Ling, C.; Shao, M.; Fan, Z.; Zhang, H. Preparation of Au@Pd Core–Shell

Nanorods with fcc-2H-fcc Heterophase for Highly Efficient Electrocatalytic Alcohol Oxidation. *J. Am. Chem. Soc.* **2022**, *144*, 547–555.

(51) Wang, Q.; Chen, F.; Tang, Q.; Guo, L.; Gebremariam, T. T.; Jin, T.; Liu, H.; Kou, B.; Li, Z.; Bian, W. Transition from core-shell to Janus segregation pattern in AgPd nanoalloy by Ni doping for the formate oxidation. *Appl. Catal., B* **2020**, *270*, No. 118861.

(52) Tang, Q.; Chen, F.; Wang, Q.; Jin, T.; Guo, L.; Wu, Y.; Yu, S.; Li, Z. Surface reconstruction of AgPdF and AgPd nanoalloys under the formate oxidation reaction. *J. Mater. Chem. A* **2021**, *9*, 23072–23084.



Contents lists available at ScienceDirect

Journal of Electroanalytical Chemistry

journal homepage: www.elsevier.com/locate/jelechem

Phosphorous incorporation into palladium tin nanoparticles for the electrocatalytic formate oxidation reaction

Guillem Montaña-Mora^a, Xueqiang Qi^{a,b,*}, Xiang Wang^a, Jesus Chacón-Borrero^a, Paulina R. Martinez-Alanis^a, Xiaoting Yu^c, Junshan Li^d, Qian Xue^b, Jordi Arbiol^{e,f}, Maria Ibáñez^{g,*}, Andreu Cabot^{a,f,*}

^aCatalonia Institute for Energy Research – IREC, Jardins de les Dones de Negre 1, 2^a pl., Sant Adrià de Besòs, Spain

^bSchool of Chemistry and Chemical Engineering, Chongqing University of Technology, Chongqing 400054, China

^cJiangsu Key Laboratory of Advanced Catalytic Materials and Technology, School of Petrochemical Engineering, Changzhou University, Changzhou 213164, China

^dInstitute of Advanced Study, Chengdu University, Chengdu 610106, China

^eCatalan Institute of Nanoscience and Nanotechnology (ICN2), CSIC and BIST, Campus UAB, Bellaterra, 08193 Barcelona, Catalonia, Spain

^fICREA Pg. Lluís Companys, 08010 Barcelona, Catalonia, Spain

^gIST Austria, Am Campus 1, 3400 Klosterneuburg, Austria

ARTICLE INFO

Keywords:

Formate oxidation reaction
Electrocatalysis
Palladium tin phosphide
Direct formate fuel cell

ABSTRACT

The deployment of direct formate fuel cells (DFFCs) relies on the development of active and stable catalysts for the formate oxidation reaction (FOR). Palladium, providing effective full oxidation of formate to CO₂, has been widely used as FOR catalyst, but it suffers from low stability, moderate activity, and high cost. Herein, we detail a colloidal synthesis route for the incorporation of P on Pd₂Sn nanoparticles. These nanoparticles are dispersed on carbon black and the obtained composite is used as electrocatalytic material for the FOR. The Pd₂Sn_{0.8}P-based electrodes present outstanding catalytic activities with record mass current densities up to 10.0 A mg_{cat}⁻¹, well above those of Pd_{1.8}Sn/C reference electrode. These high current densities are further enhanced by increasing the temperature from 25 °C to 40 °C. The Pd₂Sn_{0.8}P electrode also allows for slowing down the rapid current decay that generally happens during operation and can be rapidly re-activated through potential cycling. The excellent catalytic performance obtained is rationalized using density functional theory (DFT) calculations.

1. Introduction

Fuel cells, characterized by high efficiencies of conversion from chemical to electrical energy, are an appealing alternative to conventional fossil fuel-based combustion technologies. Among the possible energy carriers, liquid and solid C₁ and C₂ fuels, such as ethanol, methanol, formic acid, or formate, are particularly attractive. Such fuels can be directly produced from CO₂ reduction, thus enabling a zero-CO₂ energy cycle, and offer advantages in terms of safety, storage, and transportation over carbon-free energy carriers such as hydrogen, hydrazine, or ammonia [1].

Direct formic acid fuel cells (DFAFCs) have received special attention due to their high energy density, low fuel crossover, and superior theoretical cell potential of 1.45 V, which is well above that of direct ethanol fuel cells, 1.14 V, and direct methanol fuel cells, 1.21 V. Despite these advantages, DFAFCs have not reached the market

because of drawbacks associated with the use of an acid medium, including moderate stability related to the degradation of the electrodes and membrane, and the toxicity and corrosiveness of formic acid at high concentration.

As an alternative to DFAFCs, direct formate fuel cells (DFFCs) have received much less attention despite their several key advantages [2–7]. The use of a solid formate salt is beneficial in terms of storage and transportation over liquid formic acid. Formate is also characterized by much lower toxicity and corrosiveness than formic acid, and therefore it can be used at higher concentrations [3,6]. Besides, DFFC present faster kinetics due to the rapid O₂ reduction reaction (ORR) kinetics in alkaline medium when compared with an acid environment [8].

However, the performance and overall cost-effectiveness of DFFCs strongly depend on the performance of the catalyst activating the formate oxidation reaction (FOR). FOR can proceed through two main

* Corresponding authors at: School of Chemistry and Chemical Engineering, Chongqing University of Technology, Chongqing, 400054, China (X. Qi); IST Austria, Am Campus 1, 3400 Klosterneuburg, Austria (M. Ibáñez); Catalonia Institute for Energy Research – IREC, Jardins de les Dones de Negre 1, 2^a pl., Sant Adrià de Besòs, Spain (X. Qi, A. Cabot).

E-mail addresses: xoqi@cqut.edu.cn (X. Qi), mibanez@ist.ac.at (M. Ibáñez), acabot@irec.cat (A. Cabot).

<https://doi.org/10.1016/j.jelechem.2023.117369>

Received 20 December 2022; Received in revised form 15 March 2023; Accepted 20 March 2023

Available online 23 March 2023

1572-6657/© 2023 Elsevier B.V. All rights reserved.

pathways [9]. A first pathway is the direct formate oxidation to CO_2 . This is the most convenient mechanism for electrochemical application because it is the fastest and most energetically efficient. The second pathway is the indirect reaction that involves the initial formation of intermediate CO_{ads} that is afterward oxidized to CO_2 .

As a drawback of DFFCs, the demanding FOR requires the use of noble metal catalysts such as Pt and Pd. Among FOR electrocatalysts, Pt generally displays the highest initial activities, but it also suffers from poor stability [10–14]. Pt-based catalysts generally drive FOR through the indirect path, producing CO_{ads} that strongly bind to the surface active sites, thus rapidly deactivating the catalyst [15]. Besides being slightly more abundant and less expensive than Pt, Pd also shows higher long-term activity and durability, which has positioned Pd as the state-of-the-art FOR catalyst [2–4,16–20]. However, pure Pd catalysts still suffer from too elevated cost, and unsatisfactory activity and durability for the deployment of cost-effective commercial DFFC [21]. While competition between the two FOR mechanisms exist in pure Pd catalysts, Pd oxidizes formate mainly through the direct pathway [22]. During this process, formate decomposes into surface adsorbed H_{ads} and CO_{2ads} [23]. H_{ads} binds strongly to the Pd active sites, which is generally assumed to block the adsorption of unreacted formate molecules and, consequently, reduce the catalytic activity [24–26]. Besides, the production of CO_{ads} through the minoritarian indirect reaction pathway also affects the catalyst's long-term activity.

Several strategies have been developed to overcome the limitations of Pd catalysts. The main approach is the alloying of palladium with other metallic or non-metallic elements. This alloying targets three main objectives: i) to optimize the palladium electronic energy levels to tune the adsorption energy of precursors/intermediates/products; ii) to provide additional surface adsorption/reaction sites; and iii) to minimize the amount of Pd used. In this scenario, numerous noble metal Pd-based alloys have been tested, including Pd–Ag [27–29], Pd–Rh [30], Pd–Au [31,32], Pd–Ag–Ir [33], Pd–Ag–Ru [34], Pd–Ag–Rh [35], or Pd–Au–Ag [36]. Besides, the alloying of Pd with abundant metals such as Sn, Cu, Ni, or Co is not only particularly interesting in terms of cost but also to promote the interaction with hydroxyl groups [24,37,38]. The formation of M–OH weakens the adsorption of poisoning intermediates such as CO_{ads} and H_{ads} . As an example, J. Noborikawa et al. demonstrated $\text{Pd}_{87}\text{Cu}_{13}/\text{C}$ to have 1.8 times higher activity than monometallic Pd/C [39]. Qiao Wang et al. showed that the incorporation of Cu into AgPd resulted in a factor 1.2 mass activity increment and improved stability compared to the binary compound [24]. Besides, Sankar et al. reported $\text{Pd}_{2.3}\text{Co}/\text{C}$ with a mass activity of $2.5 \text{ A mg}_{Pd}^{-1}$ and PdNi/VC with $4.5 \text{ A mg}_{Pd}^{-1}$, well above that of Pd/C [38,40].

Among the different Pd alloys, PdSn is particularly interesting both in terms of cost and performance in oxidation reactions. We and others have demonstrated that the incorporation of tin remarkably improves the palladium resistance towards poisoning and the electrooxidation catalytic activity by both electronic and geometrical effects [41–48]. Several previous works have tested Pd–Sn alloys for the formic acid oxidation reaction (FAOR) [49–53]. Liu et al. showed Pd_2Sn as the most effective catalyst in comparison with other Pd_xSn_y alloys and pure Pd/C [51]. Wang et al. obtained PdSn alloy nanoparticles on carbon nanotubes with 1.81 times higher activity and superior stability towards FAOR than the palladium counterpart. Additionally, Hwang et al. deposited PdSn on Ti and demonstrated excellent performance in the interconversion between CO_2 and formic acid [52,53]. Surprisingly, very few studies have focused on the application of Pd–Sn alloys as FOR electrocatalysts in DFFCs. Recently, Sasidharan et al. reported a $\text{Pd}_{85}\text{Sn}_{15}$ alloy with an excellent FOR activity of 5.7 A mg^{-1} , which is more than 3.5 times that of Pd/C, and prominent stability [54]. Additionally, Hosseini-Benhangi developed a novel class of non-metal flow batteries using bifunctional CO_2 /formate electrocatalysis based on binary PdSn and ternary PdSnPb and PdSnIn alloys [55].

Phosphorus is an inexpensive non-metallic element with abundant valence electrons. Its alloying with metals modify the metals electronic state, facilitating the adsorption of hydroxyl species and hampering the adsorption of poisoning compounds and the dissolution of metal ions from the catalyst surface. To the best of our knowledge, no studies have reported the use of palladium phosphides for FOR. However, Pd–P and Pd–M–P alloys have been demonstrated as efficient catalysts for the FAOR [56–61]. As an example, the ternary PdNiP exhibits a remarkable improvement in electrocatalytic activity towards formic acid, methanol, ethanol oxidation, and hydrogen evolution reactions compared to the binary PdNi [62–65]. Besides, we demonstrated the incorporation of P to PdSn alloys to significantly improve the catalyst performance towards the ethanol oxidation reaction [66].

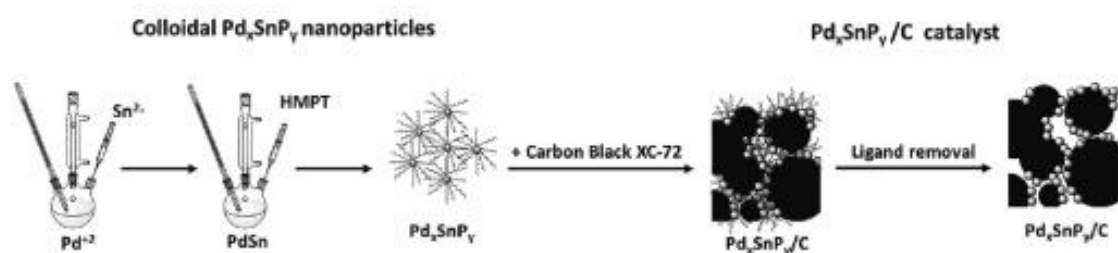
In this work, we demonstrate that the incorporation of phosphorus into PdSn nanoparticles results in a significant improvement of the FOR electrocatalytic performance. Using a colloidal synthesis method, Pd–sn–P particles are prepared and afterward supported onto carbon black. The FOR activity and stability of the produced composite electrodes are experimentally analyzed. Besides, the outstanding performances obtained are rationalized using DFT calculations.

2. Results and discussion

2.1. Catalyst physico-chemical properties

As detailed in the experimental section (Supporting Information, SI), phosphorus-containing palladium tin-based catalysts were prepared through a four-step approach (Scheme 1). In the first step, colloidal Pd–Sn nanoparticles were grown from the co-reduction of Pd(acac)₂ and Sn(OAc)₂ at 230 °C using oleylamine as both solvent and reducing agent, and trioctylphosphine and methylamine hydrochloride as stabilizers and shape-directing agents [67]. Afterwards, phosphorus was incorporated into the Pd–Sn nanoparticles through reaction with hexamethylphosphorous triamide (HMPT) at 300 °C. In a third step, Pd–sn–P nanoparticles were supported onto carbon black Vulcan XC-72 to maximize the particle dispersion for electrochemical application. Once supported, the nanoparticle surface ligands were removed using an acid treatment and posterior annealing under an inert atmosphere to obtain a ligand-free electrocatalyst [67–74].

Transmission electron microscopy (TEM) analysis of the produced Pd–sn–P nanoparticles shows them to be characterized by elongated geometries with an average length of 20 nm and an average thickness of 9 nm (Fig. 1a). Scanning electron microscopy with energy-dispersive X-ray spectroscopy (SEM-EDS) and inductively coupled plasma mass spectrometry (ICP-MS) data confirmed the presence of the three elements with an atomic ratio of Pd/Sn/P = 2/0.8/1 (Fig. S1b). The powder X-ray diffraction (XRD) pattern of the $\text{Pd}_2\text{Sn}_{0.8}\text{P}$ particles resembles that of an orthorhombic Pd_2Sn phase with space group $Pnma$ (JCPDS 01–89–2057, Fig. 1b). Fig. 1c shows a representative high-resolution TEM (HRTEM) image of the $\text{Pd}_2\text{Sn}_{0.8}\text{P}$ nanoparticles. The fast Fourier transform (FFT) of the magnified detail matched that of the Pd_2Sn orthorhombic $Pnma$ phase, consistent with XRD data. No additional phases, particularly the binary phosphides SnP (JCPDS 03–065–9787) and PdP (JCPDS 01–077–1421), were detected by HRTEM and XRD analyses (Figure S5). Fig. 1d displays a TEM image of the $\text{Pd}_2\text{Sn}_{0.8}\text{P}$ particles homogeneously dispersed onto carbon black, after the purification and annealing process. High-angle annular dark-field scanning transmission electron microscopy (HAADF-STEM) and electron energy loss spectroscopy (EELS) analysis of the supported particles showed a uniform distribution of the three elements throughout each nanoparticle and between nanoparticles (Fig. 1e). To evaluate the electrocatalytic activity variation with the incorporation of phosphorus, binary $\text{Pd}_{1.8}\text{Sn}$ and ternary $\text{Pd}_2\text{Sn}_{0.8}\text{P}_{1.8}$ containing a larger amount of P were also prepared (Fig. S1a and S1c). $\text{Pd}_{1.8}\text{Sn}$ and Pd_2



Scheme 1. Schematic view of the process used to prepare the palladium tin phosphide-based catalyst.

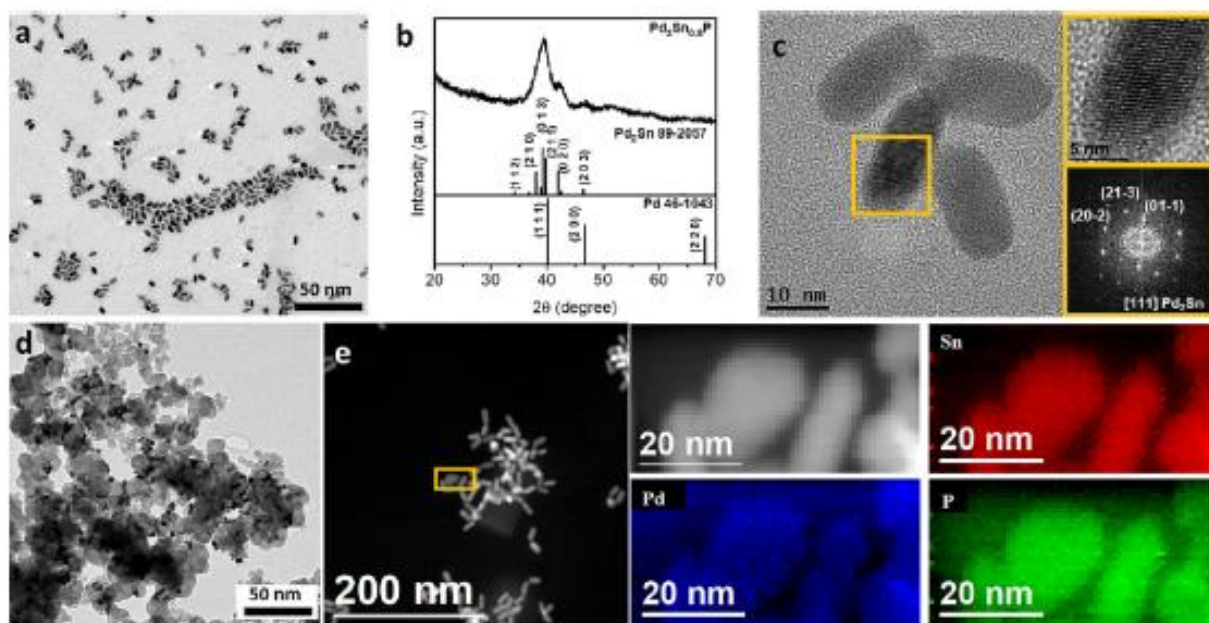


Fig. 1. Structural and chemical characterization of Pd₂Sn_{0.8}P nanoparticles. (a) TEM micrograph. (b) XRD pattern. (c) HRTEM micrograph, detail of the orange squared region and its corresponding indexed FFT. (d) TEM image of the Pd₂Sn_{0.8}P nanoparticles supported onto carbon black. (e) HAADF-STEM general image of the Pd₂Sn_{0.8}P nanoparticles (left) and HAADF-STEM magnified detail of the orange squared region on the left with the corresponding EELS elemental composition maps (right): Pd (blue), Sn (red) and P (green). (For interpretation of the references to colour in this figure legend, the reader is referred to the web version of this article.)

Sn_{0.8}P_{1.8} also displayed elongated morphologies (Figure S2 and S3, respectively) and a structure similar to the orthorhombic Pd₂Sn phase (Figure S4 and S6, respectively).

Fig. 2 displays the X-ray photoelectron spectroscopy (XPS) spectra of Pd₂Sn_{0.8}P nanoparticles. The high-resolution Pd 3d XPS spectrum has the main doublet at 335.6 eV (3d_{5/2}) attributed to metallic Pd,

and another less intense doublet at 337.2 eV (3d_{5/2}) assigned to Pd²⁺. The Sn 3d XPS spectrum also displays two doublets, at 484.8 eV (Sn 3d_{5/2}) and 487.0 eV (Sn 3d_{3/2}), that are assigned to a metallic Sn and an oxidized Sn²⁺ component, respectively. In this case, the oxidized Sn component is majoritarian. Figure S7 shows a comparison of the XPS spectra of Pd-Sn alloys with and without phosphorous.

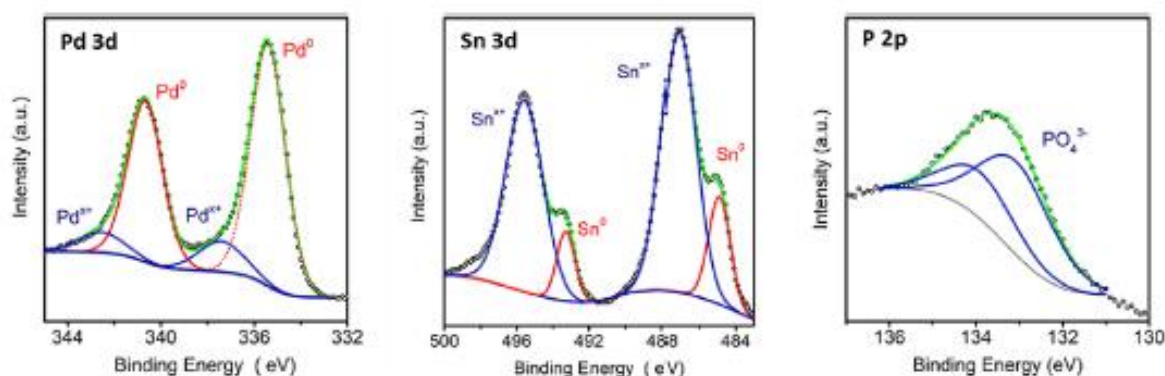


Fig. 2. High-resolution Pd 3d, Sn 3d, and P 2p XPS spectra of the Pd₂Sn_{0.8}P catalyst.

mulation of adsorbed intermediate species (H_{ads} and/or CO_{ads}) that deactivate the catalyst active sites [22,25]. $Pd_{1.6}Sn/C$ was deactivated after 2000 s while for both phosphide catalysts the mass current was still ca. $0.1 \text{ A mg}_{Pd}^{-1}$ after 5500 s and 4200 s for $Pd_2Sn_{0.8}P/C$ and $Pd_2Sn_{0.8}P_{1.8}/C$, respectively. Thus, the incorporation of P not only increases the FOR activity but also the stability against the adsorption of poisoning species.

Fig. 4 shows the dependence on temperature of the FOR electrochemical activity obtained from the three palladium-based catalysts. At 40°C , the current density significantly increased and the onset potential diminished for the phosphorized catalysts. This improved performance is related to the fact that a higher temperature lowers the relative reaction energy barrier, decreasing the overpotential and facilitating the desorption of CO_2 . The faster product desorption allows a higher rate of unreacted formate molecules to reach the catalyst's active sites, incrementing the current density.

To remove the accumulated poisoning species, a rapid potential scan to oxidize and reduce the Pd surface was tested. Fig. 5 shows the regeneration capacity of the three tested catalysts. After every 30 min of chronoamperometric test, the catalysts were re-activated by performing 2 CV cycles in the potential range -0.9 V to 0.4 V (vs Hg/HgO). All three catalysts demonstrate a high activity recovery and stability throughout the process.

3. DFT calculations

DFT calculations were used to gain insight into the mechanism behind the outstanding FOR performance experimentally measured from $Pd_2Sn_{0.8}P$ catalysts. In aqueous conditions, the $HCOO^-$ oxidation to CO_2 could occur through the following elementary steps:



The top-view and side-view structures of the optimized pristine Pd_2Sn and $Pd_2Sn_{0.8}P$ and the corresponding adsorption structures of $*HCOO$ and $*CO_2$ are shown in Figure S10. The computational Gibbs free energy of $*HCOO$ oxidation to $*CO_2$ was calculated comparatively on Pd_2Sn and $Pd_2Sn_{0.8}P$ (Fig. 6a,b). It can be found that the free energy decreases in the first and second steps involving the $*HCOO$ oxidation to adsorbed $*CO_2$, thus they are energy-favorable exothermic reactions. However, the last step from adsorbed $*CO_2$ to free CO_2 is an endothermic reaction, involving an energy barrier of 0.57 eV on Pd_2Sn (001) and just 0.33 eV on $Pd_2Sn_{0.8}P$ (001). Thus it can be deemed that the $Pd_2Sn_{0.8}P$ (001) performs better activity than the Pd_2Sn (001) because of a significantly decreased adsorption energy of CO_2 after the incorporation of phosphorous into the Pd_2Sn system. That is, the adsorption energy of CO_2 on $Pd_2Sn_{0.8}P$ (001) surface is only about -0.33 eV , which is 0.24 eV above that on Pd_2Sn (001) surface (Fig. 6b). The modulation of the electronic structure of $Pd_2Sn_{0.8}P$ through introducing P to the Pd-Sn system may play a dominant role during the reaction [75,76]. In addition, the adsorption energy of $HCOO$ on Pd_2Sn (001) is -1.23 eV , and -1.42 eV on $Pd_2Sn_{0.8}P$ (001). We need to point out that we further calculated the indirect FOR pathway, but this calculation yielded an energy barrier of the oxidation of $HCOO$ to CO of more than 3 eV on $Pd_2Sn_{0.8}P$, pointing at a less favorable path.

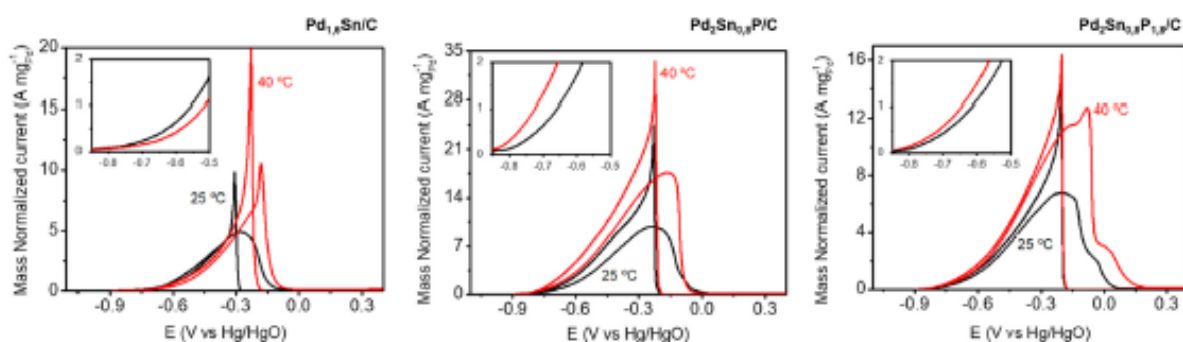


Fig. 4. CV voltammograms of $Pd_{1.6}Sn/C$, $Pd_2Sn_{0.8}P/C$ and $Pd_2Sn_{0.8}P_{1.8}/C$ at 25°C (black line) and 40°C (red line). (For interpretation of the references to colour in this figure legend, the reader is referred to the web version of this article.)

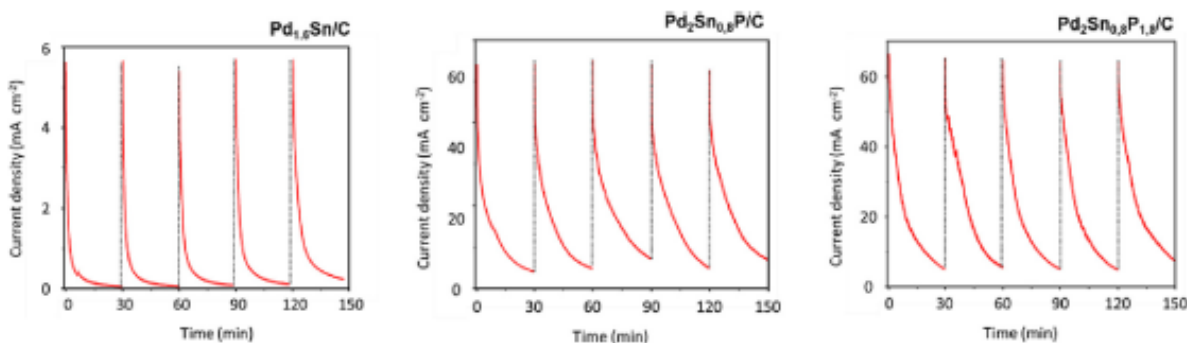


Fig. 5. Successive chronoamperometric curves of the $Pd_{1.6}Sn/C$, $Pd_2Sn_{0.8}P/C$ and $Pd_2Sn_{0.8}P_{1.8}/C$ catalysts regenerated every 30 min using two CV cycles (vertical lines).

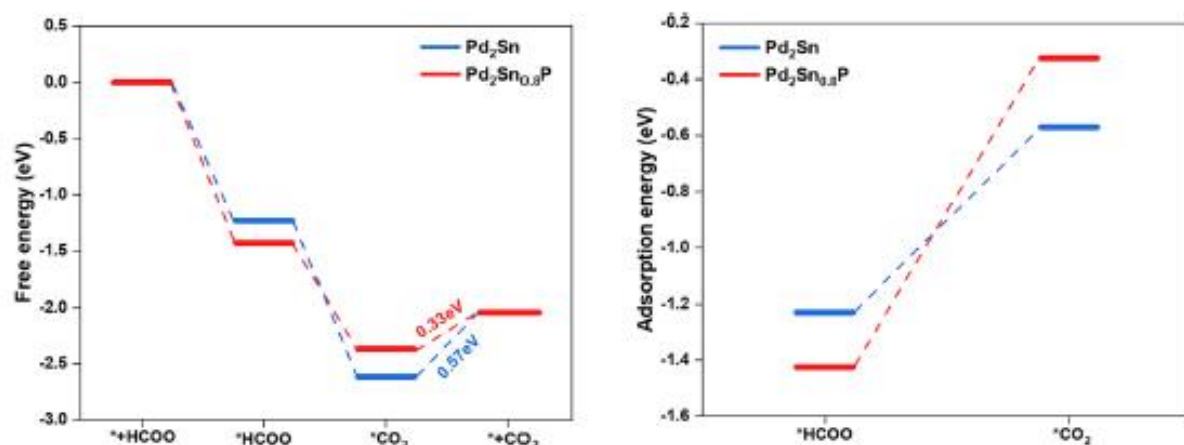


Fig. 6. (a) Change of Gibbs free energy according to reactions of (4–6) on Pd₂Sn and Pd₂Sn_{0.8}P. (b) Adsorption energy of HCOO and CO₂ on Pd₂Sn and Pd₂Sn_{0.8}P.

The decreased interaction after P doping was further confirmed by the calculation of the charge density difference as shown in Fig. 7. The moderate difference in HCOO adsorption energy is also reflected in the charge density difference in HCOO-Pd₂Sn and HCOO-Pd₂Sn_{0.8}P systems (Fig. 7a,c). A significantly lower charge redistribution difference between CO₂ and Pd₂Sn_{0.8}P (001) in Fig. 7b was obtained compared with the system CO₂-Pd₂Sn (001) in Fig. 7d, implying a lower interaction. Thus, the desorption of CO₂ from Pd₂Sn_{0.8}P (001) is much easier than from Pd₂Sn, which facilitates the re-exposure of active sites on the surface. The partial density of states (PDOS) is shown in Fig. 7e. The interaction of the p orbital of P and the d orbital of Pd can be

found around the Fermi level. The d band of Pd was expanded after the P doping. The d-band center of Pd₂Sn is -2.82 eV, while it decreased to -3.34 eV in the Pd₂Sn_{0.8}P. This decrease in the d-band center explains the decreased adsorption energy for the adsorbed species.

4. Conclusions

In summary, we demonstrated that through a phosphorization process, the electrocatalytic performance of Pd-Sn catalysts towards FOR

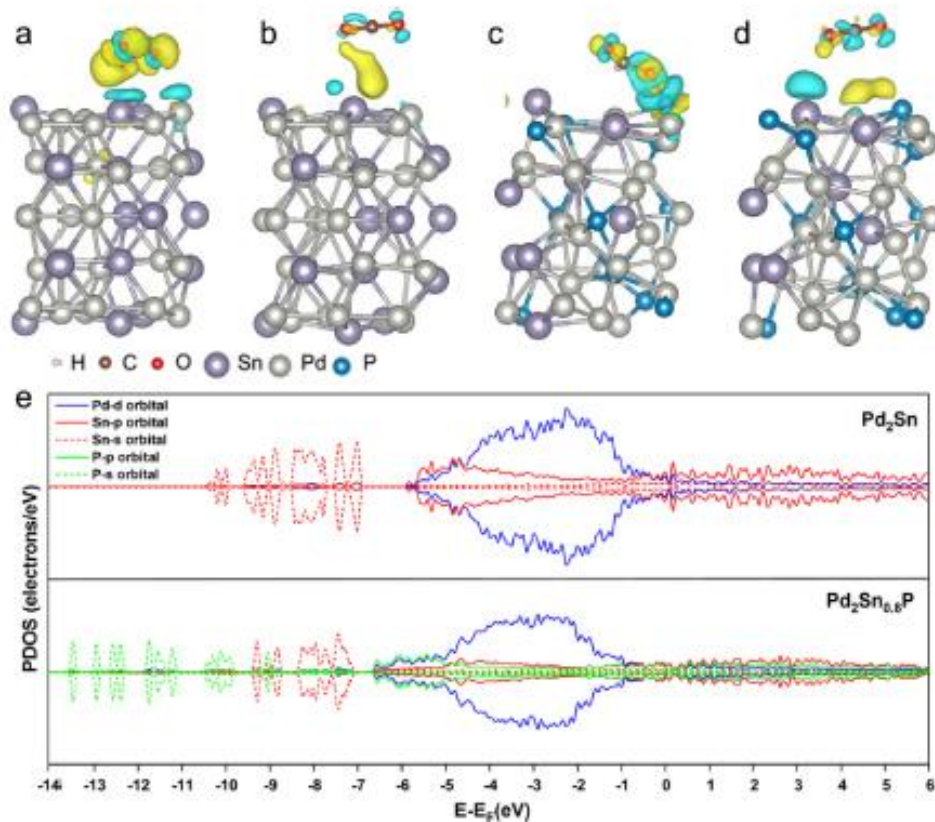


Fig. 7. Charge density difference plots of (a) Pd₂Sn-HCOO, (b) Pd₂Sn-CO₂, (c) Pd₂Sn_{0.8}P-HCOO and (d) Pd₂Sn_{0.8}P-CO₂. The isosurface value is $0.00025 \text{ e} \text{ \AA}^{-3}$. The blue region means charge depletion while the yellow region means charge accumulation. (e) PDOS of Pd₂Sn and Pd₂Sn_{0.8}P. (For interpretation of the references to colour in this figure legend, the reader is referred to the web version of this article.)

can be strongly enhanced. Palladium tin phosphide catalysts were obtained by a colloidal process, in which the binary Pd-Sn was first obtained and, subsequently, phosphorized by HMPPT at 300 °C. Pd₂-Sn_{0.8}P/C catalysts exhibited not only higher activity and stability than Pd_{1.6}Sn/C and Pd/C catalysts but also the highest mass-specific current densities reported so far. Furthermore, activity can be boosted by increasing the temperature from 25 °C to 40 °C. While a rapid current decay throughout the chronoamperometric test was obtained, especially for Pd/C and Pd_{1.6}Sn/C samples, the catalysts could be regenerated using two CV cycles. Finally, DFT results confirmed that the presence of P favors the desorption of CO₂ thus reducing the energy barrier of the rate-limiting step.

CRedit authorship contribution statement

Guillem Montaña-Mora: Conceptualization, Investigation, Methodology, Writing – original draft. **Xueqiang Qi:** Software, Formal analysis, Writing – original draft, Writing – review & editing. **Xiang Wang:** Investigation. **Jesus Chacón-Borrero:** Formal analysis, Software. **Paulina R. Martínez-Alanis:** Resources. **Xiaoting Yu:** Methodology. **Junshan Li:** Methodology. **Qian Xue:** Software, Formal analysis. **Jordi Arbiol:** Writing – review & editing, Formal analysis, Resources. **Maria Ibáñez:** Resources, Supervision. **Andreu Cabot:** Conceptualization, Supervision, Writing – review & editing, Project administration.

Declaration of Competing Interest

The authors declare that they have no known competing financial interests or personal relationships that could have appeared to influence the work reported in this paper.

Acknowledgements

This work was carried out within the framework of the project Combenergy, PID2019-105490RB-C32, financed by the Spanish MCIN/AEI/10.13039/501100011033. ICN2 is supported by the Severo Ochoa program from Spanish MCIN / AEI (Grant No.: CEX2021-001214-S). IREC and ICN2 are funded by the CERCA Programme from the Generalitat de Catalunya. Part of the present work has been performed in the frameworks of the Universitat de Barcelona Nanoscience PhD program. ICN2 acknowledges funding from Generalitat de Catalunya 2021SGR00457. This study was supported by MCIN with funding from European Union NextGenerationEU (PRTR-C17.11) and Generalitat de Catalunya. The authors thank the support from the project NANOGEN (PID2020-116093RB-C43), funded by MCIN/AEI/10.13039/501100011033/ and by "ERDF A way of making Europe", by the European Union. The project on which these results are based has received funding from the European Union's Horizon 2020 research and innovation programme under Marie Skłodowska-Curie grant agreement No. 801342 (Tecnospring INDUSTRY) and the Government of Catalonia's Agency for Business Competitiveness (ACCIÓ). J. Li is grateful for the project supported by the Natural Science Foundation of Sichuan (2022NSFSC1229). M.L. acknowledges funding by ISTA and the Werner Siemens Foundation.

Appendix A. Supplementary data Additional information for experimental and theoretical methods. SEM-EDS and XRD analysis of Pd_{1.6}Sn, Pd₂Sn_{0.8}P, and Pd₂Sn_{0.8}P_{1.8}. TEM images of Pd_{1.6}Sn and Pd₂Sn_{0.8}P_{1.8}. Catalysts regeneration of the three catalysts. Optimized structures before and after the adsorption of *HCOO and *CO₂ on Pd₂Sn (a-c) and Pd₂Sn_{0.8}P

Supplementary data to this article can be found online at <https://doi.org/10.1016/j.jelechem.2023.117369>.

References

- [1] T. Vo, K. Purohit, C. Nguyen, B. Biggs, S. Mayoral, J.L. Haan, Formate: An Energy Storage and Transport Bridge between Carbon Dioxide and a Formate Fuel Cell in a Single Device, *ChemSusChem* 8 (2015) 3853–3858.
- [2] X. Su, Z. Pan, L. An, Performance characteristics of a passive direct formate fuel cell, *Int. J. Energy Res.* 43 (2019) 7433–7443.
- [3] A.M. Bartrom, J. Ta, T.Q. Nguyen, J. Her, A. Donovan, J.L. Haan, Optimization of an anode fabrication method for the alkaline Direct Formate Fuel Cell, *J. Power Sources* 229 (2013) 234–238.
- [4] L.Q. Wang, M. Bellini, J. Filippi, M. Follero, A. Lavacchi, M. Innocenti, A. Marchionni, H.A. Miller, F. Vizza, Energy efficiency of platinum-free alkaline direct formate fuel cells, *Appl. Energy* 175 (2016) 479–487.
- [5] K. Tran, T.Q. Nguyen, A.M. Bartrom, A. Sadiki, J.L. Haan, A fuel-flexible alkaline direct liquid fuel cell, *Fuel Cells* 14 (2014) 834–841.
- [6] J. Jiang, A. Wledekowski, Prospective direct formate fuel cell, *Electrochem. Commun.* 18 (2012) 41–43.
- [7] A.M. Bartrom, J.L. Haan, The direct formate fuel cell with an alkaline anion exchange membrane, *J. Power Sources* 214 (2012) 68–74.
- [8] X. Ge, A. Sumbaja, D. Wu, T. An, B. Li, F.W.T. Goh, T.S.A. Hor, Y. Zong, Z. Liu, Oxygen reduction in alkaline media: From mechanisms to recent advances of catalysts, *ACS Catal.* 5 (2015) 4643–4667.
- [9] L. An, R. Chen, Direct formate fuel cells: A review, *J. Power Sources* 320 (2016) 127–139.
- [10] M. Rosenbaum, U. Schröder, F. Scholz, Investigation of the electrocatalytic oxidation of formate and ethanol at platinum black under microbial fuel cell conditions, *J. Solid State Electrochem.* 10 (10) (2006) 872–878.
- [11] S.-H. Han, H.-M. Liu, J. Bai, X.L. Tian, R.Y. Xia, J.-H. Zeng, J.-X. Jiang, Y.u. Chen, Platinum-Silver Alloy Nanoballoon Nanoassemblies with Super Catalytic Activity for the Formate Electrooxidation, *ACS Appl. Energy Mater.* 1 (3) (2018) 1252–1258.
- [12] S.G. da Silva, J.C.M. Silva, G.S. Buzzo, A.O. Neto, M.H.M.T. Assumpção, Use of PtAu/c electrocatalysts toward formate oxidation: Electrochemical and fuel cell considerations, *Mater. Renew. Sustain. Energy* 5 (4) (2016).
- [13] X. Yu, A. Manthiram, Catalyst-selective, scalable membraneless alkaline direct formate fuel cells, *Appl. Catal. B Environ.* 165 (2015) 63–67.
- [14] A. Nacys, V. Kovalevskij, E. Norius, An Enhanced Oxidation of Formate on PdNi / Ni Foam Catalyst in an Alkaline Medium, (2022).
- [15] J. John, H. Wang, E.D. Rus, H.D. Abruna, Mechanistic studies of formate oxidation on platinum in alkaline medium, *J. Phys. Chem. C* 116 (2012) 5810–5820.
- [16] J. Ding, Z. Liu, X. Liu, J. Liu, Y. Deng, X. Han, C. Zhong, W. Hu, Mesoporous Decoration of Freestanding Palladium Nanoribbons Boosts the Electrocatalysis Capabilities toward Formic Acid and Formate Oxidation, *Adv. Energy Mater.* 9 (2019) 1–8.
- [17] V. Galvan, D.E. Glass, A.P. Baxter, G.K.S. Prakash, Reduced Graphene Oxide Supported Palladium Nanoparticles for Enhanced Electrocatalytic Activity toward Formate Electrooxidation in an Alkaline Medium, *ACS Appl. Energy Mater.* 2 (10) (2019) 7104–7111.
- [18] M.V. Pagliaro, M. Bellini, J. Filippi, M.G. Follero, A. Marchionni, H.A. Miller, W. Oberhauser, F. Vizza, Hydrogen production from the electrooxidation of methanol and potassium formate in alkaline media on carbon supported Rh and Pd nanoparticles, *Inorganica Chim. Acta* 470 (2018) 263–269.
- [19] X. Li, H. Hodson, C. Batchelor-McMuley, L. Shao, R.G. Compton, Improving Formate and Methanol Fuels: Catalytic Activity of Single Pd Coated Carbon Nanotubes, *ACS Catal.* 6 (2016) 7118–7124.
- [20] H. Hwang, S. Hong, J.W. Kim, J. Lee, Optimized electrode structure for performance and mechanical stability in a direct formate fuel cell using cation ionomer, *Sustain. Energy Fuels* 4 (4) (2020) 1899–1907.
- [21] S. Zhang, Y. Shao, G. Yin, Y. Lin, Recent progress in nanostructured electrocatalysts for PEM fuel cells, *J. Mater. Chem. A* 1 (2013) 4631–4641.
- [22] J.-Y. Wang, H.-X. Zhang, K. Jiang, W.-B. Cai, From HCOOH to CO at Pd Electrodes: A Surface-Enhanced Infrared Spectroscopy Study, *J. Am. Chem. Soc.* 133 (2011) 14876–14879.
- [23] T. Takamura, F. Mochimaru, Adsorption and oxidation of formate on palladium in alkaline solution 14 (1969) 111–119.
- [24] Q. Wang, F. Chen, L. Guo, T. Jin, H. Liu, X. Wang, X. Gong, Y. Liu, Nanoalloying effects on the catalytic activity of the formate oxidation reaction over AgPd and AgCuPd aerogels, *J. Mater. Chem. A* 7 (27) (2019) 16122–16135.
- [25] M. Choun, S. Hong, J. Lee, Adsorbed Hydrogen as a Site-Occupying Species in the Electrocatalytic Oxidation of Formate on Pd/C in Alkaline Medium, *J. Electrochem. Soc.* 165 (2018) J3266–J3270.
- [26] Y.I. Zhou, J. Liu, J. Ye, Z. Zou, J. Ye, J. Gu, T. Yu, A. Yang, Poisoning and regeneration of Pd catalyst in direct formic acid fuel cell, *Electrochim. Acta* 55 (17) (2010) 5024–5027.
- [27] Q. Tang, F. Chen, Q. Wang, T. Jin, L. Guo, Y. Wu, S. Yu, Z. Li, Surface reconstruction of AgPdF and AgPd nanoalloys under the formate oxidation reaction, *J. Mater. Chem. A* 9 (40) (2021) 23072–23084.
- [28] L. Guo, F. Chen, T. Jin, H. Liu, N. Zhang, Y. Jin, Q. Wang, Q. Tang, B. Pan, Surface reconstruction of AgPd nanoalloy particles during the electrocatalytic formate oxidation reaction, *Nanoscale* 12 (5) (2020) 3469–3481.
- [29] J. Wang, C. Liu, A. Lushington, N. Cheng, M.N. Banks, A. Riese, X. Sun, Pd on carbon nanotubes-supported Ag for formate oxidation: The effect of Ag on anti-poisoning performance, *Electrochim. Acta* 210 (2016) 285–292.

- [30] J. Bai, Q.-i. Xue, Y. Zhao, J.-X. Jiang, J.-H. Zeng, S.-B. Yin, Y.u. Chen, Component-Dependent Electrocatalytic Activity of Ultrathin PdRh Alloy Nanocrystals for the Formate Oxidation Reaction, *ACS Sustain. Chem. Eng.* 7 (2) (2019) 2830–2836.
- [31] S.G. da Silva, J.C.M. Silva, G.S. Buzzo, E.V. Spinacé, A.O. Neto, M.H.M.T. Assumpção, PdAu/C Electrocatalysts as Anodes for Direct Formate Fuel Cell, *Electrocatalysis* 6 (5) (2015) 442–446.
- [32] Y. Li, Y. He, W. Yang, A high-performance direct formate-peroxide fuel cell with palladium-gold alloy coated foam electrodes, *J. Power Sources* 278 (2015) 569–573.
- [33] Y. Jin, F. Chen, T. Jin, L. Guo, J. Wang, Mesoporous PdAgIr nanoalloys to catalyze formate oxidation with an unprecedentedly low onset potential, *J. Mater. Chem. A* 8 (48) (2020) 25780–25790.
- [34] T.T. Gebremariam, F. Chen, B. Kou, L. Guo, B. Pan, Q. Wang, Z. Li, W. Bian, PdAgRu nanoparticles on polybenzimidazole wrapped CNTs for electrocatalytic formate oxidation, *Electrochim. Acta* 354 (2020) 136678.
- [35] Y. Jin, Y. Jin, F. Chen, F. Chen, L. Guo, L. Guo, J. Wang, J. Wang, B. Kou, B. Kou, T. Jin, T. Jin, H. Liu, H. Liu, Engineering Two-Dimensional PdAgRh Nanoalloys by Surface Reconstruction for Highly Active and Stable Formate Oxidation Electrocatalysis, *ACS Appl. Mater. Interfaces* 12 (2020) 26694–26703.
- [36] B. Pan, F. Chen, B. Kou, J. Wang, Q. Tang, L. Guo, Q. Wang, Z. Li, W. Bian, J. Wang, Unexpectedly high stability and surface reconstruction of PdAuAg nanoparticles for formate oxidation electrocatalysis, *Nanoscale* 12 (21) (2020) 11659–11671.
- [37] L. Chen, L. Lu, H. Zhu, Y. Chen, Y. Huang, Y. Li, L. Wang, Improved ethanol electrooxidation performance by shortening Pd-Ni active site distance in Pd-Ni-P nanocatalysts, *Nat. Commun.* 8 (2017) 1–9.
- [38] S. Sankar, G.M. Anilkumar, T. Tamaki, T. Yamaguchi, Cobalt-Modified Palladium Bimetallic Catalyst: A Multifunctional Electrocatalyst with Enhanced Efficiency and Stability toward the Oxidation of Ethanol and Formate in Alkaline Medium, *ACS Appl. Energy Mater.* 1 (2018) 4140–4149.
- [39] J. Noborikawa, J. Lau, J. Ta, S. Hu, L. Scudiero, S. Derakhshan, S. Ha, J.L. Haan, Palladium-copper electrocatalyst for promotion of oxidation of formate and ethanol in alkaline media, *Electrochim. Acta* 137 (2014) 654–660.
- [40] S. Sankar, G.M. Anilkumar, T. Tamaki, T. Yamaguchi, Binary Pd–Ni Nanoalloy Particles over Carbon Support with Superior Alkaline Formate Fuel Electrooxidation Performance, *ChemCatChem* 11 (19) (2019) 4731–4737.
- [41] A.N. Geraldes, D. Furtunato Da Silva, J.C. Martins Da Silva, O. Antonio De Sá, E.V. Spinacé, A.O. Neto, M. Coelho Dos Santos, Palladium and palladium-tin supported on multi wall carbon nanotubes or carbon for alkaline direct ethanol fuel cell, *J. Power Sources* 275 (2015) 189–199.
- [42] L.X. Ding, A.L. Wang, Y.N. Ou, Q. Li, R. Guo, W.X. Zhao, Y.X. Tong, G.R. Li, Hierarchical Pd-Sn alloy nanosheet dendrites: An economical and highly active catalyst for ethanol electrooxidation, *Sci. Rep.* 3 (2013) 1–7.
- [43] W. Du, K.E. Mackenzie, D.F. Milano, N.A. Deskins, D. Su, X. Teng, Palladium-tin alloyed catalysts for the ethanol oxidation reaction in an alkaline medium, *ACS Catal.* 2 (2) (2012) 287–297.
- [44] C. Wang, Y. Wu, X. Wang, L. Zou, Z. Zou, H. Yang, Low temperature and surfactant-free synthesis of Pd₂Sn intermetallic nanoparticles for ethanol electro-oxidation, *Electrochim. Acta* 220 (2016) 628–634.
- [45] R. Sarawathy, R. Suman, P. Malin Bruntha, D. Khanna, V. Chelmsamy, Mn-doped nickel titanate (Ni_{1-x}Mn_xTiO₂) as a promising support material for PdSn electrocatalysts for methanol oxidation in alkaline media, *RSC Adv.* 11 (46) (2021) 28829–28837.
- [46] H. You, F. Gao, C. Wang, J. Li, K. Zhang, Y. Zhang, Y. Du, Rich grain boundaries endow networked PdSn nanowires with superior catalytic properties for alcohol oxidation, *Nanoscale* 13 (42) (2021) 17939–17944.
- [47] J. Liang, S. Li, Y. Chen, X. Liu, T. Wang, J. Han, S. Jiao, R. Gao, Q. Li, Ultrathin and defect-rich intermetallic Pd₂Sn nanosheets for efficient oxygen reduction electrocatalysis, *J. Mater. Chem. A* 8 (31) (2020) 15665–15669.
- [48] Z. Luo, J. Lu, C. Flor, R. Nafria, A. Genç, J. Arbiol, J. Llorca, M. Ibañeta, J.R. Morante, A. Cabot, Pd₂Sn [010] nanorods as a highly active and stable ethanol oxidation catalyst, *J. Mater. Chem. A* 4 (42) (2016) 16706–16713.
- [49] Dandan Tu, B. Wu, B. Wang, C. Deng, Y. Gao, Gao, A highly active carbon-supported PdSn catalyst for formic acid electrooxidation, *Appl. Catal. B Environ.* 103 (1–2) (2011) 163–168.
- [50] D. Chen, S. Pei, Z. He, H. Shao, J. Wang, K. Wang, Y. Wang, Y. Jin, High active PdSn binary alloyed catalysts supported on B and N codoped graphene for formic acid electro-oxidation, *Catalysts* 10 (7) (2020) 751.
- [51] Z. Liu, X. Zhang, Carbon-supported PdSn nanoparticles as catalysts for formic acid oxidation, *Electrochem. Commun.* 11 (8) (2009) 1667–1670.
- [52] R.-X. Wang, Y.-J. Pan, Z.-R. Liang, J.-M. Zhang, Z.-Y. Zhou, S.-G. Sun, PdSn nanocatalysts supported on carbon nanotubes synthesized in deep eutectic solvents with high activity for formic acid electrooxidation, *RSC Adv.* 6 (65) (2016) 60400–60406.
- [53] E. Hwang, H. Kim, H. Park, T. Lim, Y.-T. Kim, S.H. Ahn, S.-K. Kim, Pd–Sn alloy electrocatalysts for interconversion between carbon dioxide and formate/formic acid, *J. Nanosci. Nanotechnol.* 17 (10) (2017) 7547–7555.
- [54] S. Sasidharan, A.A. Sasikala Devi, R. Jose, T. Tamaki, A.M. Gopinathan, T. Yamaguchi, Alkaline Formate Oxidation with Colloidal Palladium-Tin Alloy Nanocrystals, *ACS Appl. Energy Mater.* 5 (1) (2022) 266–277.
- [55] P. Hosseini-Benhangi, C.C. Gyenge, E.L. Gyenge, The carbon dioxide redox flow battery: Bifunctional CO₂ reduction/formate oxidation electrocatalysis on binary and ternary catalysts, *J. Power Sources* 495 (2021) 229752.
- [56] J. Duan, Z. Xiang, H. Zhang, B. Zhang, X. Xiang, Pd-Co₂P nanoparticles supported on N-doped biomass-based carbon microsheet with excellent catalytic performance for hydrogen evolution from formic acid, *Appl. Surf. Sci.* 530 (2020) 147191.
- [57] Z. Yu, X.-K. Wei, J. Xu, Y. Li, A. Araujo, J.L. Faria, R.E. Dunin-Borkowski, L. Liu, Multifunctional Noble Metal Phosphide Electrocatalysts for Organic Molecule Electro-Oxidation, *ACS Appl. Energy Mater.* 4 (2) (2021) 1593–1600.
- [58] L. Peng, J. Chang, K. Jiang, H. Xue, C. Liu, W. Bin Cai, W. Xing, J. Zhang, Nanostructured palladium catalyst poisoning depressed by cobalt phosphide in the electro-oxidation of formic acid for fuel cells, *Nano Energy* 30 (2016) 355–361.
- [59] Y. Bao, H. Liu, Z. Liu, F. Wang, L. Peng, Pd/FeP catalyst engineering via thermal annealing for improved formic acid electrochemical oxidation, *Appl. Catal. B Environ.* 274 (2020) 119106.
- [60] T.-J. Wang, Y.-C. Jiang, J.-W. He, F.-M. Li, Y.u. Ding, P. Chen, Y.u. Chen, Porous palladium phosphide nanotubes for formic acid electrooxidation, *Carbon Energy* 4 (3) (2022) 283–293.
- [61] K.C. Poon, B. Khezri, Y. Li, R.D. Webster, H. Su, H. Sato, A highly active Pd-P nanoparticle electrocatalyst for enhanced formic acid oxidation synthesized via stepwise electrodeless deposition, *Chem. Commun.* 52 (17) (2016) 3556–3559.
- [62] Z. Yu, J. Xu, I. Amorim, Y. Li, L. Liu, Easy preparation of multifunctional ternary PdNiP/C catalysts toward enhanced small organic molecule electro-oxidation and hydrogen evolution reactions, *J. Energy Chem.* 58 (2021) 256–263.
- [63] J. Chang, L. Peng, C. Liu, W. Xing, X. Hu, An effective Pd-Ni₂P/C anode catalyst for direct formic acid fuel cells, *Angew. Chemie - Int. Ed.* 53 (1) (2014) 122–126.
- [64] S. Wang, J. Chang, H. Xue, W. Xing, L. Peng, Catalytic Stability Study of a Pd-Ni₂P/C Catalyst for Formic Acid Electrooxidation, *ChemElectroChem* 4 (5) (2017) 1243–1249.
- [65] X. Liang, B.o. Liu, J. Zhang, S. Lu, Z. Zhuang, Ternary Pd-Ni-P hybrid electrocatalysts derived from Pd-Ni core-shell nanoparticles with enhanced formic acid oxidation activity, *Chem. Commun.* 52 (74) (2016) 11143–11146.
- [66] X. Yu, J. Liu, J. Li, Z. Luo, Y. Zuo, C. Xing, J. Llorca, D. Nasou, J. Arbiol, K. Pan, T. Kleinhans, Y. Xie, A. Cabot, Phosphorous incorporation in Pd₂Sn alloys for electrocatalytic ethanol oxidation, *Nano Energy* 77 (2020) 105116.
- [67] D. Yang, Z. Liang, P. Tang, C. Zhang, M. Tang, Q. Li, J.J. Blendscho, J. Li, M. Heggen, R.E. Dunin-Borkowski, M. Xu, J. Llorca, J. Arbiol, J.R. Morante, S.L. Chou, A. Cabot, A High Conductivity 1D s-d Conjugated Metal-Organic Framework with Efficient Polysulfide Trapping-Diffusion-Catalysis in Lithium-Sulfur Batteries, *Adv. Mater.* 34 (2022) 1–11.
- [68] C. Zhang, B. Fei, D. Yang, H. Zhan, J. Wang, J. Diao, J. Li, G. Henkelman, D. Cai, J. J. Blendscho, J.R. Morante, A. Cabot, Robust Lithium-Sulfur Batteries Enabled by Highly Conductive WS₂-Based Superlattices with Tunable Interlayer Space, *Adv. Funct. Mater.* 32 (24) (2022) 2201322.
- [69] M. Li, D. Yang, J.J. Blendscho, X.u. Han, C. Zhang, K. Liu, J. Diao, J. Li, J. Wang, M. Heggen, R.E. Dunin-Borkowski, J. Wang, G. Henkelman, J.R. Morante, J. Arbiol, S.-L. Chou, A. Cabot, Enhanced Polysulfide Conversion with Highly Conductive and Electrocatalytic Iodine-Doped Bismuth Selenide Nanosheets in Lithium-Sulfur Batteries, *Adv. Funct. Mater.* 32 (26) (2022) 2200529.
- [70] X. Wang, X. Han, R. Du, Z. Liang, Y. Zuo, P. Guardia, J. Li, J. Llorca, J. Arbiol, R. Zheng, A. Cabot, Unveiling the role of counter-anions in amorphous transition metal-based oxygen evolution electrocatalysts, *Appl. Catal. B Environ.* 320 (2023) 121988.
- [71] R. Du, K. Xiao, B. Li, X. Han, C. Zhang, X. Wang, Y. Zuo, P. Guardia, J. Li, J. Chen, J. Arbiol, A. Cabot, Controlled oxygen doping in highly dispersed Ni-loaded g-C₃N₄ nanotubes for efficient photocatalytic H₂O₂ production, *Chem. Eng. J.* 441 (2022) 135999.
- [72] X. Wang, X.u. Han, R. Du, C. Xing, X. Qi, Z. Liang, P. Guardia, J. Arbiol, A. Cabot, J. Li, Cobalt Molybdenum Nitride-Based Nanosheets for Seawater Splitting, *ACS Appl. Mater. Interfaces* 14 (37) (2022) 41924–41933.
- [73] D. Yang, M. Li, X. Zheng, X.u. Han, C. Zhang, J. Jacs Blendscho, J. Llorca, J. Wang, H. Hao, J. Li, G. Henkelman, J. Arbiol, J.R. Morante, D. Mitin, S. Chou, A. Cabot, Phase Engineering of Defective Copper Selenide toward Robust Lithium-Sulfur Batteries, *ACS Nano* 16 (7) (2022) 11102–11114.
- [74] X. Wang, J. Li, Q. Xue, X.u. Han, C. Xing, Z. Liang, P. Guardia, Y. Zuo, R. Du, L. Balcells, J. Arbiol, J. Llorca, X. Qi, A. Cabot, Sulfate-Decorated Amorphous-Crystalline Cobalt-Iron Oxide Nanosheets to Enhance O-O Coupling in the Oxygen Evolution Reaction, *ACS Nano* 17 (1) (2023) 825–836.
- [75] Y. Zhou, Q. Wang, X. Tian, J. Chang, L. Peng, Electron-enriched Pt induced by CoSe₂ promoted bifunctional catalytic ability for low carbon alcohol fuel electro-reforming of hydrogen evolution, *J. Energy Chem.* 75 (2022) 46–54.
- [76] Y. Zhou, Y. Kuang, G. Hu, X. Wang, L. Peng, An effective Pt-Co/Te/NC catalyst of bifunctional methanol electrolysis for hydrogen generation, *Mater. Today Phys.* 27 (2022).

Accepted Article

Title: Oxophilic Sn to promote glucose oxidation to formic acid in Ni nanoparticles

Authors: Guillem Montaña Mora, Karol V. Mejia-Centeno, Xueqiang Qi, Qian Xue, Jesus Chacón-Borrero, Francesco Salutari, Maria Chiara Spadaro, Teresa Andreu, Germán Salazar-Alvarez, Frank Güell, Jordi Llorca, Jordi Arbiol, Paulina R. Martinez-Alanis, and Andreu Cabot

This manuscript has been accepted after peer review and appears as an Accepted Article online prior to editing, proofing, and formal publication of the final Version of Record (VoR). The VoR will be published online in Early View as soon as possible and may be different to this Accepted Article as a result of editing. Readers should obtain the VoR from the journal website shown below when it is published to ensure accuracy of information. The authors are responsible for the content of this Accepted Article.

To be cited as: *ChemSusChem* **2024**, e202401256

Link to VoR: <https://doi.org/10.1002/cssc.202401256>

